Université de Liège
Faculté des Sciences

Ejections de matière par les astres : des étoiles massives aux quasars



par

Damien HUTSEMEKERS

Docteur en Sciences
Chercheur Qualifié du FNRS

Dissertation présentée en vue de l'obtention
du grade d'Agrégé de l'Enseignement Supérieur

2003

Illustration de couverture : la nébuleuse du Crabe, constituée de gaz éjecté à grande vitesse par l'explosion d'une étoile en supernova. Cliché obtenu avec le VLT et FORS2, ESO, 1999.

Table des matières

Préface et remerciements **5**

Introduction **7**

Articles **21**

I Les nébuleuses éjectées par les étoiles massives **23**

1 HR Carinae : a Luminous Blue Variable surrounded by an arc-shaped nebula **25**

2 The nature of the nebula associated with the Luminous Blue Variable star WRA751 **37**

3 A dusty nebula around the Luminous Blue Variable candidate HD168625 **45**

4 Evidence for violent ejection of nebulae from massive stars **57**

5 Dust in LBV-type nebulae **63**

II Quasars de type BAL et microlentilles gravitationnelles **73**

6 The use of gravitational microlensing to scan the structure of BAL QSOs **75**

7 ESO & NOT photometric monitoring of the Cloverleaf quasar **89**

8 Selective gravitational microlensing and line profile variations in the BAL quasar H1413+117 **99**

9 An optical time-delay for the lensed BAL quasar HE2149-2745 **113**

III Quasars de type BAL : polarisation 127

10 A procedure for deriving accurate linear polarimetric measurements 129

11 Optical polarization of 47 quasi-stellar objects : the data 137

12 Polarization properties of a sample of Broad Absorption Line and gravitationally lensed quasars 145

13 The optical polarization of radio-loud and radio-intermediate Broad Absorption Line quasi-stellar objects 157

14 The polarization properties of Broad Absorption Line QSOs : observational results 165

15 Spectropolarimetry of the iron low-ionization Broad Absorption Line quasar Q0059-2735 177

IV Orientation à grande échelle de la polarisation des quasars 185

16 Evidence for very large-scale coherent orientations of quasar polarization vectors 187

17 Confirmation of the existence of coherent orientations of quasar polarization vectors on cosmological scales 209

Préface et remerciements

Dans cet ouvrage, nous présentons une sélection de travaux de recherches effectués essentiellement durant la dernière décennie et traitant des éjections de matière par les étoiles massives et les quasars.

Après une courte introduction décrivant nos principaux résultats et le contexte dans lequel ils s'inscrivent, nous regroupons en quatre parties nos articles originaux précédés chacun d'un bref résumé. Des mises à jour, non encore publiées, complètent certains articles.

Je tiens à exprimer ma reconnaissance à tous les collègues et amis de l'Institut d'Astrophysique et de l'Observatoire Européen Austral qui, par des collaborations ou des discussions toujours fructueuses, ont partagé mon intérêt pour les questions traitées dans cette dissertation. Ma plus profonde gratitude va également à tous ceux dont l'enthousiasme et les continuels encouragements m'ont permis de progresser dans la profession d'astrophysicien et de l'exercer dans les sites extraordinaires du Chili.

Mes remerciements vont au Fonds National de la Recherche Scientifique, à l'Observatoire Européen Austral, à l'Université de Liège, à la Communauté française de Belgique et aux Services fédéraux des affaires Scientifiques, Techniques et Culturelles, sans le soutien financier desquels les travaux présentés dans cet ouvrage n'auraient probablement pas vu le jour.

Je remercie également Jean Surdej et Jean-Pierre Swings pour avoir relu et commenté le texte de cette dissertation.

Enfin, j'aimerais remercier plus particulièrement mon épouse Véronique pour son soutien dans cette aventure que constitue le métier d'astronome.

Introduction

Etoiles, galaxies, quasars, la plupart des astres éjectent à un moment donné de leur existence une partie de la matière qui les constitue. Ce phénomène fondamental exerce une influence tant sur l'évolution des astres qui en sont le siège que sur le milieu où ils se trouvent, contribuant à l'évolution de l'Univers tout entier.

Bien que relativement peu nombreuses, les étoiles massives, extrêmement lumineuses, sont à l'origine de flux énergétiques importants, tant radiatifs que mécaniques [1]. Leur impact sur le milieu ambiant est considérable. Les étoiles massives et la matière qu'elles éjectent modifient les conditions physiques et dynamiques du milieu interstellaire, provoquant entre autres la formation de nouvelles étoiles. Par l'intermédiaire de leurs vents stellaires, de l'éjection de nébuleuses ou encore de l'explosion en supernovae, elles constituent la source principale d'enrichissement du milieu environnant en éléments lourds, résidus des réactions nucléaires qui se déroulent en leur sein. Les étoiles massives contribuent de façon essentielle à l'évolution chimique et dynamique des galaxies.

Dans certaines situations, un grand nombre d'étoiles massives peut se former en un laps de temps relativement court. Ensemble, elles dominent le rayonnement émis par la galaxie hôte. On parle alors d'une flambée d'étoiles ("starburst"). L'évolution rapide et collective de ces étoiles massives est à l'origine de super-vents galactiques riches en poussières et susceptibles de contaminer le milieu intergalactique [2]. Ces flambées d'étoiles massives sont couramment observées dans les galaxies les plus lointaines connues à l'heure actuelle et leurs vents pourraient constituer la signature des toutes premières générations d'étoiles dans les galaxies primordiales.

D'autre part, certaines galaxies peuvent devenir "actives", libérant de l'énergie gravitationnelle par accrétion de matière sur un objet central extrêmement massif [3]. L'énergie libérée par ce mécanisme fait de ces objets –noyaux actifs de galaxies et quasars– les objets les plus lumineux de notre Univers. Ces processus s'accompagnent également d'éjections de matière, soit sous forme de spectaculaires jets radio, ou encore sous forme de vents hautement ionisés dans le cas des quasars de type BAL (Broad Absorption Line) [4].

Si l'importance relative de ces deux phénomènes –flambée d'étoiles massives et activité du noyau galactique– est encore loin d'être claire notamment dans les premières phases de l'Univers (qui, des quasars ou des étoiles massives, a émis la première lumière ? [5]), il est certain que dans bon nombre de galaxies, ils peuvent coexister, rivalisant d'importance [6–8]. C'est notamment le cas des galaxies en interaction où les forces de marée, amenant gaz et poussières dans le noyau galactique, peuvent déclencher si-

multanément flambée d'étoiles et activité [9]. Ces deux phénomènes peuvent aussi se succéder, définissant peut-être une séquence évolutive "Starburst $\rightarrow$ Quasar BAL", ces derniers expulsant et détruisant le cocon de poussières laissé par les étoiles [10–12]. Etoiles massives et quasars sont donc intimement liés depuis l'aube de l'Univers.

Dans cet ouvrage, nous présentons quelques contributions à l'étude des éjections de matière par les étoiles massives et les quasars. Dans la première partie, nous rapportons les résultats d'une recherche et d'une étude systématiques des nébuleuses éjectées par les étoiles massives et plus particulièrement par les étoiles de type LBV (Luminous Blue Variable) et WR (Wolf-Rayet). Nous nous intéressons ensuite aux quasars de type BAL, dont les raies en absorption décalées vers le bleu révèlent des éjections de matière à des vitesses atteignant 20% de la vitesse de la lumière. Deux aspects sont traités : l'étude des profils de raies et plus particulièrement de leurs variations suite à des effets de microlentille gravitationnelle, et l'étude de leur polarisation. Dans la dernière partie nous discutons un résultat inattendu : la découverte d'une orientation à grande échelle de la polarisation des quasars.

Les nébuleuses éjectées par les étoiles massives

Les étoiles de type LBV sont des supergéantes évoluées extrêmement lumineuses. Elles sont caractérisées par des taux de perte de masse élevés ($\sim 5\ 10^{-5}$ $M_\odot$ an^{-1}) ainsi que par des variations photométriques et spectrales importantes et irrégulières (éruptions). Bien que très peu nombreuses (une dizaine connues dans notre Galaxie), les LBVs constituent une étape brève mais essentielle dans l'évolution des étoiles massives, entre les étoiles de type O et les Wolf-Rayet [13,14]. Les étoiles très lumineuses dont les caractéristiques physiques sont semblables à celles des LBVs mais pour lesquelles il n'y a pas d'éruption répertoriée sont considérées comme des candidates LBV[1].

Un des aspects les plus intéressants des LBVs est que certaines d'entre elles sont associées à une nébuleuse dont l'étude détaillée peut donner des indications précieuses sur l'historique des éjections de matière liées aux différentes phases de l'évolution stellaire. Parmi les LBVs galactiques, η Carinae et AG Carinae sont depuis longtemps connues pour être entourées d'une nébuleuse en expansion dont la morphologie rappelle celle des nébuleuses planétaires, tout en étant plus grandes et plus massives [15]. Plusieurs LBVs du Grand Nuage de Magellan sont également connues pour posséder des enveloppes circumstellaires détectées spectroscopiquement [16,17]. Une question vient immédiatement à l'esprit : est-on en présence d'une nouvelle classe de nébuleuses, caractéristique des étoiles massives et plus particulièrement des LBVs, ou s'agit-il d'objets particuliers voire exotiques ?

Afin de répondre à cette question, nous avons effectué une recherche et une étude systématiques de telles nébuleuses autour des LBVs et candidates LBV connues dans notre Galaxie. Contrairement aux nébuleuses planétaires dont l'étoile centrale est très

[1]Notons que la présence d'une nébuleuse circumstellaire en expansion et enrichie en produits de nucléosynthèse indique presque certainement une éruption passée

faible, l'extrême brillance des LBVs rend difficile la détection de faibles nébulosités dans leur voisinage. Bénéficiant de la qualité croissante des détecteurs CCD et des filtres à bande étroite disponibles à l'Observatoire Européen Austral (ESO, La Silla), nous avons obtenu des images de ces étoiles dans des filtres interférentiels centrés sur les raies d'émission nébulaire et sur le continuum adjacent. La différence des images obtenues dans ces deux types de filtres isole la nébuleuse en émission. Afin de diminuer la lumière "parasite" de l'étoile, certaines observations ont également été effectuées avec le coronographe intégré au spectro-imageur EFOSC du télescope de 3,6m de l'ESO. Grâce à cette technique, trois nouvelles nébuleuses ont pu être résolues autour des étoiles HR Carinae, WRA 751 et HD 168625. Leur morphologie et leur cinématique indiquent clairement leur association physique avec l'étoile centrale. Parmi les neuf LBVs et candidates LBV connues dans notre Galaxie jusqu'alors, six apparaissent donc associées à une nébuleuse[2], indiquant qu'il s'agit là d'une caractéristique essentielle de cette phase de l'évolution des étoiles massives. Ces observations sont décrites dans les articles 1, 2 et 3.

Complétant l'imagerie par des données spectroscopiques, nous avons pu déterminer les caractéristiques physiques fondamentales de ces nébuleuses et obtenir une estimation de la distance cinématique des étoiles centrales, confirmant leur grande luminosité et leur classification comme LBVs. En bon accord avec les nébuleuses de type LBV connues antérieurement, ces nébuleuses sont de faible excitation, ont une dimension de l'ordre de 1 parsec, une masse de gaz ionisé d'environ 1 masse solaire et une vitesse d'expansion voisine de 50 km s^{-1} correspondant à un âge cinématique typique de 10^4 ans. L'analyse spectroscopique révèle des anomalies d'abondances (surabondance de l'azote par rapport à l'oxygène) indiquant que ces nébuleuses sont constituées de produits de nucléosynthèse éjectés par l'étoile centrale quelques milliers d'années auparavant.

Ces caractéristiques font des nébuleuses associées aux LBVs une classe d'objets relativement homogène et différente des nébuleuses planétaires éjectées par les étoiles de faible masse. Elles sont comparables aux nébuleuses éjectées par les étoiles Wolf-Rayet de type spectral WN8[3]. Ceci est en bon accord avec l'idée que la phase LBV précède la phase Wolf-Rayet dans le schéma évolutif des étoiles très massives.

Une question importante est bien sûr comment et à quel moment se sont formées ces nébuleuses ? Sur base de nos observations, nous avons tenté de dégager quelques propriétés systématiques permettant d'apporter des éléments de réponse à ces questions. Nous avons ainsi mis en évidence une relation très claire entre la masse de la nébuleuse et la luminosité de l'étoile centrale (Article 4). La simple existence d'une telle relation suggère que ces nébuleuses ont été éjectées lors d'un événement violent et unique (consistant éventuellement en une série d'éruptions très rapprochées dans le temps). Cette relation est surtout basée sur la mesure de la masse de la poussière se trouvant dans ces nébu-

[2]En ne comptant pas P Cygni qui est associée à une nébulosité vraisemblablement d'un autre type ; voir les discussions dans les articles 2, 4, 5 et aussi [18]. Des nébuleuses ont également pu être résolues autour de quelques LBVs du Grand Nuage de Magellan, mais de façon incomplète vu leur grande distance.

[3]Il existe plusieurs types de nébuleuses associées aux Wolf-Rayet [19]. Celles qui nous intéressent ici sont constituées de matériaux éjectés par l'étoile et non encore contaminés par leur interaction avec le milieu interstellaire [20].

leuses (la masse de gaz ionisé, bien qu'en bon accord qualitatif, est plus incertaine). En effet, toutes les nébuleuses associées à des LBVs galactiques contiennent de la poussière froide ($\sim$ 100 K) rayonnant dans l'infra-rouge lointain et détectée par le satellite IRAS. Il est important de noter que si la valeur de la masse de la poussière dans une nébuleuse varie en fonction des caractéristiques des grains (dimension, composition chimique), les valeurs relatives d'une nébuleuse à l'autre n'en dépendent pas moyennant l'hypothèse raisonnable que toutes les nébuleuses de type LBV contiennent le même type de grains (Article 5). De plus, cette relation dépend peu de la distance des objets, qui n'est généralement pas déterminée avec grande précision.

Initialement établie pour les LBVs galactiques, cette relation se généralise aux LBVs du Grand Nuage de Magellan suffisamment brillantes dans l'infra-rouge lointain pour être détectées à cette distance et aux étoiles de type WN8 ayant éjecté une nébuleuse, montrant qu'il s'agit clairement du même type d'objet (Article 5). Depuis lors, quelques nouvelles candidates LBVs ont été découvertes dans notre Galaxie notamment sur base de recherches systématiques dans l'infra-rouge proche, celles-ci permettant d'identifier des étoiles très lointaines et obscurcies dans la lumière visible par l'absorption interstellaire. Tous les nouveaux objets confirmés comme candidats LBV et entourés d'une nébuleuse ont des caractéristiques en excellent accord avec la relation trouvée précédemment (cf. la mise à jour suivant l'article 5).

Cette relation "masse nébulaire - luminosité stellaire" apparaît donc comme une propriété importante des nébuleuses éjectées par les étoiles de type LBV et Wolf-Rayet. Elle apporte non seulement des contraintes sur les modèles d'évolution et de stabilité des étoiles massives [20–22], mais aussi un moyen d'évaluer la production totale de poussières par les étoiles très massives qui sont formées en grand nombre lors des flambées stellaires au sein des galaxies et des quasars.

Malgré les nombreux progrès observationnels et théoriques, les raisons physiques et le moment exact de l'éjection d'une nébuleuse par ces étoiles sont encore mal connus [23]. Il importe entre autres de comprendre pourquoi certaines LBVs n'ont pas éjecté de nébuleuse. C'est notamment le cas de P Cygni qui ne possède pas de nébuleuse comparable à celles des autres LBVs, ainsi que le cas de HD 160529 et HD 168607 pour lesquelles nous avons obtenu des images dans les mêmes conditions mais ne révélant aucune nébulosité associée (Articles 3 et 4). Une solution à cette énigme pourrait venir de l'analyse des abondances de surface de ces étoiles. En comparant par exemple P Cygni à AG Carinae et HR Carinae, nous avons noté l'état moins avancé des produits de nucléosynthèse (le rapport N/O surtout) à la surface de P Cygni (Article 2). Cela pourrait indiquer que P Cygni est dans un stade évolutif légèrement antérieur, n'ayant pas encore éjecté de nébuleuse. Une autre alternative pourrait être une plus faible rotation de P Cygni[4], réduisant le mélange des produits de nucléosynthèse et ne favorisant pas l'éjection d'une nébuleuse. La mesure de la vitesse de rotation de ces étoiles est une donnée importante qui devrait pouvoir être obtenue dans un futur proche notamment en résolvant directement le vent stellaire grâce à l'interférométrie [25].

[4]La vitesse de rotation de P Cygni est estimée à 40–50 km s^{-1} [24], ce qui n'est pas particulièrement élevé comparé à certaines étoiles massives de la séquence principale

Les quasars de type BAL

Le spectre d'un quasar normal est dominé par un continu non-thermique et des raies en émission larges. Les quasars de type BAL (quasars BAL en abrégé) montrent en sus de larges raies en absorption (Broad Absorption Lines) apparaissant à des longueurs d'onde plus courtes que les raies en émission (voir des exemples dans les articles 8 et 9). Ce décalage vers le bleu des raies en absorption révèle la présence d'éjections de matière à des vitesses élevées. Dans certains cas, émission et absorption sont contigües et forment un profil dit de type P Cygni, assez comparable à ceux que l'on observe dans les étoiles massives sujettes à des pertes de masse, sinon qu'ils indiquent des vitesses d'éjection 10 fois plus grandes ($\sim 0{,}1c$) et des taux de perte de masse 10^5 fois plus élevés (~ 1 $M_\odot$ an^{-1}). Environ un quasar sur dix est un quasar BAL [26].

De telles éjections de matière conduisent évidemment à se poser de multiples questions. Quelles sont leur origine et leur évolution ? Pourquoi seuls certains quasars en sont-ils le siège ? Quel lien y a-t-il avec les vents galactiques et les flambées d'étoiles ? Dans quelle mesure ces éjections contaminent-elles le milieu intergalactique ?

Malgré de nombreuses études, la nature de ce phénomène reste énigmatique. L'interprétation des données est particulièrement complexe car, contrairement aux étoiles qui peuvent être considérées comme sphériques en première approximation, on ignore la géométrie des quasars BAL (et des quasars en général), ceux-ci n'ayant jamais été résolus vu les grandes distances auxquelles ils se trouvent. Ainsi, si la région à l'origine des raies en absorption n'est pas sphérique mais ressemble plutôt à un disque ou un tore, on peut supposer que tous les quasars sont entourés de matière en expansion et que seuls les quasars dont le disque est sur la ligne de visée sont reconnus comme des quasars BAL [27]. C'est le modèle d'unification par orientation (couramment utilisé et assez bien justifié dans certains cas comme l'unification des galaxies actives de Seyfert [28]). D'un autre coté, on peut penser que la matière à l'origine des raies en absorption possède une symétrie quasi-sphérique et que les quasars BAL sont des quasars jeunes émergeant de leurs cocons de gaz et de poussière, évoluant vers les quasars "normaux" [9,11]. Cette incertitude sur la géométrie fait en sorte que la modélisation détaillée des raies spectrales apporte peu à la compréhension du phénomène BAL, les profils calculés dépendant fortement des hypothèses introduites au départ[5].

S'il est bien bien sûr très important d'accumuler un maximum de données sur ces quasars afin d'en obtenir une vision panchromatique[6], le problème le plus critique est de pouvoir fixer leur géométrie. Dans la suite de cette dissertation nous présentons quelques travaux dont l'intérêt tout particulier est d'apporter des informations –bien qu'indirectes– sur la géométrie et l'orientation des quasars BAL.

[5]Un exemple est l'interprétation de la différence entre les largeurs équivalentes des raies en émission et en absorption, généralement attribuée à une symétrie non sphérique [29]. Pourtant, en considérant d'autres ingrédients physiques comme la macro-turbulence [30] ou le simple fait de tenir compte des corrections relativistes [31], on peut reproduire, au moins qualitativement, les différences observées.

[6]Comme par exemple la spectroscopie infra-rouge ou encore la spectroscopie à haute-résolution. De telles observations donnent des informations sur les conditions physiques règnant dans la région de formation des raies, voire parfois sur la distance entre cette région et le noyau central [32,33].

Ainsi, nous discutons l'utilisation de l'effet de microlentille gravitationnelle pour "zoomer" les régions internes du quasar. Ensuite, nous étudions leur polarisation optique. Celle-ci, révélatrice des écarts à la symétrie sphérique, offre l'équivalent de multiples lignes de visée.

• Profils de raies et effets de microlentille gravitationnelle

Lorsqu'une galaxie se trouve sur la ligne de visée d'un quasar lointain, son potentiel gravitationnel dévie les rayons lumineux en provenance du quasar. Plusieurs images du même objet peuvent être observées, séparées de quelques secondes d'arc et largement amplifiées. C'est l'effet de lentille gravitationnelle [34]. En plus de cet effet global dû à la galaxie-lentille, des étoiles de cette galaxie peuvent agir individuellement. On parle alors de microlentilles gravitationnelles [35]. La masse d'une étoile étant beaucoup plus faible que celle de la galaxie, les micro-images produites ne peuvent être résolues mais une nette amplification d'une des macro-images peut être observée. La section efficace (rayon d'Einstein) projetée d'une telle microlentille étant voisine de la dimension communément admise pour la source du rayonnement continu du quasar, on s'attend à une amplification significative du continuum, les raies en émission supposées formées dans une région beaucoup plus étendue ne subissant globalement aucun effet.

Cet effet de microlentille gravitationnelle ouvre clairement de nouvelles perspectives pour l'étude de la structure interne des quasars. En se déplacant au sein de la galaxie, l'étoile microlentille passe petit à petit devant le quasar, zoomant l'une après l'autre les régions ou parties de régions à l'origine du continuum et des raies spectrales. A partir des variations spectrales induites par ce "scanner naturel", on peut espérer reconstruire –au moins partiellement– la structure interne du quasar, impossible à résoudre directement.

Dans un premier article (Article 6), nous étudions l'effet possible d'une lentille gravitationnelle sur le spectre d'un quasar de type BAL, en considérant deux modèles communément admis. Dans le premier modèle, la région à l'origine des raies BAL est constituée de petits nuages opaques n'occultant qu'une partie du continuum et ne contribuant pas aux raies en émission. Dans le second cas, nous considérons un modèle de type P Cygni, c'est-à-dire un vent continu de symétrie sphérique. Ces deux modèles constituent des cas extrêmes et de nombreuses solutions intermédiaires peuvent représenter adéquatement les quasars BAL (comme par exemple un modèle de type P Cygni axisymétrique). Entre autres à l'aide de simulations numériques, nous montrons que les variations spectrales attendues lors du passage d'une microlentille devant le quasar sont très différentes selon le type de modèle choisi. La détection d'un événement microlentille dans un quasar de type BAL devrait donc permettre de discriminer les différents types de modèles et de contraindre la géométrie de ces objets.

Afin de détecter un événement microlentille, il importe de suivre photométriquement les quasars multiples. Nous avons ainsi participé à plusieurs de ces suivis photométriques (Article 7 ; [36,37]) dont le but premier est de déterminer la constante de Hubble en mesurant le retard avec lequel une variation intrinsèque du quasar est détectée dans ses différentes images. Les variations résiduelles révèlent l'influence possible de microlentil-

les. C'est notamment le cas du quasar BAL H1413+117 dont le suivi photométrique est présenté dans l'article 7. Une variation résiduelle de la composante D est observée, suggérant une amplification de cette composante par effet microlentille.

Outre cette variation photométrique, la composante D du quasar H1413+117 montre des différences spectrales par rapport aux trois autres composantes ([38], Article 8). Cette différence se marque notamment dans une partie du profil en absorption. Elle a été interprétée par un effet microlentille et plus particulièrement par l'amplification sélective d'un nuage BAL absorbant [38].

Dans l'article 8, nous discutons à nouveau cette interprétation en tenant compte d'une amplification affectant à la fois le nuage absorbant et le continuum adjacent. L'effet résultant n'étant que différentiel, les différences spectrales induites sont faibles. En considérant des modèles génériques de microlentilles gravitationnelles, nous montrons que cette interprétation est possible mais qu'elle nécessite un ajustement fin des paramètres et notamment une localisation très précise d'un nuage opaque par rapport aux caustiques. D'autre part, une interprétation en termes de modifications de profils de type P Cygni standards n'est pas possible : en effet, dans ce type de modèle, toutes les longueurs d'onde sont affectées simultanément (Article 6). Une interprétation basée sur l'amplification du continuum par rapport à une zone en émission étendue à l'origine d'un profil de raie en émission complexe est par contre envisageable. Bien entendu, ne disposant que d'observations obtenues à une seule époque, il reste toujours possible que les spectres résultent d'une variation intrinsèque du quasar, détectée avec retard dans la composante D.

Dans une mise à jour suivant l'article 8 nous discutons une seconde série de spectres obtenus quatre ans plus tard avec le télescope spatial Hubble. En plus de différences spectrales intrinsèques affectant les quatre composantes, il est remarquable de constater que la différence observée dans le profil en absorption de la composante D est restée quasi identique durant tout ce laps de temps. Cette observation confirme l'existence d'un effet microlentille et rend l'hypothèse de l'amplification sélective d'un nuage absorbant difficilement tenable.

En fait ces observations peuvent s'expliquer très simplement si l'on admet que la variation observée dans le profil en absorption est due à une émission sous-jacente, non affectée par l'effet microlentille. Dans ce cas, il est aisé de séparer absorption et émission du profil observé. Une telle séparation apporte des informations sur la formation des profils de raies et donc sur la géométrie du flux de matière. Nous montrons de fait que les profils ainsi extraits révèlent l'existence d'un disque équatorial dans un vent en expansion, en bon accord avec les observations spectropolarimétriques présentées plus loin et avec certains modèles théoriques.

Ces résultats montrent clairement tout l'intérêt du phénomène microlentille pour résoudre la structure des quasars de type BAL. Bien sûr, avec deux époques d'observations seulement, on est loin d'un "scan" complet. Des observations supplémentaires, prises à intervalles réguliers, sont donc particulièrement souhaitables.

Dans le dernier article de cette série (Article 9), nous discutons les spectres d'un quasar double de type BAL, HE 2149-2745. Ici encore des différences spectrales, et plus particulièrement des différences de largeurs équivalentes des raies en émission, suggèrent

l'existence d'un effet microlentille. Contrairement au cas de H1413+117, aucune différence n'est observée dans les profils en absorption. Par contre, la structure des profils en émission n'est pas tout à fait identique dans les deux composantes, suggérant que la région à l'origine des raies en émission pourrait être partiellement résolue par la microlentille. Au moins une seconde époque d'observations est nécessaire pour confirmer ces hypothèses.

• La polarisation des quasars de type BAL

Dès les années quatre-vingt, plusieurs études [39,40] mettent en évidence le fait que la lumière qui nous vient de certains quasars, dont des quasars de type BAL, peut être polarisée linéairement. Bien que les niveaux de polarisation soient faibles, de l'ordre de quelques pour cent, c'est une découverte importante. En effet, la polarisation linéaire due à la diffusion ou à la réflexion de la lumière par des particules (poussières, électrons libres) donne des informations précieuses sur la géométrie d'un objet sans qu'il soit nécessaire de le résoudre spatialement. Si la région diffusant la lumière possède la symétrie sphérique, la polarisation résultante est nulle, tandis qu'une polarisation non nulle –même faible– indique un écart important à la symétrie sphérique. Dans le cas des quasars BAL, l'analyse de la polarisation peut donc servir à fixer plus précisément la géométrie de leurs éjections de matière.

Comme ces premières études ne contenaient que quelques rares quasars de type BAL, les plus brillants généralement, une investigation plus systématique de la polarisation de ces objets s'avérait nécessaire, d'autant que le développement de l'instrumentation permettait d'obtenir des mesures de polarisation de plus en plus précises pour des objets faibles. A l'aide du télescope de 3,6m de l'ESO et du spectro-imageur EFOSC, nous avons donc entamé une étude systématique de la polarisation optique des quasars BAL. Outre une série de mesures de la polarisation linéaire dans des filtres à bande large, nous avons également effectué la spectropolarimétrie de certains d'entre eux. Cette technique donne la dépendance spectrale de la polarisation. On peut en extraire le spectre polarisé, c'est-à-dire la partie de la lumière réfléchie par les particules. Si ces particules ne sont pas sur la ligne de visée directe, elles constituent un "miroir" capable de fournir à la fois une vue "périscopique" de l'intérieur du quasar et une ligne de visée décalée traversant éventuellement d'autres parties du vent en expansion. Cette technique a été amplement utilisée pour démontrer que les galaxies de Seyfert 1 et 2 ne sont en fait que des objets identiques vu sous des angles différents [28].

Mesurer une polarisation de quelques pour cent pour des objets faibles, nécessite des observations à très haut rapport signal sur bruit. La soustraction précise de la polarisation du ciel nocturne ainsi qu'une photométrie adéquate sont indispensables. Dans les articles 10, 11 et 12, nous décrivons en détail la technique observationnelle utilisée ainsi que la méthode de réduction spécialement mise au point. Typiquement, nos mesures sont entachées d'une incertitude de 0,2% sur le niveau de polarisation, soit beaucoup moins que dans les études précédentes. La polarisation instrumentale résiduelle est également trouvée très faible. Enfin, nous discutons la contamination possible due à la polarisation

interstellaire dans notre Galaxie et nous montrons que virtuellement tout quasar dont le degré de polarisation excède 0,6% est intrinsèquement polarisé.

Dans les articles 12, 13 et 14, nous présentons les résultats de notre étude systématique de la polarisation des quasars BAL. Nous montrons tout d'abord qu'en tant que classe d'objets, les quasars BAL sont significativement plus polarisés que les quasars non-BAL et que, parmi les quasars BAL, les plus polarisés sont ceux qui possèdent des raies de faible ionisation en absorption.

Afin de comprendre l'origine de cette polarisation, nous tentons ensuite de la relier aux propriétés spectroscopiques de ces quasars, quantifiées en une série d'indices spectraux : pente du continuum, rapport de flux radio / optique, indices de balnicité et de détachement[7] des raies BAL, etc. L'analyse statistique est effectuée sur base de méthodes non-paramétriques. Un des résultats les plus intéressants est la mise en évidence d'une corrélation significative entre la polarisation du continuum et l'indice de détachement des raies BAL dans le sens où les quasars montrant des profils de type P Cygni sont les plus polarisés. Une analyse statistique en composantes principales [41] indique que cette corrélation est dominante et constitue donc une des caractéristiques importantes de la physique des quasars BAL.

Ces résultats peuvent s'interpréter assez simplement dans le cadre d'un modèle axisymétrique où l'éjection de matière se fait à partir d'un disque, sous forme par exemple d'un vent continu. Ce modèle assez générique a fait l'objet de plusieurs études théoriques [42–45]. Dans ce cas, la forme des profils de raies et la polarisation dépendent toutes deux de l'orientation du disque par rapport à la ligne de visée. Lorsque le disque est vu sur la tranche, des profils de type P Cygni sont produits et la polarisation générée par diffusion dans le vent est alors maximale, soit par un pur effet géométrique (dépendant de l'extension verticale du vent et de son opacité ; Article 12, [46]), soit parce que le continu direct est plus atténué. Dans ce cas, l'indice de détachement pourrait constituer une mesure de l'inclinaison du disque. Bien sûr, de nombreuses variantes à ce modèle sont possibles, mais il reste clair qu'un flux de matière ayant la symétrie sphérique ne peut reproduire les observations.

Dans un addendum suivant l'article 14, nous présentons nos observations spectropolarimétriques. Comme précédemment nous avons essayé de dégager quelques tendances générales sur base d'analyses statistiques. Ainsi, nous avons pu identifier une relation possible entre l'indice de détachement et le rapport des profondeurs des raies en absorption mesurées dans le spectre polarisé et dans le spectre total. Un telle relation s'interprète assez naturellement dans le cadre du modèle que nous venons de discuter.

Pour le quasar BAL H1413+117, la spectropolarimétrie est décrite un peu plus en détail. En effet, en usant d'une méthode basée sur l'effet de microlentille gravitationnelle (Article 8), nous avions suggéré pour H1413+117 un modèle de vent à deux composantes,

[7] L'indice de balnicité est une largeur équivalente modifiée de la raie de CIV λ1549 en absorption. C'est une mesure de l'intensité du phénomène BAL dans un quasar. L'indice de détachement d'une raie BAL est une mesure assez complexe de l'écart entre la raie en émission et la raie en absorption [27]. Les raies BALs montrant des profils de type P Cygni ont un indice de détachement faible.

dont un disque. Bien que distinct[8], ce modèle n'en a pas moins les caractéristiques essentielles du modèle générique. Il est remarquable de constater que les observations spectropolarimétriques, qui sont caractérisées par une rotation de l'angle de polarisation dans les raies en absorption et par le fait que seule l'absorption du disque est observée dans le spectre polarisé, sont en excellent accord avec ce modèle de vent à deux composantes proposé tout à fait indépendamment.

De tout ceci, il ressort que le modèle générique explique assez bien l'ensemble des observations tant spectropolarimétriques que celles interprétées en termes d'effet microlentille. Des effets sur les spectres dus à l'orientation du disque par rapport à la ligne de visée sont bien sûr attendus, comme par exemple la relation observée entre l'indice de détachement et la polarisation, mais ils n'impliquent nullement que quasars BAL et non-BAL sont en fait des objets identiques vus sous des angles différents[9].

Enfin, nous terminons cette partie par une étude spectropolarimétrique détaillée d'un quasar de type BAL exceptionnel : Q0059-2735. Ce quasar possède la particularité de montrer des raies de FeII en absorption qui, contrairement aux raies BAL fortement ionisées, ne sont pas plus polarisées que le continuum tout en étant détectées dans le spectre polarisé. Ce comportement indique une localisation et/ou une région de formation distincte. Ces observations sont en accord avec l'idée que le spectre de Q0059-2735 est un mélange de spectres de quasar et de starburst [50,51]. Dans le cadre de cette interprétation, les raies de FeII seraient dues à du gaz éjecté par des supernovae issues d'une flambée d'étoiles récente et donc formées bien au delà de la région à l'origine des raies BAL classiques. Ces caractéristiques pourraient indiquer que Q0059-2735 est un quasar jeune au sein d'une séquence évolutive. Elles posent la question de l'existence d'un lien entre le phénomène BAL et les flambées d'étoiles massives.

Polarisation des quasars et grandes structures

Les galaxies, et très probablement les quasars, s'organisent en diverses structures dans l'Univers. On peut dès lors se demander si la matière éjectée par les quasars peut influencer la formation et l'évolution de structures plus grandes, ou si, inversément, ce sont ces structures, c'est-à-dire leurs champs gravitationnels et/ou magnétiques, qui ont un effet sur la formation des quasars et de leurs éjections de matière. Bien que ces questions fondamentales aient fait l'objet de plusieurs études théoriques [52–54] et de quelques avancées observationnelles [55,56] –surtout à l'échelle des amas et superamas–, elles restent essentiellement ouvertes.

Dans le cadre de notre étude de la polarisation des quasars, nous avons mis en évidence un effet d'orientation qui pourrait apporter des éléments de réponses à ces questions, ou encore à l'identification de l'énigmatique matière sombre omniprésente dans l'Univers. Ces travaux sont repris dans les articles 16 et 17.

[8]En plus du vent issu du disque (disk wind), on suppose l'existence d'une composante polaire (polar wind)

[9]Cette idée d'unification est d'ailleurs battue en brêche par une série d'observations très récentes [47–49]

Tout d'abord, nous avons constaté dans un de nos échantillons de quasars polarisés que, dans une certaine région du ciel, les angles de polarisation des quasars ne sont pas distribués de façon aléatoire comme on pourrait s'y attendre mais concentrés autour d'une certaine direction. Autrement dit, les vecteurs polarisation apparaissent orientés de façon cohérente ou encore alignés entre eux et ceci dans un volume bien défini de l'Univers. C'est un résultat tout à fait surprenant et inattendu.

Afin de vérifier cet effet, nous avons construit un plus grand échantillon de quasars en rassemblant des mesures de polarisation publiées dans la littérature. Nous avons aussi développé des tests statistiques adaptés au problème. Appliqués à ce nouvel échantillon, ces tests confirment l'existence d'une orientation cohérente de la polarisation des quasars, sur des échelles spatiales de l'ordre du gigaparsec. Une première explication qui vient immédiatement à l'esprit est un biais instrumental ou encore une contamination due à la polarisation interstellaire. Mais rien ne vient étayer ces hypothèses, d'autant que l'effet d'orientation affecte des quasars éloignés et non les quasars situés sur la même ligne de visée mais à plus faible distance.

Supposant cet effet réel, on peut dès lors définir une région du ciel où l'on prédit à l'avance les valeurs que peuvent prendre les angles de polarisation. Il suffit ensuite de mesurer la polarisation de quasars situés dans cette région et de vérifier si oui ou non les angles nouvellement mesurés tombent dans l'intervalle prédit. Ce test très simple, décrit et réalisé dans l'article 17, confirme également l'existence d'un effet d'orientation à grande échelle de la polarisation des quasars[10].

Les échelles auxquelles ces alignements sont détectés suggèrent un effet d'importance cosmologique. Deux types d'interprétations sont possibles. D'une part, on peut supposer que l'angle de polarisation est lié à la géométrie des quasars et définit un axe caractérisant leur structure. Dans ce cas, ce sont les quasars eux-mêmes qui seraient alignés sur des grandes échelles, peut-être suite à l'influence d'un champ magnétique cosmologique lors de leur formation. Bien que très spéculatif, un tel scénario a déjà été envisagé dans le cadre de la formation des galaxies [53,54,57,58]. D'autre part, on peut invoquer un mécanisme affectant la propagation de la lumière. Par exemple, la conversion de photons en axions[11] est dichroïque au sein d'un champ magnétique [59,60] et pourrait donc conduire à un alignement tel qu'on l'observe. Dans ce scénario, l'effet d'alignement permettrait d'identifier les constituants de la matière sombre, comme par exemple ces hypothétiques axions. Malheureusement il est difficile dans ce cadre d'expliquer pourquoi les quasars situés à plus faible distance ne sont pas alignés de la même façon et pourquoi les relations observées entre la polarisation des quasars et leurs propriétés intrinsèques ne sont pas détruites. Notons que quelques études récentes [60–62] confirment indépendamment nos résultats et/ou proposent des interprétations plus complexes. Mais seules de nouvelles données permettront de déterminer les caractéristiques de cet effet d'orientation et d'en comprendre l'origine.

[10]Notons que de nouvelles mesures obtenues très récemment et non encore publiées confirment de façon plus significative encore les résultats rapportés ici

[11]L'axion est une particule pseudo-scalaire de faible masse prédite par plusieurs extensions au modèle standard de la physique des particules. C'est un bon candidat pour la matière sombre froide dans l'Univers

Conclusions et perspectives ...

Les travaux présentés dans cette dissertation illustrent la diversité et la complexité du phénomène d'éjection de matière dans les astres. Ils s'inscrivent parmi les nombreux résultats récents montrant à quel point les différents constituants de l'Univers ne peuvent être considérés comme isolés, mais interagissent entre eux, acteurs d'une évolution collective et globale et ce peut-être jusqu'aux plus grandes structures.

De nombreux points restent évidemment obscurs, souvent faute d'observations homogènes en nombre suffisant. Nul doute cependant que le formidable déploiement des nouveaux moyens d'investigation prévus pour les années à venir y apportera quelques réponses. Citons par exemple le lancement des satellites infra-rouge SIRTF et Herschel qui permettront d'étudier avec précision la poussière dans les nébuleuses de type LBV, y compris dans d'autres galaxies. Citons encore les cent mille quasars détectés par le Sloan Digital Sky Survey (SDSS), dont environ dix pour cent sont des quasars BAL, et qui pourront être analysés sur base d'une sélection rigoureuse d'échantillons homogènes. Enfin, mentionnons le défi de l'interférométrie optique et sub-millimétrique qui devrait permettre de résoudre quasi directement la structure interne des quasars les plus proches.

Références

1. Maeder, A., Conti, P. 1994, ARA&A 32, 227
2. Heckman, T. 2000, Phil. Trans. R. Soc. Lond. A 358, 2077, and references therein
3. Krolik, J.H. 1998, "Active Galactic Nuclei : from the Central Black Hole to the Galactic Environment", Princeton University Press
4. Crenshaw, D.M., et al. 2002, " Mass Outflow in Active Galactic Nuclei : New Perspectives", ASP Conf. Ser. Vol. 255, San Francisco
5. Silk, J., Rees, M. 1998, A&A 331, L1
6. Cid Fernandes, R., et al. 2001, ApJ 558, 81, and references therein
7. Hill, T., et al. 1999, AJ 117, 111, and references therein
8. Kunth, D., Contini, T. 1999, in "Wolf-Rayet Phenomena in Massive Stars and Starburst Galaxies", Van der Hucht et al. (eds), IAU Symp. 193, 725
9. Canalizo, G., Stockton, A. 2001, ApJ 555, 719
10. Sanders, D.B., et al. 1988, ApJ 328, L35
11. Canalizo, G., Stockton, A. 2002, in " Mass Outflow in Active Galactic Nuclei : New Perspectives", Crenshaw et al. (eds), ASP Conf. Ser. 255, 195
12. Lípari, S., et al. 2003, MNRAS 340, 289
13. Humphreys, R.M., Davidson, K. 1994, PASP 106, 1025
14. Nota, A., Lamers, H.J.G.L.M. 1997, "Luminous Blue Variables : Massive Stars in Transition", ASP Conf. Ser. Vol. 120, San Francisco
15. Stahl, O. 1987, A&A 182, 229, and references therein
16. Walborn, N.R. 1982, ApJ 256, 452
17. Stahl, O., Wolf, B. 1986, A&A 158, 371
18. Smith, N. 2002, MNRAS 336, L22
19. Chu, Y.-H. 1981, ApJ 249, 195
20. Smith, L. 1996, in "Wolf-Rayet Stars in the Framework of Stellar Evolution", Vreux et al. (eds), 33^{rd} Liège Int. Astrophys. Coll., 381
21. Maeder, A. 1997, in "Luminous Blue Variables : Massive Stars in Transition", Nota & Lamers (eds), ASP Conf. Ser. 120, 374
22. Stothers, R.B., Chin, C.-w. 1996, ApJ 468, 842
23. Lamers, H.J.G.L.M., et al. 2001, ApJ 551, 764
24. Busche, J.R., Hillier, D.J. 2002, BAAS 200, 7417
25. Dessart, L., Chesneau, O. 2002, A&A 395, 209
26. Arav, N., et al. 1997, "Mass Ejection from Active Galactic Nuclei", ASP Conf. Ser. Vol. 128, San Francisco
27. Weymann, R.J. et al. 1991, ApJ 373, 23
28. Antonucci, R. 1993, ARA&A 31, 473
29. Hamann, F., et al. 1993, ApJ 415, 541
30. Surdej, J., Hutsemékers, D. 1987, A&A 177, 42
31. Hutsemékers, D. 1993, ApJ 417, 97

32. Hall, P.B., Hutsemékers, D., et al. 2003, ApJ 593, 189
33. Hutsemékers, D., Hall, P.B., Brinkmann, J. 2003, A&A, submitted
34. Schneider, P., Ehlers, J., Falco, E. 1992, "Gravitational lenses", Springer, Berlin.
35. Chang, K., Refsdal, S. 1979, Nature 282, 561
36. Daulie, G., et al. 1993, in "Gravitational Lenses in the Universe", J. Surdej et al. (eds.), 31^{st} Liège Int. Astrophys. Coll., 181
37. Courbin, F., et al. 1995, A&A 303, 1
38. Angonin, M.C., et al. 1990, A&A 233, L5
39. Moore, R.L., Stockman, H.S. 1984, ApJ 279, 465
40. Stockman, H.S., Moore, R.L., Angel, J.R.P. 1984, ApJ 279, 485
41. Lamy, H., Hutsemékers, D. 2003, A&A, in preparation
42. Murray, N., et al. 1995, ApJ 451, 498
43. de Kool, M., Begelman, M.C. 1995, ApJ 455, 448
44. Königl, A., Kartje, J.F. 1994, ApJ 434, 446
45. Emmering, R.T., Blandford, R.D., Shlosman, I. 1992, ApJ 385, 460
46. Brown, J.C., McLean, I.S. 1977, A&A 57, 141
47. Becker, R.H., et al. 2000, ApJ 538, 72
48. Jiang, D.R., Wang, T.G. 2003, A&A 397, L13
49. Yuan, M.J., Wills, B.J. 2003, astro-ph/0306518
50. Cowie, L.L., et al. 1994, ApJ 432, L83
51. Egami, E., et al. 1996, AJ 112, 73
52. Furlanetto, S.R., Loeb, A. 2001, ApJ 556, 619
53. Reinhardt, M. 1971, ApS&S 10, 363
54. Wasserman, I. 1978, ApJ 224, 337
55. West, M.J. 1991, ASP Conf. Ser. 21, 290
56. West, M.J. 1994, MNRAS 268, 79
57. Greyber, H. D. 1998, AIP Conf. Proc. 431, 73
58. Greyber, H. D. 2003, AIP Conf. Proc. 666, 365
59. Harari, D., Sikivie, P. 1992, Phys. Lett. B, 289, 67
60. Jain, P., Panda, S., Sarala, S. 2002, Phys. Rev. D 66, 5007
61. Jain, P., Narain, G., Sarala, S. 2003, astro-ph/0301530
62. Bezerra, V. B., Mosquera Cuesta, H. J., Ferreira, C. N. 2003, Phys. Rev. D 67, 4011

Articles

Première partie

Les nébuleuses éjectées par les étoiles massives

Article 1

HR Carinae : a Luminous Blue Variable surrounded by an arc-shaped nebula

D. Hutsemékers, E. Van Drom : Astron. Astrophys. 248, 141 (1991)

Cet article est le premier d'une série consacrée aux étoiles de type LBV (Luminous Blue Variable) et plus particulièrement à la recherche et l'étude systématiques des nébuleuses qui les entourent. Nous étudions ici l'étoile HR Carinae, une des rares LBVs connues dans notre Galaxie.

A partir d'observations spectroscopiques à moyenne et haute résolution, nous montrons que HR Car subit, sur une base de temps inférieure à l'année, des variations spectrales importantes, typiques des LBVs. Plusieurs composantes sont détectées dans le vent stellaire avec des vitesses variant au cours du temps.

La mesure de la vitesse radiale héliocentrique de l'étoile à partir des raies interdites de FeII donne une distance cinématique de 5,4 kpc pour HR Car, confirmant qu'il s'agit là d'une des étoiles les plus lumineuses de notre Galaxie.

Sur base d'images obtenues au travers de filtres étroits isolant les raies d'émission nébulaires, nous rapportons la découverte d'une nébuleuse de faible excitation entourant partiellement HR Car. La mesure d'une vitesse d'expansion radiale estimée à environ 50 km s^{-1} et d'une surabondance de l'azote par rapport à l'oxygène indiquent que cette nébuleuse contient des produits de nucléosynthèse éjectés par l'étoile il y a environ 10000 ans.

1991A&A...248..141H

Astron. Astrophys. 248, 141–149 (1991)

ASTRONOMY AND ASTROPHYSICS

HR Carinae: a luminous blue variable surrounded by an arc-shaped nebula ⋆

D. Hutsemékers and E. Van Drom

European Southern Observatory, La Silla, Casilla 19001, Santiago 19, Chile

Received October 31, 1990; accepted January 3, 1991

Abstract. We present new, high and medium dispersion spectroscopic observations of the luminous blue variable (LBV) star HR Car, showing that this star has a multiple shell expanding atmosphere and undergoes spectral variations apparently correlated with the light variations similarly to the other LBVs. Most striking are the very broad emission wings (FWZI $\sim 3000\,\mathrm{km\,s^{-1}}$) of the Balmer lines, reminiscent from the broad lines observed in the spectra of Of and WR stars.

We also derive a kinematic distance of 5.4 kpc and a bolometric magnitude of $-9^{\mathrm{m}}.4$, putting HR Car among the most luminous stars of the Galaxy.

From the analysis of narrow band filter imagery, we report on the discovery of an arc-shaped jet-like nebula associated with HR Car.

Spectroscopic observations of this nebula reveal an emission nature with very low excitation. As the star itself, the nebula is characterized by a significant N/O overabundance, probably due to the presence of nuclear processed material ejected by the star.

Key words: luminous blue variable stars – mass-loss – emission nebulae – HR Car

1. Introduction

HR Car is one of the few luminous blue variables (LBVs) known in our Galaxy. These stars are very luminous evolved supergiants characterized by irregular outbursts or eruptions. Although no more than ten LBVs have been observed in the Galaxy and the Large Magellanic Cloud, they are generally considered as a short but important stage in massive star evolution towards the WR stage. They constitute a quite unique group for understanding the physics of the stars near the Humphreys-Davidson stability limit (Humphreys 1989).

One of the most interesting characteristics of the LBVs is certainly that some of them are surrounded by a small nebula apparently formed of matter ejected by the star and giving evidence for enrichment by nuclear processed material. These nebulae therefore constitute an important clue for understanding the LBV phenomenon and the evolutionary status of these stars. Such nebulae are well-known around η Car and AG Car, which are, with P Cyg and HR Car, the 4 confirmed galactic LBVs. If the presence of a circumstellar nebula around P Cyg is possible but doubtful, nothing was ever detected around HR Car (Stahl 1989).

Since HR Car is by far the less studied of the galactic LBVs, the goal of this paper is to present new observations of this star and more particularly the discovery of a nebulosity around it.

HR Car (= HD 90177 = CPD $-58°2145$ = MWC 202 = He 3-407) is known to be a B2I P Cygni-type star with [Fe II] and Fe II emission lines, undergoing irregular slow light variations of approximately 1.5 mag as well as spectral variations on a period of a few months (Carlson & Henize 1979). It has a very high luminosity which is comparable to that of AG Car and P Cyg (Viotti 1971). From the photometric study of the light variations, van Genderen et al. (1990) clearly show that HR Car suffers S Dor type variations similar to those reported for AG Car and P Cyg.

A detailed infrared spectroscopic investigation has been performed by McGregor et al. (1988) who reported the presence of cool dust around HR Car and a variable spectrum characterized by strong [Fe II] emission lines and weak CO first overtone emission. They also found that HR Car is losing mass at a variable rate with an average value of $6\ 10^{-7}\,M_{\odot}\,\mathrm{yr}^{-1}$. Ultraviolet observations were recently analysed by Shore et al. (1990) who assign to HR Car an ultraviolet spectral type B4–5 and confirm its very high luminosity. They find that the Si IV and C IV resonance lines are weak as in the spectrum of other P Cygni type stars.

In the remainder, we present medium and high dispersion spectroscopic observations of HR Car as well as imaging and spectroscopic observations of the nebula found in its surroundings.

2. The observations

The observations of HR Car were carried out at the European Southern Observatory (ESO) during the period December 1988–June 1990. For all the observations, spectroscopy and imaging, the detectors were high resolution CCD chips of type RCA SID 503, 1024×640 pixels, each $15\,\mu\mathrm{m}^2$.

The usual calibration frames (bias, darks, flat-fields as well as spectra of HeAr, ThAr and spectrophotometric standard stars) have been obtained. The reduction was done with the standard IHAP and MIDAS packages available at ESO.

In most cases, we have obtained more than one frame for a given spectroscopic or imaging configuration. All these frames were reduced individually before their eventual comparison and/or addition.

Send offprint requests to: D. Hutsemékers, Institut d'Astrophysique, Université de Liège, 5, av. de Cointe, B-4000 Liège, Belgium

⋆ Based on observations collected at the European Southern Observatory (ESO, La Silla)

© European Southern Observatory • Provided by the NASA Astrophysics Data System

1991A&A...248..141H

Table 1. Imaging observations of HR Car

Date	Instrument	Filter	λ_c/FWHM (Å)	Exposure time	Seeing
16/12/88	2.2 m + DC	[N II]	6595/23	10 s	0".8
		Continuum	6026/261	1 s	0".9
29/03/89	2.2 m + DC	Hα + [N II]	6554/20	5 s + 10 s	0".9
		[N II]	6595/23	2 × 10 s	0".9
		[N II]	6595/23	5 min + 10 min	1".3
		Continuum	6026/261	2 × 1 s	0".7
23/06/89	2.2 m + DC	Hα + [N II]	6572/40	1 min + 5 min	2".0
		[N II]	6593/36	5 min	2".5
		[O III]	5006/66	2 × 5 min	2".2
27/04/90	2.2 m + DC	Hα + [N II]	6572/40	2 × 5 min	1".4
		[N II]	6580/20	4 × 10 min	1".3
		[S II]	6735/26	15 min	1".4
		[O III]	5007/27	10 min	1".5
29/04/90	2.2 m + DC	[N II]	6580/20	30 s + 10 min	1".0
30/04/90	2.2 m + DC	Continuum	6450/61	1 min	1".2
28/06/90	3.6 m + EFOSC	Hα + [N II]	6548/63	4 × 2 min + 2 × 6 min	1".4
		[O III]	5006/66	3 min	2".0

2.1. *Imaging*

The images of HR Car and its nebula were obtained using the 2.2 m telescope equipped with the Direct Camera (DC) and the 3.6 m telescope equipped with the EFOSC camera (Melnick et al. 1989). At the 2.2 m and 3.6 m telescopes, the RCA CCD pixel size of 15 μm corresponds to 0".175 and 0".337 on the sky, respectively. We essentially used narrow-band interference filters centered on the spectral lines of Hα, [N II], [S II], [O III] and a red continuum. In order to avoid saturation effects, some frames were also obtained at the 3.6 m telescope by positioning on the stellar image the 8".0 occulting spot of the EFOSC coronographic mode. A summary of these imaging observations is given in Table 1, together with the filter characteristics.

The search for faint nebulosities near bright objects is always a difficult task: the image of the star is generally saturated while filters of lower quality may produce some ghosts, both effects contaminating the direct surroundings of the stellar image. In order to be sure that the observed nebulosity is not due to such a contamination, we have repeated our imaging observations with various filters and CCDs, also moving the object at different positions on the CCD. When detected, the features discussed in Sect. 4 are present on all the frames obtained with a given filter.

2.2. *Spectroscopy*

Low dispersion spectrograms of HR Car and its nebula were obtained at the 1.52 m and 2.2 m telescopes equipped with a Boller and Chivens spectrograph (Heydari-Malayeri et al. 1989). They cover the 3500–6800 Å spectral range. They were obtained at different epochs with the aim of detecting spectral variations. Each time a nebular spectrum was recorded, a stellar one was taken with the same setting in order to allow a comparison independent of the calibration. In most cases the Hα line did not reach the saturation level, the signal to noise ratio being increased by repeated exposures. Higher dispersion spectrograms were obtained with the same equipment in the 4430–4920 Å spectral range, an important region for the spectral classification of luminous early-type stars.

HR Car was also observed at high dispersion with the CASPEC spectrograph attached to the 3.6 m telescope (Pasquini & D'Odorico 1989). The 31.6 lines mm^{-1} grating was used with a 300 lines mm^{-1} cross dispersion grating and a $f/1.5$ camera. The high resolution RCA CCD was used in the 2 × 2 binned mode. The spectra were centered on the Hα and Hγ-Hβ spectral regions, the first one being slightly underexposed in the continuum.

Higher dispersion spectrograms were obtained more or less one year later with the CES spectrograph attached to the CAT telescope (Lindgren & Gilliotte 1989). Two regions were considered, centered on the Hα and the He I λ5876 – Na I D spectral lines. We should note that a ghost is present in the flat-fields at the He I λ5876 position hampering a good reduction at this wavelength. In order to derive precise radial velocities from these spectra, we have also observed two radial velocity standard stars: HD 168454 and HD 186791.

Finally, a spectrum of the nebula around HR Car was also obtained with the EFOSC spectrograph attached to the 3.6 m telescope (Melnick et al. 1989).

For the nebular spectra obtained at the 1.5 m telescope, the 2".0 wide slit was positionned at a distance of ~16" from the star and with a PA ≃ 60°, in order to cross the SE arcs (see Sect. 4). At the 3.6 m telescope, the 0".75 wide slit was oriented E-W and positionned 15" S of the star. We should note that the spectra are partially contaminated by the light from the bright star. But, since this contamination is spatially well defined on the nebular spectrum, it can be quite easily removed during the reduction procedure.

All the spectra have been sky-subtracted, this substraction taking also into account the eventual contamination by the faint ambient nebula in which HR Car is embedded and seen on the ESO/SRC sky survey R plates.

Table 2 gives a summary of the spectroscopic observations.

© European Southern Observatory • Provided by the NASA Astrophysics Data System

1991A&A...248..141H

Table 2. Spectroscopic observations of HR Car and its nebula

Date	Instrument	Spectral range (Å)	Resolution (Å)	Exposure time	Object
14/04/89	1.5 m + B&C	4430–4920	0.98	10 + 20 min	Star
18/06/89	3.6 m + CASPEC	4050–5120	~0.3	1 min + 5 min	Star
18/06/89	3.6 m + CASPEC	6050–7140	~0.4	1 min	Star
14/02/90	1.5 m + B&C	3500–5430	3.8	2 min + 4 × 60 s	Star
15/02/90	2.2 m + B&C	5100–6850	3.4	2 min + 3 × 30 s	Star
10/05/90	CAT + CES	6535–6592	0.12	1 min + 2 × 5 min	Star
12/05/90	CAT + CES	5860–5910	0.11	2 × 30 min	Star
13/05/90	CAT + CES	5860–5910	0.11	30 min	Star
15/05/90	1.5 m + B&C	4820–6800	4.7	60 s	Star
15/05/90	1.5 m + B&C	4820–6800	4.7	2 × 30 min + 60 min	Nebula
17/05/90	1.5 m + B&C	3570–5510	4.9	90 s + 180 s	Star
17/05/90	1.5 m + B&C	3570–5510	4.9	2 × 60 min	Nebula
19/05/90	1.5 m + B&C	4820–6800	4.7	60 min	Nebula
28/06/90	3.6 m + EFOSC	3600–7000	6.4	10 min	Nebula

3. The star

3.1. *Analysis of the spectrum*

The spectrum of HR Car is dominated by strong Balmer emission lines showing P Cygni type profiles superimposed on very broad (FWZI $\simeq$ 3000 km s^{-1}) emission features, the profiles of the upper members of the series being dominated by absorption. Moderately strong emission lines due to [Fe II] and Fe II are also observed, the latter ones with P Cygni type profiles. Spectral lines due to He I, N II, Si II, Si III, and Mg II are seen in absorption. Strong Ca II and Na I absorption lines are detected, most probably of circumstellar/interstellar origin, the diffuse interstellar bands being also very prominent.

Representative parts of the spectrograms recorded at the most separated epochs are illustrated in Figs. 1 and 2. Despite the unequal spectral dispersions, definite differences can be seen: the absorption lines of He I, N II, Si III as well as the [Fe II] emission lines are stronger in April 89 while the Fe II lines are stronger in May 90. According to their epoch of observation, the other spectra show intermediate characteristics, the CASPEC spectrograms obtained in June 89 being not too different from the April 89 spectrum. On the basis of the Si II, Si III, Mg II, and He I absorption lines, we have determined an equivalent spectral type B3I in April 90 and B9I in May 90. The He I λ4471/Mg II λ4481 line ratio is quite illustrative of this variation (Fig. 2).

It is particularly interesting to remark that between these two epochs, HR Car has apparently brightened (see Fig. 3) so that the spectral variations are most probably linked to the light variations. This behavior is quite common in LBVs (see for example the well-documented and similar behavior of S Dor, R127 or R71 reported by Leitherer et al. 1985; Stahl et al. 1983; or Wolf et al.

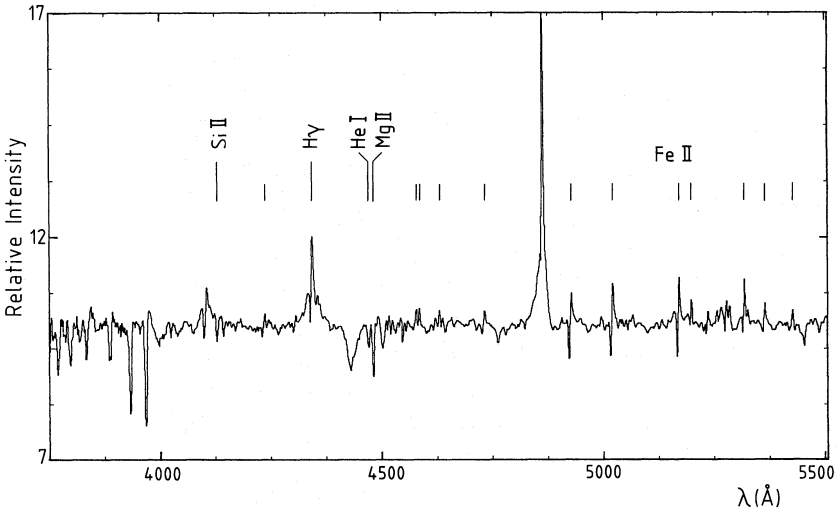


Fig. 1. The normalized blue spectrum of HR Car observed with the 1.52 m telescope in May 90. A few lines of interest are indicated. The non-labeled marks indicate Fe II lines

© European Southern Observatory • Provided by the NASA Astrophysics Data System

1991A&A...248..141H

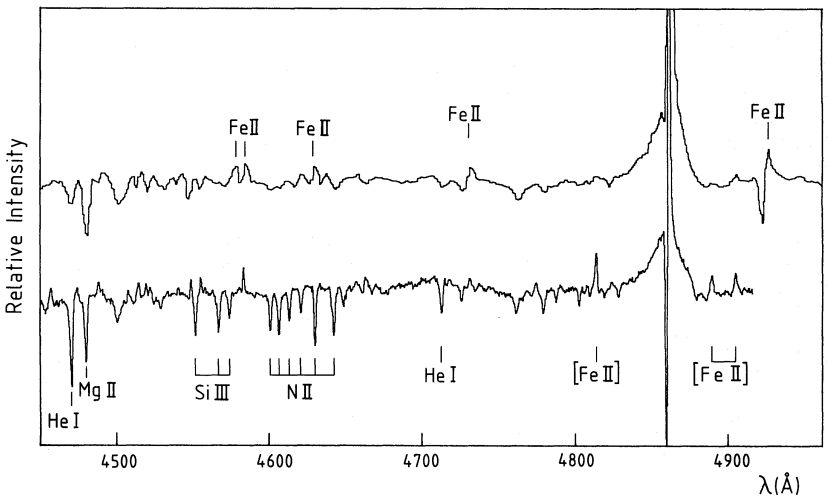


Fig. 2. Comparison of two spectrograms of HR Car recorded at the 1.52 m telescope in April 89 (*lower*) and May 90 (*upper*)

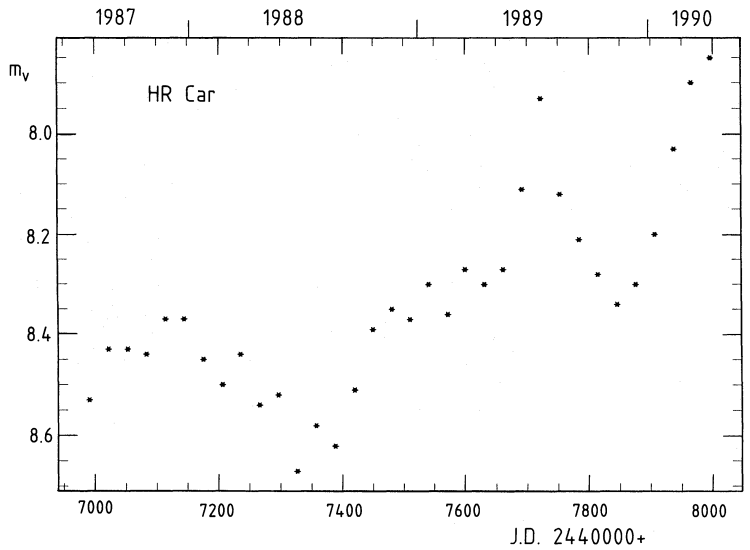


Fig. 3. The visual light curve of HR Car from the observers of the Royal Astronomical Society of New Zealand (Bateson 1987–1990)

1981, respectively): during brightening, these stars are surrounded by a cool dense envelope which hampers the observation of the true stellar features observed at minimum.

The spectrum of HR Car obtained in April 89 is quite remarkable in the sense that the N II lines are well seen while no O II can be detected contrary to normal B supergiants or P Cygni itself where O II is at least as intense as N II (see for example the atlas by Walborn & Fitzpatrick 1990, and Yamashita et al. 1977). This fact, already noticed by Carlson & Henize (1979), probably indicates a N/O overabundance in the atmosphere of HR Car. A similar deficiency of oxygen lines has been reported for the galactic LBV AG Car (Caputo & Viotti 1970; see also Hutsemékers & Kohoutek 1988).

Radial velocities have been measured for most lines on the high dispersion CASPEC spectrograms recorded in June 89. They are given in Table 3 while a few line profiles of interest are illustrated in Fig. 4. We should note that similar velocities were measured for the less numerous lines observed in the April 89 spectrum. The heliocentric systemic velocity of HR Car was measured from the [Fe II] emission lines: $+22\,\mathrm{km\,s^{-1}}$ ($\sigma/\sqrt{n} = 4\,\mathrm{km\,s^{-1}}$ for $n = 9$ lines). The lines of He I, Mg II, Si II, Si III, N II are only slightly blueshifted by typically $15\,\mathrm{km\,s^{-1}}$ with respect to the star, such motions being quite common in the atmospheres of supergiants. The He I lines have in addition a weak blue wing extending up to $\sim -102\,\mathrm{km\,s^{-1}}$. Very different are the P Cygni type profiles of the Balmer and Fe II lines which show two absorption components significantly displaced to the shorter wavelengths. These components probably reveal the presence of two extended shells in the atmosphere of HR Car. Compared to the most blueshifted absorption component, the less blueshifted one is stronger for the upper Balmer lines than for the lower members of the series. If the excitation is higher near the star, this suggests that the less blueshifted component is formed nearer to the star.

© European Southern Observatory • Provided by the NASA Astrophysics Data System

1991A&A...248..141H

Table 3. Mean radial velocities (km s^{-1}) relative to the star of the absorption lines of the different ions observed in the CASPEC spectrograms of HR Car

Ion	Velocity
H I	−105
	− 36
Fe II	−104
	− 31
He I	− 1
N II	− 10
Mg II	− 16
Si II	− 15
Si III	− 14

Figure 5 illustrates the variations of the Hα line profile between June 89 and May 90. The less blueshifted absorption component shows only little radial velocity variation (it even seems to be present in the spectra obtained in 1987 by Bandiera et al. 1989) while the high velocity one is significantly displaced to the blue. Since the radial velocity of the stable component is not too different from the radial velocity of some of the higher excitation lines (Table 3), we may think that this component is formed in more or less the same part of the atmosphere. If this is true and if the highest excitation lines are formed the deepest in the atmosphere, it indicates that, near the star, the envelope is slightly accelerated outwards. The other absorption component, whose radial velocity relative to the star changes from −105 km s^{-1} to −140 km s^{-1} between June 89 and May 90, is probably formed in

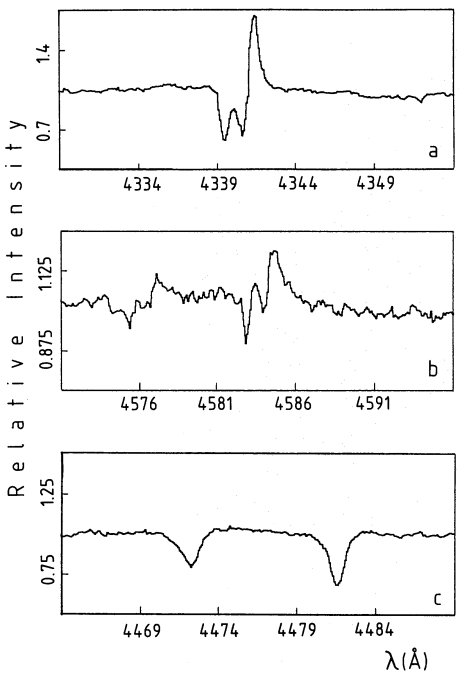


Fig. 4a–c. The line profiles of Hγ (**a**), Fe II λ4583 (**b**), He I λ4471 (**c**) and Mg II λ4481 (**c**) from the CASPEC spectrograms obtained in June 89

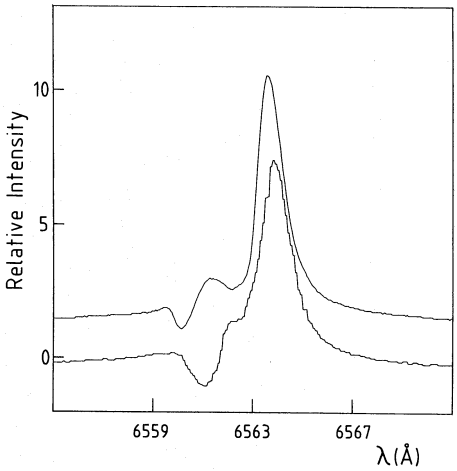


Fig. 5. Comparison of the Hα line profiles obtained in June 89 with CASPEC (*lower*) and May 90 with the CAT+CES (*upper*). The spectra have been rebinned in wavelength to take into account the difference in the motion of the earth between these two epochs

a more extended and more rapidly expanding shell becoming less optically thick with time. We should remark that in the May 90 CAT+CES spectrum, the He I λ5876 line shows 2 absorption components at −38 and −135 km s^{-1} relative to the star. The peculiar behavior of this line was already noticed in the spectrum of R 127 by Stahl et al. (1983).

From the blue wing of the Balmer and Fe II lines observed in the CASPEC spectra, we have measured the terminal velocity of the wind which is found equal to ∼145 km s^{-1}. Half the FWZI of the [Fe II] lines is somewhat lower than this value: ∼125 km s^{-1}. If the [Fe II] lines are formed outer than the region where the Balmer lines are formed, in lower density regions, this indicates that either the wind is decelerating at large distances from the star, probably because of its interaction with old remnants, or the material ejected before had a lower velocity. Let us finally note that the terminal velocity of the wind measured one year later from the Hα profile (Fig. 5) has increased to ∼170 km s^{-1}.

One of the most striking characteristics of the spectrum of HR Car is certainly the presence of very broad wings (FWZI ∼ 3000 km s^{-1}) superimposed on the Balmer emission lines. A faint broad emission of similar width may also be present around the He I λ4713 absorption lines, which, on our April 89 spectrum, is the only one sufficiently unblended to detect such a faint feature. Spectra of other stars have been obtained with the same instrumental setting and reduced on the same way with no equivalent bump at λ4713 so that it is reasonable to think that this feature is real. We should notice that broad He I emission lines have been reported in the spectrum of R 127 (Stahl et al. 1983).

In the spectrum of P Cygni and AG Car, the broad wings of the Balmer lines have been interpreted as due to non-coherent scattering of the emission line photons by free electrons (Bernat & Lambert 1978; Wolf & Stahl 1982). In the case of HR Car, this interpretation does not seem very satisfactory: the equivalent width ratio of the broad to the narrow residual emission is rather high (about 10 for Hδ) and greater by a factor 5 for Hδ than for Hβ (see Fig. 1). In order to reproduce the broad wings of both Hδ and Hβ by electron scattering, we need quite different electron optical depths which means quite different loci of formation of

© European Southern Observatory • Provided by the NASA Astrophysics Data System

these lines, a situation which is not supported by net differences in the radial velocities. Also, with such high electron optical depths, we should detect broad emission lines associated with the brightest Fe II lines, these lines being as intense as Hδ or Hγ (see Fig. 1) with nearly equal radial velocities (cf. Table 3). Finally, the Hβ broad emission wings appear rather asymmetric, more extended to the blue, while scattering by electrons preferentially produces wings more extended to the red (Auer & Van Blerkom 1972). All these observational characteristics are significantly different from those described by Bernat & Lambert (1978) for the case of P Cygni. We therefore think that these broad lines more likely reveal the presence of high velocity motions in the atmosphere of HR Car, as the He I broad lines observed in the spectrum of R 127 (Stahl et al. 1983). Since emission lines with such a large Doppler broadening are only seen in the spectrum of WR stars and of some extreme Of stars – superimposed on narrower emission lines for these latter ones (Underhill et al. 1989) –, this may indicate that the atmosphere of HR Car has some properties in common with those of Of and WR stars, therefore supporting a possible evolutionary link.

3.2. *Distance and stellar parameters*

From the heliocentric velocity of the star, we can estimate the kinematic distance of HR Car. Adopting $+22\pm4\,\mathrm{km\,s^{-1}}$ as the systemic velocity of HR Car, we derive its velocity relative to the local standard of rest, $v_{\mathrm{lsr}} = +9\,\mathrm{km\,s^{-1}}$. This value is equal to that reported by Humphreys et al. (1989) for AG Car which is located in the same region of the sky, so that a similar reasoning can be followed in order to derive the kinematic distance of HR Car. We find 5.4 ± 0.4 kpc which is greater than the value of 2.5 kpc generally adopted considering its belonging to the Carina OB association. Such a large distance for HR Car is in agreement with the very strong interstellar lines observed in its spectrum. The Na I D lines are illustrated in Fig. 6. At least five absorption components are clearly seen, with velocities up to $-86\,\mathrm{km\,s^{-1}}$. Such high velocity components seem quite common in the Carina nebula (Walborn 1982). The presence of an absorption component at an heliocentric velocity of $+22\,\mathrm{km\,s^{-1}}$, similar to that of the star, indicates that the light coming from HR Car crosses interstellar material moving at positive radial velocities, giving some support to the large distance we derived. We should remark that an absorption component of Na I is also detected with a similar velocity in the spectrum of a neighbouring star, He 3-519, in agreement with the suggestion that this component has an interstellar origin.

Using the magnitudes and parameters of HR Car determined by van Genderen et al. (1990): $V = 8\overset{\mathrm{m}}{.}4$, $A_V = 3\overset{\mathrm{m}}{.}1$, $T_{\mathrm{eff}} \simeq 14\,000$ K, $BC \simeq -1$ as well as the new distance of 5.4 kpc, we find a bolometric magnitude of $M_{\mathrm{bol}} \simeq -9\overset{\mathrm{m}}{.}4$. If corrected for the distance, a similar value can be obtained from the data of Shore et al. (1990) which are derived from ultraviolet observations. As noted by van Genderen et al. (1990), such a value of the bolometric magnitude will be in better agreement with the LBV amplitude-luminosity relation found by Wolf (1989). With these values for the distance and bolometric magnitude, the average mass-loss rate of $6\,10^{-7}\,M_{\odot}\,\mathrm{yr^{-1}}$ determined by McGregor et al. (1988) amounts to $2\,10^{-6}\,M_{\odot}\,\mathrm{yr^{-1}}$.

The stellar parameters that we just derived confirm the LBV nature of HR Car by putting it in the upper part of the HR diagram between S Dor and R 71 (see e.g. the HR diagram displayed by Wolf 1989). Also the higher mass-loss rate is more typical of that of other LBVs.

4. The nebula

4.1. *The optical morphology*

First, looking at the ESO/SRC sky survey plates, we can see that HR Car does not belong to a particular star cluster and is embedded in a faint extended nebula which is apparently not related to the star itself.

A CCD image in the Hα+[N II] filter of the direct surroundings of HR Car is illustrated by Fig. 7. Two nebular arcs are definitely seen in the SE direction. They are located at 13″ and 17″ from the star and are ~2″ wide. The stellar image also shows a diffuse aspect in the NW direction suggesting that the nebulosity is extended in this direction and therefore has a bipolar geometry with a SE-NW axis. Especially interesting is the condensation located 6″ SE from the star: it is diffuse and elongated in the direction of the nearest arc, looking like a jet originating from the

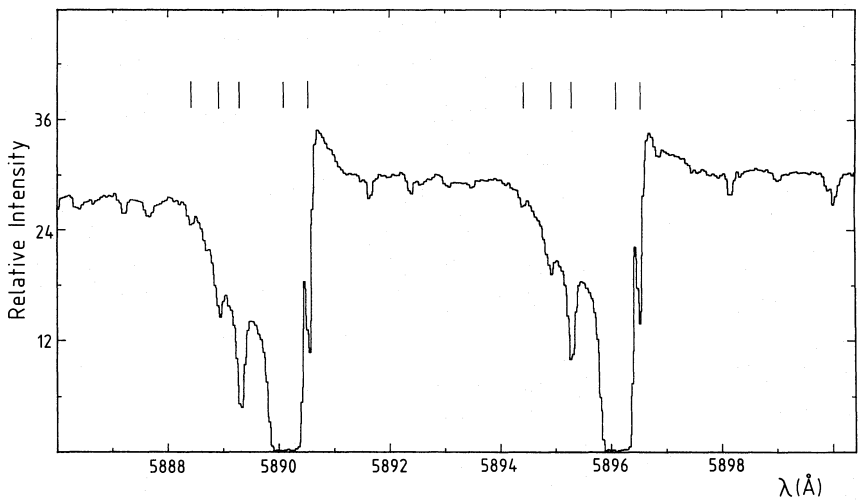


Fig. 6. The profiles of the Na I D lines observed with the CAT+CES in May 90. Five absorption components are indicated. They have heliocentric radial velocities of −86, −60, −41, +0.3 and +22 km s^{-1}

© European Southern Observatory • Provided by the NASA Astrophysics Data System

1991A&A...248..141H

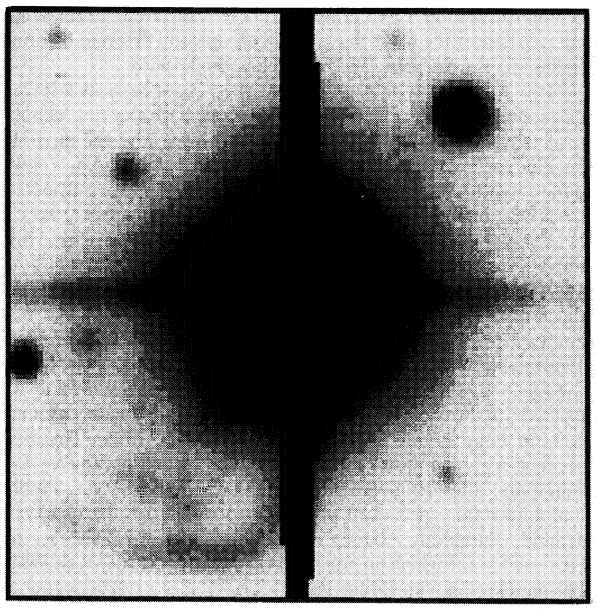


Fig. 7. Sum of the two best seeing (~1".2 FWHM) images (2 min exposure each) obtained at the 3.6 m telescope + EFOSC with a good quality Hα + [N II] filter. The intensity scale is logarithmic. North is up, east to the left. The field is 35" × 35". The vertical and horizontal features are instrumental, due to the overexposition of the stellar image. The other features may be considered as real (see text)

stellar core. Despite some net differences, this kind of geometry is reminiscent from that of the nebula associated with AG Car where a jet has recently been found in addition to an overall bipolar geometry (Paresce & Nota 1989).

The nebular features discussed above are detected on all the images obtained in the [N II] and Hα + [N II] filters, including those obtained in the EFOSC coronographic mode which are unsaturated but of less good seeing. These features are nevertheless absent on the images obtained with the [O III] and continuum filters. This suggests that the nebula is not of reflective nature but of emission type.

On the good seeing and unsaturated images of HR Car, we can also see a faint star clearly resolved and located at 3".7 E, 0".2 S of HR Car. In the red continuum filter used on March 89, this companion is about 5^m fainter than HR Car and $0^m.4$ brighter than the star seen 15" NW of HR Car.

4.2. The spectrum and physical characteristics

The spectrum of the nebula, which essentially refers to the arcs, consists of the Balmer emission lines seen up to Hγ (Hδ is very faint but probably present) as well as the [N II] λλ6548–6583 and the [S II] λλ6716–6723 forbidden lines (Fig. 8). [N I] λ5199 is also probably present but faint. The spectrum is remarkable by the low excitation and the absence of oxygen lines, namely the [O I] λ6300, [O II] λλ3726–3729 and [O III] λλ4959–5007 lines. As from the spectrum of the star, this suggests a net N/O overabundance.

Despite some differences in the location of the slit, the spectra obtained at various epochs are essentially the same. Also, we have not detected any significant spatial variation of the nebular spectrum except radial velocity differences up to $\sim 50\,\mathrm{km\,s^{-1}}$ between small regions in the two arcs, the greatest arc being the most redshifted. This velocity difference was measured in the May 90 spectra from the spatial profile of the [N II] lines. It is rather high and may indicate that the arcs are strongly related to the stellar wind, as also suggested by the morphology.

With so few observed lines it is not easy to derive quantitative parameters for the nebula. We can nevertheless try to constrain some of them. Assuming case B recombination with $T_e = 10^4$ K, we derive from the observed Hα/Hβ and Hγ/Hβ ratios the logarithmic extinction coefficient: $c \simeq 1.4$. This extinction corresponds to $A_V \simeq 3$, a value which is nearly the same as the value derived from the stellar photometry (see Sect. 3.2) suggesting that no additional extinction occurs inside the nebula. Both the measured $F(\lambda)/F(\mathrm{H}\beta)$ and the corrected $I(\lambda)/I(\mathrm{H}\beta)$ emission line ratios are given in Table 4.

From the [N II] lines, we can estimate the electron temperature T_e. Since the [N II] λ5755 lines is not convincingly detected in our spectra, only an upper limit to the temperature can be obtained. With $I([\mathrm{N\,II}])/I(\mathrm{H}\beta) \leqq 0.03$, we find $T_e \leqq 12\,500$ K. We may therefore adopt in the following the electron temperature $T_e = 10^4$ K. From the [S II] line ratio, we derive the electron density: $n_e = 600\,\mathrm{cm^{-3}}$. These values are rather typical of H II regions and not too different from those obtained by Mitra & Dufour (1990) for the nebula associated with AG Car.

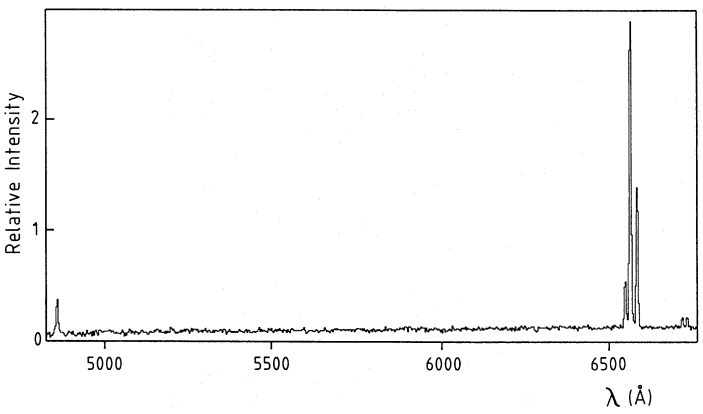


Fig. 8. The red part of the spectrum of the nebular arcs associated with HR Car. It was obtained in May 90 with the 1.52 m telescope. The Hβ, Hα, [N II] and [S II] lines are clearly identified

© European Southern Observatory • Provided by the NASA Astrophysics Data System

1991A&A...248..141H

Table 4. Relative intensities of the emission lines observed in the spectrum of the nebular arcs surrounding HR Car

Line	$F(\lambda)/F(H\beta)$	$I(\lambda)/I(H\beta)$
$H\gamma$	30	48
$H\beta$	100	100
$H\alpha$	846	285
[N II] λ6548	126	42
[N II] λ6583	365	123
[S II] λ6716	25	7.7
[S II] λ6731	26	8.0

Using the approximation $N/O = N^+/O^+$, which seems reasonable for low excitation H II regions (Pagel 1990; see also Mitra & Dufour 1990), we may calculate a lower limit of this abundance ratio, the [O II] λ3727 line being not detected in our spectra. Considering the [O II] lines due to the ambient nebula, which are well seen in our spectrograms, in order to fix the limit of visibility of the lines in this spectral region, we adopt $I([O\,II])/I(H\beta) \leqq 0.5$. We therefore obtain $N/O \geqq 0.4$, assuming for the nebula a simple one layer model in the low density limit. This value is significantly greater than the normal N/O abundance known in H II regions, 0.07 (Shaver et al. 1983), suggesting that the nebula contains nuclear processed material ejected by the star. We should remark that the presence of CO, detected by McGregor et al. (1988), could not easily explain this abundance anomaly since this CO is apparently formed in high density regions nearer the star.

Finally, adopting the distance of 5.4 kpc for HR Car, the projected distance of the arcs from the star is 0.34 and 0.45 pc while they are approximately 0.05 pc wide. If we assume that these arcs are confined in a cone originating from the star, we can roughly estimate their mass: $\sim 0.15\,M_\odot$, using the electron density determined above. With an expansion velocity of the order of a few 10 km s^{-1}, the arcs have a kinematic age of the order of 10^4 yr.

5. Discussion and conclusions

The present observations show that the characteristics of HR Car, including its variations, are very similar to those of other LBVs, belonging either to the Galaxy or to the LMC. This strengthens the view that these stars undergo the same kind of physical processes, essentially dominated by a variable mass-loss.

The presence in the spectrum of HR Car of broad emission lines indicative of high Doppler velocities suggests a link with the Of and WR stars which are the only stars known to display very broad lines in their spectra. The overabundance of N relative to O, in agreement with the predictions of the models of Maeder (1987) for massive stars, also supports the interpretation that HR Car is an evolved star in a transition stage towards WR stars.

The observations are also consistent with the view that the nebula surrounding HR Car is constituted, at least in part, of enriched material ejected by the star.

If we except the case of P Cygni which is still a matter of controversy (Stahl 1989), all the galactic LBVs are now shown to be surrounded by a nebula apparently related to the mass-loss of the star. Also the new LBV candidate WRA 751, recently discovered by Hu et al. (1990), is embedded in a faint emission nebula (de Winter 1990; Hutsemékers & Van Drom 1991) while many LBVs of the LMC have spectroscopically detected circumstellar shells (Walborn 1982b; Stahl & Wolf 1986).

It is particularly interesting that the nebula around HR Car has some common morphological features with the ring nebula associated with AG Car, namely the bipolarity and the possible jet. Since such a morphology is most naturally explained by a close binary hypothesis, it gives some support to this interpretation for the LBV phenomenon itself, as proposed by Gallagher (1989).

The nebula around HR Car shares other characteristics with the AG Car nebula like the low excitation, the physical conditions and the N/O overabundance (Mitra & Dufour 1990). However, the nebula surrounding AG Car looks more massive (Stahl 1987) and partly of reflective nature, especially the jet (McGregor et al. 1988b; Paresce & Nota 1989). This difference is in agreement with the fact that the amount of cool dust, which is assumed to be located in the visible nebula, has been found greater around AG Car than around HR Car (McGregor et al. 1988). The dust content may therefore constitute an important parameter for classifying the nebulosities associated with early-type highly luminous stars, especially if we compare with the nebulae observed around luminous Bep supergiants like HD 87643 or CD $-42°11721$ which are much more reflective (Surdej et al. 1981; Hutsemékers & Van Drom 1990).

Acknowledgements. It is a pleasure to thank here M. Heydari-Malayeri for kindly carrying out the CASPEC observations and reading the manuscript. It is also a pleasure to thank J. Surdej for a critical reading of the manuscript.

References

Auer L.H., Van Blerkom D., 1972, ApJ 178, 175
Banderia R., Focardi P., Altamore A., Rossi C., Stahl O., 1989, Physics of Luminous Blue Variables, IAU Coll. 113, p. 279
Bateson F.-M., 1987–1990, Circulars of the Roy. Astron. Soc. of New Zealand
Bernat A.P., Lambert D.L., 1978, PASP 90, 520
Caputo F., Viotti R., 1970, A&A 7, 266
Carlson E.D., Henize K.G., 1979, Vistas Astron. 23, 213
de Winter D., 1990 (private communication)
Gallagher J.S., 1989, Physics of Luminous Blue Variables, IAU Coll. 113, p. 185
Heydari-Malayeri M., Jarvis B., Gilliotte A., 1989, ESO Operating Manual No. 9
Hu J.Y., de Winter D., Thé P.S., Pérez M.R., 1990, A&A 227, L17
Humphreys R.M., 1989, Physics of Luminous Blue Variables, IAU Coll. 113, p. 3
Humphreys R.M., Lamers H.J.G.L.M., Hoekzema N., Cassatella A., 1989, A&A 218, L17
Hutsemékers D., Kohoutek L., 1988, A&AS 73, 217
Hutsemékers D., Van Drom E., 1990, A&A 238, 134
Hutsemékers D., Van Drom E., 1991, A&A, in press
Leitherer C., Appenzeller I., Klare G., Lamers H.J.G.L.M., Stahl O., Waters L.B.F.M., Wolf B., 1985, A&A 153, 168
Lindgren H., Gilliote A., 1989, ESO Operating Manual No. 8
Maeder A., 1987, A&A 173, 247
McGregor P.J., Finlayson K., Hyland A.R., Joy M., Harvey P.M., Lester D.F., 1988b, ApJ 329, 874
McGregor P.J., Hyland A.R., Hillier D.J., 1988, ApJ 324, 1071
Melnick J., Dekker H., D'Odorico S., 1989, ESO Operating Manual No. 4, ESO, Garching

© European Southern Observatory • Provided by the NASA Astrophysics Data System

1991A&A...248..141H

Mitra P.M., Dufour R.J., 1990, MNRAS 242, 98
Pagel B.E.J., 1991, Dynamical and Chemical Evolution of Galaxies, eds. Franco, Matteucci (in press)
Parese F., Nota A., 1989, ApJ 341, L43
Pasquini L., D'Odorico S., 1989, ESO Operating Manual No. 2
Shaver P.A., McGee R.X., Newton L.M., Danks A.C., Pottasch S.R., 1983, MNRAS 204, 53
Shore S.N., Brown D.N., Bopp B.W., Robinson C.R., Sanduleak N., Feldman P.D., 1990, ApJS 73, 461
Stahl O., 1987, A&A 182, 229
Stahl O., 1989, Physics of Luminous Blue Variables, IAU Coll. 113, Kluwer, Dordrecht, p. 149
Stahl O., Wolf B., 1986, A&A 158, 371
Stahl O., Wolf B., Klare G., Cassatella A., Krautter J., Persi P., Ferrari-Toniolo M., 1983, A&A 127, 49
Surdej A., Surdej J., Swings J.P., Wamsteker W., 1981, A&A 93, 285
Underhill A.B., Gilroy K.K., Hill G.M., 1989, AJ 98, 1063
van Genderen A.M., Thé P.S., Heemskerk M., Heynderickx D., van Kampen E., Kraakman H., Larsen I., Remijn L., Wanders I., van Weeren N., 1990, A&AS 82, 189
Viotti R., 1971, PASP 83, 170
Walborn N.R., 1982, ApJS 48, 145
Walborn N.R., 1982b, ApJ 256, 452
Walborn N.R., Fitzpatrick E.L., 1990, PASP 102, 379
Wolf B., 1989, A&A 217, 87
Wolf B., Appenzeller I., Stahl O., 1981, A&A 103, 94
Wolf B., Stahl O., 1982, A&A 112, 111
Yamashita Y., Nariai K., Norimoto Y., 1977, Atlas of Representative Stellar Spectra, University of Tokyo, Tokyo

Note added in proof: On April 24 and 26, 1991, we have recorded the spectrum of HR Car at the 1.52 m + B&C telescope with a spectral resolution comparable to that of the April 89 observations. In addition to the Balmer emission lines, the April 91 spectrum essentially shows bright Fe II lines with P Cygni type profiles. These Fe II lines are stronger than in the May 90 spectrum, Fe II λ4583 being nearly as prominent as Hγ. The He I lines are very faint while no [Fe II] is detected. The Balmer line profiles still consist of P Cygni type profiles superimposed on very broad wings. These observations show that the spectrum of HR Car is still evolving, following the trend noticed between the April 89 and the May 90 observations.

© European Southern Observatory • Provided by the NASA Astrophysics Data System

Article 2

The nature of the nebula associated with the Luminous Blue Variable star WRA751

D. Hutsemékers, E. Van Drom : Astron. Astrophys. 251, 620 (1991)

Dans cet article, nous présentons les résultats d'observations de l'étoile de type LBV WRA751. Sur des images obtenues au travers de filtres étroits centrés sur les principales raies nébulaires, nous détectons clairement la présence d'une nébuleuse de forme elliptique autour de l'étoile.

La spectroscopie à moyenne et haute dispersion indique qu'il s'agit d'une nébuleuse en expansion radiale autour de WRA751. Elle est caractérisée par une faible excitation et une surabondance de l'azote par rapport à l'oxygène.

Avec la découverte des nébuleuses associées à WRA751 et HR Car (Article 1), nous mettons en évidence le fait que quasi toutes les étoiles de type LBV sont entourées d'une nébuleuse. Les caractéristiques physiques de ces nébuleuses – masse, vitesse d'expansion, âge dynamique, rapport d'abondance N/O– sont très semblables et différentes de celles des nébuleuses planétaires associées aux étoiles de faible masse.

Ces observations suggèrent que l'éjection d'une nébuleuse est une étape importante de l'évolution des étoiles massives et une caractéristique essentielle des LBVs.

1991A&A...251..620H

Astron. Astrophys. 251, 620–624 (1991)

ASTRONOMY
AND
ASTROPHYSICS

The nature of the nebula associated with the luminous blue variable star WRA 751 ⋆

D. Hutsemékers and E. Van Drom

Institut d'Astrophysique, Université de Liège, 5 av. de Cointe, B-4000 Liège, Belgium

Received April 3, accepted June 27, 1991

Abstract. We present narrow-band filter imagery as well as medium to high resolution spectroscopy of the nebula surrounding the luminous blue variable (LBV) star WRA 751.

The nebula appears as a slowly expanding H II region of low excitation characterized by a significant N/O overabundance which may be due to the presence in the nebula of nuclear processed material ejected by the star.

With the recent discovery of a nebula around HR Car, all but one known galactic LBVs are now shown to be associated with a nebula. These nebulae have rather similar physical characteristics, one of the most important being that all of them apparently contain processed material.

Key words: luminous blue variable stars –mass-loss – emission nebulae – WRA 751

1. Introduction

WRA 751 is a galactic luminous blue variable star (LBV) recently identified by Hu et al. (1990).

These stars are very luminous evolved supergiants characterized by irregular outbursts or eruptions. Although no more than ten LBVs have been observed in the Galaxy and the Large Magellanic Cloud, they are generally considered as a short but physically important stage in the evolution of massive stars towards the WR stage. They constitute a quite unique group for studying the physics of the stars near the Humphreys-Davidson stability limit (Humphreys 1989).

One of the most interesting characteristics of the LBVs is certainly that some of them are surrounded by a small nebula apparently formed of matter ejected by the star and giving evidence for enrichment by nuclear processed material. The analysis of these nebulae may provide some important clues for understanding the LBV phenomenon and the evolutionary status of these stars.

Since, up to now, very few have been observed, we have started a systematic search and study of the nebulosities associated with luminous emission-line stars in order to better constrain their properties and to know if they constitute a new, quite homogeneous class of nebulae (Hutsemékers & Van Drom 1991b). Some results have already been presented for the cases of *CD*–42°11721 and HR Car (Hutsemékers & Van Drom 1990, 1991a). The current paper is devoted to the analysis of new observations of the nebula surrounding the LBV star WRA 751.

WRA 751 (= He3-591) has first been classified as a possible WR star by Henize (Roberts 1962) and later as a Bep type star by Carlson & Henize (1979). These authors have found that the spectrum of WRA 751 is characterized by strong Fe II and [Fe II] emission lines which can be as prominent as the Hβ emission line. On the basis of a photometric and spectroscopic investigation, Hu et al. (1990) suggest WRA 751 as a candidate for a new LBV. They report that this star is variable, very luminous ($M_{bol} = -9^m.6$) and has an equivalent spectral type O9.5. By comparing the spectral energy distributions, and more specifically the IR excesses, they note a definite similarity with AG Car and HR Car, two well known galactic LBVs which also show bright Fe II emission lines in their spectra. In a more detailed study confirming the LBV nature of WRA 751 (de Winter 1990), they also find that this star is most probably embedded in a nebulosity.

In the remainder of this paper, we present narrow-band CCD imagery and medium to high resolution spectroscopy of the nebula associated with WRA 751.

2. The observations

The observations of WRA 751 were carried out at the European Southern Observatory (ESO, La Silla). For all the observations, spectroscopy and imagery, the detectors were high resolution CCD chips of type RCA SID 503, 1024 × 640 pixels, each 15 μm^2.

The usual calibration frames (bias, darks, flat-fields as well as spectra of HeAr, ThAr and spectrophotometric standard stars) have been obtained. The reduction was performed using the standard IHAP and MIDAS packages available at ESO.

In most cases, we have obtained more than one frame for a given spectroscopic or imaging configuration. All these frames were reduced individually before their eventual comparison and/or addition.

2.1. Imagery

The images of WRA 751 and its nebula were obtained using the 2.2 m telescope equipped with the direct camera and the 3.6 m

Send offprint requests to: D. Hutsemékers

⋆ Based on observations collected at the European Southern Observatory (ESO, La Silla)

© European Southern Observatory • Provided by the NASA Astrophysics Data System

1991A&A...251..620H

Table 1. Imaging observations of WRA 751 and its nebula

Date	Instrument	Filter	λ_c/FWHM (Å)	Exposure time (min)	Seeing
27/04/90	2.2 m	[N II]	6580/20	5+10+15+30	1.″6
27/04/90	2.2 m	[O III]	5007/27	15	1.″8
29/04/90	2.2 m	Hα+[N II]	6572/40	15	1.″2
29/04/90	2.2 m	[N II]	6580/20	20	1.″0
29/04/90	2.2 m	[O III]	5007/27	60	1.″3
30/04/90	2.2 m	continuum	6450/61	10	1.″2
28/06/90	3.6 m+EFOSC	Hα+[N II]	6548/63	2+3	1.″4

Table 2. Spectroscopic observations of the nebula surrounding WRA 751

Date	Instrument	Spectral range (Å)	Resolution (Å)	Exposure time (min)
10/05/90	CAT+CES	6535–6592	0.12	2×30+60
15/05/90	1.5 m+B&C	4820–6800	4.7	15+30
16/05/90	1.5 m+B&C	4820–6800	4.7	60
17/05/90	1.5 m+B&C	3570–5510	4.9	2×60
18/05/90	1.5 m+B&C	3570–5510	4.9	60
19/05/90	1.5 m+B&C	4820–6800	4.7	60
28/06/90	3.6 m+EFOSC	3600–7000	6.4	10
01/12/90	1.5 m+B&C	4550–7450	5.3	50

telescope equipped with the EFOSC camera (Melnick et al. 1989). At the 2.2 m and 3.6 m telescopes, the RCA CCD pixel size of 15 μm corresponds to 0.″175 and 0.″337 on the sky, respectively. We essentially used narrow-band interference filters centered on the spectral lines of Hα, [N II], [O III] and a red continuum.

A summary of these imaging observations is given in Table 1, together with the filter characteristics.

We should notice that in nearly all frames, the image of WRA 751 does not reach the saturation level.

2.2. *Spectroscopy*

Low dispersion spectrograms of the nebula surrounding WRA 751 were obtained at the 1.52 m telescope equipped with a Boller and Chivens spectrograph (Heydari-Malayeri et al. 1989). They cover the 3570–7450 Å spectral range. In May 90, the 2.″0 wide slit was oriented E–W and positioned in order to cross the northern part of the nebula, i.e. at ~9″ from the star. In December 90, the spectrum was recorded using a 1.″1 wide slit oriented E–W and positioned ~8″ south of the star. An additional spectrogram was obtained with the EFOSC spectrograph attached to the 3.6 m telescope (Melnick et al. 1989), the 0.″75 wide slit being positioned north of the star and oriented E–W as in the May 90 B&C observations.

Because the slit has to be positioned quite near the star which is comparatively bright, the spectrum of the nebula is often contaminated by the stellar one. Fortunately, most of this contamination is spatially well defined on the two-dimensional spectrum and can therefore be eliminated during the reduction procedure. For the spectrograms obtained under bad seeing conditions, a small contamination is still present, its most unpleasant effect on the nebular spectrum being an increase of the Hα emission line intensity relative to other nebular emission lines like [N II] or [S II], Hα being very prominent in the spectrum of the star itself. We should therefore keep in mind that even for the good spectrogram discussed in the next section and for which the contamination is certainly small, the Hα emission line intensity might be slightly overestimated. Excepting this effect, the spectra recorded at different epochs essentially show the same features.

Higher dispersion spectrograms centered on the Hα emission line were obtained with the CES spectrograph attached to the CAT telescope (Lindgren & Gilliotte 1989), the full-length 2.″0 wide slit (decker removed) being positioned on the star.

The spectra of the nebula have been sky-subtracted, this subtraction taking also into account the eventual contamination due to the very faint diffuse nebulosity in which WRA 751 looks embedded. This ambient nebulosity, which does not seem related to WRA 751, is detectable on the ESO/SRC sky survey plates and most probably belongs to the Carina nebula located in front of the star.

Table 2 gives a summary of the spectroscopic observations.

3. The characteristics of the nebula

3.1. *The optical morphology*

Figure 1 illustrates an image of WRA 751 and its surroundings obtained in the Hα+[N II] light. The image clearly shows the presence of a nebula around WRA 751, whose morphology,

© European Southern Observatory • Provided by the NASA Astrophysics Data System

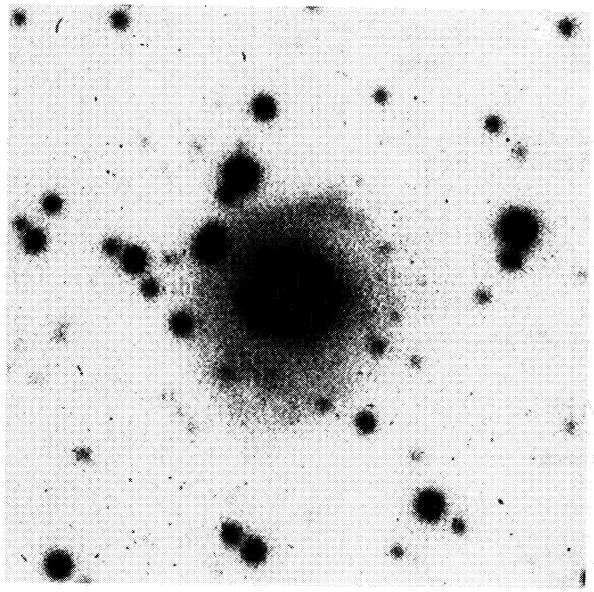


Fig. 1. An image of WRA 751 and its nebula in the Hα + [N II] light. This image is the weighted sum of the frames obtained at the 2.2 m telescope with the Hα + [N II] and [N II] filters. On all these frames the stellar image was not saturated. The resultant seeing is 1″.3 FWHM. The field is 1′ × 1′. North is up, east to the left

mainly symmetric relative to the star, gives evidence for a physical association. The nebula is roughly circular, 22″ in diameter, and slightly elongated in the NW–SE direction. It is apparently not detached from the star. The surface brightness is not uniform: the easter part of the nebula is brighter than the western part while an arc-shaped condensation is well seen at the NW edge. On our best seeing image, a similar feature is suspected at the opposite SE edge, as well as some filamentary condensations to the west.

On the frames obtained with the [O III] and continuum filters the nebula is not detected indicating that it is not of reflective nature but mainly of emission type.

We should also notice that WRA 751 is located in a rather crowded field of stars, two of them being quite near: one is located at 3″.2 E, 0″.8 S from WRA 751 and the other at 2″.9 N, 0″.7 E. The first of these stars, easter of WRA 751, is only 2^{m}.5 fainter in the [O III] filter and should therefore be taken into account in doing precise photometry.

3.2. The spectrum and physical characteristics

The optical spectrum of the nebula surrounding WRA 751 essentially consists of the Balmer emission lines Hα and Hβ in addition to the [N II] λλ 6548–6583 and [S II] λλ 6716–6731 forbidden lines (Fig. 2). It is quite remarkable by the low excitation, the strong Hα/Hβ ratio as well as the absence of oxygen lines like [O I] λ 6300, [O II] λλ 3726–3729 or [O III] λλ 4959–5007. Since the blue [O II] lines, if present, may be difficult to see due to the strong extinction indicated by the Hα/Hβ ratio, we have searched for the [O II] λλ 7320–7330 lines which are not observed in the spectrum recorded in December 90. Compared to the presence of bright [N II] lines in the spectrum, the absence or weakness of oxygen lines for three stages of ionization suggests a significant N/O overabundance in the nebula.

Assuming case B recombination with $T_e = 10^4$ K, we use the Hα/Hβ ratio to determine the logarithmic extinction coefficient $c(\mathrm{H}\beta) \simeq 3.1$ which corresponds to $A_V \simeq 6.5$. This high value confirms, in the limit of the uncertainties, the large extinction towards WRA 751 already found by Hu et al. (1990) from photometric observations. The corrected emission line ratios $I(\lambda)/I(\mathrm{H}\alpha)$ are given in Table 3, together with the measured ratios $F(\lambda)/F(\mathrm{H}\alpha)$.

Since the [N II] λ 5755 emission line is not observed in our spectra, only an upper limit to the electron temperature T_e may be estimated. Adopting $I([\mathrm{N\,II}]\lambda 5755)/I([\mathrm{N\,II}]\lambda 6548 + \lambda 6583) \leqq 0.03$, we find $T_e \leqq 15000$ K. The electron density is derived from the [S II] line ratio: $n_e \simeq 400\,\mathrm{cm}^{-3}$ (Aller, 1984). These values are typical of normal H II regions. Considering the [N II]/Hα, [S II]/Hα and [O III]/Hβ line ratios in the framework of classification diagrams like those constructed by Veilleux & Osterbrock (1987), we can see that the spectrum of the nebula associated with WRA 751 is compatible with the spectrum of a photoionized H II region in which N is overabundant relative to H while S/H is

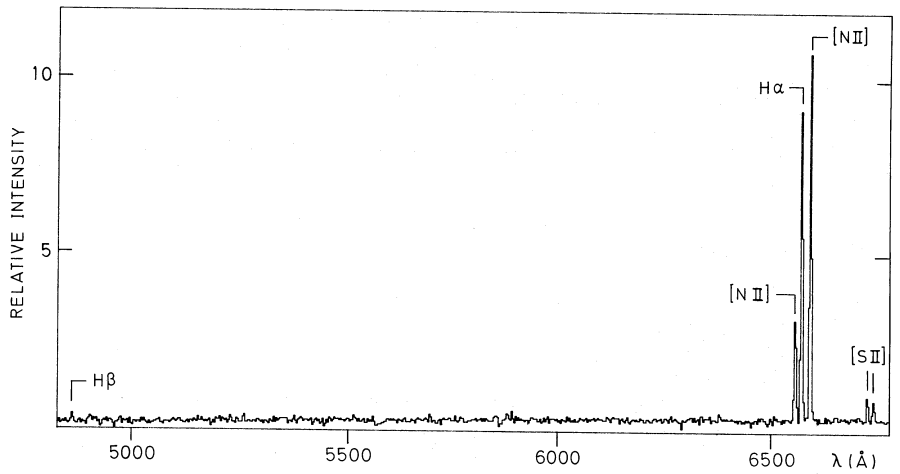


Fig. 2. A good red spectrum of the northern part of the nebula surrounding WRA 751. It was obtained on May 19, 1990 with the B&C spectrograph attached to the 1.52 m telescope

© European Southern Observatory • Provided by the NASA Astrophysics Data System

1991A&A...251..620H

Table 3. Relative intensities of the emission lines observed in the spectrum of the nebula surrounding WRA 751

Line	$F(\lambda)/F(\mathrm{H}\alpha)$	$I(\lambda)/I(\mathrm{H}\alpha)$
Hβ	2.8:	35:
Hα	100	100
[N II] λ6548	37	37
[N II] λ6583	113	113
[S II] λ6716	6.7	5.8
[S II] λ6731	6.3	5.4

normal. It is very interesting to notice that these emission line ratios are nearly identical to those measured in the spectrum of M1–67, the ring nebula surrounding the WN 8 star 209 BAC, in which Esteban et al. (1991) have recently found a remarkable abundance pattern i.e. a strong N/O overabundance due to both N/H enhancement and O/H deficiency.

Bright nebular [N II] lines are also well seen on the CES spectra, superimposed on the stellar spectrum and significantly narrower than the stellar Hα emission line. These lines are resolved in two peaks of nearly equal brightness suggesting that the nebula is expanding. From the separation of the peaks, we measure an expansion velocity of $\sim 26\,\mathrm{km\,s^{-1}}$, while the FWHM/2 gives $\sim 39\,\mathrm{km\,s^{-1}}$. In fact, the [N II] and Hα lines are spatially resolved on the two-dimensional CES spectra, clearly extending out of the stellar spectrum (see Fig. 3). The [N II]/Hα intensity ratio measured on this spatially extended nebular spectrum is in agreement with the values reported in Table 3. Despite the low signal-to-noise ratio (the observations were not initially intended for this purpose), we can see that the overall velocity distribution of these lines roughly corresponds to the symmetric expansion of a sphere of non uniform brightness, more material being redshifted than blueshifted at least for this position of the slit (Fig. 3). Very interesting is the fact that the part of the [N II] lines which is superimposed on the stellar spectrum has a much greater intensity. These lines may be partially formed near the star but not in the stellar wind whose terminal velocity, measured from the Hα P Cygni type profile, amounts to $190\,\mathrm{km\,s^{-1}}$. On low dispersion spectra of the star recorded at the same time as those of the nebula (in May 90), faint [S II] lines are clearly observed in addition to the [N II] ones but with an intensity ratio $I(\lambda 6716)/I(\lambda 6731) \simeq 0.6$ indicating that a much higher electron density, $n_e \simeq 2500\,\mathrm{cm^{-3}}$, prevails closer to the star. On the other hand, the intensity of these [S II] lines relative to the [N II] lines is the same as in Table 3, giving no indication for a different excitation mechanism. These observations suggest that the nebula is extending up to close to the star, its density increasing towards the center with apparently no change of the expansion velocity. They also indicate that the distribution of matter in the nebula significantly departs from the spherical symmetry, as suspected from the imagery.

Finally, adopting a kinematic distance of 7 kpc determined from the heliocentric radial velocity of the [N II] lines, $+24\,\mathrm{km\,s^{-1}}$, and in good agreement with the distance suggested by the large extinction (Hu et al. 1990), the nebula has a radius of 0.38 pc. Assuming a constant expansion velocity of $26\,\mathrm{km\,s^{-1}}$, this radius corresponds to a kinematic age of $1.5\,10^4$ years. With the approximation that the nebula is spherical and homogeneous, we may also give a rough estimate for the mass of the ionized gas: $\sim 3.2\,M_\odot$.

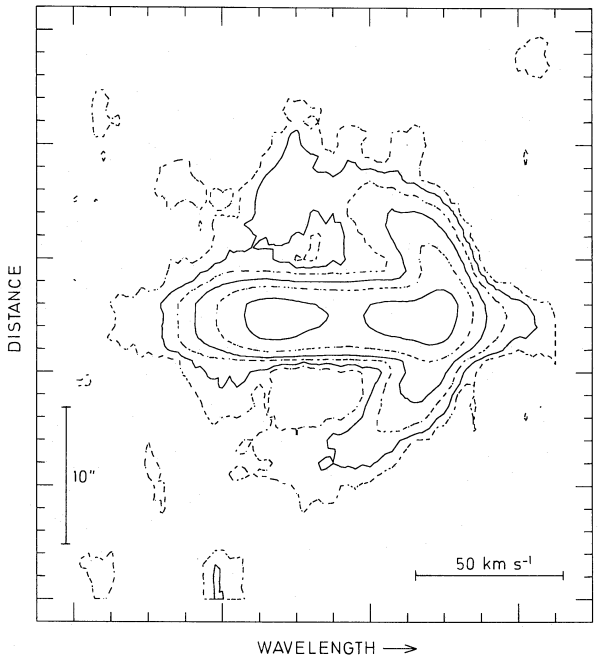


Fig. 3. Smoothed contour plots of the [N II] λ 6583 emission line observed in the CAT + CES spectrum of WRA 751. The adjacent stellar continuum has been subtracted. Between the contours, the intensity increases by a factor 2. The slit was roughly oriented NE–SW, NE at the top (because the field is rotating at the CAT, the orientation of the slit is not precisely known)

4. Discussion and conclusions

From the present observations, the nebula associated with WRA 751 appears as an expanding H II region of low excitation and non uniform brightness. It shows a significant N/O overabundance which suggests that it is constituted, at least in part, of processed material most probably ejected by the star whose mass-loss, as for other LBVs, should be quite strong. The data are in agreement with the interpretation that WRA 751 is a very luminous evolved star.

The presence of a nebula around WRA 751 strengthens the perspective that the formation of a nebula is an important characteristic of the LBV evolutionary stage: if we except P Cygni, all the other galactic LBVs – η Car, AG Car, HR Car as well as the possibly related star He 3-519 – are embedded in nebulosities while many LBVs of the LMC have spectroscopically detected circumstellar shells (Walborn 1982; Wolf & Stahl 1986), some of them being resolved by direct imagery (Stahl 1987). Despite definite differences, the physical and chemical characteristics prevailing in the nebula associated with WRA 751 are in first approximation remarkably similar to those reported for the nebulae surrounding AG Car and HR Car (Mitra & Dufour 1990; Hutsemékers & Van Drom 1991a). Also the nebulae resolved around two LMC Ofpe/WN9 stars and the one around He3-519 have comparable masses and densities (Stahl 1987). The majority of these nebulae seem to constitute a class of objects whose characteristics, significantly different from those of classical planetary nebulae, appear rather homogeneous, suggesting that their formation may be due to a common physical mechanism. We should nevertheless remark that, unlike the case of AG Car, the nebula surrounding

© European Southern Observatory • Provided by the NASA Astrophysics Data System

1991A&A...251..620H

WRA 751 does not appear detached from the star, suggesting that it is due more to a continuous mass-loss rather than to a sudden outburst.

In this view, it is striking that P Cygni, whose luminosity is intermediate between that of AG Car and HR Car (Humphreys 1989), is not surrounded by a comparable nebulosity (the radio arc detected in the vicinity of P Cygni is not really comparable (Baars & Wendker 1987; Lamers 1989; see also Stahl 1989). But, if the stellar spectra of both AG Car and HR Car are, at some epochs, nearly identical to that of P Cygni, they nevertheless reveal a much stronger N/O overabundance: the oxygen lines are practically absent from the spectra of AG Car and HR Car (Caputo & Viotti 1970; Hutsemékers & Kohoutek 1988; Hutsemékers & Van Drom 1991a) while they are well seen in that of P Cygni (Luud 1967). Since a significant N/O overabundance is also observed in the nebulae surrounding AG Car and HR Car (Mitra & Dufour 1990; Hutsemékers & Van Drom 1991a), it is tempting to say that the ejection of a nebula arises at a peculiar moment of the LBV stage, when a sufficient amount of nuclear processed matter is present at the stellar surface. In this view, P Cygni could be in a younger evolutionary stage than AG Car and HR Car. It would be worthwile to obtain a high resolution spectrum of WRA 751 near the minimum phase in order to see if this star also shows such a strong N/O overabundance as AG Car and HR Car.

Finally, it is particularly interesting that the physical conditions prevailing in the nebula associated with WRA 751 are apparently similar to those prevailing in some WR ring nebulae like M1–67, especially if we consider the N/O ratio (Vilchez & Esteban 1991; Esteban et al. 1991). This gives further support to the idea that there exists a close relationship between these two classes of stars.

It is definitely clear that before one draws definite conclusions more nebulae of this kind should be known and studied. In a future work, we will analyse other objects which could be related to those discussed in this paper.

Acknowledgements. Part of this work was done when the authors were at the European Southern Observatory, La Silla. This research is also supported in part by contract ARC 90/94-140 "Action de recherche concertée de la Communauté Française" (Belgium).

References

Aller L. H., 1984, Physics of Gaseous Nebulae. Reidel, Dordrecht
Baars J. W. M., Wendker H. J., 1987, A&A 181, 210
Caputo F., Viotti R., 1970, A&A 7, 266
Carlson E. D., Henize K. G., 1979, Vistas Astron. 23, 213
de Winter D., 1990 (private communication)
Esteban C., Vilchez J. M., Smith L. J., Manchado A., 1991, A&A 244, 205
Heydari-Malayeri M., Jarvis B., Gilliotte A., 1989, ESO Operating Manual No. 9
Hu J. Y., de Winter D., Thé P. S., Pérez M. R., 1990, A&A 227, L17
Humphreys R. M., 1989, Physics of Luminous Blue Variables. IAU Coll. 113, Kluwer, Dordrecht, p. 3
Hutsemékers D., Kohoutek L., 1988, A&AS 73, 217
Hutsemékers D., Van Drom E., 1990, A&A 238, 134
Hutsemékers D., Van Drom E., 1991a, A&A 248, 141
Hutsemékers D., Van Drom E., 1991b (in preparation)
Lamers H. J. G. L. M., 1989, Physics of Luminous Blue Variables. IAU Coll. 113, Kluwer, Dordrecht, p. 135
Lindgren H., Gilliote A., 1989, ESO Operating Manual No 8
Luud L. S., 1967, SvA 11, 211
Melnick J., Dekker H., D'Odorico S., 1989, ESO Operating Manual No 4
Mitra P. M., Dufour R. J., 1990, MNRAS 242, 98
Roberts M. S., 1962, AJ 67, 79
Stahl O., 1987, A&A 182, 229
Stahl O., 1989, Physics of Luminous Blue Variables, IAU Coll. 113, Kluwer, Dordrecht, p. 149
Stahl O., Wolf B., 1986, A&A 158, 371
Veilleux S., Osterbrock D. E., 1987, ApJS 63, 295
Vilchez J. M., Esteban C., 1991, Wolf-Rayet stars and Interrelations with Other Massive Stars in Galaxies. IAU Symp. 143, Reidel, Dordrecht, p. 379
Walborn N. R., 1982, ApJ 256, 452

© European Southern Observatory • Provided by the NASA Astrophysics Data System

Article 3

A dusty nebula around the Luminous Blue Variable candidate HD168625

D. Hutsemékers, E. Van Drom, E. Gosset, J. Melnick : Astron. Astrophys. 290, 906 (1994)

En utilisant les mêmes techniques que précédemment ainsi que l'imagerie dans le proche infra-rouge, nous rapportons la découverte d'une nébuleuse de type LBV autour de l'étoile HD168625, une supergéante de type B.

Nous montrons que cette nébuleuse complexe consiste en une coquille de gaz et de poussière en expansion d'où semble émerger une nébuleuse bipolaire en émission. Nous notons également que la poussière diffusant la lumière stellaire s'étend au-delà du gaz ionisé.

Malgré une masse plus faible, les caractéristiques physiques que nous mesurons pour cette nébuleuse sont compatibles avec celles des autres nébuleuses de type LBV, suggérant que HD168625 est bien une étoile de ce type, même si des variations photométriques importantes n'ont pas été détectées.

Enfin, nous notons l'absence de nébulosité autour de la LBV voisine HD168607.

1994A&A...290..906H

Astron. Astrophys. 290, 906–914 (1994)

ASTRONOMY
AND
ASTROPHYSICS

A dusty nebula around the luminous blue variable candidate HD 168625*

D. Hutsemékers[1], E. Van Drom[1], E. Gosset[1], and J. Melnick[2]**

[1] Institut d'Astrophysique, Université de Liège, 5 av. de Cointe, B-4000 Liège, Belgium
[2] European Southern Observatory, La Silla, Casilla 19001, Santiago 19, Chile

Received 14 March 1994 / Accepted 25 May 1994

Abstract. On the basis of narrow-band visible and near-infrared imagery as well as high-resolution spectroscopy, we report the discovery of a new LBV-type nebula around the B supergiant HD 168625. We find that it essentially consists of a dusty expanding shell from which seems to emerge a bipolar emission nebula, the whole embedded in a reflection nebulosity. The inner shell is stratified: the continuum emission arises beyond the ionized gas, and is possibly due to scattering of stellar light by large dust grains or to non-equilibrium dust emission. The unexpected presence of unidentified infrared emission bands (UIRs) in the spectrum of this object is also discussed.

We finally report the non-detection of a comparable nebula around the nearby LBV HD 168607.

Key words: luminous blue variable stars – circumstellar matter – emission nebulae – dust – HD 168625 – HD 168607

1. Introduction

Luminous blue variables (LBVs) are extreme supergiant stars located in the Hertzsprung-Russell (HR) diagram near the Humphreys-Davidson limit. They are generally thought to represent a short-lived intermediate stage in the evolution of massive stars from O to WR stars (cf. reviews by Humphreys 1989; Hillier 1992; Wolf 1992). About ten LBVs are presently known in our Galaxy.

One of the most remarkable characteristics of LBVs is that some of them are surrounded by a ring nebula apparently constituted of nuclear processed material ejected by the star (cf. reviews by Stahl 1989; Chu 1991; Smith 1993). In order to see if the association with a nebula is a generic property of these stars, we have searched for nebulosities around galactic LBV candidates using CCD imaging through narrow-band filters which isolate nebular lines. In addition to the previously known nebulae surrounding η Car, AG Car, and He3-519, nebulae have been found around HR Car and WRA751 (Hutsemékers & Van Drom 1991a, 1991b). The present paper is devoted to the study of a new case of LBV-type ring nebula, detected around HD 168625.

HD 168625 (= He3-1681 = SAO161375) is a very luminous B-type star which has been recently studied by Chentsov & Luud (1989) and van Genderen et al. (1992). We adopt the stellar parameters used by van Genderen et al. (1992), i.e. a distance d = 2.2 kpc, a bolometric magnitude $M_{\rm bol} = -8.6$, and an effective temperature $T_{\rm eff}$ = 12 000 K. While located in the same part of the HR diagram as HR Car and HD 168607, two bona fide LBVs (e.g. van Genderen et al. 1992), HD 168625 was not recognized as a LBV due to the weakness of its emission lines and to the low amplitude of its photometric variations. But, HR Car itself would be discarded from the LBV class if only classified using its position in the "Maximum light amplitude – Effective temperature" diagram of van Genderen et al. (1992). Also P Cyg and η Car would not be recognized as LBVs without the historical evidence for outbursts which occurred centuries ago. The photometric behavior is therefore not sufficient to invalidate the classification of HD 168625 as a LBV, especially if we note that spectral variations have possibly been observed: the spectral type of HD 168625 quoted in the literature varies between B2 (Popper & Seyfert 1940), B8 (Morgan et al. 1955), and B5.6 (Chentsov & Luud 1989), while the spectral type of HD 168607, located only $\sim 1'$ apart and described by the same authors, always remained between B8 and B9.4. Further, although weak, Hα is clearly seen on our high resolution spectrograms with a P Cygni line profile indicating a wind terminal velocity of $\sim$ 250 km s^{-1}, typical of LBVs. Also, like most LBVs known to be associated with a nebula, HD 168625 is surrounded by cool dust detected by the Infrared Astronomical Satellite IRAS (Chentsov & Luud 1989; Hutsemékers 1994, hereafter Paper I). With the discovery of an optical nebula around it, we consider that HD 168625 is a good LBV candidate.

The present paper is divided as follows: in Sect. 2, we present the imaging and spectroscopic observations. The characteristics

Send offprint requests to: D. Hutsemékers

* Based on observations collected at the European Southern Observatory (ESO, La Silla)

** Also, chercheur qualifié au FNRS

© European Southern Observatory • Provided by the NASA Astrophysics Data System

1994A&A...290..906H

Table 1. Visible imaging observations

Date	Instrument	Filter (ESO n°)	λ_c/FWHM	Seeing
11/03/91	2.2m + CCD#5	Hα + [NII] (#436)	6560/63 Å	1.″5
22/04/91	3.6m + EFOSC1 + CCD#8	Hα + [NII] (#691)	6566/61 Å	1.″7
23/04/91	3.6m + EFOSC1 + CCD#8	Hα + [NII] (#691)	6566/61 Å	1.″1
23/04/91	3.6m + EFOSC1 + CCD#8	Continuum (#695)	6645/63 Å	0.″9
15/05/91	3.6m + EFOSC1 + CCD#8	Hα + [NII] (#691)	6566/61 Å	1.″7
15/05/91	3.6m + EFOSC1 + CCD#8	Continuum (#695)	6645/63 Å	1.″7
30/04/92	3.6m + EFOSC1 + CCD#26	Hα + [NII] (#691)	6566/61 Å	1.″2
30/04/92	3.6m + EFOSC1 + CCD#26	Continuum (#695)	6645/63 Å	1.″2
13/05/93	3.6m + EFOSC1 + CCD#26	Gunn z (#615)	8382/bb Å	1.″0
15/05/93	2.2m + EFOSC2 + CCD#19	Gunn z (#619)	8420/bb Å	1.″0

Table 2. Near-infrared imaging observations

Date	Filter	$\lambda_c/\Delta\lambda$	Seeing
10/05/93	H_2	2.121/0.039 μm	1.″6
10/05/93	Brγ	2.164/0.037 μm	1.″4
10/05/93	Continuum	2.177/0.038 μm	1.″4
10/05/93	CO	2.365/0.088 μm	1.″5
12/05/93	Continuum	2.177/0.038 μm	1.″6

of the nebula are described in Sect. 3. A few comments on the circumstellar environment of the nearby LBV HD 168607 are given in Sect. 4, while discussion and conclusions form the last section.

2. The observations

The observations have been carried out at the European Southern Observatory (ESO, La Silla) from March 1991 to July 1993, using the 3.6m telescope equipped with the EFOSC1 spectrometer and camera (Melnick et al. 1989), the 2.2m telescope equipped with the direct camera, the EFOSC2 spectrometer and camera (Melnick 1993) and the infrared camera IRAC2 (Moorwood et al. 1992), the 1.4m CAT telescope feeding the CES spectrometer (Lindgren & Gilliotte 1989). More information on the telescopes, detectors and filters may be found in the ESO Users manual (Schwarz & Melnick 1993).

All the reductions were performed using standard procedures in the MIDAS application package developed at ESO.

2.1. Visible imagery

We have obtained CCD images of HD 168625 and its surrounding nebula using broad- and narrow-band filters, the latter centered on Hα and a nearby continuum. The journal of observations is given in Table 1. The numbers characterizing CCDs and filters are those currently in use at ESO.

In this paper, we mainly consider the EFOSC1 imaging observations of April 92 and May 93, obtained in better seeing conditions and with a cleaner CCD. The CCD#26 is a TEK 512×512 with 27×27 μm^2 pixels corresponding to 0.″61×0.″61 on the sky. The April 92 observations consist of 1^m and 5^m exposures obtained in both the Hα+[NII] and continuum filters. The 8″ coronographic spot of EFOSC1 was centered at best on the star to avoid effects due to saturation. Faint spikes nevertheless remain. For calibration purposes, $0^s.1$ unsaturated exposures of the unmasked star were also secured in both filters, as well as 1^m exposures of the AG Car nebula in the Hα+[NII] filter with the same coronographic spot. The May 93 images consist of 20^s exposures obtained in a broad-band Gunn z filter with the 3″ coronographic spot centered on the star. Due to a better alignment of the Lyot stop, the faint contaminating spikes are no longer present. Dark-subtraction and flat-fielding were performed in the standard way.

It is important to note that the observations obtained in worse but different conditions essentially confirm the results presented in Sect. 3, within the limits fixed by their lower quality.

2.2. Near-infrared imagery

Near-infrared images of HD 168625 and its nebula were obtained in May 93 using the IRAC2 camera and narrow-band filters centered on various spectral lines (cf. Table 2). The detector was a Rockwell 256×256 pixel NICMOS3 array. With the B objective, the pixel size of 40 μm corresponds to 0.″27 on the sky.

For one image in a given filter, we have obtained 5 exposures of the object separated by 4 exposures of the sky successively sampling north, east, south and west of the object; one exposure consists of the average of 100 integrations of 1^s each. Even with this short integration time (the shortest possible), the images of HD 168625 are slightly saturated. Since the weather was cloudy, no calibration frames (standard stars,...) were obtained. Flat-fields were secured by taking difference images of the diffusing screen in the dome with a halogen lamp alternately on and off.

The reductions were performed as follows: after subtracting from each of the 5 object frames the median of the 4 sky

© European Southern Observatory • Provided by the NASA Astrophysics Data System

1994A&A...290..906H

Table 3. High-resolution spectroscopic observations

Date	UT (beginning)	Spectral range	Resolution	Exposure time	Position angle
12/07/93	$00^h\,00^m$	6538–6593 Å	0.12 Å	60^m	267–279°
12/07/93	$02^h\,53^m$	6538–6593 Å	0.12 Å	60^m	308–327°
12/07/93	$05^h\,03^m$	6538–6593 Å	0.12 Å	$45^m \times 2$	354–34°
13/07/93	$23^h\,52^m$	6698–6743 Å	0.12 Å	60^m	267–279°
14/07/93	$01^h\,28^m$	6698–6743 Å	0.12 Å	60^m	287–303°
14/07/93	$06^h\,40^m$	6538–6593 Å	0.12 Å	60^m	40–67°

frames, these frames were flat-fielded, cleaned for bad pixels, recentered, and finally averaged. After the reduction, faint features (spikes, ghosts, rings,...) are still present, contaminating the images (cf. Moorwood et al. 1992).

Several stars of comparable brightness have been observed and reduced similarly in order to construct a stellar profile which may eventually be subtracted. Useful mean stellar profiles without field stars have been obtained by taking the median of 4 frames centered on a given star and 90°-rotated.

2.3. High-resolution spectroscopy

High-resolution spectra of HD 168625 and its nebula were obtained in July 93 with the short camera of the CES spectrometer in wavelength ranges centered on the Hα+[NII] and [SII] $\lambda\lambda$6717–6731 emission lines. The journal of observations is given in Table 3. The seeing was typically 1.″6 and 1.″2 during the first and the second night, respectively. In spite of rather long exposure times, the nebular [SII] lines are underexposed. In order to estimate the shape of the continuum, two stars, HR6878 and HD 211998, were observed in similar conditions. The spectrum of a Th-Ar lamp has been recorded for the wavelength calibration.

The detector was a 1024×640 RCA CCD (ESO #9) with 15×15 μm^2 pixels corresponding to 0.″83 and 1.″02 along and across the slit respectively. The slit was approximately 20″ long; its width was 2.2″ for the Hα+[NII] spectral range and 2.3″ for the [SII] range. At the CAT, the position of the slit cannot be kept fixed on the sky: the field rotates around the star such that, during a given exposure, the slit sweeps a range of position angles. The position angles have been evaluated according to calculations by G. Artzner (private communication). They are given in Table 3, counted anti-clockwise from the N–S direction, north up, east to the left.

3. The characteristics of the nebula

3.1. The interstellar environment

HD 168625 and HD 168607 are twin bright stars located about 15′ southeast from the core of M17, the Omega nebula, and presumably at the same distance (cf. van Genderen et al. 1992, and references therein). Nice pictures of the Omega nebula obtained by T. Neckel with the ESO/MPI 2.2m telescope and R. West with the ESO 3.6m telescope are displayed in the atlases of Neckel & Vehrenberg (1987) and Laustsen et al. (1987), respectively. The diffuse aspect of HD 168625 may already be noticed.

On the plate shown by Laustsen et al. (1987), both stars seem to lie in some kind of cavity delimited to the north by a sharp arc in Omega nebula, to the east and to the west by faint diffuse clouds located about 8′ from the stars. The western nebulosity has a filamentary morphology reminiscent of wind-blown shells. This suggests that at least one of these stars (HD 168607, better centered on the cavity?) could be physically related to the Omega nebula.

A CCD picture of HD 168625 and its surroundings imaged with the Hα+[NII] filter is illustrated in Fig. 1. Apart from the small nebula seen immediately around HD 168625, many features are present, the most remarkable being a series of condensations within $\sim$ 1′ from HD 168625, and a dark lane immediately south. Similar condensations are also seen south of the darker region, suggesting that the nebular material is everywhere, most probably belonging to the Omega nebula. It is not clear whether these nebulosities are physically related to HD 168625 or not, but there is no indication from their morphology that they are. On the contrary, the small nebula seen around HD 168625 is clearly associated with the star, as discussed below.

3.2. Description and morphology

The nebula surrounding HD 168625 is best seen in Fig. 2 which illustrates a Hα+[NII] image, continuum subtracted. This picture is the difference of two 5^m exposure frames obtained in April 92 with the Hα+[NII] and λ6645 continuum filters. The seeing was similar during the two exposures. Before subtraction, the continuum frame was recentered and multiplied by 0.98, the ratio of the stellar fluxes in the Hα+[NII] and continuum filters measured on the frames where the image of the star is not saturated. Since the stellar intrinsic Hα emission line is faint and of P Cygni type, this ratio is mainly a continuum flux ratio and the field stars essentially disappear (when unsaturated). The instrumental spikes and stellar profile wings are also removed, therefore providing us with a rather clean image of the nebula.

The nebula surrounding HD 168625 is an emission nebula and its symmetry relative to the star indicates a physical asso-

© European Southern Observatory • Provided by the NASA Astrophysics Data System

1994A&A...290..906H

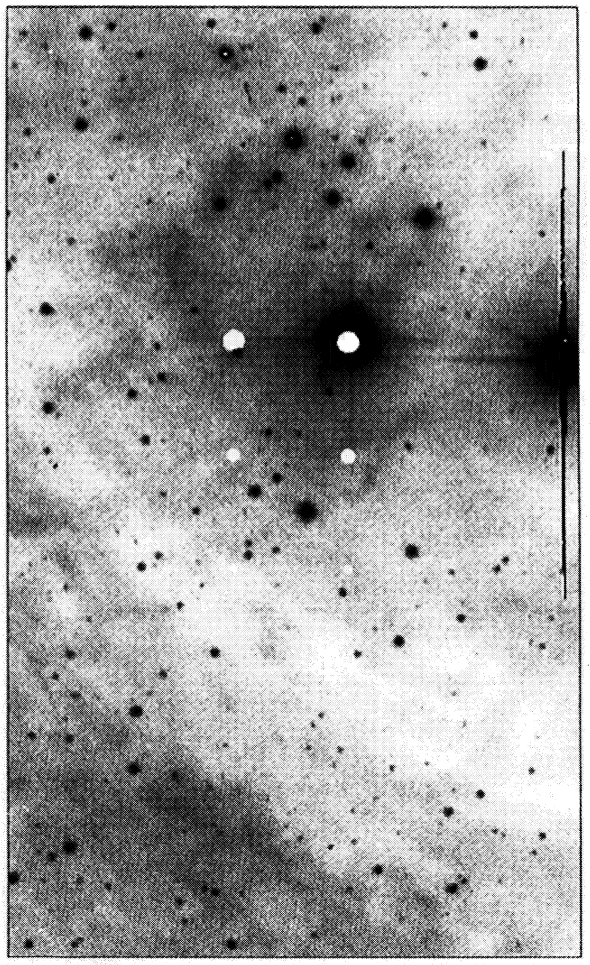


Fig. 1. An image of HD 168625 and its surroundings obtained with the Hα+[NII] filter. The field is $3' \times 5'$. North is up and east to the left. This 5^m exposure frame has been obtained on April 92 with the 3.6m telescope and EFOSC1. The six coronographic spots are clearly seen, the largest being positioned on HD 168625. A small nebula may be identified around the star. The nebular features everywhere on the frame are due to the Omega nebula. The saturated star is HD 168607, which is comparable in brightness to HD 168625. The intensity scale is logarithmic

ciation. It seems constituted of two regions:
(1) An inner $10\farcs0 \times 13\farcs5$ elliptical ring detached from the star and with a major axis oriented SE–NW. The SW part of the ring is brighter with a sharply defined outer edge.
(2) An outer nebula on which the ring seems superimposed. Its size is $\sim 16'' \times 21''$. Its major axis is oriented NE–SW, perpendicular to that of the ring. The NE part is brighter and its edge well defined on the background. It appears horn- or ansa-shaped. A similar morphology is suspected for the fainter SW part, suggesting a bipolar morphology.

The inner ring may also be seen on the images obtained with the λ6645 continuum and Gunn z filters (cf. Fig. 3). In both filters, it is slightly but definitely larger than the Hα+[NII] ring, just surrounding the latter. The outer bipolar Hα+[NII] nebula is not detected in these continuum filters. In addition, a diffuse, quite symmetric but patchy nebulosity is observed all around the star up to $\sim 20''$, contaminating the image of the ring (cf. Figs. 1 and 3). Its most remarkable feature is a clumpy elongation extending SE. This nebulosity is not seen on the difference image illustrated in Fig. 2 because it is equally present on the Hα+[NII] and λ6645 continuum frames. This, with a rough brightness decline with distance from the star, suggests that this nebulosity is mainly a reflection nebula which scatters the stellar light.

Near-infrared images of HD 168625 and its nebula are shown in Figs. 4 and 5. We did not detect any significant morphological difference between the images obtained in the different near-infrared filters. This indicates that the near-infrared emission is dominated by the continuum. We therefore only consider an average of the images, which corresponds to an effective wavelength of ~ 2.2 μm.

The ring is clearly seen in the 2.2 μm continuum. It is definitely larger ($\sim 12'' \times 15''$) than the Hα+[NII] ring, and comparable in size to that observed in the visible continuum. It is however better resolved and less contaminated by the extended reflection nebulosity which is not seen at these near-infrared wavelengths. It appears inhomogeneous with a sharp SW edge and a fainter, more diffuse NE part. The ring is possibly linked to the star in its southern part; a bar-like feature oriented SE–NW and roughly crossing the star is also apparent. As in the visible continuum, the outer bipolar Hα+[NII] nebula is not seen in the 2.2 μm continuum.

The ring appears unusually bright in the continuum: after roughly subtracting a stellar profile, we find that its surface brightness in the λ6645 continuum filter is approximately 20 % that of the Hα+[NII] ring. While this estimate is uncertain, it is too large to be only explained in terms of thermal continuum emission processes which include bound-free, free-free and two-photon recombinations of hydrogen and helium. Scattering of stellar light may be invoked. However, if we compare the continuum surface brightness of the ring to that of the outer reflection nebulosity, we note that the ring is comparatively brighter with increasing wavelengths; for example, in the λ6645 continuum filter, the SE elongation of the outer nebulosity is as bright as the ring, while it is significantly fainter in the Gunn z filter, and undetected at near-infrared wavelengths. If this progressive disappearance of the outer reflection nebulosity with increasing wavelengths is naturally explained by scattering, the different wavelength dependence of the continuum emission from the ring would require scattering by much larger grains; this is a reasonable hypothesis since the presence of large grains has already been suggested for explaining the dust properties in other LBV nebulae, like those around AG Car and η Car (McGregor et al. 1988a, 1988b; Paresce & Nota 1989). On the other hand, this excess of continuum radiation may be similar to the non-thermal non-scattering dust

© European Southern Observatory • Provided by the NASA Astrophysics Data System

1994A&A...290..906H

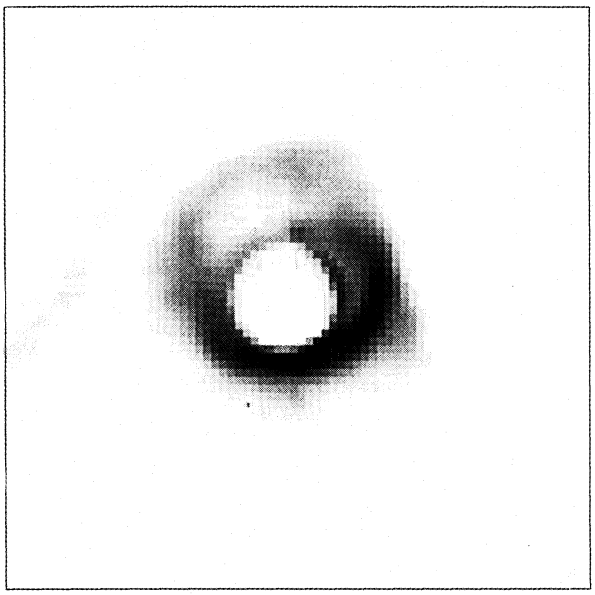


Fig. 2. A Hα+[NII] image of the nebula associated with HD 168625. This is the difference of frames obtained in April 92 with the Hα+[NII] and λ6645 continuum filters. The field is 74 pixels $\times$ 74 pixels i.e. $\sim$ 45″ $\times$ 45″; the star is at the center of the picture. North is up and east to the left. The coronographic spot is not exactly centered on the star but slightly east

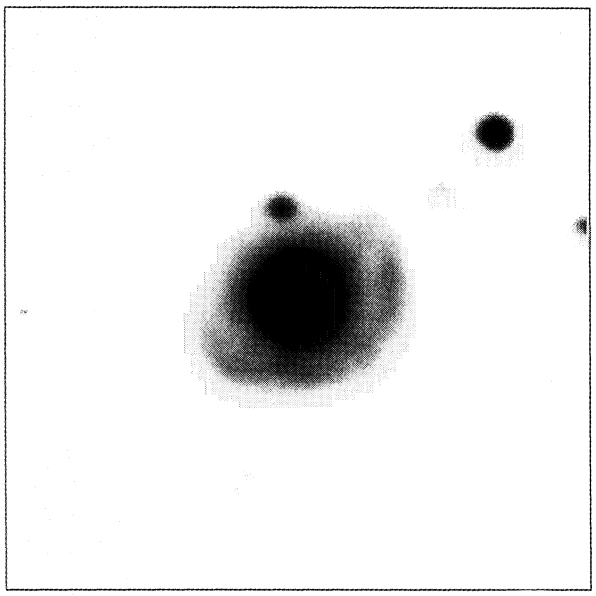


Fig. 4. A near-infrared continuum image of HD 168625 obtained in May 93. This is the average of frames obtained in different narrow-band filters. The mean effective wavelength is $\sim$ 2.2μm. The field is 167 pixels $\times$ 167 pixels i.e. $\sim$ 45″ $\times$ 45″; the star is at the center of the picture. North is up and east to the left

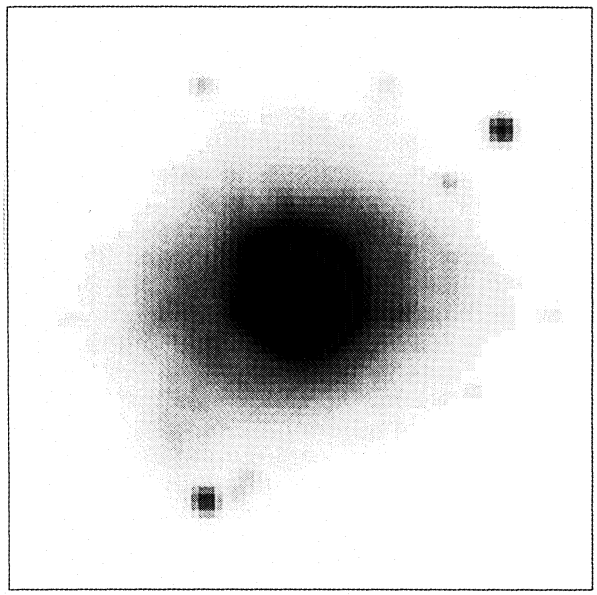


Fig. 3. A continuum image of the nebula obtained in May 93 with the Gunn z filter. The field is 74 pixels $\times$ 74 pixels i.e. $\sim$ 45″ $\times$ 45″; the star is at the center of the picture. North is up and east to the left

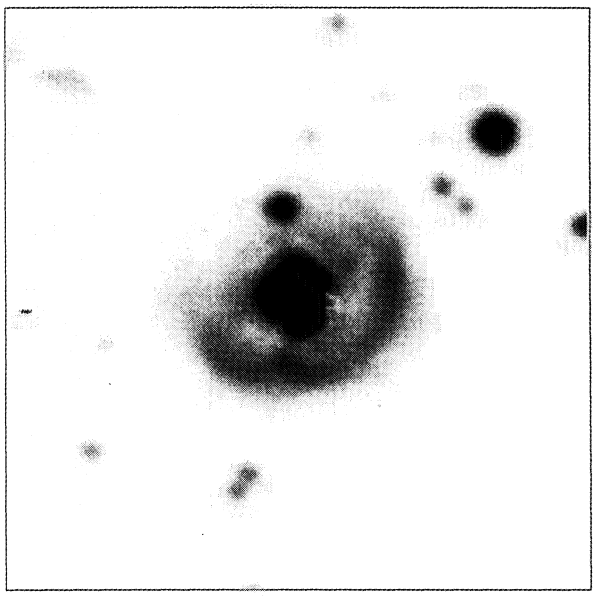


Fig. 5. Same as Fig. 4 but with a stellar profile subtracted. Since the subtraction is not perfect namely due to the saturation of the stellar images, the structure of the central part is not reliable

© European Southern Observatory • Provided by the NASA Astrophysics Data System

1994A&A...290..906H

continuum emission which has been observed in various types of nebulae. Indeed, an extended continuum emission is seen in the near-infrared spectrum of reflection nebulae (e.g. Sellgren 1989, and references therein) and young planetary nebulae (e.g. Hora et al. 1993; Likkel et al. 1994), while, at visible wavelengths, some of these objects show an extended red emission (e.g. Witt et al. 1984; Furton & Witt 1990). In some nebulae, the extended red and near-infrared continuum emissions have been mapped and shown to extend beyond the ionized gas (e.g. Furton & Witt 1990; Likkel et al. 1994), as observed in the case of the HD 168625 ring. These continuum emissions are generally attributed to non-equilibrium dust emission, and often associated with the so-called unidentified infrared emission bands (UIRs) (e.g. Sellgren 1989; Duley 1989). The presence of UIRs in the spectrum of HD 168625 (Cohen et al. 1986) therefore supports such an origin for the excess of continuum. Additional observations like spatially resolved polarization maps of the ring are needed to distinguish between this interpretation and the scattering one.

3.3. Kinematical and physical characteristics

Two-dimensional high-resolution Hα and [NII] emission line profiles are illustrated in Figs. 6 and 7 for different positions of the slit on the nebula. The two lines have rather similar profiles, Hα being more diffuse. The profiles essentially indicate that the ring is in fact a hollow ellipsoidal shell expanding at 20 ± 2 km s^{-1} along both its minor and major axes. At the distance of 2.2 kpc, the inner shell has a mean radius of 0.06 pc and a dynamic age of $3\ 10^3$ years. The outer bipolar nebula is only barely seen on one frame (lower right in Figs. 6 and 7), such that nothing definite can be said about its kinematics. Its NE part seems nevertheless slightly blueshifted by ~ 6 km s^{-1} with respect to the systemic velocity of the shell, possibly indicating that it is located closer to the observer.

The heliocentric systemic velocity of the nebula is 14 ± 3 km s^{-1}, greater or equal to the mean velocity of the Omega nebula, 5.2 ± 5 km s^{-1} (Georgelin et al. 1973). According to the galactic rotation curve in this region (e.g. Georgelin et al. 1973), this means that the distance to HD 168625 is at least as large as the distance to the Omega nebula.

From these spectroscopic observations, we measure the following line ratios, uncorrected for reddening: Hα/[NII]6584 $\simeq$ 2.6 and [SII]6717/[SII]6731 $\simeq$ 0.9. The [SII] line ratio provides us with an estimate of the electron density n_e in the nebula: $n_e \simeq 630 \pm 300$ cm^{-3}.

Taking into account the Hα/[NII] ratio and the transmission curve of the filters, we may evaluate the total Hα flux by integrating over the whole nebula (ring + outer bipolar nebula) the light received in the Hα+[NII] filter, continuum subtracted (i.e. using the image displayed in Fig. 2). The flux from the region masked by the coronographic spot has been extrapolated using the nebula mean surface brightness. The total Hα flux has been subsequently calibrated using the Hα flux of the AG Car nebula, available from the literature (e.g. Stahl 1987; de Freitas Pacheco et al. 1992; Nota et al. 1992) and measured on frames obtained during the same observing run (cf. Sect. 2.1). The Hα flux from the HD 168625 nebula finally amounts to 4.6 ± 0.7 10^{-13} erg cm^{-2} s^{-1}, uncorrected for reddening. The uncertainty mainly accounts for errors in evaluating the contribution due to the part of the nebula masked by the coronographic spot. In order to estimate the nebular $E(B-V)$, we used a low-resolution (also low-quality) nebular spectrum, obtained in April 92 with EFOSC1. The slit was oriented N–S and positioned $\sim 17''$ east from the star, crossing a faint arc-like feature (cf. Fig. 2). From the Hα/Hβ ratio, we derive $E(B-V) = 0.75 \pm 0.1$. This value is smaller than the stellar $E(B-V) = 1.46 \pm 0.12$ (e.g. van Genderen et al. 1992). This may indicate that there is a significant circumstellar reddening. On the other hand, this nebular feature, probably a condensation in the Omega nebula, is not clearly associated with HD 168625, and the difference of reddenings may suggest that HD 168625 and its nebula are located beyond the Omega nebula, or on its far side. Spectroscopy of the ring around HD 168625 is needed to estimate the actual nebular $E(B-V)$. With $E(B-V) \simeq 0.75$, the de-reddened Hα flux amounts to $F_{H\alpha} = 2.5 \pm 0.9\ 10^{-12}$ erg cm^{-2} s^{-1}; this was the value used in Paper I. With $E(B-V) \simeq 1.46$, we have $F_{H\alpha} = 1.2 \pm 0.4\ 10^{-11}$ erg cm^{-2} s^{-1}.

From the Hα flux, the electron density and the distance, we can evaluate M_i, the mass of the ionized gas. Using formulae given in e.g. Aller (1984), and $F_{H\alpha} \simeq 2.5\ 10^{-12}$ erg cm^{-2} s^{-1}, we find $M_i \simeq 7\ 10^{-3}\ M_\odot$ (Paper I). With $F_{H\alpha} \simeq 1.2\ 10^{-11}$ erg cm^{-2} s^{-1}, we have $M_i \simeq 3\ 10^{-2}\ M_\odot$. From the IRAS fluxes, we also found that cool ($T_d \simeq 124$ K) dust is present in the nebula, and that its mass M_d amounts to $\sim 3\ 10^{-4}\ M_\odot$ (Paper I). It is interesting to note that with the largest value for the ionized gas mass in the nebula around HD 168625, the slope of the LBV nebula "$\log M_i - \log L$" relation found in Paper I is in better agreement with the slope of the "$\log M_d - \log L$" relation.

4. The nebular environment of the nearby LBV HD 168607

Since the nearby star HD 168607 is also a LBV, we have similarly searched for a nebulosity around it. While observed in the same conditions as HD 168625, including with EFOSC1 and IRAC2, nothing has been detected in the vicinity of this star. Also, no nebular line may be seen on high-resolution CAT+CES spectra obtained with exposure times as long as those for HD 168625. Finally, IRAS did not detect any cool dust around HD 168607. We can therefore safely conclude that HD 168607 is not associated with a LBV-type nebula.

On the other hand, HD 168607 is possibly at the origin of a wind-blown shell in the Omega nebula, as suggested by its position almost at the center of a cavity (cf. Sect. 3.1). Its heliocentric velocity (4–10 km s^{-1}, Chentsov 1980) is in quite good agreement with that of the Omega nebula, 5.2 ± 5 km s^{-1} (Georgelin et al. 1973).

5. Discussion and conclusions

Our observations confirm that HD 168625 is at least as distant as the Omega nebula and the nearby LBV HD 168607. Further

© European Southern Observatory • Provided by the NASA Astrophysics Data System

1994A&A...290..906H

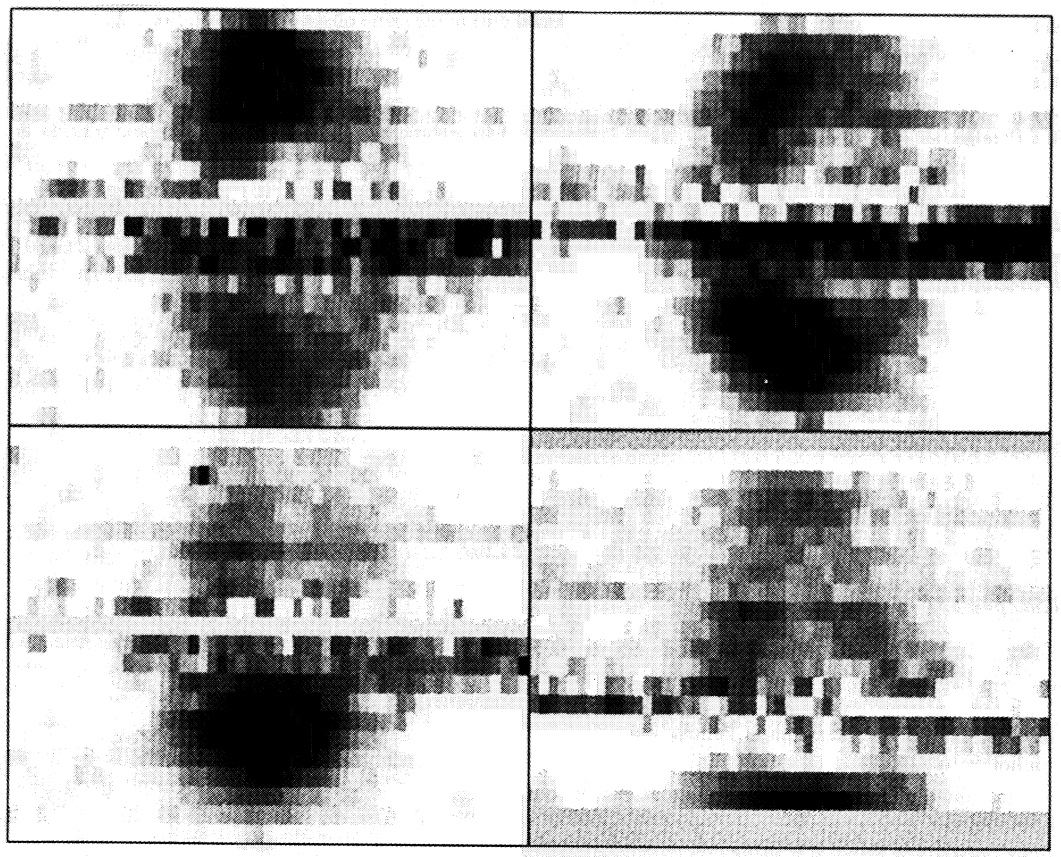


Fig. 6. Two-dimensional Hα emission line profiles from the nebula surrounding HD 168625. The four frames correspond to different position angles of the slit (cf. Table 3): $\sim 273°$ (upper left), $\sim 318°$ (upper right), $\sim 14°$ (lower left), and $\sim 54°$ (lower right). The size of each frame is 2.75 Å $\times$ 22 pixels, i.e. ~ 125 km s^{-1} $\times$ 18″. The spectrum of the star has been subtracted from the two-dimensional spectra, after its replication using the spatial profile of the continuum on each side of the line. This subtraction is not perfect and a noisy strip is still present. On the last frame the star is not at the center of the slit

support to this result comes from high-resolution observations of the NaI D line profiles obtained by one of us (E.G.), and showing that interstellar absorption occurs at higher positive velocities in the spectrum of HD 168625 than in the spectrum of HD 168607. HD 168625 is therefore a very luminous star, possibly a LBV. The nebula found around HD 168625 cannot be considered as a planetary nebula: it is better classified as a LBV-type nebula.

While our observations are not sufficient to build a detailed model, the following picture may be sketched: the nebula essentially consists of a dusty expanding shell from which seems to emerge a bipolar emission nebula, the whole embedded in a reflection nebulosity whose relation with the star is unclear. The shell is stratified: the dust continuum emission (either due to dust scattering or to non-equilibrium dust emission) arises beyond the ionized gas.

Although this kind of morphology is more typical of young planetary nebulae, it may be observed in some other LBV nebulae. The nebula around η Car is constituted of a dusty inner part –the homunculus– and outer emission nebulosities (Walborn 1976). On our images of the nebula around AG Car (often considered as the prototype of the class), we can clearly see a small and faint loop north of the ring: it has a N–S symmetry axis, an opening angle of $\sim 50°$, and peaks 28″ north from the star. This structure probably corresponds to the northern part of the bipolar outflow spectroscopically detected by Smith (1991), giving evidence that a faint bipolar nebula is also associated with AG Car in addition to the bright ring. Further, on the near-infrared images of HD 168625 described in Sect. 3.2, we note the presence of elongations inside the continuum-emitting ring: these are reminiscent of the dusty jet-like condensations around AG Car which also extend beyond the region where the Hα ring peaks (cf. Paresce & Nota 1989).

The kinematical and physical properties of the nebula are consistent with those commonly reported for LBV nebulae (cf. Smith 1993; Paper I and references therein). The size and the expansion velocity are smaller than in the representative AG Car nebula, but comparable to those of the η Car and WRA751

© European Southern Observatory • Provided by the NASA Astrophysics Data System

1994A&A...290..906H

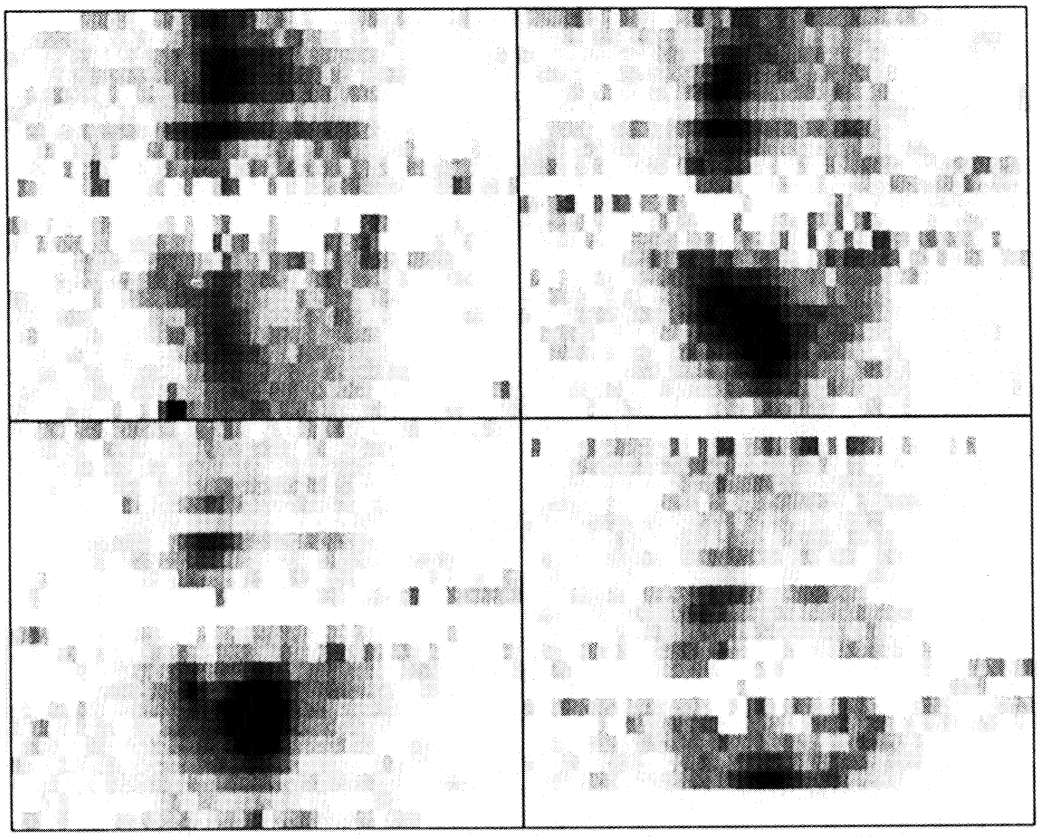


Fig. 7. Same as Fig. 6 but for the [NII] λ6584 emission line

nebulae, respectively. The nebular mass is smaller but nevertheless fitting the "nebular mass – stellar luminosity" relations of Paper I.

A peculiarity of HD 168625 is the presence in its spectrum of unidentified infrared emission bands (UIRs) which most probably arise in the nebular environment. Indeed, UIRs are detected in a variety of nebulae, including reflection nebulae, HII regions and planetary nebulae. These bands are generally attributed to polycyclic aromatic hydrocarbon molecules (PAHs); they are stronger in the spectrum of planetary nebulae where high C/O abundance ratios prevail (e.g. Cohen et al. 1986, 1989 and references therein). On the contrary, the nebula around HD 168625 is expected to contain CNO-synthesis products, as other LBV nebulae which are commonly N-rich. Furthermore, from the comparison of medium-resolution stellar spectra obtained in the $\lambda\lambda$4050–4950 spectral range with spectra displayed in the atlas of Lennon et al. (1992), we confirm the classification of HD 168625 as a mid-B type supergiant with normal absorption lines of CII, NII, OII, and SiIII (see also Chentsov & Luud 1989); it is therefore likely that the photospheric abundances of HD 168625 are modified by CNO processed material, as those of other galactic B-type supergiants (Lennon et al. 1993). The detection of relatively strong UIR bands in the spectrum of HD 168625 is unexpected, but may indicate that a large C/O abundance ratio is not essential for the formation of UIRs in this kind of nebulae, like, may be, in the case of pre-main sequence objects (e.g. Geballe et al. 1989). On the other hand, it is possible that the UIR emitting material has not been ejected by the star, but is of interstellar origin, possibly due to the nearby Omega nebula where UIR features are known to be enhanced

© European Southern Observatory • Provided by the NASA Astrophysics Data System

1994A&A...290..906H

relatively to the average interstellar medium (Giard et al. 1989). It is clear that a mapping of these UIRs would be worthwhile, as well as a detailed abundance analysis of the nebula. In this context, it is worth mentioning that diffuse absorption bands (DIBs) have been detected in the spectra of HD 168625 and HD 168607 (Herbig 1975), giving some support to the suggestion by Le Bertre & Lequeux (1993) that DIBs are commonly associated with LBV-type objects.

In conclusion, we find HD 168625 surrounded by a nebula whose characteristics are consistent with other LBV-type nebulae, although it has some peculiarities making it a rather unique object which certainly deserves further study. HD 168625, and the nearby LBV HD 168607 which is not associated with a comparable LBV-type nebula, constitute an important pair of supergiants for understanding the detailed processes of massive star evolution.

Acknowledgements. It is a pleasure to thank Andrea Moneti and Hans Gemperlein for many advices about the observations with IRAC2. We also thank G. Artzner for providing us with his (unpublished) tables for determining the position of the CES slit on the sky. The SIMBAD database has been consulted for the bibliography. This research is supported in part by contracts ARC 90/94-140 "Action de recherche concertée de la Communauté Française" and SC005 "Service Centers and Research Networks of the SPPS" (Belgium).

References

Aller L.H., 1984, Physics of Thermal Gaseous Nebulae, Reidel, Dordrecht
Chentsov E.L., 1980, SvA Lett. 6, 199
Chentsov E.L., Luud L., 1989, Afz. 31, 5
Chu Y.H., 1991, In: Wolf-Rayet stars and interrelations with other massive stars in galaxies, van der Hucht K.A., Hidayat B. (eds.), IAU Symp. 143, Kluwer, Dordrecht, p. 349
Cohen M., Allamandola L., Tielens A.G.G.M., Bregman J., Simpson J.P., Witteborn F.C., Wooden D., Rank D., 1986, ApJ 302, 737
Cohen M., Tielens A.G.G.M., Bregman J., Witteborn F.C., Rank D., Allamandola L., Wooden D., de Muizon M., 1989, ApJ 341, 246
Duley W.W., 1989, In: Interstellar dust, Allamandola L.J., Tielens A.G.G.M. (eds), IAU Symp. 135, Kluwer, Dordrecht, p. 141
de Freitas Pacheco J.A., Damineli Neto A., Costa R.D.D., Viotti R., 1992, A&A 266, 360
Furton D.G., Witt A.N., 1990, ApJ 364, L45
Geballe T.R., Noll K.S., Whittet D.C.B., Waters L.B.F.M., 1989, ApJ 340, L29
van Genderen A.M., van den Bosch F.C., Dessing F., Fehmers G.C., van Grunsven J., van der Heiden R., Janssens A.M., Kalter R., van der Meer R.L.J., van Ojik R., Smit J.M., Zijderveld M.J., 1992, A&A 264, 88
Georgelin Y.M., Georgelin Y.P., Roux S., 1973, A&A 25, 337
Giard M., Pajot F., Lamarre J.M., Serra G., Caux E., 1989, A&A 215, 92
Herbig G.H., 1975, ApJ 196, 129
Hillier D.J., 1992, In: The atmospheres of early-type stars, Heber U., Jeffery C.S. (eds.), Springer, Berlin, p. 105
Hora J.L., Deutsch L.K., Hoffmann W.F., Fazio G.G., Shivanandan K., 1993, ApJ 413, 304
Humphreys R.M., 1989, In: Physics of Luminous Blue Variables, Davidson K., Moffat A.F.J., Lamers H.J.G.L.M. (eds.), IAU Coll. 113, p.3
Hutsemékers D., Van Drom E., 1991a, A&A 248, 141
Hutsemékers D., Van Drom E., 1991b, A&A 251, 620
Hutsemékers D., 1994, A&A 281, L81 (Paper I)
Laustsen S., Madsen C., West R.M., 1987, Exploring the southern sky, Springer-Verlag, Berlin, p. 183
Le Bertre T., Lequeux J., 1993, A&A 274, 909
Lennon D.J., Dufton P.L. Fitzsimmons A., 1992, A&AS 94, 569
Lennon D.J., Dufton P.L. Fitzsimmons A., 1993, A&AS 97, 559
Likkel L., Morris M., Kastner J.H., Forveille T., 1994, A&A 282, 190
Lindgren H., Gilliotte A., 1989, ESO operating manual n° 8, ESO, Garching
McGregor P.J., Hyland A.R., Hillier D.J., 1988a, ApJ 324, 1071
McGregor P.J., Finlayson K., Hyland A.R., Joy M., Harvey P.M., Lester D.F., 1988b, ApJ 329, 874
Melnick J., 1993, EFOSC2 operating manual, ESO, Garching
Melnick J., Dekker H., D'Odorico S., 1989, ESO operating manual n° 4, ESO, Garching
Morgan W.W., Code A.D., Whitford A.E., 1955, ApJS 2, 41
Moorwood A., Finger G., Biereichel P., Delabre B., van Dijsseldonk A., Huster G., Lizon J.-L., Meyer M., Gemperlein H., Moneti A., 1992, The Messenger 69, 61
Neckel T., Vehrenberg H., 1987, Atlas of Galactic Nebulae Part II, Treugesell-Verlag, Düsseldorf, p. 43
Nota A., Leitherer C., Clampin M., Greenfield P., Golimowski D.A., 1992, ApJ 398, 621
Paresce F., Nota A., 1989, ApJ 341, L83
Popper D.M., Seyfert C.K., 1940, PASP 52, 401
Schwarz H.E., Melnick J., 1993, The ESO users manual, ESO, Garching
Sellgren K., 1989, In: Interstellar dust, Allamandola L.J., Tielens A.G.G.M. (eds), IAU Symp. 135, Kluwer, Dordrecht, p. 103
Smith L.J., 1991, In: Wolf-Rayet stars and interrelations with other massive stars in galaxies, van der Hucht K.A., Hidayat B. (eds.), IAU Symp. 143, Kluwer, Dordrecht, p. 385
Smith L.J., 1993, In: Circumstellar matter in the late stages of stellar evolution, Clegg R.E.S., Meikle P., Stevens I.R. (eds.), 34th Herstmonceux Conference, Cambridge, in press
Stahl O., 1987, A&A 182, 229
Stahl O., 1989, In: Physics of Luminous Blue Variables, Davidson K., Moffat A.F.J., Lamers H.J.G.L.M. (eds.), IAU Coll. 113, p. 149
Walborn N.R., 1976, ApJ 204, L17
Witt A.N., Schild R.E., Kraiman J.B., 1984, ApJ 281, 708
Wolf B., 1992, In: Nonisotropic and variable outflows from stars, Drissen L., Leitherer C., Notta A. (eds.), PASPC 22, p. 327

This article was processed by the author using Springer-Verlag LaTeX A&A style file version 3.

© European Southern Observatory • Provided by the NASA Astrophysics Data System

Article 4

Evidence for violent ejection of nebulae from massive stars

D. Hutsemékers : Astron. Astrophys. 281, L81 (1994)

Dans cet article plus général, nous rapportons les résultats de notre recherche systématique de nébuleuses autour des LBVs de notre Galaxie et plus particulièrement la découverte d'une relation entre la masse de la nébuleuse et la luminosité de l'étoile centrale. Cette relation est valable tant pour la masse de la poussière présente dans la nébuleuse que pour la masse de gaz ionisé (bien que la mesure de cette dernière quantité soit plus incertaine).

L'existence même d'une telle relation et le fait que quelques LBVs ne sont pas associées à une nébuleuse suggèrent que leur formation est due à une éjection de matière violente et unique plutôt qu'à une perte de masse continue. La relation "masse nébulaire – luminosité stellaire" que nous trouvons est en accord avec certaines prédictions théoriques.

1994A&A...281L..81H

Astron. Astrophys. 281, L81–L84 (1994)

ASTRONOMY AND ASTROPHYSICS

Letter to the Editor

Evidence for violent ejection of nebulae from massive stars

D. Hutsemékers

Institut d'Astrophysique, Université de Liège, 5 av. de Cointe, B-4000 Liège, Belgium

Received 4 November 1993 / Accepted 19 November 1993

Abstract. We report the results of a systematic search for nebulae around Luminous Blue Variables (LBVs) and the discovery of a strong correlation between the mass of the nebulae and the luminosity of the central stars. This correlation holds for both the dust and ionized gas masses of the nebulae.

The existence of a "nebular mass – stellar luminosity" relation and the fact that not all LBVs are presently associated with a nebula give evidence against a continuous mass-loss mechanism for the formation of these nebulae. Further, the good agreement found between the observed relation and predictions by Maeder (1989), suggests that all these nebulae may be due to a violent ejection of matter caused by an instability of structural origin.

Key words: Luminous Blue Variable stars – mass-loss – emission nebulae

1. Introduction

Luminous Blue Variables (LBVs) are extreme supergiant stars located in the Hertzprung-Russell diagram near the Humphreys-Davidson instability limit (Humphreys & Davidson 1979). They are generally thought to represent a short-lived intermediate stage in the evolution of massive stars from O to WR stars (Maeder 1989, Humphreys 1989). About ten LBVs are presently known in our Galaxy.

One of the most remarkable characteristics of LBVs is the presence of a ring nebula surrounding some of them (Stahl 1989). In order to see if the association with a nebula is a generic property of these stars, we have searched for nebulosities around galactic LBV candidates using CCD imaging through narrow-band filters which isolate nebular lines. In addition to the previously known nebulae around η Car, AG Car, and He3-519, three new nebulae have been found surrounding HR Car, WRA751, and HD168625 (Hutsemékers & Van Drom 1991a, 1991b, Hutsemékers et al. 1993, hereafter Papers I, II and III). Nothing has been detected around HD160529 and HD168607.

Spectroscopic investigations of LBV nebulae have revealed abundance anomalies suggesting that they are constituted of nuclear processed material ejected by the central stars (Davidson et al. 1982; Mitra & Dufour 1990; de Freitas Pacheco et al. 1992; Papers I, II). If, for η Car, the mass-loss was directly observed to occur in one great eruption (e.g. Davidson 1989), the origin of most LBV nebulae is still unclear: they may be formed either by the interaction of continuous stellar winds like planetary nebulae (e.g. Robberto et al. 1993), or by a single violent ejection of matter possibly due to an instability of atmospheric (e.g. Lamers & Fitzpatrick 1988) or structural (e.g. Maeder 1989) origin.

In order to distinguish between these interpretations, we investigate in the present work how the mass of the nebular material surrounding LBVs correlates with the luminosity of the central stars.

2. The mass of LBV nebulae

2.1. The stellar parameters

The stellar luminosities and distances of LBVs may be found in the literature. For HR Car, we use the average of our values (Paper I) and those of Van Genderen et al. (1992). For He3-519, we have obtained low and high resolution spectra of the nebula, the observations being similar to those reported in Paper II (a more detailed account of these data will be given elsewhere). From the radial velocity of the [NII] and $H\alpha$ nebular lines, a kinematic distance of 7.6 kpc has been estimated for He3-519. Its luminosity has been calculated using $V = 10.97$ (Stahl 1986) and a visual extinction $A_V = 3.9 \pm 0.4$ mag intermediate between the value derived from the nebular $H\alpha/H\beta$ ratio (~ 3.4) and the higher values (~ 4.3) suggested by Stahl (1986) and Davidson et al. (1993). Considering that He3-519 is hotter than AG Car during minimun, we use a bolometric correction $\sim$ -3.0 $\pm$ 0.3 mag.

The adopted distances and luminosities (L, expressed in solar luminosity units $L_\odot$) are given in Table 1. Since

* Based on observations collected at the European Southern Observatory (ESO) and by the Infrared Astronomical Satellite (IRAS)

© European Southern Observatory • Provided by the NASA Astrophysics Data System

1994A&A...281L..81H

the nebular masses and stellar luminosities similarly depend on the distance, the errors reported in Table 1 and 2 do not account for the uncertainties on the distances.

Table 1. Stellar parameters

Object	Distance (kpc)	$\log L/L_\odot$	Ref.
η Car	2.5	6.70 ± 0.01	1,2
AG Car	6.0	6.22 ± 0.02	3
WRA751	7.1	6.06 ± 0.20	4
He3-519	7.6	6.03 ± 0.28	5
HR Car	5.2	5.58 ± 0.12	5
HD168625	2.2	5.34 ± 0.12	6

References: (1) Van Genderen & Thé 1984, (2) Tapia et al. 1988, (3) Humphreys et al. 1989, (4) Paper II, (5) this work, (6) Van Genderen et al. 1992

2.2. The nebular dust masses

All the six LBVs associated with an optical nebula show an infrared excess at 25 and 60 μm detected by the Infrared Astronomical Satellite (IRAS) and due to the presence of cool dust around the star (Mc Gregor et al. 1988a; Chentsov & Luud 1989; Hu et al. 1990; Davidson et al. 1993). If in thermal equilibrium, the dust should lie at distances corresponding to the optical nebula, as directly seen on far-infrared images (Mc Gregor et al. 1988b; Allen 1989), or revealed by the presence of dust-scattered stellar light within the nebula (Paresce & Nota 1989; Allen 1989; Paper III). The nebular mass may therefore be estimated from the dust masses. The 100 μm measurements being not always reliable, dust masses were computed following McGregor et al. (1988a) from the 60 μm flux density, using formulae given by Soifer et al. (1986). The flux densities were obtained from the IRAS Point Source Catalog and colour corrected according to the IRAS Explanatory Supplement (1985). For η Car, the 25 μm value is taken from Mc Gregor et al. (1988). The 60 μm mass absorption coefficient K_λ is estimated by extrapolating at longer wavelengths the value at 20 μm for silicate dust (Draine & Lee 1984), using $K_\lambda \propto \lambda^{-\beta}$ with $\beta = 1.5$. The characteristic dust temperature was estimated from the 25-60 μm colour temperature and a grain emissivity proportional to $\lambda^{-\beta}$. Dust temperatures (T_d) and masses (M_d, expressed in solar mass units $M_\odot$) are given in Table 2. It should be noticed that the two LBVs imaged with no detection of any optical nebulosity, HD168607 and HD160529, do not show any infrared excess indicating the presence of dust. This suggests that these non-detections are due to the real absence of an associated nebula and not to the inability of these cooler stars to ionize their surroundings.

In Figure 1, we have reported the nebular dust mass against the luminosity of the central stars. A strong correlation between these two quantities may be seen. Changing the mass absorption coefficient of the grains affects similarly all dust masses but do not modify the relation: with $\beta = 1$ rather than 1.5, all masses are simply shifted by ~ -0.4 dex. The basic assumption is that the grain properties are essentially similar for all these nebulae, an hypothesis which, in view of the observed correlation, seems a posteriori reasonable.

2.3. The nebular ionized gas masses

The mass of the ionized gas in LBV nebulae may be evaluated independently from the total flux emitted in the $H\alpha$ line, $F(H\alpha)$, and the electron density n_e using formulae given e.g. in Aller (1984). The small dependence on the electron temperature is neglected. The $H\alpha$ fluxes of the nebulae around HD168625, HR Car, WRA751 and He3-519 have been measured by integrating over the whole nebula the light received through narrow-band filters centred on the $H\alpha$ line. For HD168625 and HR Car a continuum image has been subtracted before. Taking into account the transmission of the filters and using available spectra of the nebulae, the fluxes were de-contaminated from the [NII] lines and de-reddened with nebular $E(B-V)$ estimated from the $H\alpha/H\beta$ line ratios. Finally, the fluxes were calibrated by comparison with other nebulae for which the $H\alpha$ flux is known and which have been imaged with the same filters during the same observing run. After re-scaling to our reddening value, the $H\alpha$ flux of the He3-519 nebula is in good agreement with that reported by Stahl (1987), and the mean value is taken. For AG Car, the flux is averaged from Stahl (1987), Nota et al. (1992) and de Freitas Pacheco et al. (1992). No reliable $H\alpha$ flux is available for the η Car nebula, essentially due to the strong contamination by reflected stellar light. The electron densities were re-derived homogeneously from the observed [SII] $\lambda\lambda$ 6717,6731 line ratios. These measurements are given in Table 2, together with the derived mass of the ionized gas (M_i), and the nebular radii measured on $H\alpha$+[NII] frames.

The mass of ionized gas in LBV nebulae is reported in Figure 2 against the luminosity of the central stars, confirming the dependence of the nebular mass on the stellar luminosity. The average ionized gas-to-dust ratio is comparable to values reported for other objects like planetary nebulae or HII regions. The slope of the "$\log M_i - \log L$" relation is apparently steeper when compared to the "$\log M_d - \log L$" one. It is possible that the ionized fraction of the total gas is smaller in the nebulae around HR Car and HD168625, as could be expected from the lower temperature and luminosity of these stars. The detection of molecular gas in the vicinity of HR Car but not around AG Car nor around η Car (Mc Gregor et al. 1988a) could support this view.

© European Southern Observatory • Provided by the NASA Astrophysics Data System

1994A&A...281L..81H

Table 2. Nebular parameters

Object	Radius (pc)	T_d (K)	$\log M_d/M_\odot$	$\log F(H\alpha)$ ($ergs\,cm^{-2}s^{-1}$)	$\log n_e$ (cm^{-3})	$\log M_i/M_\odot$
η Car	0.15	133 ± 8	-1.41 ± 0.12			
AG Car	0.50	88 ± 5	-2.00 ± 0.15	-9.76 ± 0.05	2.77 ± 0.10	0.60 ± 0.15
WRA751	0.40	103 ± 5	-2.23 ± 0.11	-10.29 ± 0.15	2.56 ± 0.20	0.43 ± 0.35
He3-519	1.02	73 ± 3	-2.23 ± 0.12	-10.55 ± 0.15	2.56 ± 0.15	0.24 ± 0.30
HR Car	0.43	100 ± 4	-3.02 ± 0.10	-11.20 ± 0.20	2.72 ± 0.15	-0.91 ± 0.35
HD168625	0.11	124 ± 7	-3.51 ± 0.12	-11.60 ± 0.15	2.80 ± 0.20	-2.14 ± 0.35

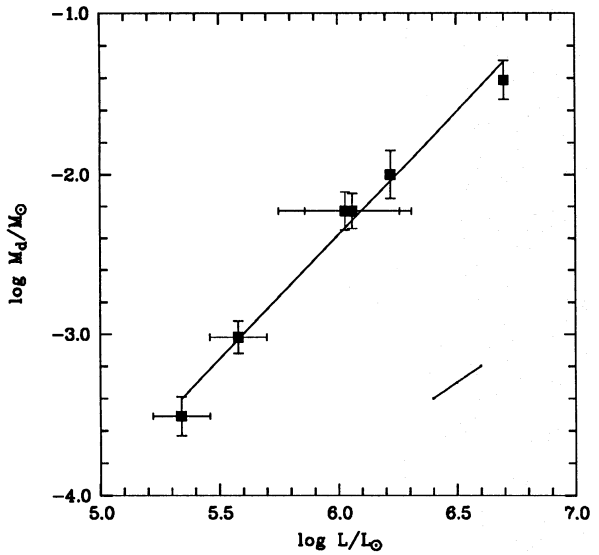


Fig. 1. Dust mass of LBV nebulae reported as a function of the luminosity of the central stars. The straight line resulting from a least square fit is plotted and illustrates the strong correlation between the nebular dust masses and the stellar luminosities. The error bars do not account for the uncertainties on the distances since both mass and luminosity similarly depend on it. A typical uncertainty on the distances is represented by the small oblique error bar.

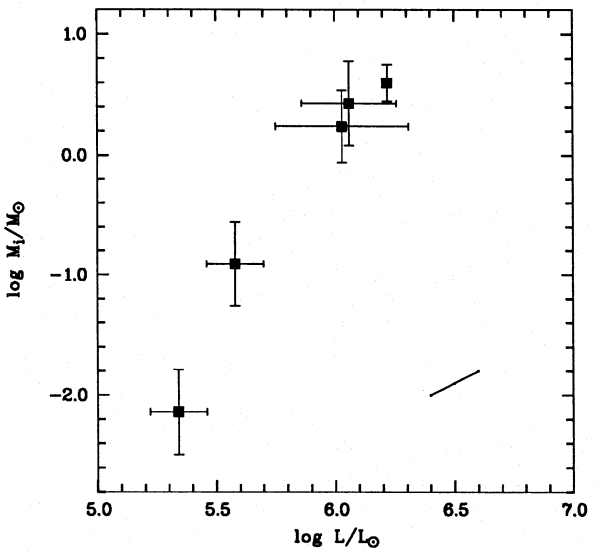


Fig. 2. Ionized gas mass of LBV nebulae reported as a function of the luminosity of the central stars. The uncertainties on the ionized gas masses are larger due to the difficulty of measuring a reliable $H\alpha$ flux for faint nebulae near bright stars and of obtaining a good estimate of the average electron density.

2.4. A "nebular mass-stellar luminosity" relation

The relation between the nebular mass M_{neb} and the stellar luminosity L is therefore better expressed by

$$\log(\frac{M_{neb}}{M_\odot}) = (1.55 \pm 0.10)\ \log(\frac{L}{L_\odot}) + C, \qquad (1)$$

fitting a straight line to the data displayed in Figure 1. If M_{neb} refers to the dust mass (computed with $\beta = 1.5$), $C = -11.7 \pm 0.1$. If we assume that the total gas-to-dust ratio is comparable in all LBV nebulae, M_{neb} may refer to the total nebular mass and the constant C may be fixed using the gas mass of the AG Car nebula ($M_{neb} \simeq 4.0 M_\odot$) which is presently the nebula with the best available mass estimate and known to be density bounded (Robberto et al. 1993). In this case, $C \simeq -9.0$.

3. Discussion and Conclusions

The mere existence of a relation between the mass of the LBV nebulae and the luminosity of the central stars constrains the models proposed to explain the formation of such nebulae. If LBV nebulae result from matter continuously ejected during a previous evolutionary stage and swept up by the present stellar wind, we expect the nebular mass to continuously increase with time. Since at the considered evolutionary stage, a massive star keeps its luminosity nearly constant (e.g. Maeder 1989), such an interpretation would imply that the LBVs of our sample

© European Southern Observatory • Provided by the NASA Astrophysics Data System

have exactly the right age to have their nebular masses correlated with their luminosities, which is very unlikely. Further, if this kind of interpretation is correct, we would also expect nebulae around all LBVs including HD160529 ($\log L/L_\odot \simeq 5.50$, Sterken et al. 1991) and HD168607 ($\log L/L_\odot \simeq 5.38$, Van Genderen et al. 1992). The existence of a relation between the mass of LBV nebulae and the luminosity of the central stars therefore argues against the continuous mass-loss mechanism for explaining the formation of these nebulae. The absence of any correlation between the nebular masses and radii (cf. Table 2) also supports this view.

Maeder (1989) has given an estimate of the maximum possible mass ΔM ejected in one episode during some dynamical time scales: if R and M denote the radius and mass of the star, $\Delta M \propto R^{5/2}M^{-3/2}L$. Using the mass-luminosity relation for massive stars $M \propto L^{0.47}$ (Lamers & Fitzpatrick 1988), and the maximum stellar radius $R \propto L^{1/2}$ which is independent of the effective temperature (Wolf 1989), we find $\Delta M \propto L^{1.55}$, in excellent agreement with the relation found observationally (Eq. 1). This suggests that a structural instability mechanism may be at the origin of the ejection of the LBV nebulae. In this case, the maximum possible mass could be ejected during a single violent event occuring at the LBV evolutionary stage, possibly when the stars are located in the region of the HR diagram where the relation $R \propto L^{1/2}$ is valid for most LBVs (cf. Wolf 1989). It is also interesting to note that the two LBVs without nebulae are cooler than HR Car and HD168625 which are of comparable luminosities, as can be expected from stars having not yet ejected their outer layers.

The reality of a relation between the mass of LBV nebulae and the luminosity of the central stars seems well established giving some evidence that a single violent ejection is at the origin of all these nebulae. However, the exact shape of the observed relation will only be known with certainty if the total mass of the nebula can be evaluated, including the mass of the molecular gas. Also, the status of faint nebulosities, like those recently detected around P Cygni (Johnson et al. 1992) which apparently contain much less material and are only marginally associated with dust (Waters & Wesselius 1986; Luud et al. 1988) should be clarified.

Clearly, the functional dependence of a "nebular mass -stellar luminosity" relation for massive stars may constrain evolutionary models and instability mechanisms like those proposed by Maeder (1989) and Stothers and Chin (1993). It may also provide us with a useful tool for evaluating the mass deposition into the ISM during the LBV stage. It will be interesting to obtain similar data for LBV nebulae in other galaxies (e.g. LMC) in order to see if this relation depends on the metallicity.

Acknowledgements. It is a pleasure to thank J. Surdej for reading the manuscript. This research is supported in part by contracts ARC 90/94-140 "Action de recherche concertée de la Communauté Française" and SC005 " Service Centers and Research Networks of the SPPS" (Belgium).

References

Allen, D.A., 1989, *MNRAS* **241**, 195
Aller, L.H., 1984, *Physics of Thermal Gaseous Nebulae*, Reidel, Dordrecht
Chentsov, E.L., Luud, L., 1989, *Astrophys.* **31**, 5
Davidson, K., Humphreys, R. M., Hajian, A., Terzian, Y., 1993, *ApJ* **411**, 336
Davidson, K., Walborn, N.R., Gull, T.R., 1982, *ApJ* **254**, L47
Davidson, K., 1989, *Physics of Luminous Blue Variables*, IAU Coll. 113, p.101
Draine, B.T., Lee, H.M., 1984, *ApJ* **285**, 89
de Freitas Pacheco, J.A., Damineli Neto, A., Costa, R.D.D., Viotti, R., 1992, *A&A* **266**, 360
van Genderen, A.M., Thé, P.S., 1984, *Sp. Sc. Reviews* **39**, 317
van Genderen, A.M. et al., 1992, *A&A* **264**, 88
Hu, J.Y., de Winter, D., Thé, P.S., Pérez, M.R., 1990, *A&A* **227**, L17
Humphreys, R.M., Davidson, K., 1979, *ApJ* **232**, 409
Humphreys, R.M., 1989, *Physics of Luminous Blue Variables*, IAU Coll. 113, p.3
Humphreys, R.M., Lamers H.J.G.L.M., Hoekzema, N., Cassatella, A., 1989, *A&A* **218**, L17
Hutsemékers, D., Van Drom, E., 1991a, *A&A* **248**, 141 (Paper I)
Hutsemékers, D., Van Drom, E., 1991b, *A&A* **256**, 620 (Paper II)
Hutsemékers, D. et al., 1993, in preparation (Paper III)
Johnson, D.R.H., Barlow, M.J., Drew, J.E., Brinks, E., 1992, *MNRAS* **255**, 261
Lamers , H.J.G.L.M., Fitzpatrick, E.L., 1988, *ApJ* **324**, 279
Luud, L., Tuvikene T., Ruusalepp, M., 1988, *Astrophys.* **29**, 97
Maeder, A., 1989, *Physics of Luminous Blue Variables*, IAU Coll. 113, p. 15
McGregor, P.J., Hyland, A.R., Hillier D.J., 1988a, *ApJ* **324**, 1071
McGregor, P.J., Finlayson, K., Hyland, A.R., Joy, M., Harvey, P.M., Lester, D.F., 1988b, *ApJ* **329**, 874
Mitra P.M., Dufour R.J., 1990, *MNRAS* **242**, 98
Nota, A., Leitherer, C., Clampin, M., Greenfield, P., Golimowski, D.A., 1992 *ApJ* **398**, 621
Paresce, F., Nota, A., 1989, *ApJ* **341**, L883
Robberto, M., Ferrari, A., Nota, A., Paresce, F., 1993 *A&A* **269** , 330
Soifer , B.T., Rice, W.L., Mould, J.R., Gillett, F.C., Rowan Robinson, M., Habing, H.J., 1986, *ApJ* **304**, 651
Stahl, O., 1986, *A&A* **164**, 321
Stahl, O., 1987, *A&A* **182**, 229
Stahl, O., 1989, *Physics of Luminous Blue Variables*, IAU Coll. 113, p. 149
Sterken, C., Gosset, E., Juttner, A., Stahl, O., Wolf, B., Axer, M., 1991, *A&A* **182**, 229
Stothers, R.B., Chin, C.-W, 1993, *ApJ* **408**, L85
Tapia, M., Roth, M., Marraco, H., Ruiz, M.T., 1988, *MNRAS* **232**, 661
Waters, L.B.F.M., Wesselius, P.R., 1986, *A&A* **155**, 104
Wolf, B., 1989, *A&A* **246**, 441

© European Southern Observatory • Provided by the NASA Astrophysics Data System

Article 5

Dust in LBV-type nebulae

D. Hutsemékers : in Luminous Blue Variables : Massive Stars in Transition, A. Nota, H. Lamers (eds.), A.S.P. Conference Series 120, 316 (1997)

Dans cet article, certaines propriétés des nébuleuses associées aux LBVs sont passées en revue et plus particulièrement celles liées à la présence de poussière.

Nous montrons tout d'abord que toutes les nébuleuses de type LBV contiennent de la poussière froide rayonnant dans l'infra-rouge lointain et, qu'à cet égard, les nébuleuses de type LBV du Grand Nuage de Magellan (LMC) ne diffèrent pas de celles de notre Galaxie. Nous montrons que les LBVs du LMC suivent également la relation "masse nébulaire – luminosité stellaire" ainsi que les nébuleuses associées aux étoiles Wolf-Rayet de type WN8, généralisant la relation établie précédemment pour les nébuleuses galactiques (Article 4). Ces résultats appuient l'hypothèse d'un lien évolutif entre les LBVs et les étoiles de type WN8.

Enfin, nous montrons que dans quelques cas, on peut détecter la lumière stellaire diffusée par les poussières et ceci jusqu'à des distances excédant les dimensions de la nébuleuse de gaz ionisé.

De nouvelles nébuleuses de type LBV ayant été découvertes après la publication de cet article, nous présentons une mise à jour de la relation "masse nébulaire – luminosité stellaire" qui se voit confirmée.

Luminous Blue Variables : Massive Stars in Transition
ASP Conference Series, Vol. 120, 1997
A. Nota and H.J.G.L.M. Lamers, eds.

Dust in LBV-type Nebulae

Damien Hutsemékers[1]

Institut d'Astrophysique, 5 av. de Cointe, B-4000 Liège, Belgium

Abstract. Some systematic properties of dust in LBV-type nebulae are reviewed, on the basis of the far-infrared thermal emission measured by the IRAS satellite, and the scattering of visible stellar light.

1. Introduction

In the framework of a systematic study of infrared properties of emission-line stars, McGregor et al. (1988a) found that LBVs are surrounded by cool dust, while B[e] stars are predominantly associated with hot dust (although a few objects like η Car, or the B[e] star HD87643, both embedded in nebulosities, are simultaneously associated with hot and cool dust). They showed that, if in equilibrium, the cool dust must lie at large distances from the star, most probably in the optical nebula surrounding some of these objects. McGregor et al. (1988b) subsequently resolved the far-infrared emission from AG Car, showing that it actually arises within the optical nebula.

Table 1 summarizes the present situation for Galactic and Large Magellanic Cloud (LMC) LBVs, together with four Galactic WR stars associated with ejecta-type nebulae (Esteban et al. 1992). For the Galactic objects, there is a nearly one-to-one correlation between the presence of cool dust and that of a nebula. Also, HD160529 and HD168607 have been imaged with no detection of any optical nebulosity, and do not show any infrared excess indicating the presence of dust. For the LMC objects, the observations are much more incomplete: due to the larger distance, only the biggest nebulae have been resolved (Nota et al. 1995, 1996). The fluxes measured by IRAS are low, or contaminated by a relatively high background: only three objects are detected at 25 and 60 μm with a color temperature significantly different from that of the background. Nevertheless, the presence of cool dust in two nebulae, the detection in S119 of an excess at 25 μm, as well as the fact that the nebula around R71 is spectroscopically detected (Stahl & Wolf 1986) and probably very small (see next section), suggest that the nebulae around LMC LBVs are not different from the Galactic ones as far as dust is concerned.

The only nebula without dust is that around P Cygni: at a distance of 1.8 kpc, and assuming a dust-to-gas ratio comparable to that estimated in other nebulae, far-infrared emission (other than wind free-free emission) should have been detected. Compared to the other objects, this is not the only difference of

[1]Also, Chercheur Qualifié au Fonds National de la Recherche Scientifique, FNRS Belgium

Table 1. Dust and nebulae around LBV and WR stars

Object	Type	Optical nebulosity?	Dust?
η Car	LBV	yes	cool + hot
AG Car	LBV	yes	cool
HR Car	LBV	yes	cool
WRA751	LBV	yes	cool
P Cygni	LBV	yes	no
HD160529	LBV	no	no
HD168607	LBV	no	no
HD168625	LBV?	yes	cool
He3-519	Of/WN	yes	cool
R127	LBV	yes	cool
R71	LBV	$\sim$	cool
S Dor	LBV	?	?
R110	LBV	?	?
R143	LBV	yes?	?
BE294	LBV	?	?
S61	Of/WN	yes	cool
S119	Of/WN	yes	$\sim$
BE381	Of/WN	yes	?
HD269927c	Of/WN	?	?
R99	Of/WN	?	?
R84	Of/WN	?	?
S9	Of/WN	?	?
WR124 /M1-67	WN8	yes	cool
WR40 /RCW58	WN8	yes	cool
WR136 /NGC6888	WN6	yes	cool
WR6 /S308	WN5	yes	cool

the P Cygni nebula: it has a much smaller ionized gas mass, as well as different morphology, excitation mechanism, and abundance pattern (Johnson et al. 1992, Barlow et al. 1994, Nota et al. 1995). This possibly suggests a different origin.

2. Dust properties derived from the far-infrared emission

For an optically thin cloud of N dust grains of uniform size, composition, and temperature, the received flux density is equal to

$$F_\nu = N \frac{\pi a^2}{d^2} Q_\nu \, B_\nu(T_d), \tag{1}$$

where a is the grain radius, T_d the grain temperature, and d the distance to the cloud. In the far-infrared, the grain efficiency Q_ν is $\propto \nu^\beta$ with $\beta \simeq 1-2$, and T_d may be derived from two values of F_ν measured at different wavelengths. Dust temperatures are reported in Table 2, for $\beta = 1.5$. Whatever the nature of the central object, the dust temperature correlates with the optical nebular radius (Fig. 1a), hotter dust being in smaller nebulae, as expected at least in first approximation if the dust is mixed with the ionized gas or very close to it. On the basis of this correlation, one can predict the size of the nebula around R71 in the LMC: with $T_d = 127$ K, we expect $R_{neb} \sim 0.1$ pc, or $0\farcs3$.

Table 2. Dust properties in LBV and WR nebulae

Object	d(kpc)	$\log(L/L_\odot)$	R_{neb}(pc)	T_d(K)	$\log(M_d/M_\odot)$
η Car	2.5	6.70	0.08	133	-1.41
AG Car	6.0	6.22	0.50	88	-2.00
HR Car	5.2	5.58	0.43	100	-3.02
WRA751	7.1	6.06	0.40	103	-2.23
HD168625	2.2	5.34	0.08	124	-3.51
He3-519	7.6	6.03	1.0	73	-2.23
R127	51.	6.12	1.0	85	-2.04
R71	51.	5.90	?	128	-2.29
S61	51.	6.03	0.3:	99	-2.50
WR124 /M1-67	4.5	5.97	0.92	69	-2.51
WR40 /RCW58	2.5	5.78	3.1	59	-2.77
WR136 /NGC6888	1.8	5.74	3.7	62	-2.22
WR6 /S308	1.8	5.50	9.2	55	-2.43

For the Galactic LBVs, data are from Hutsemékers (1994, Paper I), with the difference that optical nebular radii measured in the continuum are preferred whenever available. Nebular radii are from Clampin et al. (1993) for R127, Stahl (1987) for S61, and from Esteban et al. (1993) for the WR nebulae. Stellar luminosities are from Stahl et al. (1983) for R127, Wolf et al. (1987) for S61, and Lennon et al. (1994) for R71. For the WR stars, we used the absolute magnitudes from Hamann et al. (1995) together with the bolometric corrections from L.F. Smith et al. (1994). The distances are also from Hamann et al. (1995), except for WR124 (Crawford & Barlow 1991). Whenever necessary, parameters are re-scaled to the adopted distances. Dust temperatures and masses are calculated as in Paper I, following McGregor et al. (1988a), i.e. using the 25 and 60 μm IRAS flux densities (color-corrected when necessary), β=1.5, and K_{60}=230 cm^{2}g^{-1}. For the LMC LBVs, IRAS flux densities are from the IRAS PSC when available with good accuracy, otherwise from Schwering (1989). For the WR nebulae, the IRAS flux densities are from the IRAS PSC (M1-67) and from Mathis et al. (1992). Estimates of uncertainties are discussed in Paper I.

The total dust mass may be evaluated using the relation (Hildebrand 1983)

$$M_d = \frac{F_\nu \; d^2}{B_\nu(T_d)\, K_\nu} \; , \tag{2}$$

where $K_\nu = 3\, Q_\nu / 4\, a\, \rho$, and ρ is the density of the grain material. Adopting a suitably weighted average of K_ν, Eq. 2 may be used to estimate the total dust mass without detailed knowledge of the grain size distribution. Dust masses are reported in Table 2, using $K_\nu = 230$ cm^{2}g^{-1} at 60 μm. Considering only Galactic LBVs, we found in Paper I a correlation between the nebular dust mass and the stellar luminosity. Fig. 1b illustrates this relation. The LMC LBVs seem to behave similarly, although the dust masses are more uncertain (due to the lower IRAS fluxes). The two WN8 objects are in excellent agreement with the LBVs, supporting the relationship suggested by Smith et al. (1994) and Crowther et al. (1995). On the contrary, S308 and NGC6888 (WN5-6) do not follow the general trend, possibly indicating that these nebulae -more massive- are not, or no longer, constituted of similar material, or that they have a different origin and/or progenitor (Mathis et al. 1992, Smith 1996).

It is important to note that, due to our poor knowledge of grain properties, orders-of-magnitude differences exist in *absolute* dust mass estimates when different grain models are considered. However, if we change β and K_ν for all

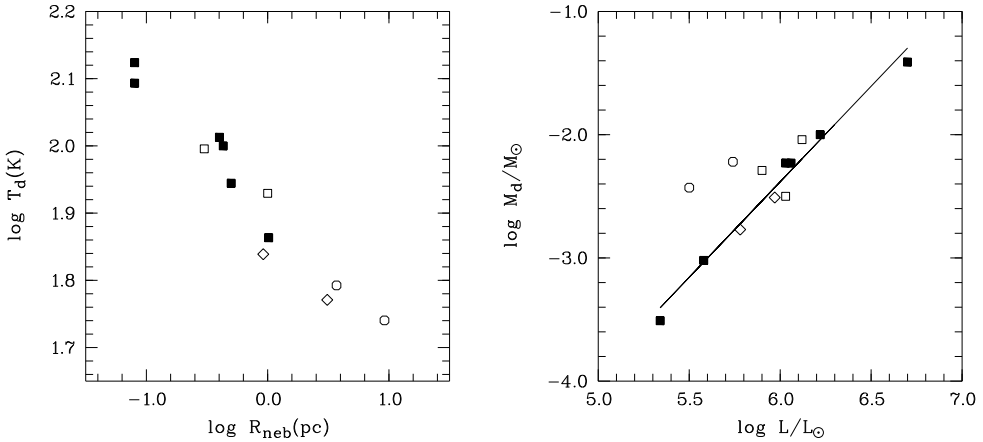


Figure 1. (A, left) The nebular dust temperature as a function of the optical nebular radius. (B, right) The nebular dust mass as a function of the stellar luminosity; the fitted line is based on Galactic LBVs (filled squares, cf. Paper I). Open squares represent LMC LBVs, losanges WN8, circles WN5-6.

objects, *relative* dust masses are essentially unchanged, and the slope of the "$\log M_d - \log L$"relation is unaffected. This can be seen in eliminating T_d from Eq. 2: within a good approximation, $M_d \simeq 1.7\,10^{-4}\,(1.85)^\beta\,K_{60}^{-1}\,d^2\,F_{\nu_{25}}^{-0.71}\,F_{\nu_{60}}^{1.71}$, if F_ν is in Jy, K_ν in cm^{2}g^{-1}, d in kpc. The basic assumption is that the grain properties are similar in all LBV-type nebulae (i.e. LBV+WN8 nebulae), an hypothesis which in view of the observed correlation seems a posteriori reasonable. Also, systematic differences in luminosities like those reported between empirical estimates and values derived from models will not affect the correlation as long as these differences remain systematic.

Further, it is interesting to consider the highly reddened objects G79.9+0.46, G25.5+0.2, and M1-78, suspected to contain LBV or WN central stars (Higgs et al. 1994, Subrahmanyan et al. 1994, Gussie 1995). For G79.9+0.46, the IRAS flux densities from Waters et al. (1996) give $\log M_d = -1.87$ at $d = 2$ kpc; this perfectly fits the correlation in Fig. 1b with $\log L/L_\odot = 6.30$ from Higgs et al. (1994), supporting the LBV nebula identification. On the contrary, the dust masses evaluated for G25.5+0.2 ($d \simeq 14$ kpc) and M1-78 ($d \simeq 8$ kpc) using IRAS PSC flux densities ($\log M_d = -1.22$ and -1.13, respectively) are definitely larger than for any other object (cf. Table 2), casting some doubts on their identification as LBV-type nebulae.

More detailed modelling has been carried out in a few cases, providing some information on the grains. After considering several models, McGregor et al. (1988b) and Hyland & Robinson (1991) concluded that large grains ($a \simeq 1$ μm) dominate in the AG Car nebula. The preponderance of large grains was also suggested in the η Car homunculus (Mitchell & Robinson 1986), and possibly in He3-519 (Davidson et al. 1993), while Mathis et al. (1992) showed that complex distributions of small grains may reproduce the observations in three WR nebulae.

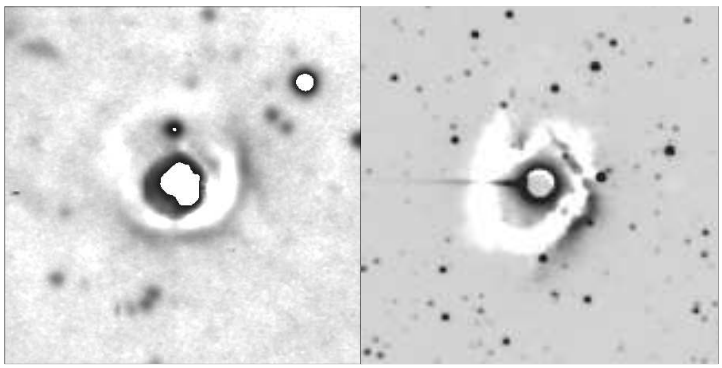


Figure 2. (A, left) HD168625: a 2.2 μm continuum image divided by a Hα+[NII] one, both from Hutsemékers et al. (1994). (B, right) AG Car: a red continuum image divided by a Hα+[NII] one, both obtained with the ESO 3.6m telescope + EFOSC. The darker regions in the nebulae are those where dust scattering dominates. Note that the AG Car nebula is also detected at 2.2 μm but the image, fainter, is of poor quality.

3. LBV-type nebulae as reflection nebulae

In addition to the well-known η Car homunculus, dust scattering has been convincingly detected in two LBV-type nebulae: AG Car (Viotti et al. 1988), and HD168625 (Hutsemékers et al. 1994). Why not in other LBV-type nebulae? Assuming the continuum surface brightness $S_{cont} \propto S_{H\alpha}/R_{neb}$, it appears that the other LBV-type nebulae are expected to be considerably fainter in the continuum, and therefore probably yet to be discovered as reflection nebulae.

The reflection nebula around AG Car has neutral colors relative to the star, while that around HD168625 is abnormally red. In both cases, this suggests the presence of large grains (Paresce & Nota 1989, Hutsemékers et al. 1994). Dust scattering seems to extend to the near-IR (as in η Car, Allen 1989), although this continuum could be due to the so-called extended 2.2 μm emission observed in many reflection nebulae (Sellgren et al. 1996). Imaging polarimetry could distinguish between these two hypotheses. In fact, detailed studies are complicated by the fact that LBVs are variable in magnitude and color, the light reaching the nebula with a time delay (typically one year for AG Car, which is comparable to the time-scale of the stellar variations).

The size and shape of the reflection nebulae are in rough agreement with the Hα nebulae, although clear differences exist (cf. Nota et al. 1995, and Fig. 2). For HD168625, the reflection nebula extends beyond the Hα ring, outlining the southern rim; this is also the case in some parts of the AG Car nebula, and for the HR Car nebula (Voors et al. 1997).

4. Conclusions

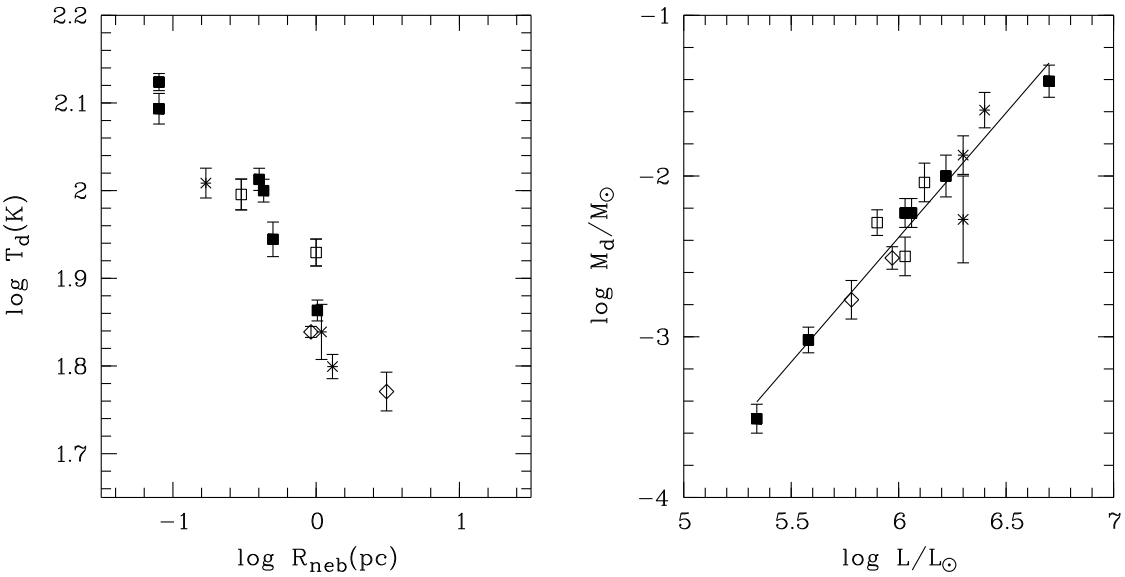
• Dust is a main feature of LBV-type nebulae (= LBV+WN8 nebulae, except P Cygni).
• Dust and ionized gas nebulae have roughly similar size and shape, but their

detailed morphology differs.
• The smaller nebulae have the hotter dust, and the most luminous stars have the most massive nebulae. The latter relation ($M_d \propto L^{1.5}$) constrains the instability and/or nebula formation mechanisms (Maeder 1997, Stothers & Chin 1996).
• There are several indications for the presence of large dust grains ($a \simeq 1\mu$m). The grain composition is unclear: silicate features are detected in η Car and R71 (Roche et al. 1993), while PAH emission is observed in HD168625 and AG Car (Cohen et al. 1986, Trams et al. 1997).

References

Allen, D.A. 1989, MNRAS, 241, 195
Barlow, M.J., Drew, J.E., Meaburn, J., Massey, R.M. 1994, MNRAS, 268, L29
Cohen, M., Allamandola, L., Tielens, A.G.G.M., et al. 1986, ApJ, 302, 737
Clampin, M., Nota, A., Golimowski, D.A., et al. 1993, ApJ, 410, L35
Crawford, I.A., Barlow, M.J. 1991, A&A, 249, 518
Crowther, P.A., Smith, L.J., Hillier, D.J., Schmutz, W. 1995, A&A, 293, 427
Davidson, K., Humphreys, R.M., Hajian, A., Terzian, Y. 1993, ApJ, 411, 336
Esteban, C., Smith, L.J., Vílchez, J.M., Clegg, R.E.S 1993, A&A, 272, 299
Esteban, C., Vílchez, J.M., Smith, L.J., Clegg, R.E.S 1992, A&A, 259, 629
Gussie, G.T. 1995, PASA, 12, 31
Hamann, W.R., Koesterke, L., Wessolowski, U. 1995, A&A, 299, 151
Higgs, L.A., Wendker, H.J., Landecker, T.I. 1994, A&A, 291, 295
Hildebrand, R.H. 1983, QJRAS, 24, 267
Hutsemékers, D. 1994, A&A, 281, L81 (Paper I)
Hutsemékers, D., Van Drom, E., Gosset, E., Melnick, J. 1994, A&A, 290, 906
Hyland, A.R., Robinson, G. 1991, Proc. ASA, 9, 124
Johnson, D.R.H., Barlow, M.J., Drew, J.E., Brinks, E. 1992, MNRAS, 255, 261
Lennon, D.J., Wobig, D., Kudritzki, R.P., Stahl, O. 1994, Space Sci.Rev., 66, 207
Maeder, A. 1997, these proceedings
Mathis, J.S., Cassinelli, J.P., van der Hucht, K.A., et al. 1992, ApJ, 384, 197
McGregor, P.J., Hyland, A.R., Hillier, D.J. 1988a, ApJ, 324, 1071
McGregor, P.J., Finlayson, K., Hyland, A.R., et al. 1988b, ApJ, 329, 874
Mitchell, R.M., Robinson, G. 1986, MNRAS, 222, 347
Nota, A., Livio, M., Clampin, M., Schulte-Ladbeck, R. 1995, ApJ, 448, 788
Nota, A., Pasquali, A., Drissen, L., et al. 1996, ApJS, 102, 383
Paresce, F., Nota, A. 1989, ApJ, 341, L83
Roche, P.F., Aitken, D.K., Smith, C.H. 1993, MNRAS, 262, 301
Schwering, P.B.W. 1989, A&AS, 79, 105
Sellgren, K., Werner, M.W., Allamandola, L.J. 1996, ApJS, 102, 369
Smith, L.F., Meynet, G., Mermilliod, J.C. 1994, A&A, 287, 835
Smith, L.J. 1996, Proc. 33rd Liège Int. Astrophys. Coll., Vreux et al. (ed.), 381
Smith, L.J., Crowther, P.A., Prinja, R.K. 1994, A&A, 281, 833
Stahl, O. 1987, A&A, 182, 229
Stahl, O., Wolf, B. 1986, A&A, 158, 371
Stahl, O., Wolf, B., Klare, G., et al. 1983, A&A, 127, 49
Stothers, R.B., Chin, C.W. 1996, ApJ, 468, 842
Subrahmanyan, R., Ekers, R.D., Wilson, W.E, et al. 1994, MNRAS, 268, 304
Trams, N.R., Waters, L.B.F.M., Voors, R.H.M. 1997, these proceedings
Viotti, R., Cassatella, A., Ponz, D., Thé, P.S. 1988, A&A, 190, 333
Voors, R.H.M., Waters, L.B.F.M., Lamers, H.J.G.L.M., et al. 1997, these proceedings
Waters, L.B.F.M., Izumiura, H., Zaal., P.A., et al. 1996, A&A, 313, 866
Wolf, B., Stahl, O., Seifert, W. 1987, A&A, 186, 182

Update
The "Nebular Mass – Stellar Luminosity" relation



This figure is similar to Fig. 1, but updated with recent data from the literature. Three galactic LBV candidates recently discovered in infrared surveys are added (with the symbol ✳). The agreement with the previously observed trends is excellent, strengthening the reality of the "nebular mass – stellar luminosity" relation. The new LBV candidates are G79.9+0.46 (Sect. 2 and Voors et al. 2000), AFGL 2298 (Ueta et al. 2001, Pasquali & Comeron 2002, Clark et al. 2003), and WRAY 17-96 (Egan et al. 2002). Already questionned in Sect. 2, G25.5+0.2 is probably not a LBV ; indeed, it shows a near-infrared spectrum different from the spectrum of other members of this class (Clark et al. 2000). For clarity, the Wolf-Rayet ring nebulae S308 and NGC 6888 are not plotted here (cf. Sect. 2).

References

- Clark, J.S., et al., 2000, ApJ 541, L67
- Clark, J.S., et al., 2003, A&A 403, 653
- Egan, M.P., et al., 2002, ApJ 572, 288
- Pasquali, A., Comerón, F., 2002, A&A 382, 1005
- Voors, R.H.M., et al., 2000, A&A 362, 236
- Ueta, T., et al., 2001, ApJ 548, 1020

Deuxième partie

Quasars de type BAL et microlentilles gravitationnelles

Article 6

The use of gravitational microlensing to scan the structure of BAL QSOs

D. Hutsemékers, J. Surdej, E. Van Drom : Astrophys. Space Science 216, 361 (1994)

Nous considérons ici l'utilisation de l'effet de microlentille gravitationnelle pour sonder la structure interne des quasars de type BAL.

Une microlentille gravitationnelle peut en effet "zoomer" certaines régions de formation des raies spectrales, modifiant de façon significative le spectre émergeant. Lorsque cette microlentille se déplace, elle induit des variations spectrales caractéristiques.

Considérant les deux modèles généralement proposés pour expliquer la formation des raies BAL, nous calculons l'effet attendu du passage d'une telle microlentille gravitationnelle. Nous constatons que les variations spectrales simulées diffèrent sensiblement. L'observation régulière d'un tel événement microlentille, "scannant" la structure interne du quasar, devrait donc permettre de distinguer les différents modèles.

En addendum, nous donnons quelques détails et résultats supplémentaires relatifs à la déformation des profils de type P Cygni par une microlentille gravitationnelle (le cas des nuages absorbants étant discuté en détail dans l'article 8).

The Use of Gravitational Microlensing to Scan the Structure of BAL QSOs

D. Hutsemékers, J. Surdej* and E. Van Drom
Institut d'Astrophysique, Université de Liège, 5, av. de Cointe, B-4000 Liège, Belgium

Abstract. Approximately 10% of the QSOs show broad absorption lines (BAL) in their spectra which, if interpreted in terms of Doppler velocities, reveal the presence of high velocity gas outflows. One of these BAL QSOs is known to be gravitationally lensed. It therefore constitutes a good candidate to search for microlensing effects, i.e. the selective amplification of different line forming regions. Considering current models for the BAL region, we have investigated the effects of moving microlenses on the line profiles, and we conclude that these effects strongly depend on the adopted model. A regular spectroscopic monitoring of lensed BAL QSOs would therefore be highly valuable to distinguish between the various models proposed so far to interpret the origin of broad absorption lines.

Key words: BAL QSOs, Gravitational lensing

1 Introduction

The BAL QSOs constitute a class of approximately 10% of the total number of QSOs. Their spectra are characterized by broad absorption lines (BALs), blue-shifted with respect to the emission, and indicating gas outflows at very high Doppler velocities, up to 0.2 c (see e.g. Turnshek 1988, for a review).

In order to interpret these line profiles, two main classes of kinematical and geometrical models have been proposed for the BAL region (BALR).

1) In the *cloud model* (Junkkarinen 1983; Weymann *et al.* 1985), the absorption is assumed to arise in a large number of small clouds, the total solid angle subtended by these clouds being fairly small as seen from the continuum source. These clouds do not significantly contribute to the emission lines which are formed as in normal QSOs. In this case, BAL QSOs are essentially normal QSOs which just turn out to be adequately oriented, i.e. with their absorbing clouds located along the line-of-sight.

2) For the *P Cygni type model* (Scargle *et al.* 1970; Drew & Boksenberg 1984) the absorption is produced in a relatively smooth flow having roughly the spherical symmetry (but in which discrete clouds may be embedded). In this case, the absorbing material may contribute to the emission lines and, more specifically, it can be at the origin of emission observed at high velocities. BAL QSOs may consist of a physically different class of QSOs, eventually being normal QSOs seen at another evolutionary stage.

It is clear that these two models are rather extreme, and that hybrids are possible.

* Also, Maître de Recherches au FNRS

Astrophysics and Space Science **216**: 361–365, 1994.
© 1994 *Kluwer Academic Publishers. Printed in Belgium.*

Also, there seems to exist subclasses of BAL QSOs, like the low-ionization or the PHL5200-type BAL QSOs, which probably necessitate slightly different modeling.

Since one of these BAL QSOs is known to be gravitationally lensed (Magain *et al.* 1988), the selective magnification of some line forming regions is expected, revealing the structure of the QSO. Considering the two proposed types of BALR models, we have investigated microlensing effects on simulated BAL profiles. In this framework, we discuss the case of the lensed BAL QSO H1413+117, deriving some possible constraints on the flow models.

2 The effects of gravitational microlensing on BALs

Microlensing corresponds to the gravitational lens effect due to a star or a group of stars (which may belong to a galaxy) located along the line-of-sight. While the separation between the micro-images is too small to be detected ($\sim 10^{-6}$ arcsec), microlensing can be at the origin of a strong (de-) magnification of the source, or of parts of it (Chang & Refsdal 1979, 1984; Kayser *et al.* 1986).

Microlensing is characterized by an effective lensing size, the so-called projected Einstein radius which essentially depends on the lens (star) mass, and by generic magnification patterns made of critical points and lines (the caustics). If a source with a size comparable to the Einstein radius of the lens crosses these caustics, it is (de-) magnified and the flux of radiation received by a distant observer is (de-) amplified.

For typical QSO and lens distances, the projected Einstein radius of a solar mass lens becomes comparable to the size of the continuum emitting region of QSOs. A microlensing event will therefore (de-)magnify the continuum emitting region but not the broad emission line region (BELR) which is generally assumed to be much more extended. The projected BALR, on the other hand, coincides with the continuum emitting region, such that microlenses can magnify the BALR, or parts of it (cf. the individual clouds if any), relative to the BELR. Since microlenses are moving with respect to the source, they can act as scanners of the QSO BALR with typical timescales of months (for the case of H1413+117).

Considering simple cloud and P Cygni type models for the BALR, we have investigated the possible effects of microlenses on the line profiles (cfr. Hutsemékers 1993, and Hutsemékers *et al.* 1992, 1993), adopting the Schwarzschild and Chang-Refsdal lens models which contain all generic microlensing features. An example of such effects is illustrated in Figure 1. We namely found that the two BALR models have rather different signatures when affected by microlensing effects. Basic differences may be summarized as follows:

• for the *cloud model*:

- clouds with different optical depths and smaller than the continuum region may be selectively magnified, inducing variations in the absorption profiles; for sufficiently small black clouds, the relative profile variation is directly proportional to the radius of the magnified cloud;

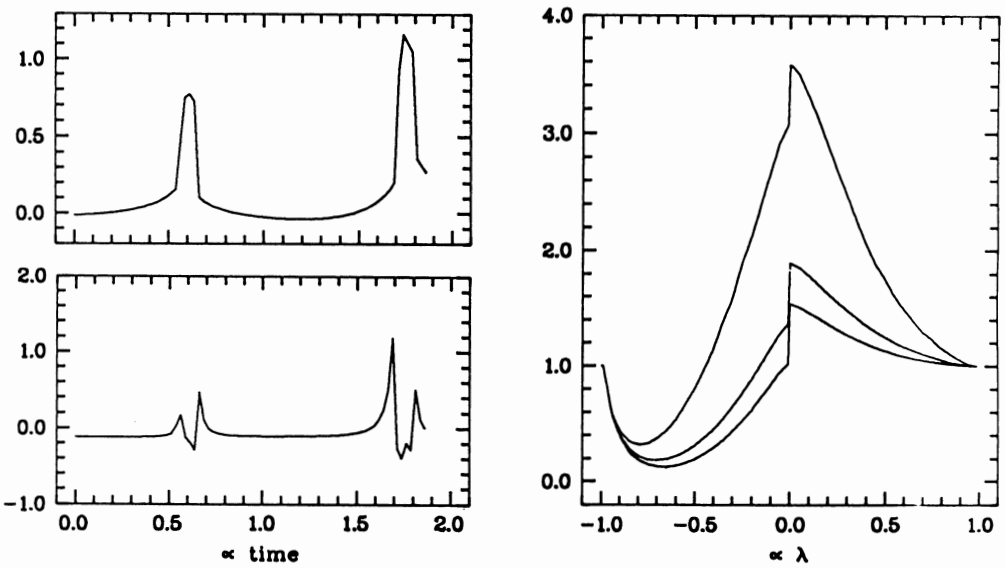


Fig. 1. Example of microlensing effects when a BAL QSO crosses a caustic pattern in the source plane, the P Cygni type model being assumed for the BALR and the Chang-Refsdal model for the microlens. In the first figure (upper left) the magnitude difference is plotted against a quantity proportional to the time, illustrating the variation of the continuum flux. The second figure (lower left) illustrates the corresponding variation of the total equivalent width of the line profiles. The last figure shows resulting P Cygni type profiles at selected moments.

- it is likely that only some parts (i.e. some velocities) of the profile are affected;
- depending on the optical depth of the magnified cloud, the variations in the absorption line may be uncorrelated with those of the emission line equivalent width;
- since the continuum region is simultaneously magnified, this effect, only differential, remains small or then requires a very precise lensing configuration;

• for the *P Cygni type model*:

- strong modifications of the P Cygni type profiles are induced, including possible enhancements of the emission;
- the behaviour is essentially the same at all velocities;
- the variations in the absorption line are correlated with those of the emission line equivalent width;
- the total equivalent width variation shows a characteristic behaviour (Fig. 1).

It seems therefore clear that the effects due to microlensing may constitute a powerful tool for distinguishing between the BALR models, provided that a regular spectroscopic monitoring becomes available.

3 Microlensing in H1413+117

The lensed BAL QSO H1413+117 consists of 4 images roughly forming a 1"×1" square. Evidence for microlensing in one of the image (D) was first reported by Kayser *et al.* 1990, on the basis of photometric variations. Further evidence comes from the fact that the spectrum of image D is slightly different from that of the other images (Angonin *et al.* 1990). The CIV and SiIV line profiles are similarly affected, in contrast with the intrinsic variations reported in the spectra of other BAL QSOs (see e.g. Barlow *et al.* 1992, and references therein).

The emission line differences may be easily interpreted by a microlensing effect: if the continuum emitting region is magnified, and the BELR is not affected as expected for a normal lens, the emission line equivalent width decreases as observed, after normalization to the amplified continuum. The difference observed in the absorption lines then arise because of

- the selective magnification of a small cloud optically thicker than the average; but this kind of interpretation necessitates very large continuum amplifications on short time scales,
- the apparent dimming of an emission line located at high velocities and superimposed on the varying part of the absorption line.

This latter interpretation is more viable in terms of microlensing, but requires the intrinsic emission line to be double-peaked. Such an intrinsic emission line profile is quite unusual and not typical of standard P Cygni type profiles. Ad-hoc models with turbulence may possibly account for such line profiles (Hutsemékers 1994). It is also striking to notice that the velocity separation between these two emission peaks exactly corresponds to the velocity separation between the Lyα and NV emission lines, possibly giving support to some line locking effects in driving the flow.

4 Conclusions

The different BALR models have clearly different signatures during a microlensing event. Microlensing events may therefore constitute a powerful tool for distinguishing between the BALR models provided that a regular spectroscopic monitoring of H1413+117 becomes available. In all cases the expected characteristics of the variations induced by microlensing are different from those reported for intrinsic variations.

If the spectral differences observed between the images of the quadruple QSO H1413+117 are actually due to microlensing effects, they are more convincingly interpreted by adopting a non-standard P Cygni type model for the BAL region. However, only the study of the temporal evolution of the observed spectral differences will provide us with more definite conclusions.

Although difficult, a spectroscopic monitoring of BAL QSOs known to be lensed, or located behind a galaxy, is badly needed.

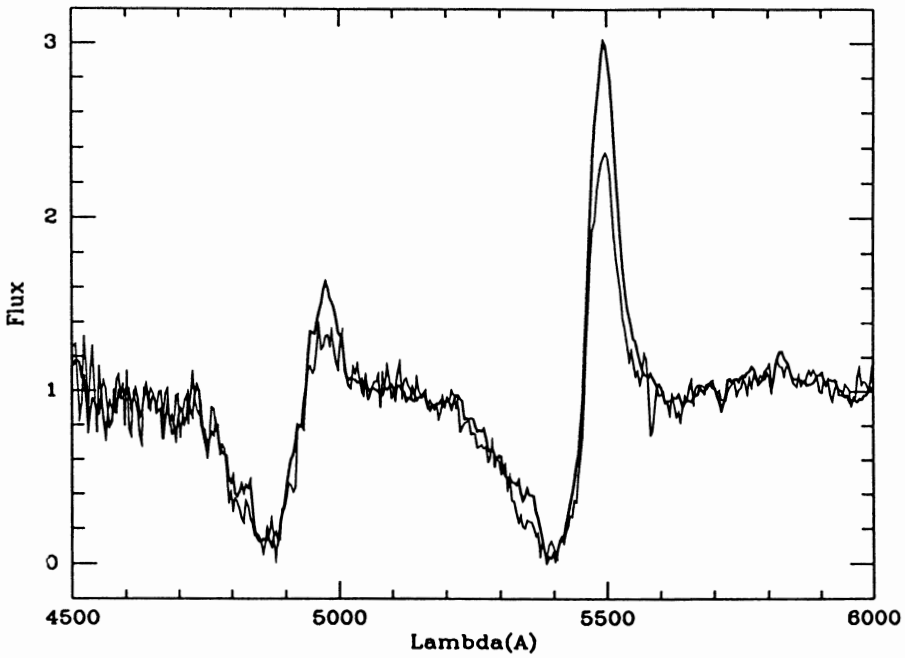


Fig. 2. The differences of the SiIV and CIV line profiles between the normalized spectrum of the component D of the BAL QSO H1413+117 (thin line) and the average spectrum (thick line) of the three other components (A,B,C) (cfr. Angonin et al., 1990, and Hutsemékers, 1993)

References

Angonin, M.C., Remy, M., Surdej, J., Vanderriest, C.: 1990, *A&A* **233**, L5
Barlow, T.A, Junkkarinen V.T., Burbidge, E.M., Weymann, R.J., Morris, S.L., Korista, K.T.: 1992, *Ap.J.* **397**, 81
Chang K., Refsdal, S.: 1979, *Nature* **282**, 561
Chang K., Refsdal, S.: 1984, *A&A* **132**, 168
Drew, J.E., Boksenberg, A.: 1984, *MNRAS* **211**, 813
Hutsemékers, D.: 1993, *A&A*, in press
Hutsemékers, D.: 1994, in preparation
Hutsemékers, D., Surdej, J., Van Drom, E.: 1992, *Gravitational lenses. Lecture Notes in Physics Vol. 406* , Kayser R., Schramm T., Nieser, L. (eds.), Springer-Verlag, p.373
Hutsemékers, D., Surdej, J., Van Drom, E.: 1993, in preparation
Junkkarinen, V.: 1983, *Ap.J.* **265**, 73
Kayser, R., Refsdal, S., Stabell, R.: 1986, *A&A* **166**, 36
Kayser, R., Surdej, J., Condon, J.J., Kellermann, K.I., Magain, P., Remy, M., Smette, A.: 1990, *Ap.J.* **364**, 15
Magain, P., Surdej, J., Swings, J.P., Borgeest, U., Kayser, R., Kühr, H., Refsdal, S., Remy, M.: 1988, *Nature* **334**, 327
Scargle, J.D., Caroff, L.J., Noerdlinger, P.D.: 1970, *Ap.J.* **161**, L115
Turnshek D.A.: 1988, *QSO Absorption Lines: Probing the Universe*, Blades, J.C., Turnshek, D.A., Norman, C. (eds.), Cambridge, p. 17
Weymann, R., Turnshek, D.A., Christiansen, W.A.: 1985, *Astrophysics of Active Galaxies and Quasi Stellar Objects*, Miller (ed.), Oxford, p.333

Addendum
Deformation of P Cygni line profiles by gravitational microlensing effects

The formalism

We consider a spherically symmetric atmosphere expanding around a central core, the source of the continuum. The flow is accelerated outwards. In the framework of the Sobolev approximation, the source function as well as the total optical depth may be evaluated *locally* in each point of the envelope. Measured by the observer, the normalized line profile at a frequency ν is simply expressed by (cf. Hutsemékers 1993) :

$$F_\nu \;=\; \int_{\Sigma_\nu} \frac{S_\nu}{I_\nu^c}\,(1-e^{-\tau_\nu})\;2p\;dp \;+\; \int_{\Sigma_\nu} e^{-\tau_\nu}\;2p\;dp\,,$$

where S_ν is the Sobolev source function, τ_ν the Sobolev optical depth, I_ν^c the intensity of the continuum emitted by the core, and p the impact parameter expressed in units of the core radius (see the figure). The integration is performed over the so-called surfaces of equal frequency ν, denoted Σ_ν.
The magnification of the source by a microlens located along the line of sight can be accounted for by simply multiplying each elementary emitting surface in the source plane by an amplification factor A which is characterized by a microlens model and the projected distance between the lens and the core. Since the amplification is not symmetric with respect to the quasar center, the line profile function then reads

$$F_\nu \;=\; \frac{\int\int S_\nu\,(1-e^{-\tau_\nu})\,A(p,\theta)\;p\;dp\;d\theta \;+\; \int\int I_\nu^c\,e^{-\tau_\nu}\,A(p,\theta)\;p\;dp\;d\theta}{\int\int I_\nu^c\,A(p,\theta)\;p\;dp\;d\theta}$$

which simplifies to

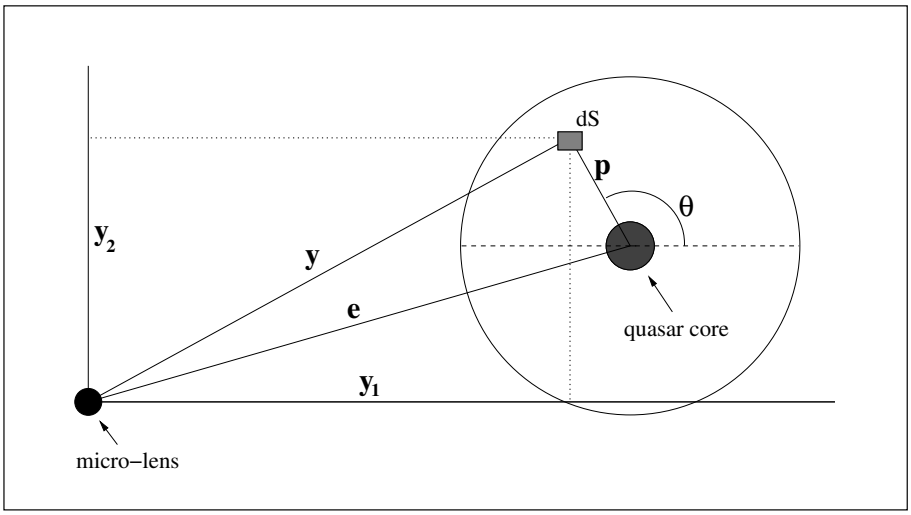
$$F_\nu \;=\; \int_0^{p_{\max}} \frac{S_\nu}{I_\nu^c}\,(1-e^{-\tau_\nu})\,\frac{A^\star(p)}{A_c^\star}\;2p\;dp \;+\; \int_0^1 e^{-\tau_\nu}\,\frac{A^\star(p)}{A_c^\star}\;2p\;dp$$

if we define

$$\begin{aligned} A^\star(p) &= \frac{1}{2\pi}\int_0^{2\pi} A(p,\theta)\;d\theta \\ A_c^\star &= \int_0^1 A^\star(p)\;2p\;dp\,. \end{aligned}$$

The amplification factor $A(p,\theta)$ depends on the adopted microlens model. A generic model is the so-called Chang-Refsdal microlens which is basically a point-mass lens perturbed by the gravitational field of the host galaxy. The amplification factor may be computed[1] in each point of the source plane as a function of several parameters. It shows typical

[1] See Schneider et al. (1992) for a complete derivation of the amplification factor in the case of a Chang-Refsdal microlens



The geometry in the source plane

caustic patterns like those illustrated in the series of figures below. The amplification factor also depends on the size of the quasar core relative to the microlens effective radius in the source plane (the so-called Einstein radius, projected onto the source plane), and on their relative distance. By moving the quasar within such a caustic pattern, different amplification factors apply to different sub-regions of the wind, inducing deformations of the P Cygni line profiles.

Numerical calculations

A series of numerical calculations are given in the following figures. Each figure shows the track in the caustic pattern, the photometric light curve, the equivalent width curve, and 3 examples of P Cygni line profiles taken at different epochs along the light curve (cf. the tick marks between the flux and equivalent width diagrams).
The first two pages of figures illustrate the effect of different tracks and/or caustic patterns. For each case, two different values of the core radius (expressed in units of the Einstein radius) are considered. The same outflow model is used (i.e. a typical P Cygni type model with pure resonance scattering and a smooth opacity law).
The last page illustrates the effect of microlensing on different outflow models, i.e. a model with significant collisional excitation, a model with an opacity shell inside the flow, and a model with both the shell and the collisional excitation.

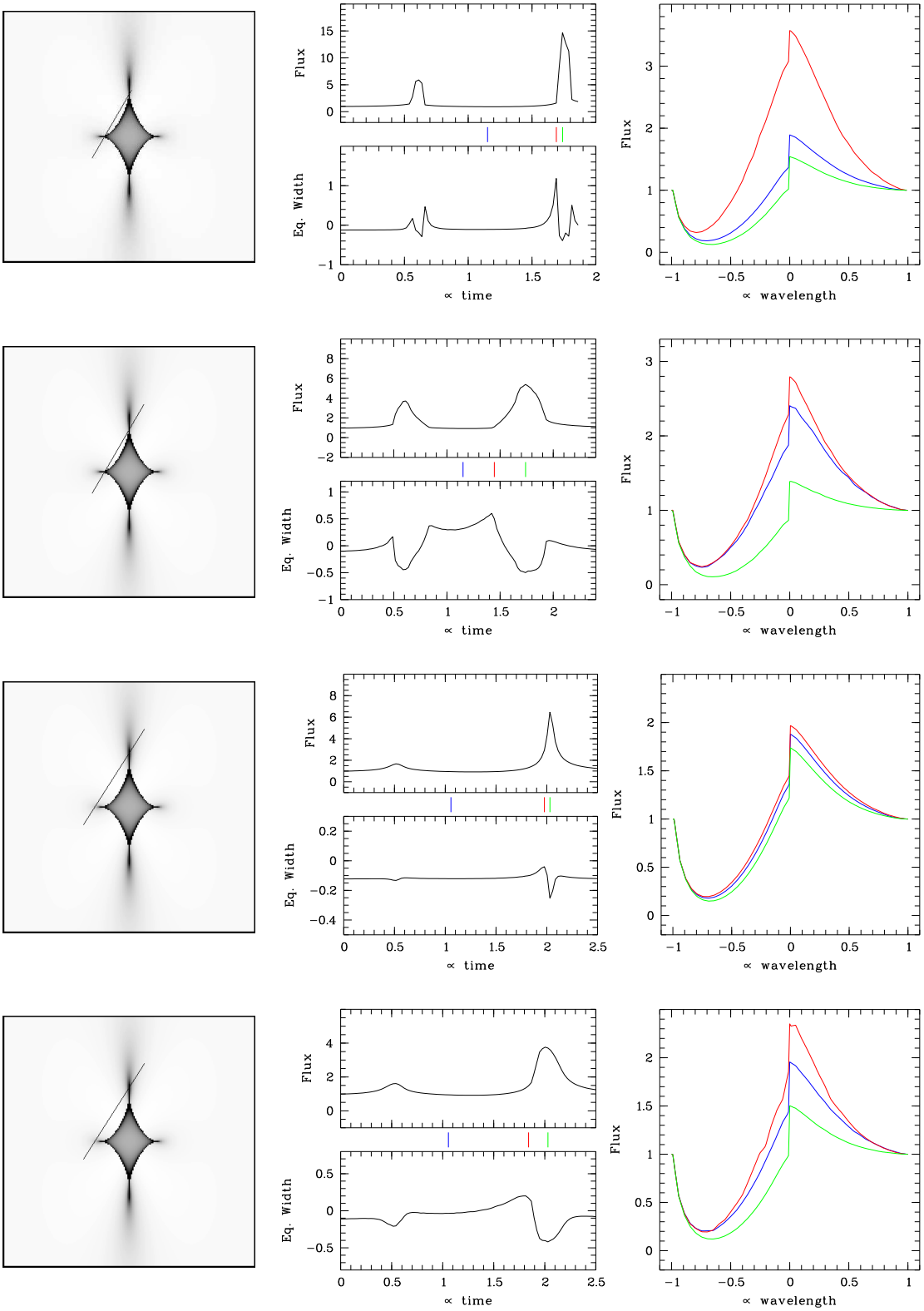
Results

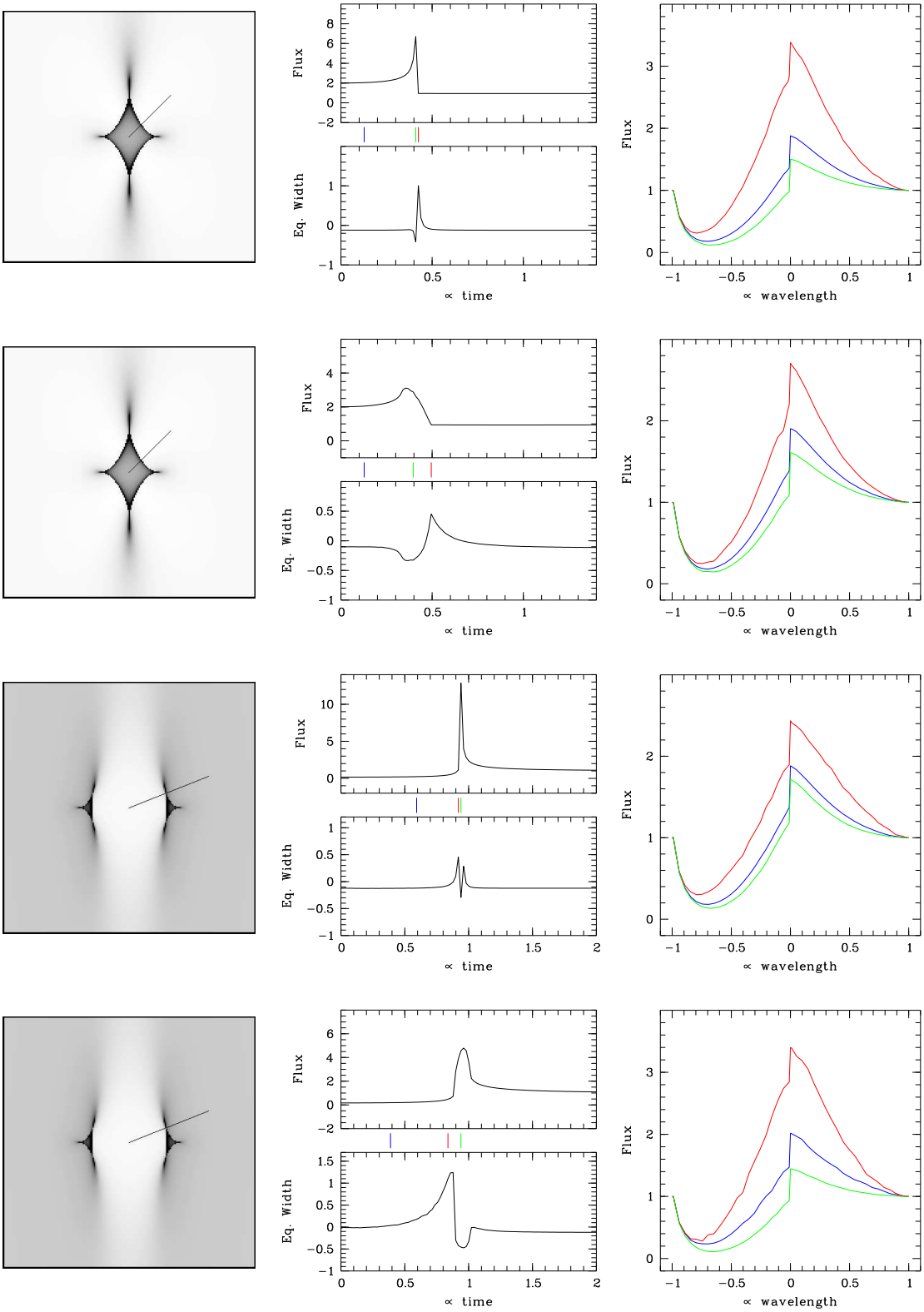
It is clear from the illustrated profiles that microlensing can induce significant deformations of P Cygni line profiles. Both emission and absorption may be enhanced. In some cases, the modified profiles can even mimic pure emission or pure absorption. It is important to notice that when deformations are significant, all velocities are affected such that only global variations are seen (as opposed to the possible appearance of narrow peaks in the profiles for example).
The enhancement of the emission part of the profile is rather unexpected since emission is usually thought to come from regions much larger than the continuum source (and consequently much larger than the Einstein radius). This enhancement may be explained

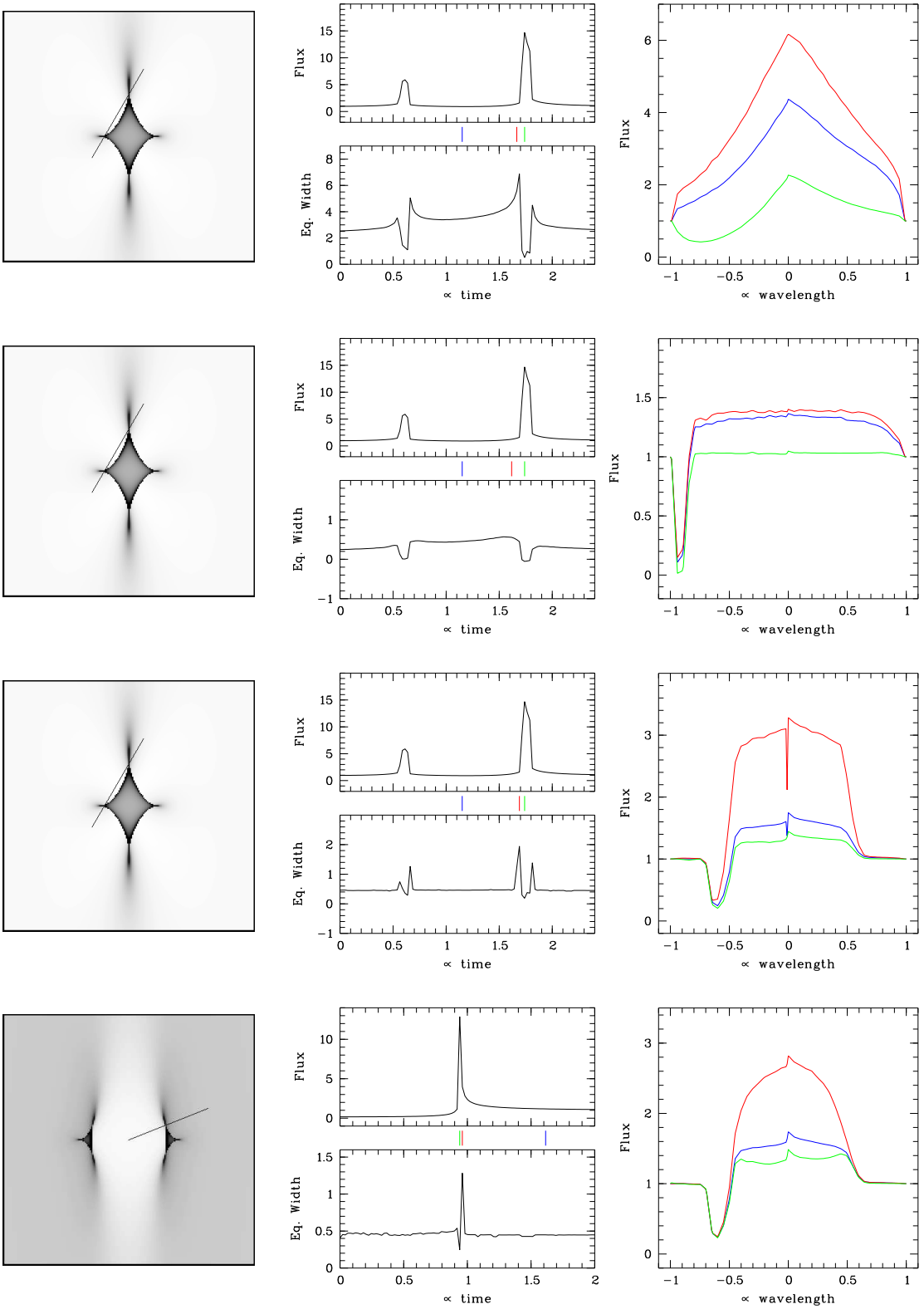
by the fact that the source function is large close to the core, rapidly decreasing outwards ; the amplification of the emission then occurs just before or after the magnification of the continuum source.
Whatever the caustic pattern or the outflow model, the profile deformations and the equivalent width curves show a characteristic behavior. Also, the first order moment W_1 of the line profiles (e.g. Hutsemékers & Surdej, 1990) is found to remain constant whatever the deformations induced by the microlensing effect. This important property may be easily understood : along a given line of sight, microlensing amplification similarly affects positive and negative velocities in the profile, producing symmetric variations which cancel each other when computing W_1.

References

- Hutsemékers, D., 1993, ApJ 417, 97
- Hutsemékers, D., Surdej, J., 1990, ApJ 361, 367
- Schneider, P., Ehlers, J., Falco, E., 1992, Gravitational lenses (Springer, Berlin).


Flux
Eq. Width
∝ time
Flux
∝ wavelength


Flux
Eq. Width
∝ time
Flux
∝ wavelength


Flux
Eq. Width
∝ time
Flux
∝ wavelength

Article 7

ESO & NOT photometric monitoring of the Cloverleaf quasar

R. Østensen, M. Remy, P.O. Lindblad, S. Refsdal, R. Stabell, J. Surdej, P.D. Barthel, P.I. Emanuelsen, L. Festin, E. Gosset, O. Hainaut, P. Hakala, M. Hjelm, D. Hutsemékers, M. Jablonski, A.A. Kaas, H. Kristen, S. Larsson, P. Magain, B. Pettersson, A. Pospieszalska-Surdej, A. Smette, J. Teuber, B. Thomsen, E. Van Drom : Astron. Astrophys. Suppl. 126, 393 (1997)

Cet article présente les résultats d'un suivi photométrique du quasar quadruple de type BAL H1413+117, réalisé à La Silla (ESO) et à La Palma (NOT) de 1987 à 1994. Le but est d'étudier les variations de chacune des quatre images individuellement, afin de mesurer le délai temporel entre les composantes (ce délai est relié aux paramètres cosmologiques fondamentaux) et/ou de détecter toute anomalie révélant un effet de microlentille.

Une analyse détaillée montre que les quatre composantes varient de façon significative et quasiment en parallèle, de sorte que seule une limite supérieure du délai temporel peut être estimée. Par contre, la courbe de lumière de la composante D présente des écarts au comportement général, indiquant la présence probable d'un effet de microlentille gravitationnelle.

ASTRONOMY & ASTROPHYSICS
SUPPLEMENT SERIES

Astron. Astrophys. Suppl. Ser. **126,** 393-400 (1997)

ESO & NOT photometric monitoring of the Cloverleaf quasar⋆,⋆⋆

R. Østensen[1], M. Remy[2], P.O. Lindblad[3], S. Refsdal[4], R. Stabell[5], J. Surdej[2,⋆⋆⋆], P.D. Barthel[6], P.I. Emanuelsen[1], L. Festin[7], E. Gosset[2,†], O. Hainaut[8], P. Hakala[9], M. Hjelm[3], J. Hjorth[10], D. Hutsemékers[2,⋆⋆⋆], M. Jablonski[5], A.A. Kaas[3], H. Kristen[3], S. Larsson[3], P. Magain[2‡], B. Pettersson[7], A. Pospieszalska-Surdej[2], A. Smette[6], J. Teuber[11], B. Thomsen[12], and E. Van Drom[2]

[1] Institute of Mathematical and Physical Sciences, University of Tromsø, N-9037 Tromsø, Norway
[2] Institut d'Astrophysique, Université de Liège, Belgium
[3] Stockholm Observatory, S-13336 Saltsjöbaden, Sweden
[4] Hamburger Sternwarte, Gojenbergsweg 112, D-21029, Germany
[5] Institute of Theoretical Astrophysics, University of Oslo, Box 1029 Blindern, N-0315 Oslo, Norway
[6] Kapteyn Astronomical Institute, Rijksuniversiteit, Landleven 12, Postbus 800, 9700 AV Groningen, The Netherlands
[7] Astron. Obs. Box 515, S-751 20 Uppsala, Sweden
[8] Institute for Astronomy, 2680 Woodlawn Drive, Honolulu HI 96822, U.S.A.
[9] Helsinki University Observatory, Tahtitorninmaki, SF-00014 Helsinki, Finland
[10] NORDITA, Blegdamsvej 17, DK-2100 Copenhagen, Denmark
[11] Copenhagen University Observatory, Juliane Maries Vej 30, DK-2100 Copenhagen, Denmark
[12] Institute of Physics and Astronomy, University of Aarhus, DK-8000 Aarhus C, Denmark

Received November 18, 1996; accepted March 18, 1997

Abstract. The Cloverleaf quasar, H1413+117, has been photometrically monitored at ESO (La Silla, Chile) and with the NOT (La Palma, Spain) during the period 1987–1994. All good quality CCD frames have been successfully analysed using two independent methods (i.e. an automatic image decomposition technique and an interactive CLEAN algorithm). The photometric results from the two methods are found to be very similar, and they show that the four lensed QSO images vary significantly in brightness (by up to 0.45 mag), nearly in parallel. The lightcurve of the D component presents some slight departures from the general trend which are very likely caused by micro-lensing effects. Upper limits, at the 99% confidence level, of 150 days on the absolute value for the time delays between the photometric lightcurves of this quadruply imaged variable QSO, are derived. This is unfortunately too large to constrain the lens model but there is little doubt that a better sampling of the lightcurves should allow to accurately derive these time delays. Pending a direct detection of the lensing galaxy (position and redshift), this system thus constitutes another good candidate for a direct and independent determination of the Hubble parameter.

Key words: gravitational lensing — techniques: image processing — quasars: H1413+117

1. Introduction

The Cloverleaf quasar, H1413+117, was discovered to be a quadruply imaged QSO by Magain et al. (1988). Since then, it has been photometrically monitored essentially as part of the ESO Key-Program *Gravitational Lensing* (La Silla) and as part of the *Gravitational Lens Monitoring Program* at the Nordic Optical Telescope (NOT) on the island of La Palma. This quasar, at a redshift of 2.55, and with an apparent visual magnitude of 17, is one of the brightest members of the class of broad absorption line (BAL) QSOs. In addition, its spectrum shows at least three narrow absorption line systems at redshifts $z = 1.44$, 1.66 and 2.07. These are attributed to intervening gas

Send offprint requests to: rolf.stabell@astro.uio.no

⋆ Based on observations collected at the European Southern Observatory (La Silla, Chile) and with the Nordic Optical Telescope (La Palma, Spain).

⋆⋆ Table 1. Logbook for the ESO and NOT observations together with photometric results for the Cloverleaf quasar. This long table can be accessed on the WWW at the URL address: http://vela.astro.ulg.ac.be/grav_lens/glp_homepage.html

⋆⋆⋆ Research Director, Belgian Fund for Scientific Research (FNRS).

† Research Associate, Belgian Fund for Scientific Research (FNRS).

‡ Senior Research Associate, Belgian Fund for Scientific Research (FNRS).

clouds (Hazard et al. 1984; Drew & Boksenberg 1984; Turnshek et al. 1988), possibly associated with the lens(es) (Magain et al. 1988). Imaging of H1413+117 shows that the four lensed components are separated by approximately one arcsecond ($''$). However, no lensing object has yet been detected. The spectra of two of the four images have been found by Magain et al. (1988) to be identical, except for narrow absorption line systems at $z = 1.44$ and 1.66, which are much stronger in component B than in C. Two-dimensional spectroscopy by Angonin et al. (1990) also shows that the spectrum of component D has smaller values for the emission lines/continuum ratios and a larger equivalent width for the absorption features in the P Cygni profiles, compared to the other three lensed QSO components. This is most likely caused by micro-lensing effects. Observations from the VLA at NRAO show radio counterparts for the four QSO components, as well as an additional strong radio source between images B and D (Kayser et al. 1990), but no radio source has been found that can be associated with a lensing object.

As part of the *Gravitational Lensing* ESO Key-Program, CCD photometry of H1413+117 has been carried out with the aim of detecting photometric variability of the QSO itself, and thereby determining the time delay(s), or the signature of micro-lensing effects. Preliminary results for the four images have been presented by Arnould et al. (1993) and by Remy et al. (1996). These authors report that from 1987 to 1993 the four lensed components apparently display brightness variations quasi-simultaneously and in parallel. They set an upper limit for the time delays of roughly a few months. In addition to these variations, which are ascribed to the source, the D component has been found to show extra light variations with respect to the other components. These extra variations have been interpreted as being possibly induced by micro-lensing effects.

The astrophysical and cosmological justifications for conducting photometric monitoring programs of gravitational lens systems are summarized in Refsdal & Surdej (1992, 1994). The importance of recording well sampled and accurate lightcurves for such systems can hardly be overestimated. The ESO Key-Program observations took place during the period 1987-1993 (see Table 1, accessible on the WWW).

The original plans were to monitor the known gravitational lens systems Q2237+0305 (the Einstein Cross), UM425, Q0142 − 100 = UM673 (ESO GL1, Surdej et al. 1987, 1988) and H1413+117 (the Cloverleaf), at weekly intervals. However, because of unfavorable weather conditions, unexpected technical problems or sometimes the non-availability of a direct CCD camera at the foci of the ESO telescopes, the sampling of the photometric lightcurves has not been as frequent as initially expected. After some preliminary observations in 1990, a program was also started at the NOT, for monitoring the four gravitational lens systems Q0142 − 100, Q0957+561 (the "classical" Double Quasar), H1413+117 and Q2237+0305. Although observations were similarly aimed at weekly intervals, several large gaps in the NOT data have occurred for the same reasons as those mentioned above. Results for the Einstein Cross have been published by Østensen et al. (1996), for UM425 by Courbin et al. (1995) and for Q0142 − 100 by Hjorth et al. (1996) and Daulie et al. (1993).

In this paper we present results for the Cloverleaf, obtained using two independent methods of analysis, combining all ESO and NOT observations.

2. Observations and instrumentation

The ESO Key-Program observations of the Cloverleaf were made using several different telescopes, and with a number of different CCD detectors. All telescopes and cameras used are listed in Table 1, together with the filters, observing dates, average seeing and the name of the principal investigator(s). The ESO telescopes that were used are the 3.5 m New Technology Telescope (NTT), the 2.2 m ESO-Max Planck Institut (MPI) telescope and the Danish 1.54 m telescope (DAN) at La Silla, Chile (the ESO 3.6 m telescope has also been used occasionally).

Observations from the NOT Monitoring program were made with the 2.56 m Nordic Optical Telescope, at Roque de los Muchachos, La Palma, Canary Islands (Spain) from April 1990 to August 1994. During the first four years, a Tektronix 512 × 512 CCD camera with 0.197$''$ pixels was the only detector available. In 1994, a more sensitive 1024 × 1024 CCD camera with 0.177$''$ pixels was installed. Reasonable signal-to-noise ratios were obtained for exposure times of 4 minutes or more when the seeing was better than 1$''$. The best NOT images show point source profiles with $FWHM = 0.5''$, which clearly resolve the four optical components of the Cloverleaf. Note that a non-linearity problem with the NOT stand-by CCD camera in observations made before 1993 has been numerically corrected for (see Østensen et al. 1996).

3. Data reduction, calibration and image analysis

Two independent methods have been used to preprocess and analyse all CCD frames obtained for the Cloverleaf at ESO and with the NOT. These are described below.

3.1. Automatic image decomposition technique

Classical preprocessing (flat-field correction and bias subtraction) has been applied to the raw data using ESO MIDAS routines. Whenever necessary, CCD non-linearities have been corrected for. Other defects such as column offsets and cosmic rays have been removed before sky subtraction. On each image frame, bi-quadratic polynomial surfaces have been fitted to numerous selected empty regions of the observed fields, in order to accurately subtract the sky from each individual CCD frame.

Also in the MIDAS environment, a general, automatic procedure has been developed in order to derive the best photometric measurements of multiply imaged point sources. The magnitudes of the lensed components have been determined by fitting multiple numerical point spread functions (hereafter PSFs), using a χ^2 minimization method.

The numerical PSF has been determined by summation of the images of isolated point sources recorded on the same CCD frames as the gravitational lens system, after re-centering at the same position by bi-quadratic interpolations. Figure 1 in Kayser et al. (1990) shows a finding chart around H1413+117, with several of the used PSF stars. Star 40 has been adopted as our photometric reference. Among others, stars 8, 19, 40, 45 and 47 have frequently been used to construct the PSF. After fitting the composite PSF to the individual stars present on the CCD frame, incompatible objects were removed and the PSF redetermined. Making use of the coordinates of the stars derived from the previous fits, the linear transformation of the positions between different frames could be determined very accurately, including any relative rotation, translation and scaling.

On each individual frame, four free PSFs were first fitted to the complex QSO image, leading to positions for each of the four lensed components and preliminary values for the intensities. In Fig. 1 the relative positions of the four lensed images of the QSO are plotted. In the final measurements, the relative positions of the four PSFs have been fixed, reducing the number of free parameters from 12 to 6 (i.e. 4 intensity parameters and 2 position parameters). The values of these average relative image positions are shown in Table 2; the estimated uncertainties being $\sigma \simeq 0.008''$. A complete description of this automatic decomposition technique may be found in Remy (1996). Let us finally note that a total of 157 distinct ESO and NOT observations have been successfully analysed with the above method, even the lower quality data.

Table 2. Average relative positions of the B, C and D lensed components with respect to A, as derived from the multiple fitting of 4 free PSFs applied to a set of the 80 best ESO and NOT observations

Comp.	$\Delta\alpha$ ($''$)	$\Delta\delta$ ($''$)
A	+0.000	+0.000
B	+0.726	+0.201
C	−0.518	+0.705
D	+0.324	+1.058

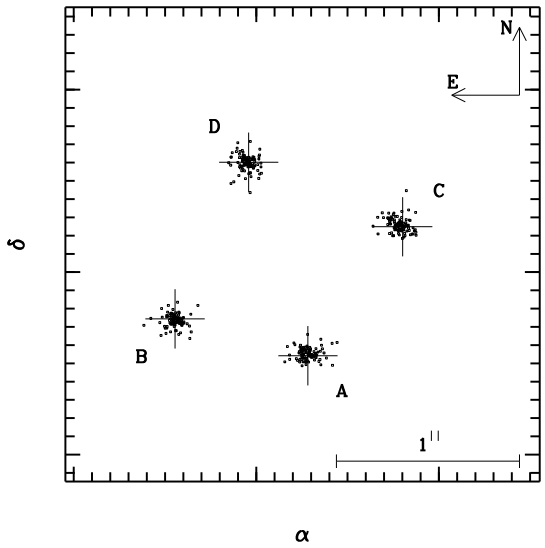


Fig. 1. Relative positions of the four lensed components of H1413+117 derived from multiple PSF fittings of the 80 best ESO and NOT observations. The four crosses in this figure refer to the adopted average relative positions of the four lensed QSO images used in subsequent PSF fittings (see Table 2)

3.2. Interactive CLEAN processing

We have independently applied the IRAF/ccdred package developed and maintained by NOAO (National Optical Astronomy Observatories, Tucson, Arizona) to preprocess the same ESO and NOT data.

A program for CLEAN deconvolution of overlapping point sources has been developed by Østensen (1994), and implemented using IDL. This program, XECClean, was especially developed for doing high precision photometry of the quadruply imaged system, Q2237+0305 (the Einstein Cross). XECClean applies a semi-analytical PSF-profile fitting procedure adopted from the DAOPHOT package by Stetson (1987) and deconvolves the images using the interactive CLEAN algorithm (Teuber 1993), where the individual images are iteratively removed, until satisfactory residuals are obtained. Unlike for the case of the Einstein Cross, the analysis of the Cloverleaf system does not suffer from the additional presence of a bright foreground lens, and it is therefore easier to determine the individual fluxes of the four QSO components.

For some of the ESO data, photometric standard stars have been simultaneously observed in the V and R bands. From this, we have calibrated in magnitude several of the used PSF stars. Adopting the numbering used by Kayser et al. (1990) for the identification of the comparison stars, we report in Table 3 their V and R magnitudes. The photometric variability of star 40 has been checked against star 45. These stars are found to be photometrically

stable with respect to each other and to other PSF stars. Since star 40 is present on all CCD frames obtained for H1413+117, it has been used as our photometric reference star.

Table 3. V and R magnitudes of PSF stars in the field of H1413+117. See Kayser et al. (1990) for a finding chart. The 1σ uncertainty on the zero point magnitude determinations is about 0.10 mag

Star	V	R
40	18.55	17.89
8	18.72	18.41
19	18.09	17.38
45	16.88	16.41
47	20.32	19.56

4. Photometric results

The relative magnitudes of the four lensed components of the Cloverleaf determined with respect to the photometric reference star 40 are also reported in Table 1. Furthermore, this table lists details of the observations together with the Modified Julian Day at the time of the observations, night averages of the photometric determinations derived from applying the automatic image decomposition technique (i.e. A_1, B_1, C_1, D_1 for the relative photometric measurements of the A-D components, respectively, and $\sigma_1(A)$, $\sigma_1(B)$, $\sigma_1(C)$, $\sigma_1(D)$, for the derived measurement uncertainties as described below) and from applying the interactive CLEAN algorithm (i.e. A_2, B_2, C_2, D_2 and σ_2 for a common value of the measurement uncertainties). The same photometric measurements with their uncertainties are plotted in Fig. 2 (automatic image decomposition technique, method 1) and in Fig. 3 (interactive CLEAN processing, method 2), as a function of the Modified Julian Day.

We describe in this paragraph how the photometric error bar with the automatic image decomposition technique has been derived for a given science frame. A simulated frame which mimics the science frame has been constructed. Gaussian profiles with comparable intensities, relative image positions and FWHM were used to simulate the real objects. Random values have been added to the simulation in a coherent way with the noise characteristics of the real frames. The simulated frame has then been reduced in exactly the same way as the real observations (including PSF determination with the same stars). This (very time consuming) simulation process has been repeated 10 times with different random noise values (still in a coherent way with the noise in the real frame). The dispersions of the derived values for each simulation of the set lead to realistic estimates for the photometric error bars (i.e. $\sigma_1(A)$, $\sigma_1(B)$, $\sigma_1(C)$, $\sigma_1(D)$). Such estimates have also been compared with the dispersion of measurements made on a series of 15 real observations, taken during the same night in the Gunn i filter (for which we assume intra-night photometric constancy): a good agreement has been found. Despite the fact that the error estimates for the automatic method are the best ones available, we cannot rule out an underestimation of the error (maximum by a factor 2) for some of the photometric data, especially those with a seeing > 1.4.

When using the interactive CLEAN algorithm, the error estimates are based on both the statistical uncertainties, as derived from the XECClean fitting, and the residuals in the CLEAN'ed image. The latter contribution includes the effects from seeing conditions and the quality of the PSF. Zero-point errors occurring when using a calibration star in the field, with colors different from the program object, can be as large as 0.02 magnitudes when changing from one detector to another.

Since our observations have been made using such a wide range of telescopes and CCD cameras, and since it has not been possible to maintain exactly the same set of filters throughout the monitoring period, some additional uncertainties are introduced in our data. However, all estimates show that these errors should be small compared to those due to the photometric decomposition of the four lensed QSO images.

5. Discussion

Comparison between the photometric lightcurves illustrated in Figs. 2 and 3 for the A, B, C and D lensed components of H1413+117 reveals a remarkably good match between the measurements derived using the two independent image analysis methods described in the previous section. Figure 4 compares the photometric measurements and their uncertainties derived using the two independent methods. Except for a few isolated data points, there is a very good overall agreement between these independent photometric determinations.

From our two observations in the B band (see Table 1), we note that the B component is weaker than the C component, while being almost equal in the V band (see Fig. 2 and Fig. 3). Image B is also markedly stronger than image C in the I band than in the R band (see Table 1 for the independent photometric measurements). This is consistent with differential reddening caused by dust in the lensing galaxy along the different light paths of the lensed components. The prominence of absorption lines at redshifts $z = 1.44$, 1.66 in the spectrum of component B supports this interpretation (Magain et al. 1988) and

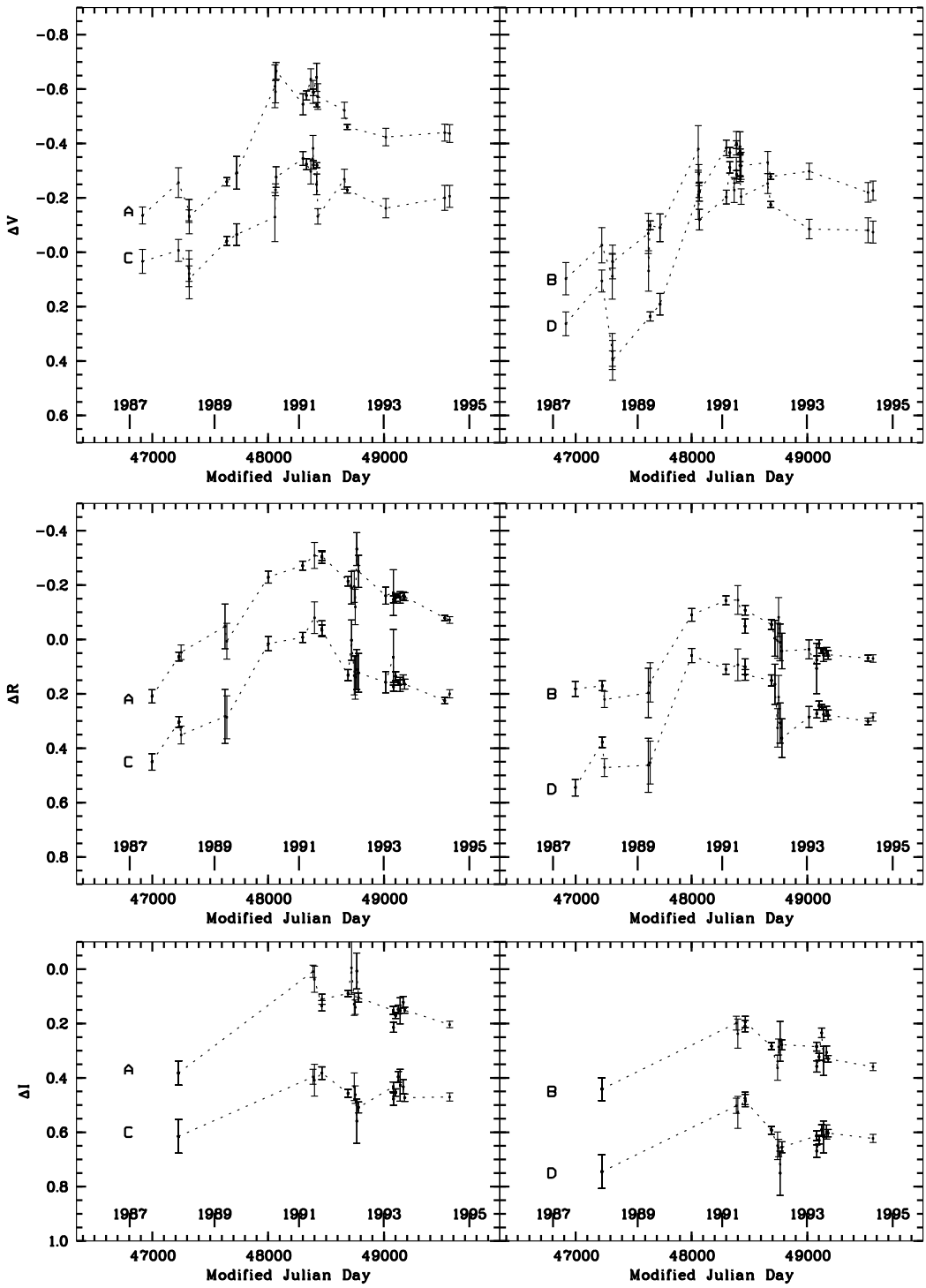


Fig. 2. Relative V, R and I magnitudes of the four lensed components of H1413+117 with respect to the photometric reference star as a function of the Modified Julian Day. These measurements are the results of applying the automatic image decomposition technique (see text, method 1)

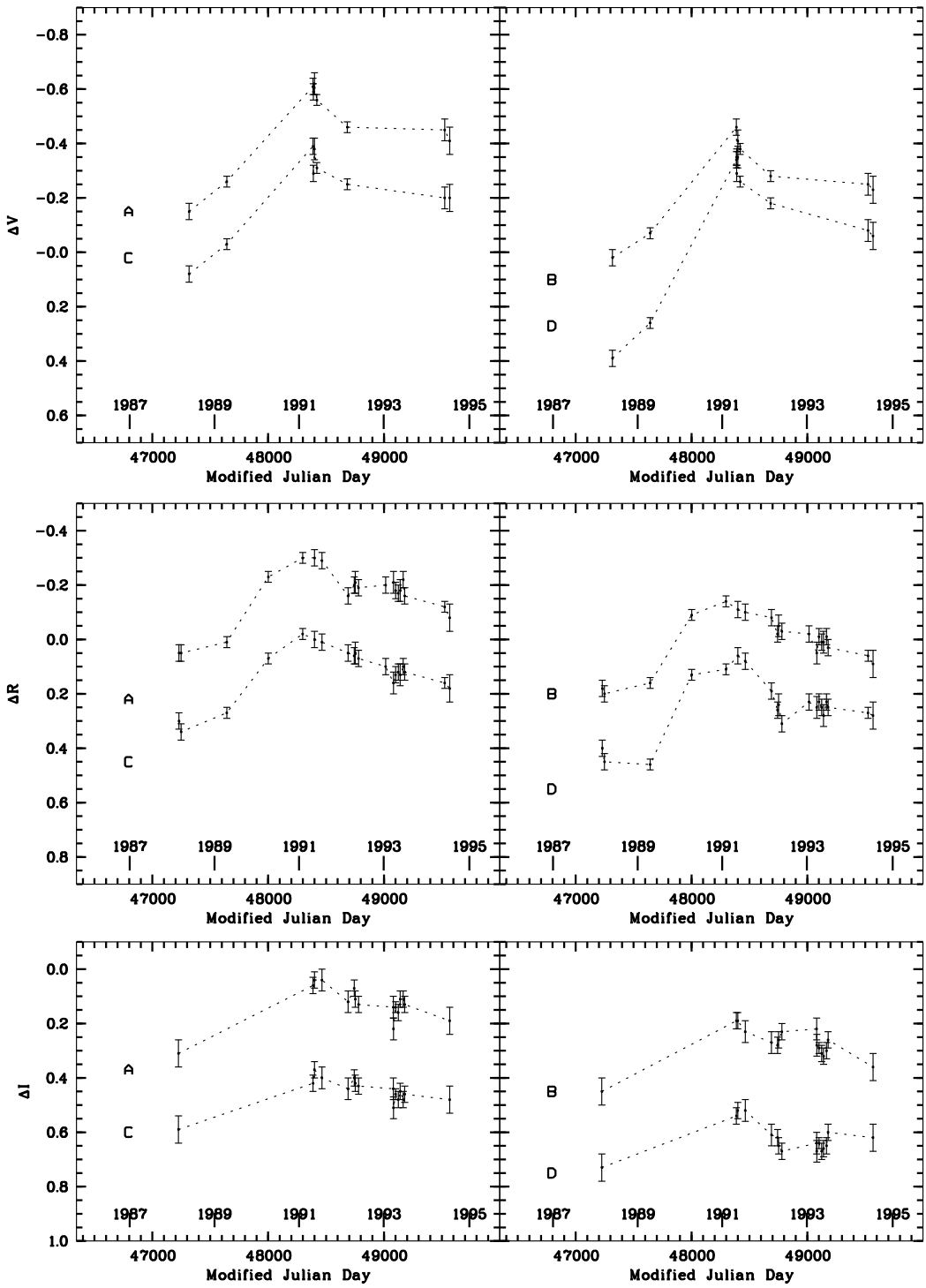


Fig. 3. Relative V, R and I magnitudes of the four lensed components of H1413+117 with respect to the photometric reference star as a function of the Modified Julian Day. These measurements are the results of applying the interactive CLEAN algorithm (see text, method 2)

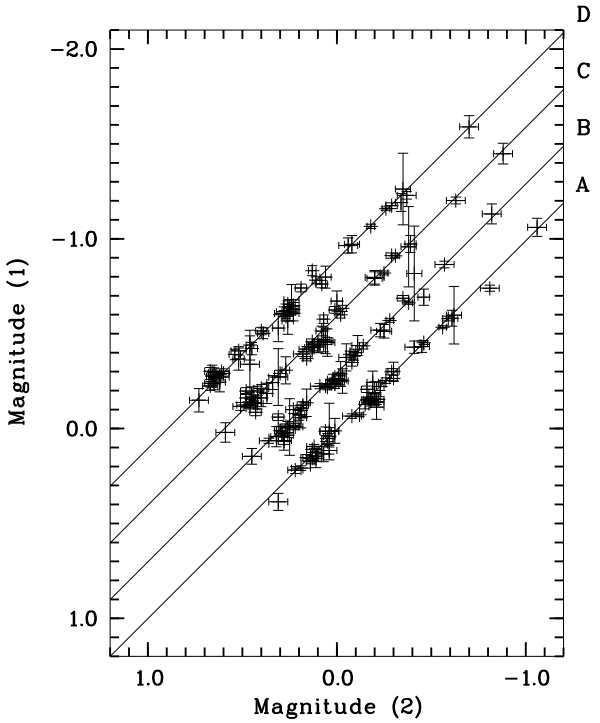


Fig. 4. Relative magnitudes for the A, B, C and D lensed components of H1413+117 (all filters), with respect to the reference photometric star, derived using the automatic image decomposition technique (1) and the interactive CLEAN algorithm (2). The diagonal lines represent curves of perfect match between the two methods. Note that for the sake of clarity, the measurements pertaining to B, C, D and their associated diagonal lines have been translated by constant values with respect to the results for A

suggests searching for the lensing object(s) at those redshifts, in the vicinity of the B component.

The lightcurves for the A, B and C components clearly vary in a parallel fashion in all filters, starting at a minimum luminosity in 1988, at the beginning of the ESO observation series, and peaking in 1991. The time delay for this system is expected to be shorter than one month (Kayser et al. 1990), so the quasi-simultaneous variations observed for these three components are consistent with intrinsic variations, as previously noted by Arnould et al. (1993) and Remy et al. (1996).

In order to avoid windowing effects on the time delay determinations (see Kayser 1993), the V and R lightcurves of component A, derived with method 1, have been smoothed using a simple low-pass spline with cut-off frequency of about (2 weeks)$^{-1}$. The magnitude differences between the data and the smoothed curve fall approximately within the 3σ limit. Nevertheless, the χ^2 for those magnitude differences, in a given filter, is found to be too high by a factor 4, at least. This could indicate the existence of photometric variations at higher frequencies but also of non-Gaussian errors or an oversmoothing of the data. In the next step of the analysis, the two smoothed lightcurves for component A (one for R and one for V) have been numerically translated in the epoch–magnitude diagram $(\Delta t, \Delta m)$. For a given value of $(\Delta t, \Delta m)$, the corresponding χ^2 between the observations of a given component and the point of the translated smoothed lightcurve at the same epoch has been computed. As the high frequency variations disallow a direct statistical interpretation of the χ^2 values, the latter ones have been normalized in two ways.

If we assume that the smoothed lightcurve of A should be compatible with the A data, the χ^2 for each component have been normalized to the minimum χ^2 of A (solid contours in Fig. 5). Considering the A data points, the derived $\chi^2(\Delta t, \Delta m)$ contour at the 99% confidence level (combined for the V and R filters in Fig. 5), extends to about ± 150 days. This sets a lower limit on the accuracy of the time delay determination based on this technique with the present data. For the B and C components, the time delays corresponding to a minimum χ^2 computed independently for the two filters (not represented) are found to be non-consistent. This accounts for the relatively smaller size of the 99% compatibility domain of the combined χ^2 for components B and C (see Fig. 5). No acceptable values for the χ^2 were found for the D component at the 99% confidence level. This is a definite indication for an abnormal behavior of the D lightcurve, incompatible with the simple interpretation in terms of time delay.

The χ^2 for each component has also been normalized to the local minimum of that component (dashed contours in Fig. 5). With this normalization, differences in the curves which would be incompatible with the hypothesis of the time delay phenomenon are hidden. An upper limit of about 150 days on the absolute value for the time delays remains. All the curves are thus also compatible with zero time delay.

We conclude that the present lightcurves of the Cloverleaf quasar are not sufficiently well sampled and/or accurate in order to estimate precise values for the time delays, only upper limits can be set. However, given the noticeable intrinsic photometric variability of H1413+117, we feel confident that a better sampling of the lightcurves will lead to an accurate determination of the time delays for this system.

Analysis of our observations does not show any clear sign of micro-lensing activity for the A, B and C components. The photometric variations for the D component, however, deviate somewhat from the parallel behavior seen for the other three lensed QSO images. Particularly during the 1992 season, there is a steep decrease in the flux of this component by approximately 0.1 magnitude during three months, while the other components remain

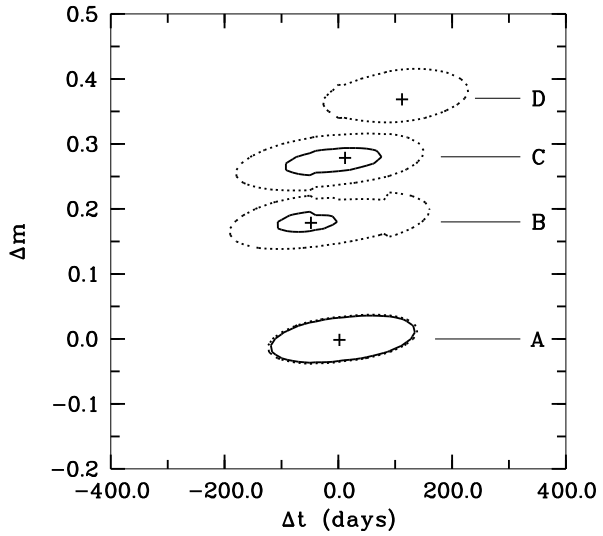


Fig. 5. 99% confidence level contours for the χ^2 of the differences between a smoothed lightcurve of component A, translated by Δt in epoch and Δm in magnitude, and the measurements of the four components, as derived by method 1. The smoothed lightcurve has been defined by a spline interpolation of the A measurements; hence the differences in epoch and magnitudes are relative to A. The χ^2 computed independently for the V and R data have been combined in the present diagram and normalized to the minimum χ^2 for A (solid contours) or to the minimum χ^2 for the given component (dashed contours). Crosses indicate the positions of the minima

relatively constant. The event is seen in both the I and R bands, whereas the V and B bands have insufficient observations to substantiate this. Variations during 1988 for the D component reported by Remy et al. (1996) in the V band were also interpreted as being possibly caused by micro-lensing. Angonin et al. concluded from spectra obtained on March 7, 1989 that the continuum of image D was slightly bluer than the other three images. From our observations in 1988 and 1994 we find no significant blue excess in the D component to within 0.03 mag. Unfortunately the observations from 1989 are not of sufficient quality to draw any definite conclusions.

In conclusion, pending a direct identification of the lensing galaxy, the multiply imaged QSO H1413+117 constitutes a very good candidate for a direct and independent determination of the Hubble parameter H_0. A photometric monitoring of this optical source, with optimal time coverage, should be organized in the near future. International collaboration will be essential for its success.

Acknowledgements. RØ would like to thank the STScI, the Norwegian Research Council and the Stockholm Observatory for financial support during a two month stay at STScI. MR and JS would like to thank B. Revenaz for his help at STScI and the PRODEX grant "Gravitational Lensing with HST" for financial support. AS thanks for financial support under grant no 781-73-058 from the Netherlands Foundation for Research in Astronomy (ASTRON) which receives its funds from the Netherlands Organisation for Scientific Research (NWO).

References

Angonin M.-C., Remy M., Surdej J., Vanderriest C., 1990, A&A 233, L5
Arnould P., Remy M., Gosset E., et al., 1993, Proc. 31st Liège Int. Astrophysical Coll. "Gravitational Lenses in the Universe", Surdej J. et al. (eds.), p. 169
Courbin F., Magain P., Remy M., et al., 1995, A&A 303, 1
Daulie G., Hainaut O., Hutsemékers D., et al., 1993, Proc. 31st Liège Int. Astrophysical Coll. "Gravitational Lenses in the Universe", Surdej J. et al. (eds.), p. 181
Drew J.E., Boksenberg A., 1984, MNRAS 211, 813
Hazard C., Morton D.C., Terlevich R., McMahon R., 1984, ApJ 282, 33
Hjorth J., Refsdal S., Stabell R., et al., 1996 (submitted to A&A)
Kayser R., Surdej J., Condon J.J., et al., 1990, ApJ 364, 15
Kayser R., 1993, Proc. 31st Liège Int. Astrophysical Coll. "Gravitational Lenses in the Universe", Surdej J. et al. (eds.), p. 5
Magain P., Surdej J., Swings J.-P., et al., 1988, Nat 334, 325
Østensen R., 1994, Cand. Scient. Thesis, University of Tromsø
Østensen R., Refsdal S., Stabell R., et al., 1996, A&A 309, 59
Refsdal S., Surdej J., 1992, Highlights Astron. 9, 3
Refsdal S., Surdej J., 1994, Rep. Prog. Phys. 56, 117
Remy M., Gosset E., Hutsemékers D., et al., 1996, IAU Symp. 173, "Astrophysical applications of Gravitational Lensing", Kochanek C.S. & Hewitt J.N. (eds.), p. 261
Remy M., 1996, Ph.D. Thesis, Liège University
Stetson P.B., 1987, PASP 99, 191
Surdej J., Magain P., Swings J.-P., et al., 1987, Nat 329, 695
Surdej J., Magain P., Swings J.-P., et al., 1988, A&A 198, 49
Teuber J., 1993, Digital Image Processing. Prentice-Hall
Turnshek D.A., Foltz C.B., Grillmair C.J., Weymann R.J., 1988, ApJ 325, 651

Article 8

Selective gravitational microlensing and line profile variations in the BAL quasar H1413+117

D. Hutsemékers : Astron. Astrophys. 280, 435 (1993)

Des différences spectrales ayant été observées entre les composantes du quasar quadruple de type BAL H1413+117 et plus particulièrement des différences dans les profils en absorption, nous tentons ici de les interpréter en considérant l'amplification sélective par une microlentille gravitationnelle d'un ou de quelques nuages absorbants.

Dans cette situation, une microlentille amplifie à la fois le nuage concerné, les nuages voisins et le continuum sous-jacent, de sorte que l'effet résultant est seulement différentiel et généralement faible.

En considérant des modèles simples mais réalistes de microlentille, nous trouvons que l'amplification sélective d'un nuage optiquement épais occultant une partie importante du continuum peut expliquer la différence spectrale observée. Mais un ajustement fin des paramètres est nécessaire et notamment une localisation très précise de l'amplification par rapport au nuage en question. La nécessité d'une configuration exceptionnelle met en doute ce type d'interprétation, tout en ne l'excluant pas.

Une autre interprétation est proposée, basée sur l'amplification du continuum par rapport à une région étendue à l'origine de profils de raies en émission complexes.

De nouvelles observations sont ensuite discutées. Elles confirment l'existence d'une amplification du continuum de la composante D, en accord avec le dernier modèle proposé. Cette amplification différentielle du continuum et des raies en émission permet la séparation des profils en absorption et en émission. Ces derniers montrent une structure double qui suggère la présence d'un disque équatorial dans le vent en expansion autour du noyau de H1413+117.

1993A&A...280..435H

Astron. Astrophys. 280, 435–442 (1993)

ASTRONOMY
AND
ASTROPHYSICS

Selective gravitational microlensing and line profile variations in the BAL quasar H1413+117

D. Hutsemékers

Institut d'Astrophysique, Université de Liège, 5, av. de Cointe, B-4000 Liège, Belgium

Received February 22, accepted May 4, 1993

Abstract. In order to interpret the spectral differences observed between the four images of the gravitationally lensed broad absorption line (BAL) quasar H 1413+117, we have investigated the effect on the line profiles of the selective magnification of individual BAL clouds by gravitational microlenses.

Since microlenses magnify both the selected cloud and the whole BAL region, this effect is only differential, and general constraints on its capability to produce spectral variations have been derived.

Considering simple but realistic models for the microlenses, we find that the selective magnification of a relatively large optically thick BAL cloud can be at the origin of the spectral differences reported between the components of H 1413+117. However, a very precise configuration is needed: the magnified cloud must be at the border of the BAL region which must itself partially lie in a region of strong de-magnification. The fine tuning of the parameters necessary to reproduce the observations either seriously questions this kind of interpretation or puts strong constraints on the lensing models.

Another interpretation of the observed line profile differences in terms of effects due to microlensing is also briefly discussed.

Key words: gravitational lensing – BAL quasars – H 1413+117

1. Introduction

The quasar H 1413+117 was first recognised as a gravitational mirage by Magain et al. (1988). Due to the presence of a gravitational lens on the line of sight (most probably an undetected galaxy), the image of this quasar is splitted into four components of comparable brightness, which roughly form a square. As shown by Magain et al. (1988) and Angonin et al. (1990, hereafter A 90), the spectra of the components are very similar, giving strong support to the lensing hypothesis.

Among the quasars presently known to the lensed, H 1413+117 is the only one to belong to the class of BAL quasars: in addition to emission lines, its spectrum displays large absorption troughs, blueshifted with respect to the emission, and usually interpreted in terms of mass outflows intrinsic to the quasar (see e.g. Weymann and Foltz 1983). H 1413+117 therefore provides us with a unique tool for studying simultaneously the gravitational lensing and BAL phenomena.

In the view, the effect of "microlenses" – i.e. individual stars generally belonging to the lensing galaxy (see e.g. Chang and Refsdal 1979, 1984; Schneider et al. 1992, hereafter S 92) – is particularly interesting: with an effective lensing size comparable to the size of the continuum emitting region, they can magnify some parts of the BAL region located in front of the continuum, therefore revealing its structure.

Evidence for microlensing effects in H 1413+117 has been suggested by Kayser et al. (1990) on the basis of photometric variations of the component D, which is expected to show the strongest influence due to microlensing. Further evidence for microlensing effects in component D has been reported by A 90. By obtaining spectra of the individual components with a bidimensional spectrograph, these authors found the normalized spectra of three of the components nearly identical while that of the component D is slightly different: the equivalent width of the emission lines is significantly smaller and the unsaturated part of the absorption profiles appears deeper (cf. Fig. 1). These characteristics are remarkably similar for the Si IV and C IV lines. It is important to notice that this behavior contrasts with the temporal variations detected in the spectra of some other BAL quasars, unrecognized to be lensed (see Barlow et al. 1992, and references therein). As done by A 90, these spectral differences may be interpreted in terms of microlensing: if a stellar-like lens magnifies the

© European Southern Observatory • Provided by the NASA Astrophysics Data System

1993A&A...280..435H

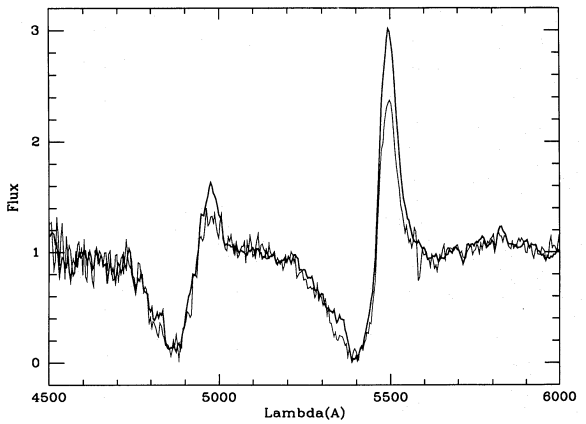


Fig. 1. The normalized spectrum of the component D of H 1413+117 (thin line) superimposed on the mean spectrum of the components A, B and C (thick line). The observations, obtained on March 7, 1989, are described in A 90 and were kindly provided by the authors. The illustrated line profiles are those of Si IV and C IV. It should be noticed that the location of the continuum is not well defined especially between Si IV and C IV

continuum region but not the broad emission line region (BELR) which is much larger, the equivalent width of the emission lines decreases. This is a classical effect suspected to be at work in several gravitational lenses. However, after renormalization to the continuum, we expect no changes in the absorption profiles since these lines are formed just in front of the continuum emitting region [1]. There are at least two possibilities to explain in terms of microlensing the differences observed in the normalized absorption profiles: (1) the varying part of the absorption profile is filled in with emission (i.e. constituting a P Cygni type profile) and the variation of the absorption is in fact due to the apparent variation of the emission; (2) the absorption region consists of small clouds of different optical depth and the microlens selectively magnifies one (or a few) of them. This latter interpretation was discussed and favored by Surdej (1990) and A 90. It is important to notice that the first interpretation requires a correlation between the variation in the normalized absorption profiles and the variation of the emission line equivalent widths, while in the second interpretation these variations may be uncorrelated, depending on the optical depth of the magnified cloud which may be optically thinner or thicker than the average. A distinction between these two interpretations, which clearly provide us with new insight on the BAL phenomenon itself, could be obtained by carrying out a regular spectral monitoring of H 1413+117.

The aim of the present paper is to investigate how quantitatively the selective magnification of BAL clouds can explain the spectral differences observed between the components of H 1413+117, considering simple but more realistic lens models than A 90. A subsequent paper (Hutsemékers et al. 1993, hereafter Paper II) will be devoted to the study of microlensing effects on P Cygni type profiles (see also Hutsemékers et al. 1992).

In Sect. 2, we derive general constraints on the selective microlensing effect in the framework of a simple BAL cloud model. We apply these constraints in Sect. 3 and 4 to the case of H 1413+117, considering the Schwarzschild and Chang-Refsdal lens models. Discussion and conclusions form the last section.

2. The selective microlensing effect

Let us assume that the absorption at a given wavelength in a line profile is due to sub-regions of different optical depth (hereafter called clouds) and located in front of a continuum emitting region of radius R. The projected size of the whole BAL formation region evidently coincides with that of the continuum. In order to evaluate the selective amplification of the light coming from individual clouds, we isolate a cloud of radius r. The emergent line profile, normalized to the continuum, can be written:

$$f = (1-\varepsilon)\, e^{-\tau_\lambda} + \varepsilon\, e^{-\tau_\lambda^*} + e(\lambda), \qquad (1)$$

where τ_λ^* is the optical depth of the considered cloud, τ_λ the average optical depth of the other clouds and $e(\lambda)$ the emission line profile. $\varepsilon = r^2/R^2$ represents the size of the cloud at the considered wavelength.

If a microlens is located on the line of sight towards one of the quasar images, it magnifies both the whole BAL region and the selected cloud, with amplitudes determined by the radii and positions of these regions relative to the lens. For adequate combinations of radii and positions, the individual cloud may be *selectively magnified* relative to the remaining of the BAL region. In this model, the modified spectrum, normalized to the amplified continuum, is expressed by

$$f_* = \left(1 - \varepsilon \frac{A_*}{A}\right) e^{-\tau_\lambda} + \varepsilon \frac{A_*}{A}\, e^{-\tau_\lambda^*} + \frac{e(\lambda)}{A}, \qquad (2)$$

A_* and A respectively denoting the (de-)amplification factors for the selected cloud and for the whole BAL and continuum regions. These amplification factors are independent of λ, the gravitational lenses being achromatic. We also assume that the microlens has no effect on the emission lines, their region of formation being much larger than the continuum region. This approach differs from that of A 90. Indeed, these authors have limited the influence of the lens

[1] It should be clear that, due to a microlensing effect, the attenuated continuum, i.e. the absorption lines, is (de-)amplified while the emission lines remain essentially unchanged. But, after renormalization to the adjacent continuum, also (de-)amplified, the normalized emission lines appear modified, while the normalized absorption profiles should be unchanged.

© European Southern Observatory • Provided by the NASA Astrophysics Data System

1993A&A...280..435H

to its Einstein radius, neglecting its effect on the remaining part of the BAL region.

By comparing the normalized emission line profiles in the spectra with and without amplification, f_*^e and f^e respectively, the factor A can be easily derived:

$$A = \frac{f^e - 1}{f_*^e - 1}. \tag{3}$$

Now, if we consider the absorption profile at a wavelength where $e(\lambda) = 0$, we have from Eqs. (1) and (2)

$$f_*^a = (1-\beta)\, f^a + \beta\, e^{-\tau_\lambda^*}, \tag{4}$$

with

$$\beta = \frac{\varepsilon}{1-\varepsilon}\left(\frac{A_*}{A} - 1\right). \tag{5}$$

If β may be evaluated, Eq. (4) allows the derivation of τ_λ^* for an individual cloud. It is easy to imagine that if the lens is moving, a spectroscopic monitoring of the variations will provide us with a complete scan of the BAL region.

Because the selective magnification is in fact due to a differential effect between the individual cloud and the whole region, the amplitude of the possible profile variations may be severely constrained. Noting that we must always have $0 \leqq e^{-\tau_\lambda^*} \leqq 1$ and $0 \leqq e^{-\tau_\lambda} \leqq 1$, we obtain from Eqs. (1)–(5), the following upper limit on the relative profile variation $\Delta f = (f^a - f_*^a)/f^a$:

$$\Delta f \leqq \Delta f^m\,(\varepsilon, A, A_*) \tag{6}$$

where

$$\Delta f^m = \beta \qquad \text{if} \quad \varepsilon \leqq \varepsilon_L, \tag{7}$$

$$\Delta f^m = \beta\, \frac{1-\varepsilon}{\varepsilon}\, \frac{1-f^a}{f^a} \qquad \text{if} \quad \varepsilon \geqq \varepsilon_L, \tag{8}$$

and

$$\varepsilon_L = 1 - f^a. \tag{9}$$

These relations give an upper limit Δf^m on the amplitude of the absorption profile variations which may be induced by a selective microlensing effect. Lower limits may be derived similarly but are not considered here because the profile variations in H 1413+117 are characterized by $f_*^a \leqq f^a$. Let us notice that no observable variation may be expected for completely saturated profiles ($f_*^a = f^a = 0$).

In many situations of interest including those discussed in Sect. 3 and 4, Δf^m increases with ε for $\varepsilon \leqq \varepsilon_L$, while for $\varepsilon \geqq \varepsilon_L$, Δf^m decreases with ε. Consequently, for all ε we have

$$\Delta f^m \leqq \Delta f_L^m = \Delta f^m(\varepsilon_L, A, A_*). \tag{10}$$

Δf_L^m constitutes the upper limit on the amplitude of the possible variations independently of any hypothesis on the size and opacity of the clouds. These relations also indicate that there is an optimal size ε_L for an individual cloud to produce the largest possible profile variation. This optimal size does not depend on the amplification factors.

This behavior may be easily understood: if the cloud is very small, it may be strongly magnified compared to its surroundings but, smaller it is, less it contributes to the profile. Since the ratio A_*/A generally decreases with ε slower than $1/\varepsilon$, the largest differential magnification effect occur for the largest clouds, provided that $\varepsilon \leqq \varepsilon_L$ (cf. Eqs. (5)–(7)]. The minimum size for a cloud to produce an observable effect is therefore also fixed by Eq. (7). For example, if $\varepsilon \ll 1$, $A_*/A \sim \varepsilon^{-n/4}$, n being equal to 1, 2 or 4 (cf. the models discussed in the following sections), and we have $\Delta f^m \sim \varepsilon^{1-n/4}$, which, for $n = 2$ (Schwarzschild lens), simply reduces to $\Delta f^m \sim r/R$. This means that the largest possible relative profile variation due to the selective magnification of a very small absorbing cloud is of the order of magnitude of the cloud radius expressed in core radii.

The amplitude of the selective magnification effect on a BAL cloud depends not only on its size and on the ratio A_*/A, but also on the difference between the optical depths τ_λ^* and τ_λ. This difference must be as large as possible to produce the most noticeable effect, and, looking at Eq. (1), we can see that there is a limit when $\varepsilon = \varepsilon_L = 1 - f^a$, i.e. when $e^{-\tau_\lambda^*} = 0$ and $e^{-\tau_\lambda} = 1$. In this case, the BAL region consists of a single optically thick cloud of size ε_L, and the differential magnification effect is maximized.

In deriving Eq. (2), we have implicitely assumed that, except in the selected cloud, the optical depth of the whole BAL region is homogeneous. If the size of the clouds is sufficiently small, this approximation is reasonable, while, in other situations, it may be unrealistic. However, this approximation does not affect our analysis. Indeed, if the clouds in the vicinity of the considered one are optically thinner than the mean value (τ_λ), they will be more magnified than the average and the limits given in Eqs. (6)–(8) still constitute upper limits. If, on the contrary, the clouds in the vicinity of the selected one are optically thicker than the average, the effective size of the cloud, defined by its opacity, should be increased and the limits evaluated with a greater value of ε. It should be clear that what we call "cloud" in this paper is only a region of different optical depth seen in projection. It may have little to do with the clouds described in the models of Weymann et al. (1985), and Begelman et al. (1990), which are very small, most probably too small to be at the origin of detectable variations due to a selective magnification effect.

In the remaining sections, we will evaluate the theoretical limit Δf^m for some simple lens models in order to see if the variations detected in the absorption line profiles of

© European Southern Observatory • Provided by the NASA Astrophysics Data System

1993A&A...280..435H

H 1413+117 may be explained by this selective magnification mechanism.

In the case of H 1413+117, we assume that the normalized, unmodified spectrum of the component D is identical to the average spectrum of the three other components. The spectra were divided according to Eq. (3), and A, the amplification factor of the whole BAL and continuum regions, estimated from the part of the C IV emission line profile where the signal-to-noise ratio is the highest i.e. where the intensity is greater than about 75% of the maximum intensity. On this part of the profile, the average values of A is equal to 1.45 ± 0.06. The uncertainty is due to the dispersion of the measurements on this part of the profile and from the uncertainty on the acceptable positions for the underlying continuum. We should notice that the values of A are not significantly different when estimated from the red side or from the blue side of this small part of the emission profile. The value derived from the center of the emission line may be slightly smaller, but it is not clear whether this is significant or not. In principle, the value of A may also be estimated from the Si IV line but it is much more dependent on the adopted underlying continuum while the signal-to-noise ratio is not as good as for C IV. In the limit of the uncertainties, the behavior of the Si IV line is nevertheless very similar to that of C IV (cf. Fig. 1).

The observed profile variation $\Delta f^{\rm obs}$ may be evaluated from the unsaturated part of C IV absorption line profile where the variations are detected and most noticeable ($\lambda \simeq 5350$ Å). In the wavelength range $\lambda\lambda$ 5330–5370 Å, the ratio $\Delta f^{\rm obs} = (f^a - f^a_*)/f^a$ is nearly constant and equal to 0.42 ± 0.06. As seen in Fig. 1, $f^a \sim 0.4$, so that $\varepsilon_L \sim 0.6$. If $\varepsilon = \varepsilon_L$, the BAL material absorbing in the wavelength range $\lambda\lambda$ 5350–5370 Å consists of a single optically thick cloud of size $\varepsilon_L = 0.6$. The absence of similar variations in the part of the profile immediately bluer suggests that, seen in projection, the BAL material absorbing at this wavelength is more homogeneous, as in the completely saturated, redder, part of the absorption profile. Such a cloud size should therefore be regarded with caution and, in the remaining, we will also consider the size $\varepsilon = 0.1$, less critical and still sufficiently large to produce a significant effect.

3. The Schwarzschild lens

Let us first assume that the continuum emitting region, the selected cloud and a Schwarzschild lens (point singularity) are centered on the line of sight. In this case, A and A_* have the well-known expressions (Liebes 1964; Refsdal 1964; S92):

$$A = \sqrt{1 + 4\frac{\eta_0^2}{R^2}} \quad \text{and} \quad A_* = \sqrt{1 + 4\frac{\eta_0^2}{r^2}}, \tag{11}$$

Table 1. Typical values of Δf_L^m computed for different combinations of ε_L and A

ε_L \ A	1.2	1.5	2.0	10.0	100.0
0.10	0.10	0.16	0.20	0.24	0.24
0.20	0.12	0.20	0.25	0.31	0.31
0.50	0.14	0.25	0.32	0.41	0.41
0.80	0.15	0.27	0.36	0.47	0.47
0.90	0.15	0.27	0.37	0.48	0.49

η_0 being the Einstein radius of the microlens projected in the source plane, i.e. $\eta_0^2 = 4GMc^{-2} D_s D_{ds} D_d^{-1}$, where M is the mass of the lens, and D_s, D_d, D_{ds} are the angular diameter distances observer–source, observer–deflector and deflector–source, respectively (cf. S92). Combining these expressions, we immediately derive

$$A_* = \sqrt{1 + \frac{A^2 - 1}{\varepsilon}}. \tag{12}$$

This relation allows us to compute β and Δf_L^m as a function of ε_L and A. Typical values are given in Table 1. Since Δf_L^m represents the largest possible relative variation, we immediately see from that Table that the selective magnification effect is essentially a small effect. It is most noticeable for the largest values of A (i.e. of the global amplification of the continuum), and impossible if the continuum is not amplified itself ($A = 1$). It should be emphasized that Δf_L^m is not very dependent on small errors on A, and that, when A is large enough, Δf_L^m no longer depends on it.

For the particular case of H 1413+117, $A = 1.45 \pm 0.06$ and $\varepsilon_L = 0.6$ imply $\Delta f_L^m = 0.24 \pm 0.02$. For $\varepsilon = 0.1$, we have $\Delta f^m = 0.15 \pm 0.01$. These values are definitely smaller than $\Delta f^{\rm obs} = 0.42 \pm 0.06$. Even if we increase the value of A by typically $\sim 10\%$, this conclusion remains unchanged due to the small dependence on A of the amplitude of the selective magnification effect[2]. This means that the selective magnification effect due to a Schwarzschild-type lens cannot explain the profile differences observed in the component D of H 1413+117.

However, if we keep the lens centered on the selected cloud but not on the whole BAL region, we may hope to increase the effect. If D is the distance between the projected center of the lens and the center of the BAL/continuum region, the amplification approximately decreases as $1 - (d/2)^2$ provided that $d = D/R \leqq 1$ (Schneider and Wagoner 1987). Eq. (12) may therefore be generalized to

[2] For example, if the emission line profiles are partially affected by the microlens, the value of A estimated with Eq. (3) could be underestimated by typically 10% (see e.g. Schneider & Wambsganss 1990).

© European Southern Observatory • Provided by the NASA Astrophysics Data System

1993A&A...280..435H

$$A_* = \sqrt{1 + \frac{A_c^2 - 1}{\varepsilon}} \tag{13}$$

where

$$A_c = A\left(1 - \frac{d^2}{4}\right)^{-1}. \tag{14}$$

In order to check the validity of this approximation, we have computed numerically the factor A_c for different values of d and η_0/R, and we found Eq. (14) to essentially constitute a good approximation. Adopting the largest possible value for d, $d = 1 - \sqrt{\varepsilon}$, we obtain $\Delta f_L^m = 0.27 \pm 0.02$ and $\Delta f^m(\varepsilon = 0.1) = 0.21 \pm 0.01$. Decentring the magnified cloud has clearly a negligible effect on the amplitude of the variations attributable to a selective magnification mechanism.

4. The Chang-Refsdal lens

If a point mass is located in a galaxy – a situation expected to occur frequently –, its gravitational potential may be perturbed by the galaxy and the resulting lens will considerably differ from the Schwarzschild model. This type of lens was first studied by Chang and Refsdal (1979, 1984) and we will refer to it as the Chang-Refsdal (CR) lens. A generic property of the CR lens amplification pattern is the presence of caustics or critical curves. When crossed by a light source, these curves are at the origin of strong magnification effects. In this situation, the amplification factors of the whole continuum region and the selected cloud may be approximated by the following expressions (cf. S92):

$$A = A_0 + \sqrt{\frac{g}{R}} \quad \text{and} \quad A_* = A_0 + \sqrt{\frac{g}{r}}, \tag{15}$$

which may be combined to give

$$A_* = A_0 + \frac{A - A_0}{\varepsilon^{1/4}}, \tag{16}$$

assuming both the cloud and the continuum simultaneously located on the critical curve. A_0 accounts for the underlying magnification related to other, distant subimages, and g is a constant, roughly $\sim \eta_0$ (Chang 1984), which can be explicitely computed for a specific lens model.

It is now straightforward to estimate typical values of Δf^m in the case of H 1413+117. For $A_0 = 1$, $\Delta f_L^m = 0.06 \pm 0.01$ and $\Delta f^m(\varepsilon = 0.1) = 0.03 \pm 0.001$, while for $A_0 = 0$, $\Delta f_L^m = 0.20$ and $\Delta f^m(\varepsilon = 0.1) = 0.09$. We can see that these values strongly depends on A_0, but remain definetely too small to explain the spectra differences observed between the images of H 1413+117.

As in the Schwarzschild case, we may hope to increase the relative magnifications of the cloud and the whole BAL region by decentring the BAL region with respect to the caustic. For a CR lens, the dependence on the distance d is rather complex and asymmetric (Chang and Refsdal 1984; see also Fig. 6.13 in S92). Fortunately, since we are interested in the maximum effect, we can only consider the portion of the curve $-1 \leqq d \leqq 0$ where the gradient of the amplification is the largest. In this part of the curve, the variation of the amplification factor with d may be simply approximated by $1 - |d|$, such that Eq. (16) may be generalized to

$$A_* = A_0 + \frac{A - A_0}{(1 - |d|)\,\varepsilon^{1/4}}, \tag{17}$$

keeping the selected cloud on the caustic.

Adopting the largest possible distance, $|d| = 1 - \sqrt{\varepsilon}$, we find for $A_0 = 1$, $\Delta f_L^m = 0.22 \pm 0.02$ and $\Delta f^m(\varepsilon = 0.1) = 0.16 \pm 0.01$, while for $A_0 = 0$, $\Delta f_L^m = 0.70$ and $\Delta f^m(\varepsilon = 0.1) = 0.51$. These latter values are obviously greater than $\Delta f^{\text{obs}} = 0.42 \pm 0.06$. In this situation, the size ε of the smallest absorbing cloud which can be at the origin of the observed line variation is $\varepsilon \sim 0.04$ (i.e. $r/R \sim 0.2$).

We can therefore conclude that the spectral differences between the images of H 1413 ± 117 may be explained by a selective magnification effect due to microlensing. However this effect requires a very precise lensing configuration: the caustic should be centered on the selected cloud while the remaining of the BAL region must be located in a region of strong de-magnification. Changing just a little bit the values of A_0 and d significantly reduces Δf^m. For example, adopting $A_0 = 0.3$, or adopting $A_0 = 0$ and $|d|$ smaller by only 10% lower $\Delta f^m(\varepsilon = 0.1)$ to the value of Δf^{obs}. Recalling also that the computed limits necessarily imply $e^{-\tau_1^*} = 0$, we see that the interpretation in terms of selective magnification requires a fine tuning of the parameters.

Since the previous analytical approach is based on approximations which may affect these conclusions, it would be valuable to check the previous results with the help of numerical simulations. Such simulations will also allow us to investigate the selective magnification effect in the vicinity of singularities not considered analytically, like the behavior near cusps.

For this purpose, we may rewrite Eq. (7)

$$\frac{A_*(r)}{A(R, d)} \geqq 1 + \frac{1 - \varepsilon}{\varepsilon}\,\Delta f^{\text{obs}}, \tag{18}$$

which, for any $\varepsilon \leqq \varepsilon_L$, gives a lower limit on the ratio A_*/A needed to explain the observations. Adopting a value for ε, light curves for extended sources of radii R and $r = R\sqrt{\varepsilon}$ may be computed numerically for selected paths of the source through the amplification patterns produced by a CR lens model. Such light curves have been extensively

© European Southern Observatory • Provided by the NASA Astrophysics Data System

1993A&A...280..435H

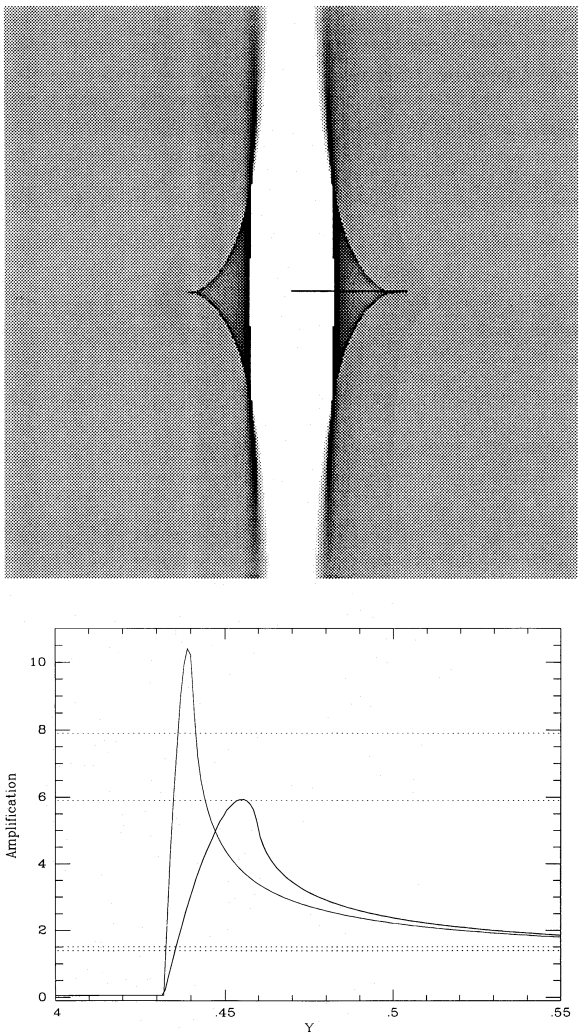


Fig. 2a and b. An example of a lensing configuration which can be at the origin of a selective magnification effect. **a** represents the amplification pattern in the source plane. A strong de-magnification region is present at the center (the darker the gray, the higher the amplification). The amplification factor has been normalized by the amplification due to the smoothed-out deflector. The shear γ and the normalized surface mass density κ_c are respectively equal to 1.1 and 0.0. The coordinates have been normalized following the relation $(Y_1, Y_2) = (\eta_1, \eta_2)/\eta_0 \sqrt{|1-\kappa_c+\gamma|}$ (the precise definition of all these quantities may be found in S92). In this figure, $-3 \leqq Y_1, Y_2 \leqq 3$. The path of the source is also drawn. **b** illustrates the values of $A_*(r)$ (thin line) and $A(R,d)$ (thick line) as a function of $Y = \sqrt{Y_1^2 + Y_2^2}$, for $\varepsilon = 0.1$ and $R/\eta_0 = 0.02$. The curve $A(R,d)$ was obtained by shifting the curve $A(R, d=0)$ by $\Delta Y = |d| R/\eta_0 \sqrt{|1-\kappa_c+\gamma|}$, where $|d| = 1-\sqrt{\varepsilon}$. The horizontal dashed lines indicate the limiting values for $A(R,d)$ and $A_*(r)$: 1.45 ± 0.06 and 6.9 ± 1.0, respectively. Near $Y \simeq 0.435$, both conditions $A(R,d) = 1.45 \pm 0.06$ and $A_*(r) \geqq 6.9 \pm 1.0$ simultaneously hold

discussed by many authors (see e.g. Kayser et al. 1986; S92). In this paper, the numerical integrations were performed in a standard way described with more details in Paper II. Let us only notice that we recover the curves presented by Grieger et al. (1989) for a single star CR lens.

In practice, we proceed as follows: by computing, for a given lens model, light curves in the vicinity of a singularity, we first estimate numerically the range of R values such that $A(R,d) = 1.45 \pm 0.06$, with $|d| \leqq 1 - \sqrt{\varepsilon}$ being the distance from the singularity (point, fold, cusp, etc.). For example, when crossing a caustics, R should roughly range from $R_{\max}$ to $\varepsilon R_{\max}$, $R_{\max}$ being of the order of g/A^2 (cf. Eqs. (15), (17)). To the range of R values corresponds a series of values $r = R\sqrt{\varepsilon}$, for which it is easy to see if $A_*(r)$ satisfies Eq. (18). In the case of H 1413+117, and for $\varepsilon = 0.1$, $A_*(r)$ should be greater than 6.9 ± 1.0. By choosing R values and paths through to amplification patterns which largely encompass the allowed ranges of R and d, it is relatively easy, without too many simulations, to check if a given lensing configuration *cannot* provide us with the needed selective magnification effect. However, if a potentially interesting configuration is identified, the parameters must be further adjusted to verify that $A_*(r)$ can satisfy Eq. (18) simultaneously with $A(R,d) = 1.45 \pm 0.06$.

Simulations were performed for various CR lens models. They essentially confirms the previous conclusions: in order to have a significant effect, the selected BAL cloud must be at the border of the BAL region, centered on a high magnification region, while the remaining of the BAL/continuum region must be strongly de-magnified. For example, the typical diamond-shaped caustics, not associated to strong de-magnification regions, cannot provide us with the needed A_*/A ratio. Nor do the cusps, and this is not too surprising: despite being greater than that due to caustics, their magnification effect remains smaller than the magnification due to a Schwarzschild lens (Schneider & Weiss 1986), while they are more extended and not contiguous to a strong de-magnification region. An example of a lensing configuration able to selectively magnify a BAL cloud is illustrated in Fig. 2. Other possible configurations are those which produce overfucusing. In all cases, fine tuning of d and A_0 is required to have a sufficient effect.

5. Discussion and conclusions

In order to interpret the absorption line differences observed between the images of the gravitational mirage H 1413+117, A90 have suggested that absorbing clouds smaller than the continuum-forming region could be selectivelly magnified by a gravitational microlens. In this paper, we investigate further this effect, on the basis of more realistic microlens models.

© European Southern Observatory • Provided by the NASA Astrophysics Data System

1993A&A...280..435H

From our study, we conclude that the selective magnification of an absorbing cloud by microlensing effects is possible but requires a very precise lensing configuration: the cloud must be located at the border of the projected continuum region, in a region of high magnification, while the remaining of the BAL region must suffer a strong de-magnification. The very fine tuning of the parameters which is needed to reproduce the observations may seriously question the plausibility of such a mechanism. However, if the profile differences may be actually attributed to this mechanism, this puts strong constraints on the lensing models for H 1413+117. Interestingly, the presence of a de-magnification region is compatible with the models proposed by Kayser et al. (1990) for H 1413+117, and more particularly with the first model which predicts the strongest dependence on microlensing for the component D ($\gamma \geqq 1$, cf. Fig. 2).

In the present paper, we have only considered single star models. However, the main results should not be very different for multiple star models, the amplification patterns still consisting of critical curves and points. Moreover, at large optical depths, multiple star models will certainly not favor the selective magnification since any differential effect will be smeared out. Even at moderate optical depths, the strong de-magnification regions of CR lens models tend to be "filled in" due to the influence of the distant stars (cf. Kayser et al. 1986).

The timescale of the variations may be roughly estimated. Adopting for the redshifts of the quasar and the deflector, $z_q = 2.55$ and $z_d = 1.55$, $H_0 = 75\,\mathrm{km\,s^{-1}\,Mpc^{-1}}$, $q_0 = 0$, the length scale η_0 may be evaluated: $\eta_0 \simeq 0.006$ pc, for a one solar mass star. Because the ratio of the distances of the quasar and the deflector is not very different from the unity, the transversal velocity V of the source relative to the microcaustics will not be strongly enhanced (cf. Kayser and Refsdal 1989). Therefore, adopting a few hundred of $\mathrm{km\,s^{-1}}$ for V, the characteristic microlensing timescale $\Delta t_0 = \eta_0/V$ is of the order of 10 years.

To produce the low amplification $A = 1.45 \pm 0.06$ with the continuum region centered on the caustic ($A_0 = 0$), R is roughly equal to η_0, which is a reasonable value for the size of the continuum emitting region. This only constitutes an order of magnitude estimate of R, the exact value depending on the strength g of the caustic. If the caustic is decentered by $|d| = 1 - \sqrt{\varepsilon}$, the radius R is smaller by a factor ε and consequently, the timescale for the variations of the continuum, Δt_c, is $\sim \varepsilon \Delta t_0$, with a maximum amplification $A_{\max} \sim A/\sqrt{\varepsilon}$. The timescale for the absorption profile variations depends on the size of the cloud and may be estimated by $\Delta t_p \sim \sqrt{\varepsilon}\,\Delta t_c \sim \varepsilon \sqrt{\varepsilon}\,\Delta t_0$. Since only a small shift of the caustic may destroy the configuration needed for the selective magnification mechanism, Δt_p certainly constitutes an upper limit on the duration of the profile variation.

For a typical value $\varepsilon \simeq 0{,}1$, we have therefore $\Delta t_c \sim 1$ yr with $\Delta m_{\max} \sim 1\overset{m}{.}6$ and $\Delta t_p \sim 0.3$ yr. In the particular case illustrated in Fig. 2, we have $\Delta t_c \simeq 0.2$ yr, $\Delta m_{\max} \simeq 2\overset{m}{.}0$, and $\Delta t_p \simeq 0.06$ yr. The profile differences observed in component D of H 1413+117 should therefore be a relatively short-lived phenomenon if attributable to this mechanism. Let us also notice that on a timescale of 1 year, photometric variations larger than 1^m have not been reported for the component D of H 1413+117 (cf. A90). If the absence of such variations is confirmed, this may again seriously questions the plausibility of the selective magnification mechanism to explain the observed spectral differences.

If this kind of interpretation seems to have some difficulties to fit the observations, this does not mean that the absorption profile differences are not due to a microlensing effect. As discussed in Sect. 1, such differences may be attributed, at least qualitatively, to the apparent variation of an emission line superimposed on the absorption profile (see also Hutsemékers et al. 1992). Assuming that the underlying C IV absorption profile is completely saturated near $\lambda \simeq 5350$ Å, as it is near $\lambda \simeq 5400$ Å (see Fig. 1), we expect, near $\lambda \sim 5350$ Å, $f_* \simeq f/A \simeq 0.28 \pm 0.02$, a value which, in the limit of the uncertainties and without any other hypothesis, is in reasonably good agreement with the measured value. This kind of interpretation, which looks promising, will be discussed in more details in a subsequent paper. Let us finally recall that the profile differences may still be attributed to an intrinsic variation observed with a time delay between the different images of H 1413+117 (cf. A90).

Since a distinction between these interpretations, and therefore new understanding on the BAL phenomenon itself, may be obtained from regular observations, we cannot stress too much the importance of carrying out a spectroscopic monitoring of H 1413+117, as well as of other BAL quasars known to suffer spectral variations or located behind a galaxy (like 1E 0104±315, cf. Schneider & Weiss 1987).

Acknowledgements. It is a pleasure to thank Jean Surdej and Eddy Van Drom for a careful reading of the manuscript. We also thank Jean Surdej for providing us with the spectra published in A90. This research is supported in part by contract ARC 90/94-140 "Action de recherche concertée de la Communauté Française" (Belgium).

References

Angonin M. C., Remy M., Surdej J., Vanderriest C., 1990, A&A 233, L5 (A90)
Barlow T. A., Junkkarinen V. T., Burbidge E. M., Weymann R. J., Morris S. L., Korista K. T., 1992, ApJ 397, 81
Begelman M. C., de Kool M., Sikora M., 1991, ApJ 382, 416
Chang K., 1984, A&A 130, 157

© European Southern Observatory • Provided by the NASA Astrophysics Data System

1993A&A...280..435H

Chang K., Refsdal S., 1979, Nature 282, 561
Chang K., Refsdal S., 1984, A&A 132, 168
Grieger B., Kayser R., Refsdal S., Stabell R., 1989, Abhandlungen auf der Hamburger Sternwarte X, 4, Hamburg
Hutsemékers D., Surdej J., Van Drom E., 1993, in preparation (Paper II)
Hutsemékers D., Surdej, Van Drom E., 1992, Gravitational lenses. Lecture Notes in Physics Vol. 406, Kayser R., Schramm T., Nieser L. (eds.), Springer, Berlin Heidelberg New York, p. 373
Kayser R., Refsdal S., 1989, Nature 338, 745
Kayser R., Refsdal S., Stabell R., 1986, A&A 166, 36
Kayser R., Surdej J., Condon J. J., Kellermann K. I., Magain P., Remy M., Smette A., 1990, ApJ 364, 15
Liebes S., 1964, Phys. Review 133, B835
Magain P., Surdej J., Swings J. P., Borgeest U., Kayser R., Kühr H., Refsdal S., Remy M., 1988, Nature 334, 327
Refsdal S., 1964, MNRAS 128, 294
Schneider P., Ehlers J., Falco E. E., 1992, Gravitational lenses, Springer, Berlin Heidelberg New York (S92)
Schneider P., Wagoner R. V., 1987, ApJ 314, 154
Schneider P., Wambsganss J., 1990, A&A 237, 42
Schneider P., Weiss R. V., 1986, A&A 164, 237
Schneider P., Weiss R. V., 1987, A&A 171, 49
Surdej J., 1990, Gravitational lensing. Lecture Notes in Physics Vol. 360, Mellier Y., Fort B., Soucail G. (eds.), Springer, Berlin Heidelberg New York, p. 57
Weymann R., Foltz C., 1983, Quasars and gravitational lenses, Swings J. P. (ed.), Liège Univ. Press, Liège, p. 538
Weymann R., Turnshek D. A., Christiansen W. A., 1985, Astrophysics of Active Galaxies and Quasi-Stellar Objects, Miller J. (ed.), Oxford Univ. Press, Oxford, p. 333

© European Southern Observatory • Provided by the NASA Astrophysics Data System

Update

Disentangling emission from absorption with microlensing : evidence for a disk in the wind of H1413+117 ?

Additional spectra of the four components of the BAL quasar H1413+117 have been obtained with the Hubble Space Telescope in 1993–1994 (see Fig. 1).
For all four components the line profiles have changed in a similar way between 1989 and 1993 : the absorption profiles extend to higher velocities in 1989, while the equivalent width of the emission lines is lower in 1993. These changes are related to a variation of the continuum brightness reported in Paper 7.
At both epochs, components A, B, and C have nearly identical spectra, while the difference with component D is qualitatively unchanged. This fact rules out the possibility that the difference seen in the spectrum of D is due to a delayed intrinsic variation, the time delay being smaller than 150 days (Paper 7) ; it supports the microlensing interpretation, the time-scale of which is expected to be around 10 years. Moreover, the brightness difference between A and D is found to decrease by ~ 0.2 magnitude in V (Paper 7). This value is in excellent agreement with the amplification factors derived from the line profiles (cf. Fig. 1), suggesting that the amplification of the D continuum due to microlensing is higher by ~ 0.2 magnitude in 1993. The stability of the effect argues against the selective magnification of an absorbing cloud as the explanation for the absorption line difference observed in component D (cf. Paper 8).
Assuming that only the continuum is amplified by the microlensing effect, we may disentangle the intrinsic absorption and emission line profiles. The results are given in Fig. 1. The intrinsic absorption profiles appear saturated starting at -2000 km s^{-1}. The emission profiles appear double-peaked, much broader than previously thought, and roughly centered on the onset velocity of the absorption (such a blueshift is commonly seen in quasars ; McIntosh et al. 1999). The profiles extracted from the 1989 and 1993 data are in good agreement. In the framework of this interpretation, the spectral difference observed between the absorption profiles in components D and A,B,C is in fact due to the presence in the absorption profile of an underlying emission which is unaffected by microlensing when the continuum is amplified. The fact that at each epoch a single amplification factor is sufficient to account for the variation of the emission line equivalent widths as well as the variation of the emission superimposed over the saturated absorption supports this interpretation.
The separation of intrinsic absorption and emission provides some clues to the geometry of the BAL region. First the coincidence in velocity between the emission and the absorption profiles indicates that at least part of the emission is formed is the wind. While a double-peaked emission profile cannot be easily produced in a spherically symmetric wind, it can be obtained assuming a dense low-velocity disk-like outflow seen edge-on and blocking part of the emission from the wind, as demonstrated by the calculations of Bjorkman et al. (1994)[1]. Such a model can reproduce the observed emission profiles as

[1]Note that in order to allow saturation in the absorption by the wind, the disk in Bjorkman's model must

simply illustrated in Fig. 2. Note that a two-component wind model is also supported by spectropolarimetric observations (cf. Part 3).
These results suggest that part of the BAL outflow in H1413+117 is disk-like, with a nearly edge-on orientation. This geometry is in agreement with several BAL outflow models (e.g. Murray et al. 1995), and may constitute a good starting point for a detailed modelling, once confirmed.

References

- Bjorkman, J.E., et al., 1994, ApJ 435, 416
- McIntosh, D.H., et al., 1999, ApJ 517, L73
- Murray, N., et al., 1995, ApJ 451, 498

be detached from the core

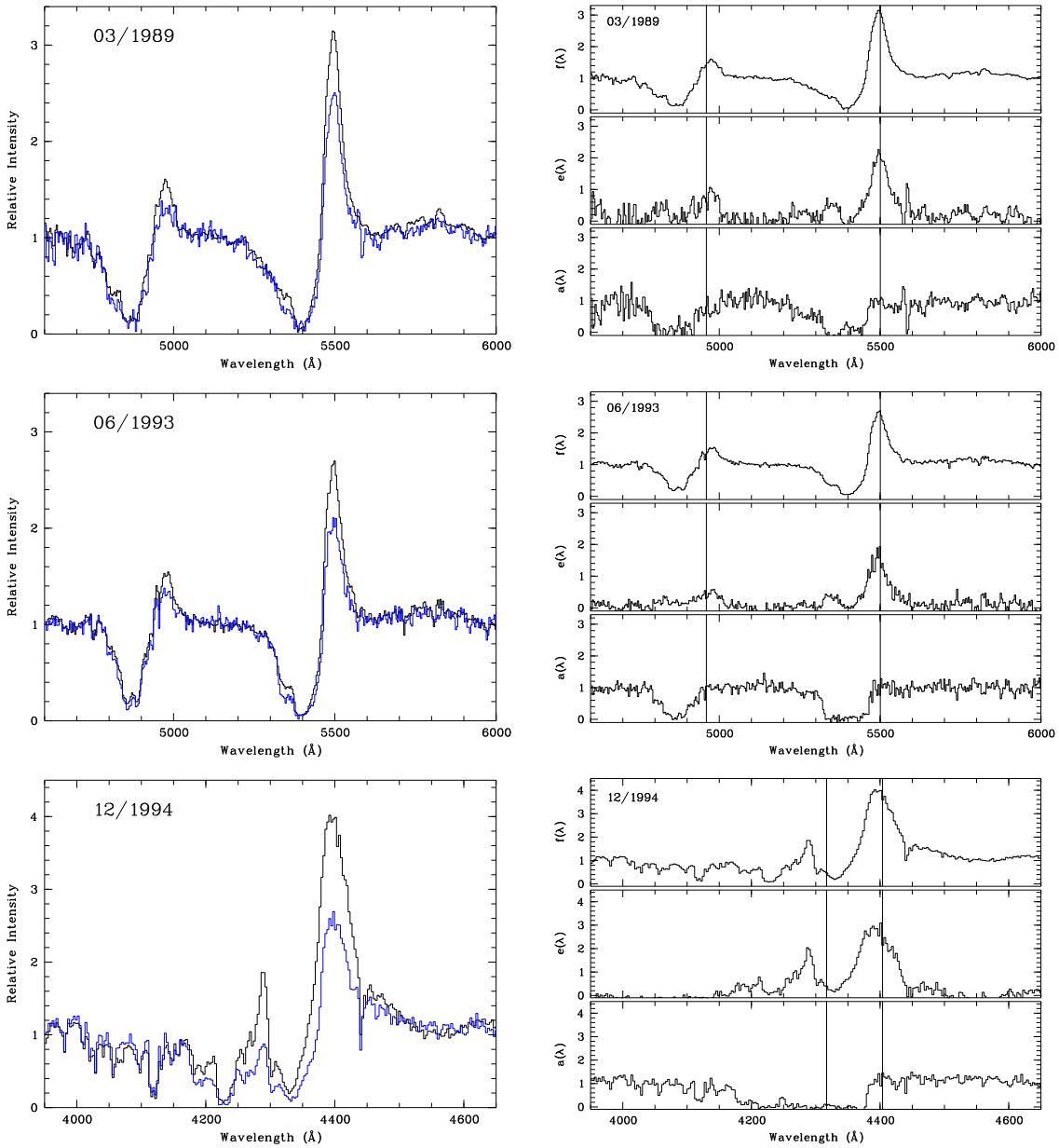


Fig. 1 : The left panels illustrate the normalized spectrum of component D of H1413+117 (thin line) superimposed on the mean normalized spectrum of components A, B, C (thick line) at 3 different epochs. The two upper panels represent the CIV and SiIV line profiles, while the bottom one shows Lyα + NV. The right panels show the normalized absorption $a(\lambda)$ and emission $e(\lambda)$ profiles extracted assuming that the spectral differences seen in component D are due to microlensing of the continuum source, the emission lines being essentially unaffected. If $f(\lambda) = a(\lambda) + e(\lambda)$ denotes the mean normalized spectrum of A,B,C, $f_D(\lambda)$ the normalized spectrum of D, and A the amplification of the continuum in D, then $a(\lambda) = e^{-\tau_\lambda} = \frac{f(\lambda) - A\, f_D(\lambda)}{1-A}$ and $e(\lambda) = A\frac{f(\lambda) - f_D(\lambda)}{A-1}$. The factor A is determined such that the emission is cancelled at best redward of the absorption profiles while keeping $a(\lambda) \geq 0$. We find $A \simeq 1.4$ for the 03/1989 data, $A \simeq 1.6$ for 06/1993, and $A \simeq 2.0$ for 12/1994. It should be emphasized that $e(\lambda)$ represents the part of the profile not affected by the microlensing effect, which is not necessarily the "pure" emission profile. The vertical lines indicate the CIV λ1549, SiIV λ1397, NV λ1240, and Lyα transitions redshifted to the systemic redshift of the quasar measured from the optical [OIII] lines, $z = 2.551$.

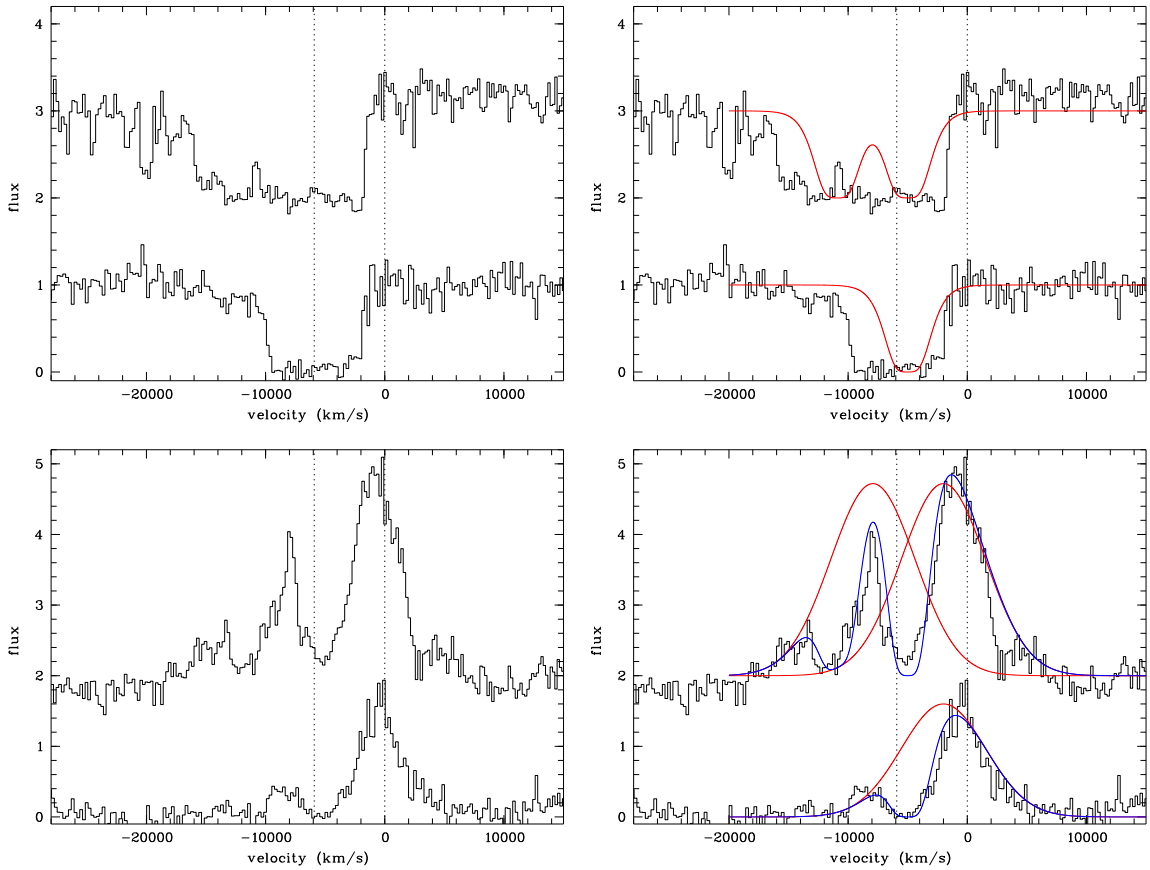


Fig. 2 : The absorption and emission line profiles extracted from the 1993–1994 data (cf. Fig. 1) are plotted here on a velocity scale in the quasar rest-frame. In each panel, the lower spectrum illustrates the results for CIV while the upper spectrum represents Lyα + NV, shifted upwards. In the top-right panel, a model for the absorption in the disk is shown, superimposed on the observed total absorption (disk + wind). It is chosen identical for all transitions. Its effect on simple emission line profiles is illustrated in the bottom-right panel, showing a fairly good agreement with the observed profiles. The simple unabsorbed emission profiles are gaussians centered on $v_{\rm min} = -2000$ km s^{-1} and assumed identical for all transitions apart from a scaling factor. It should be emphasized that they only roughly represent the true emission and more particularly the Lyα emission line which could be partially scattered by NV ions in the wind.

Article 9

An optical time-delay for the lensed BAL quasar HE 2149-2745

I. Burud, F. Courbin, P. Magain, C. Lidman, D. Hutsemékers, J.-P. Kneib, J. Hjorth, J. Brewer, E. Pompei, L. Germany, J. Pritchard, A. O. Jaunsen, G. Letawe, G. Meylan : Astron. Astrophys. 383, 71 (2002)

Cet article présente les résultats d'un suivi photométrique du quasar double de type BAL HE 2149-2745 et, en ce qui nous concerne, la détection de différences spectrales entre les deux images A et B du quasar.

On constate que la composante A apparaît plus bleue que la composante B et ceci sur une période de temps d'au moins 3 ans. En outre, les largeurs équivalentes des raies en émission sont plus faibles dans A, tandis que les largeurs équivalentes des raies en absorption –et leurs profils– sont identiques dans A et B.

Ces résultats sont compatibles avec un effet microlentille classique, amplifiant le continuum de la composante A mais pas la région plus étendue à l'origine des raies en émission. Il est intéressant de noter que la dépendance en longueur d'onde de la différence de couleur entre A et B –interprétée en termes d'effet microlentille– est similaire à celle observée pour Q2237+0305 et compatible avec le modèle standard dans lequel un disque d'accrétion constitue la source du continuum optique dans les quasars.

Des différences subtiles entre les composantes A et B sont observées dans le profil de la raie en émission CIII] λ1909, suggérant que la région à l'origine des raies en émission pourrait être partiellement résolue par l'effet microlentille.

A&A 383, 71–81 (2002)
DOI: 10.1051/0004-6361:20011731
© ESO 2002

Astronomy & Astrophysics

An optical time-delay for the lensed BAL quasar HE 2149−2745⋆

I. Burud[1,2], F. Courbin[1,3,4], P. Magain[1], C. Lidman[5], D. Hutsemékers[5,⋆⋆], J.-P. Kneib[6], J. Hjorth[7], J. Brewer[5], E. Pompei[5], L. Germany[5], J. Pritchard[5], A. O. Jaunsen[5], G. Letawe[1], and G. Meylan[2]

[1] Institut d'Astrophysique et de Géophysique, Université de Liège, Avenue de Cointe 5, 4000 Liège, Belgium
[2] Space Telescope Science Institute, 3700 San Martin Drive, Baltimore, MD 21218, USA
[3] Universidad Católica de Chile, Departamento de Astronomia y Astrofisica, Casilla 306, Santiago 22, Chile
[4] GEPI, Observatoire de Paris-Meudon, Place Jules Janssen, 92195 Meudon, France
[5] European Southern Observatory, Casilla 19, Santiago, Chile
[6] Observatoire Midi-Pyrénées (LAS), UMR 5572, 14 avenue E. Belin, 31400 Toulouse, France
[7] Astronomical Observatory, University of Copenhagen, Juliane Maries Vej 30, 2100 Copenhagen Ø, Denmark

Received 1 June 2001 / Accepted 26 November 2001

Abstract. We present optical V and i-band light curves of the gravitationally lensed BAL quasar HE 2149−2745. The data, obtained with the 1.5 m Danish Telescope (ESO-La Silla) between October 1998 and December 2000, are the first from a long-term project aimed at monitoring selected lensed quasars in the Southern Hemisphere. A time delay of 103±12 days is determined from the light curves. In addition, VLT/FORS1 spectra of HE 2149−2745 are deconvolved in order to obtain the spectrum of the faint lensing galaxy, free of any contamination by the bright nearby two quasar images. By cross-correlating the spectrum with galaxy-templates we obtain a tentative redshift estimate of $z = 0.495 \pm 0.01$. Adopting this redshift, a $\Omega = 0.3$, $\Lambda = 0.7$ cosmology, and a chosen analytical lens model, our time-delay measurement yields a Hubble constant of $H_0 = 66 \pm 8\,\mathrm{km\ s^{-1}\ Mpc^{-1}}$ (1σ error) with an estimated systematic error of $\pm 3\,\mathrm{km\ s^{-1}\ Mpc^{-1}}$. Using non-parametric models yields $H_0 = 65 \pm 8\,\mathrm{km\ s^{-1}\ Mpc^{-1}}$ (1σ error) and confirms that the lens exhibits a very dense/concentrated mass profile. Finally, we note, as in other cases, that the flux ratio between the two quasar components is wavelength dependent. While the flux ratio in the broad emission lines – equal to 3.7 – remains constant with wavelength, the continuum of the brighter component is bluer. Although the data do not rule out extinction of one quasar image relative to the other as a possible explanation, the effect could also be produced by differential microlensing by stars in the lensing galaxy.

Key words. gravitational lensing – quasars: individual: HE 2149−2745 – cosmological parameters

1. Introduction

The time-delay between the gravitationally lensed images of a distant source is a measurable parameter. Observed as the time difference between the arrival dates of a single (lensed) wavefront emitted by a distant source, it is directly related to the Hubble constant H_0 (Refsdal 1964). Obtaining accurate time-delay measurements in multiply lensed quasars can therefore yield (i) a determination of H_0 provided the mass distribution in the lens is known, or (ii) constraints on the mass distribution in a given lens, using H_0 as inferred from other methods. During the last 20 years much effort has been devoted to the observations of lensed quasars, and in particular to long-term monitoring of selected systems. Some of these are Q0957+561 (Schild 1990; Vanderriest et al. 1989), PG 1115+080 (Schechter et al. 1997), B1608+656 (Fassnacht et al. 1999) and B1600+434 (Burud et al. 2000; Koopmans et al. 2000). In this context, we have been conducting a photometric monitoring program at the Danish 1.5-m telescope at La Silla observatory (ESO, Chile) since October 1998, with the goal of measuring the time-delays in several well studied lensed quasars. We present here the first result from this program: the time-delay measurement in the two-image quasar HE 2149−2745.

The lensed nature of the BAL quasar HE 2149−2745 at $z = 2.03$ was established by Wisotzki et al. (1996). This system proves to be an easy target for monitoring at a site with reasonable seeing conditions (up to 2″): it is bright ($B = 17.3$) and the two quasar images have an

Send offprint requests to: I. Burud, e-mail: burud@stsci.edu

⋆ Based on observations made with the Danish 1.5-m telescope (ESO, La Silla, Chile) and at VLT UT1 Antu (ESO-Paranal, Chile) (Proposals: 64.O-0205(B), 65.O-0214(B), 66.A-0203(B), 67.A-0115(B), 66.B-0139(A) and HST archives ID 8175).

⋆⋆ Also Research Associate FNRS at the University of Liège, Belgium.

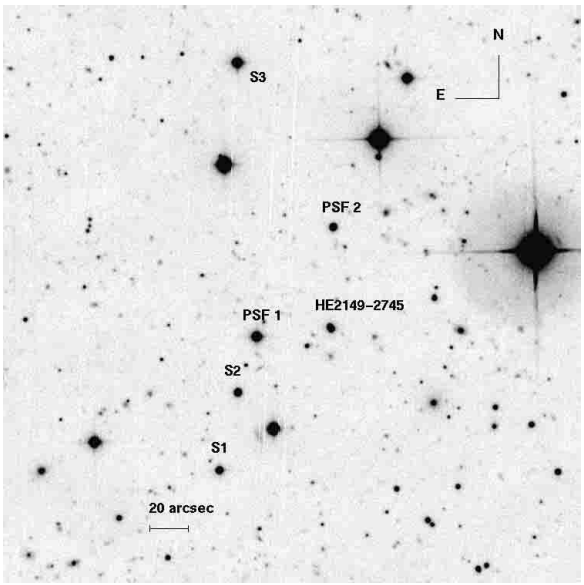


Fig. 1. Field of view $5' \times 5'$ in size around HE 2149−2745. The three reference stars (labelled S1, S2, S3) used for the photometry and the two PSF-stars (PSF1, PSF2) used in the spectral deconvolution are indicated. North is up and East to the left.

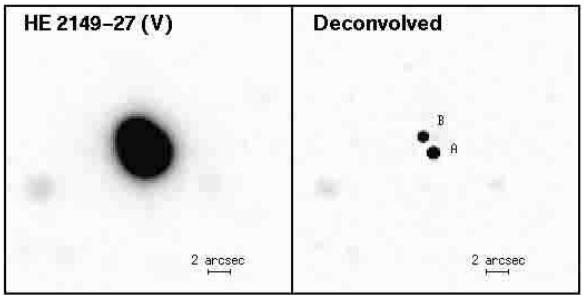


Fig. 2. *Left*: stacked V-band image of a $9'' \times 9''$ region centered on HE 2149−2745. The seeing is $\sim 2''$ and the total exposure time is $\sim$17 hours. *Right*: deconvolved image ($FWHM = 0''.4$) obtained from the simultaneous deconvolution of 57 frames. North is up and East is to the left.

Table 1. Positions of three reference stars relative to the position of the A component in HE 2149−2745.

Star	RA (arcsec)	DEC (arcsec)
S1	−48.126	136.268
S2	−57.126	−72.647
S3	−38.160	−4.145

angular separation of 1.7″. The monitoring program, the light curves and the time delay are discussed in Sects. 2–4 below.

The lensing galaxy has been detected in HST NICMOS and WFPC2 images but its redshift remains unknown. With the aim of measuring this redshift, we have obtained a spectrum of HE 2149−2745 with FORS1 at UT1 (ESO-Paranal, Chile). The analysis of the spectroscopic data is described in Sect. 5. This section also includes a discussion on the spectral differences between the two quasar components. Mass models and estimates of the Hubble constant are presented in Sect. 6. Finally, Sect. 7 summarises the main results.

2. Photometric monitoring at the 1.5 m Danish telescope

2.1. Observations and data reduction

Weekly observations of HE 2149−2745 were carried out at the Danish 1.5-m telescope at ESO-La Silla from October 1998 to December 2000. The target is visible from the beginning of June to the end of December, which results in gaps of about ∼5 months in the light curves. Apart from these gaps, very few points were missed because of poor weather or technical problems. Observations were obtained in the V and *Gunn* i bands with DFOSC (Danish Faint Object Spectrograph Camera) which has a pixel size of 0″.395. Figure 1 shows the central region of the field of view of DFOSC, i.e., 5 arcmin^2 of the 13 arcmin^2 available. The V-band was given priority because of the detector's better sensitivity at these wavelengths, but observations were also carried out in the i-band in order to monitor possible colour changes. The exposure time was set to 900 s during the first 6 months of observations. It was increased to 1800 s for the rest of the observations in order to improve the photometric quality for the faint B quasar image. For each observed data point the total exposure time was divided into three dithered exposures in order to remove cosmic rays and bad pixels. The seeing varied from 0″.7 to 2″.9, with a median of 1″.6. All the imaging data were pre-processed (bias-subtracted and flat-field corrected) using standard IRAF routines.

3. Photometry

The photometry of the blended quasar images was performed by applying the MCS deconvolution algorithm (Magain et al. 1998). This algorithm has already been used to analyze the data of several lensed quasars (e.g., Burud et al. 2000; Hjorth et al. 2001). Its main advantage is its ability to use all the data, even rather poor, irrespective of image quality and lunar phase. The final deconvolved image is produced by simultaneously deconvolving all the individual frames of the same object from all epochs. The positions of the quasar images (two in the present case) and the shape of the lensing galaxy are the same for all the images and are therefore constrained using the total S/N of the whole data-set. The intensity of the point sources are allowed to vary from image to image, hence producing the light curves.

The two quasar components are well separated in our deconvolved image of HE 2149−2745 (see Fig. 2), but the lensing galaxy remains too faint to be detected. This is

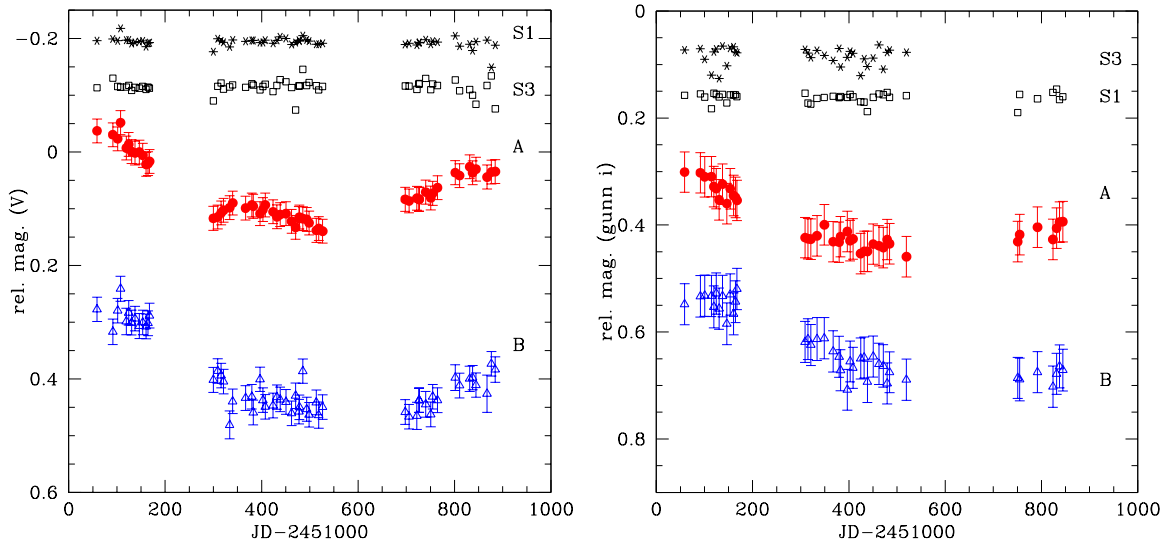


Fig. 3. Light curves of the two images A and B of HE 2149−2745 and the comparison stars S1 and S3 (Table 1). The V-band light curves are displayed on the left while the *Gunn* i-band light curves are shown on the right. The magnitudes of the quasar and stars are calculated relative to the reference star S2. The error bars include photon noise and PSF errors estimated from the deconvolution of a reference star. For display purposes, the B component is shifted by −1.3 mag and −1.2 mag in the V and *Gunn* i band, respectively, with respect to their original values. Likewise, S1 is shifted by 1.1 and 1.35, and S3 is shifted by +1.15 and +1.35 mag in the V and *Gunn* i filters, respectively. S3 was saturated in the last *Gunn* i images and is therefore not shown on the plot for these frames.

fortuitous since contamination by an extended object would complicate the analysis.

The light curves of HE 2149−2745 consist of 57 data points in the V-band and 41 points in the *Gunn* i band, as presented in Fig. 3. The points between JD 2451800 and JD 2451900 were obtained just after the installation of the new chip on DFOSC. The new chip does not have problems of charge diffusion, as the old chip had, and consequently, the effective seeing is now considerably improved. Our original PSF star, for which the ADU counts were always in the linear regime on the old CCD, became saturated on the new chip. Another PSF star further away from the target had to be used on a few frames before the exposure time was adjusted to the new chip. These points are therefore more noisy than the previous points.

The data are plotted relative to a reference star common to all images, star S2 in Table 1. Two other stars were deconvolved as well, in order to check the relative photometry and to check for systematic errors (see Table 1 for the positions of the stars). The error-bars include both photon noise and additional systematic errors, e.g., PSF errors. The latter is estimated by using one of the reference stars, as explained in Burud et al. (2000).

4. Time-delay measurement

By sliding the light curves across one another, one can make a rough "by eye" estimate of the time-delay of ∼100 days, with A leading B. Using the χ^2 minimization method described in Burud et al. (2000), a more objective value of $\Delta t = 103 \pm 12$ days is found from the V-band light curves. The i-band data are noisier and have fewer data points but the measured time-delay, $\Delta t = 104 \pm 31$ days, agrees well with the delay derived from the V-band. A simultaneous minimization of the V and i band curves gave a $\Delta t = 109 \pm 22$ days. The errors quoted here are obtained from Monte Carlo simulations of 1000 sets of light curves, assuming that the photometric errors are uncorrelated and follow a Gaussian distribution. The χ^2 minimization method was also performed on 1000 sets of curves where 5 randomly chosen data points were removed from each set. The results from these simulations yielded a time-delay of $\Delta t = 101 \pm 30$ days and $\Delta t = 107 \pm 30$ days in V and i respectively, confirming that the time-delay measurement is robust. The magnitude differences between the A and the B components are found to be 1.635 ± 0.001 mag in V and 1.505 ± 0.003 mag in the i-band. This corresponds to flux ratios of 4.51 and 4.00 in V and i bands respectively Although no erratic changes are detected in the light curves within the measurement errors, microlensing on long time scales may still be present as suggested by the VLT spectra presented in Sect. 5. Given that the V-band data contain more points and are less noisy than the i-band data, we adopt the V-band estimate of the time-delay as the best one: $\Delta t = 103 \pm 12$ days (1σ error). Figure 3 summarizes the photometric data and Fig. 4 displays the V and i-band light curves with component B shifted by 103 days.

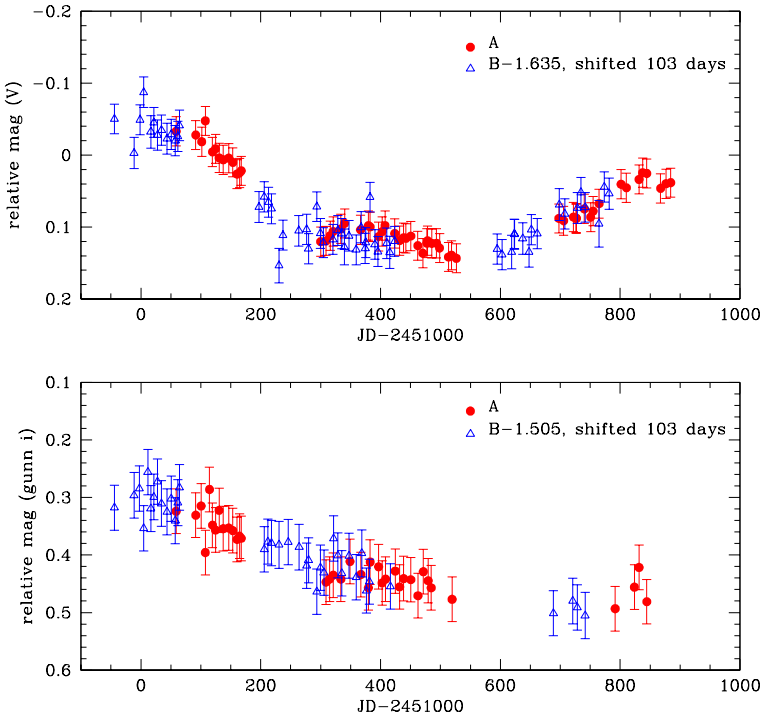


Fig. 4. The V (top) and i-band (bottom) light curves where the B curve is shifted by 103 days. The light curve of component B is shifted by 1.635 and 1.505 magnitudes in the V and i-band, respectively, with respect to their original values. The curves for the A component are as in Fig. 3.

5. Spectroscopy of HE 2149−2745

5.1. VLT spectroscopy

To convert the time-delay into an estimate of the Hubble constant, one must know the geometry of the lensing system and this includes the redshift of the lensing galaxy. For this purpose, we took an optical spectrum of HE 2149−2745 with the ESO VLT/UT1 using the Multi-Object-Spectroscopy (MOS) capability of FORS1. The observations were obtained on November 19, 2000 under fairly good seeing conditions (0.8″). The 1″ slitlets of FORS1 were aligned to obtain simultaneously the spectrum of HE 2149−2745 and of 2 PSF stars (indicated in Fig. 1) about as bright as the two quasar images. The high resolution collimator was used, resulting in a pixel size of 0.1″, in combination with the G300V grism and GG435 order sorting filter. Three exposures, each of 1000 s, were taken so that cosmic rays could be removed.

5.2. Redshift of the lensing galaxy

Using the spatial information in the spectra of the two PSF stars, the spectrum was spatially deconvolved with the spectral version of the MCS deconvolution method (Courbin et al. 2000a). The deconvolution process decomposes the data into the individual spectra of the two quasar images and the faint lensing galaxy (see Figs. 5 and 7), in a way similar to the one described in Lidman et al. (2000) for HE 1104−1805.

The lens spectrum was cross-correlated with a template spectrum of an elliptical galaxy (Kinney et al. 1996). Due to the low S/N the calculated correlations are low, nevertheless, there is a significant "bump" in the correlation function covering the redshift range $0.49 \leq z \leq 0.60$ as shown in Fig. 6. The spectrum of the lens and the template are shown in Fig. 5, where the template has been shifted vertically for clarity. The calcium H and K lines, the G-band and the Mg triplet are labeled. A measure of the reliability of the redshift estimate is given by the r-statistic of Tonry & Davis (1979), which is the signal-to-noise ratio of the main peak in the cross correlation. We find that $r = 1.9$ meaning that the signal-to-noise of the correlation peak is poor. A value above 3 is considered secure (Kurtz & Mink 1998).

As can be seen on the HST image (cf. Fig. 14) the lensing galaxy lies very close to the B image. We therefore looked for evidence of absorption in the spectrum of the background quasar. In order to remove the quasar spectral features, the B spectrum was divided by that of the A component (Fig. 8). Two, possible Ca H & K candidates were found, one at $z = 0.489$ and another at $z = 0.504$. An integrated A+B spectrum at similar resolution but covering shorter wavelengths has been published by Wisotzki et al. (1996). We looked for possible MgII absorption in

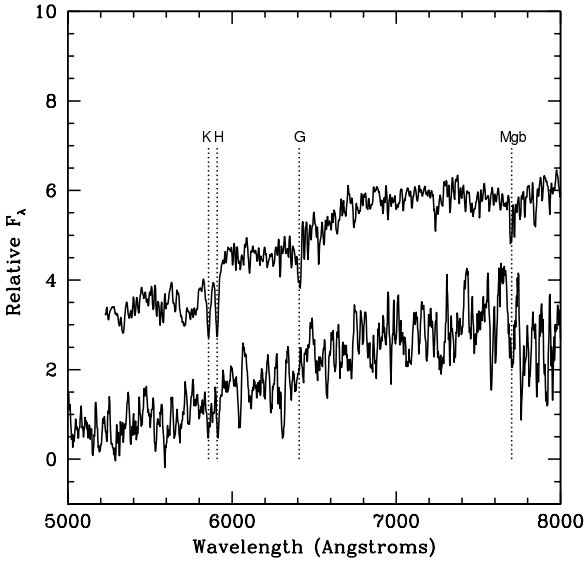


Fig. 5. Extracted spectrum of the lensing galaxy (bottom) and the template spectrum from Kinney et al. (1996) (top) used in the cross correlation. The main spectral features, calcium H and K lines, the *G*-band and the Mg triplet, are indicated by dashed vertical lines. The lens redshift is tentatively $z = 0.489$.

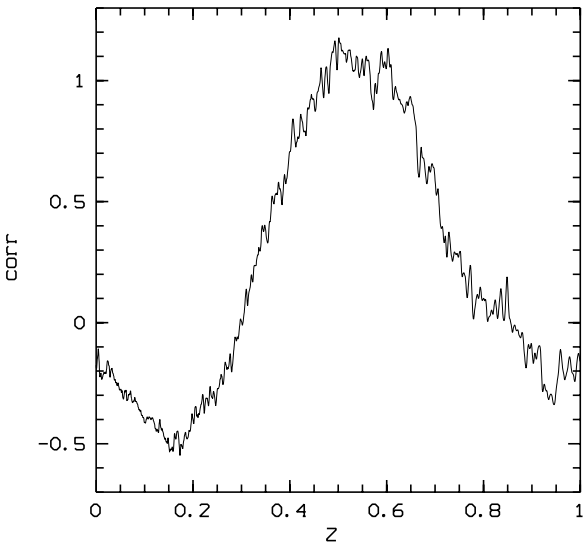


Fig. 6. Cross-correlation function of the galaxy spectrum with the galaxy template from Kinney et al. (1996). The centre of the correlation peak is at $z = 0.535$.

the quasar spectrum at the putative redshift of the lens. Unfortunately, the $z = 0.489$ line would fall in a strong absorption line of the quasar, while a candidate at $z = 0.504$ is found in the wing of a quasar emission. The signal-to-noise ratio of the lens galaxy and the Ca H and K absorption features in the B component are very low and we can not rule out any of the two estimates. We therefore take $z = 0.495 \pm 0.01$ to be the most likely redshift for the lensing galaxy. This is within the estimated redshift range

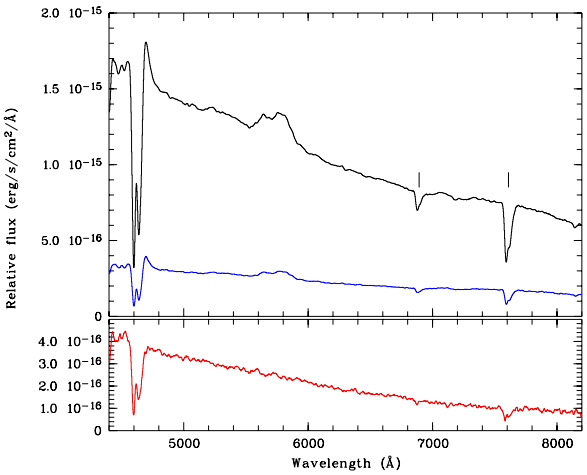


Fig. 7. *Top*: spectra of the A and B components. *Bottom*: the spectrum showing $A - 3.7 \times B$. The scaling factor is chosen to best cancel the emission lines. Telluric absorption lines are indicated.

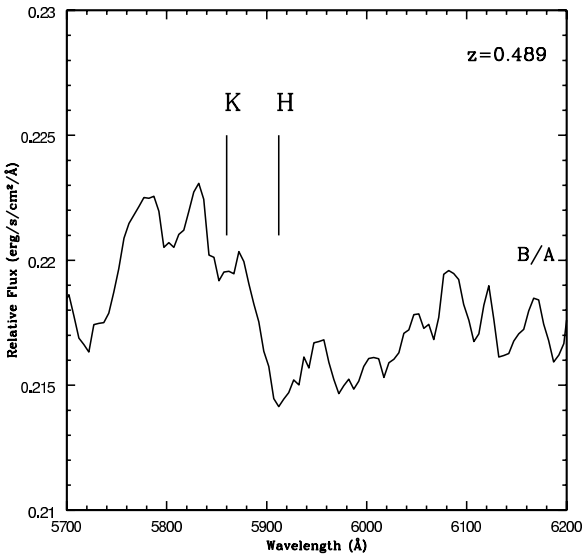


Fig. 8. Spectrum of the B component divided by that of the A component of HE 2149−2745. The plot shows a zoom on the region corresponding to possible Calcium H and K absorption due to the lens at $z = 0.489$. The bump between 5750 and 5900 Å is the residual CIII]+AlIII emission from the quasar.

$0.37 \leq z \leq 0.50$ which is based on the position of the lens in the fundamental plane (Kochanek et al. 2000).

5.3. Spectroscopy of the quasar images: Colour differences, extinction or microlensing?

The quasar spectra show that the continuum of component A is bluer than the continuum of component B (Fig. 7). This confirms the difference in flux ratio that was found from the light curves in the *V* and *Gunn*

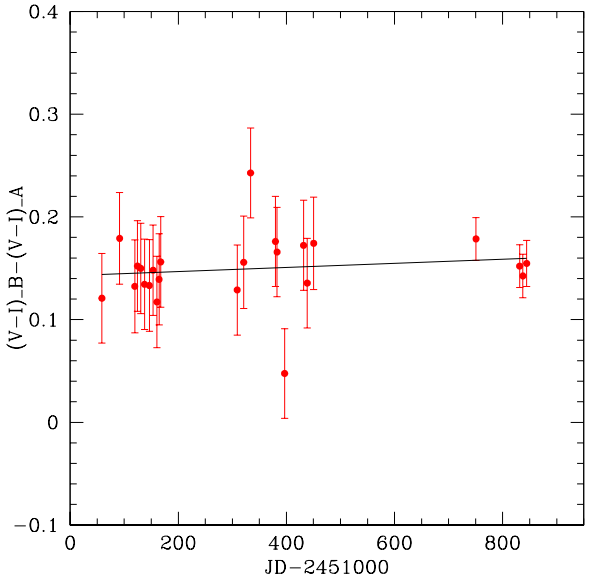


Fig. 9. Colour excess of the B component relative to the A component, $(V-I)_{\rm B}-(V-I)_{\rm A}$ as a function of time. No significant variations can be detected over a period of 900 days. The solid line shows the best fit line through the points.

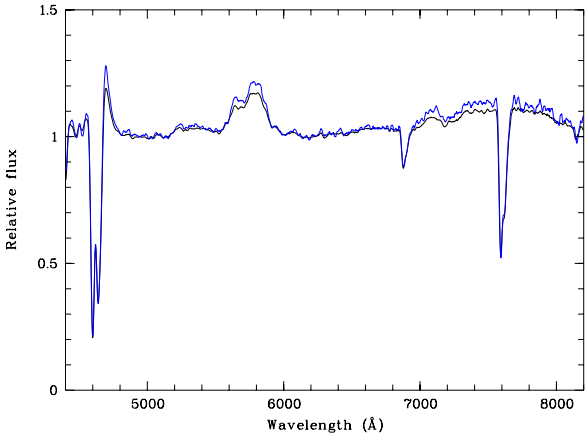


Fig. 10. The A (thick) and B (thin) spectra of HE 2149−2745 normalized to a common continuum. The equivalent widths of the emission lines, including the FeII pseudo-continuum, are smaller in A. The equivalent width of the CIV broad absorption line (∼4650 Å) is the same in both the A and B components.

i-bands (Sect. 4). We note three points of interest about these spectral differences:

1. As shown in Fig. 9 the colour difference between the quasar images does not vary during the period of our observations (∼3 years);
2. The emission line flux ratios at the date of the observation are not wavelength dependent: all emission lines cancel in the difference spectrum of Fig. 7. This difference spectrum has been produced by multiplying the spectrum of the B component by a *constant* factor of 3.7 and by subtracting it from the spectrum of the A component. Figure 10 gives a different representation of the same effect, where the spectra of the two quasar images are normalized to the same continuum. The equivalent widths of all emission lines (including the FeII pseudo-continuum) are smaller in A;
3. The CIV broad absorption line behaves as the continuum: its equivalent width is unchanged in the A and B spectra (Fig. 10).

The spectral differences cited above have essentially two possible explanations: (*i*) differential magnification due to microlensing, or (*ii*) differential reddening of the B component by the lensing galaxy.

5.3.1. Microlensing

If microlensing is present in HE 2149−2745, one expects the continuum region and the much more extended emission lines region to be affected differently (Wambsganss & Paczyński 1991). In most AGN models, the size of the continuum region depends on wavelength, and the Broad Emission Line Region (BELR) is usually believed to be larger than the continuum region by more than one order of magnitude. Since the B component is closest to the lensing galaxy we would expect that microlensing effects occur most often in the B-component. Microlensing of the A component however is also possible.

Assuming the lensed quasar in HE 2149−2745 follows the "standard" AGN model and that we are observing component A through a network of caustics produced by stars in the main lensing galaxy, one can imagine a scenario where the inner – and bluer – continuum region of the component A is being enhanced by a larger amount than the outer redder parts. As the BELR is much larger than the central AGN (even the redder parts), it remains unaffected by microlensing. This interpretation has already been proposed to explain similar spectral differences observed in the double HE 1104−1805 (Wisotzki et al. 1993, 1995; Courbin et al. 2000b).

In the case of HE 2149−2745 the Einstein radius of a typical deflector in the lens plane projected onto the source plane is ($\Omega = 0.3$, $\Lambda = 0$):

$$R_{\rm E} = \sqrt{\frac{4GM}{c^2}\frac{D_{\rm ds}D_{\rm s}}{D_{\rm d}}} = 1.3\times10^{-3}(M/0.1\ M_\odot)^{1/2}{\rm pc} \quad (1)$$

where $D_{\rm d}$, $D_{\rm s}$ and $D_{\rm ds}$ are angular diameter distances to the deflector, the source and between deflector and source respectively, and M is the mean mass of all microlenses. The duration of crossing the Einstein radius will be up to 10 years assuming a relative velocity between source and lens that is equal or larger than the velocity in the lensing galaxy which is of the order of ∼(100–400) km s^{-1} (Mould et al. 1993). Although shorter microlensing events, such as a caustic crossings, can occur, the long time scale

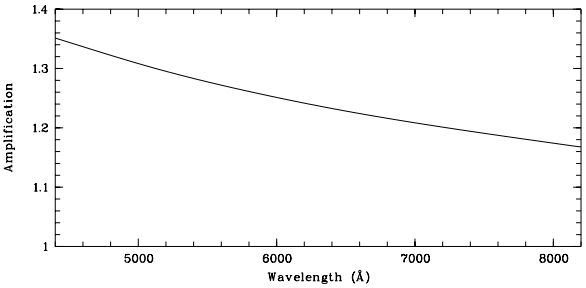


Fig. 11. The residual magnification μ of A relative to B as a function of wavelength. This magnification factor is derived by fitting the A/B continuum ratio after correcting the B spectrum by the constant factor 3.7 (as in the lower panel of Fig. 7).

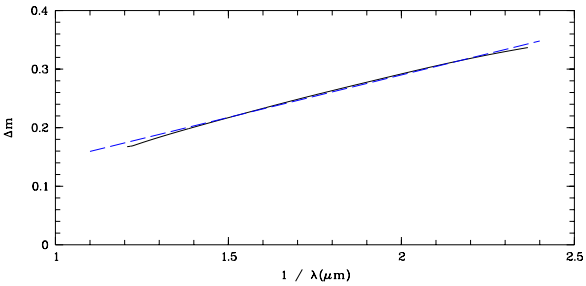


Fig. 12. The magnification of component A in magnitude ($\Delta m = 2.5 \log \mu$) as a function of inverse wavelength (solid line). The wavelength dependence is well reproduced by $\Delta m = 0.145\,/\lambda(\mu\mathrm{m})$ (dashed line).

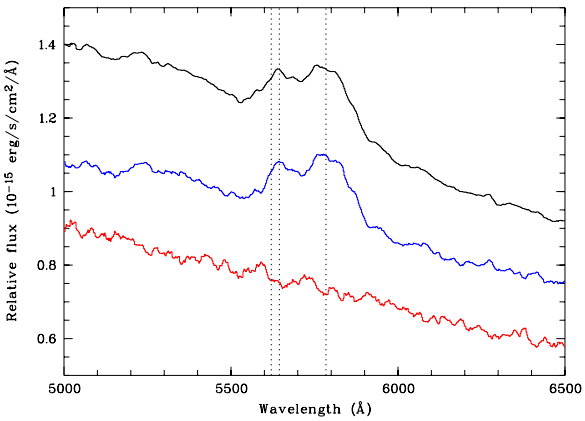


Fig. 13. An enlargement of the spectra of components A (upper) and B (middle, multiplied by 3.7), together with the difference spectrum $A - 3.7 \times B$ (lower, multiplied by 2). The region of the CIII] emission line is illustrated. The wavelengths of AlIII $\lambda\lambda$1855, 1863 and CIII] λ1909 are indicated at the redshift of the quasar ($z = 2.03$). This blend is typical of BAL quasars (Hartig & Baldwin 1986). Some subtle differences in the blue part of the line profiles may be noticed (see text).

of crossing the Einstein radius shows that an event may be present in our data, and stable over our relatively short period of observation of 900 days, as Fig. 9 would suggest.

Assuming that the continuum of A is amplified by microlensing, we may derive the wavelength dependence of the magnification from the A/B continuum ratio. This relative magnification factor μ is given in Fig. 11. It is derived by fitting the A/B continuum ratio after correcting the spectrum of B by the constant factor 3.7. The relative magnification is directly related to the size of the continuum region as a function of wavelength (e.g. Schneider et al. 1992), the precise measurement of which requires the knowledge of the background magnification μ_0 due to other distant subimages. While μ can be estimated from Fig. 11, μ_0 can only be obtained by measuring the background magnification before and after a caustic crossing event. This can be done with a spectrophotometric monitoring. In Fig. 12, we have plotted the magnification factor – expressed as a magnitude difference – as a function of the inverse wavelength. It shows a remarkably tight wavelength dependence strikingly similar to that found by Nadeau et al. (1999) for Q2237+0305. This suggests that HE 2149−2745 presently suffers a chromatic microlensing event similar (although of much longer duration) to the 1991 high-magnification event in Q2237+0305 and which was interpreted – on the basis of its colour dependence – as evidence for the thermal accretion disk model as the source of UV-visible continuum emission in quasars (cf. Nadeau et al. 1999).

While broad emission lines should be essentially unaffected by the caustic crossing, some subtle differences may arise in the line profiles if some parts of the BELR are selectively magnified (Nemiroff 1988; Schneider & Wambsganss 1990). Looking in detail at the line profiles of components A and B (Fig. 13), small differences are indeed present in the blue wing of the AlIII and CIII] emission lines. Interpreted in terms of microlensing, this could indicate that part of the BELR is being magnified. Similar profile variations are predicted by the models of Schneider & Wambsganss (1990). Interestingly, no difference in the CIV BAL profile, like those reported for the quadruple BAL quasar H1413+117; cf. Angonin et al. (1990) and Hutsemékers (1993), is noticed.

The present findings may be of importance for investigating the inner structure of quasars. Spectroscopic data obtained at regular time intervals, e.g., spectra separated by intervals corresponding to the time-delay, will test the microlensing interpretation, cancel possible time-delay effects (see Wisotzki et al. 1995) and help to probe the innermost region of quasar structure, using microlensing magnification.

5.3.2. Reddening

An alternative explanation for the observed colour difference between quasar images is that the B image is reddened by the lensing galaxy. Assuming this is true, we can estimate the amount of reddening which would correspond to the strength of the putative Ca H & K absorption

lines seen in the B spectrum (Fig. 8), if average Galactic conditions apply to the present case. From the interstellar line observations of Sembach et al. (1993), we derive a mean relation between $E(B-V)$ and the Ca K equivalent width. With a de-redshifted equivalent width ∼100 mÅ, this would imply a colour excess $E(B-V) \sim 0.05$, which corresponds to $E(V-I) \sim 0.1$, using the extinction curves of Mathis (1990), after proper redshift corrections are applied. This is compatible with the measured colour difference of 0.15 (Fig. 9). The extinction can also be estimated by fitting the magnitude difference of the A and B components as a function of wavelength (Fig. 12) with a typical extinction law. In the wavelength range of interest, the Galactic and SMC extinction curves are very similar (Pei 1992) and can be reasonably well represented by

$$A_\lambda = \frac{1.75E(B-V)}{\lambda(\mu\mathrm{m})} \qquad (2)$$

where A_λ is the extinction in magnitudes, and where the ratio of the total-to-selective extinction R_V is taken to be $R_V = 3.1$. Identifying the wavelength dependence of the magnitude difference in Fig. 12 to this extinction curve at the redshift of the lens, we have $1.75E(B-V)(1+z_{\rm lens}) = 0.145$ i.e., $E(B-V) = 0.05$ which is in agreement with what is found from the Ca H & K lines.

In the case of extinction by dust in the lens we would expect the continuum and the BELR to be equally affected. This does not seem to be the case; however, the wavelength range between CIV and the CIII]-AlIII complex is small. A more sensitive test of the dust hypothesis will be to observe H-alpha in the infra-red, as this will provide a larger wavelength baseline to measure differences.

On the basis of the available data, no interpretation of the apparent reddening can be excluded, although microlensing seems a somewhat more natural explanation for the observed spectral differences.

6. Lens modeling

The time-delay measured for HE 2149−2745 can be used to infer an estimate of H_0, based on modeling of the total gravitational potential responsible for the lensing effect. This includes the main lensing galaxy and any intervening massive cluster along the line of sight to the quasar. HE 2149−2745 is a relatively easy case to model, as there is no obvious mass concentration along the line of sight to the source apart from the main lensing galaxy. Only a marginally detected galaxy concentration is seen 30″ West and 1′ North of the main lens. In addition, the lensing galaxy is almost aligned with the two quasar images (see Figs. 1 and 14). Two different approaches can be used to convert time delays into H_0: models that involve an analytical form for the lensing galaxy, and models that involve more degrees of freedom, e.g., a pixelated surface mass density (Saha & Williams 1997; Williams & Saha 2000). We use both approaches.

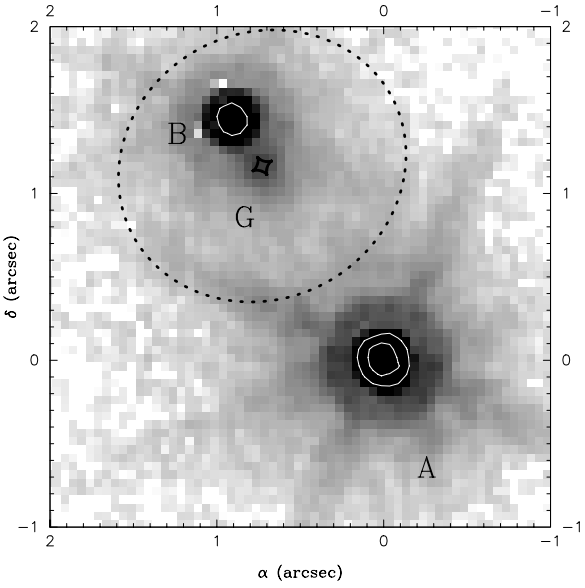


Fig. 14. Field of 3″ around HE 2149−2745, where the lensing galaxy is indicated as G, close to the faint quasar image B. Also indicated are the critical and caustic curves created by a single lensing galaxy and no external shear. The image has been obtained from the CASTLEs public survey of gravitational lenses. This I-band image comes from HST/WFPC2 (Kochanek et al.).

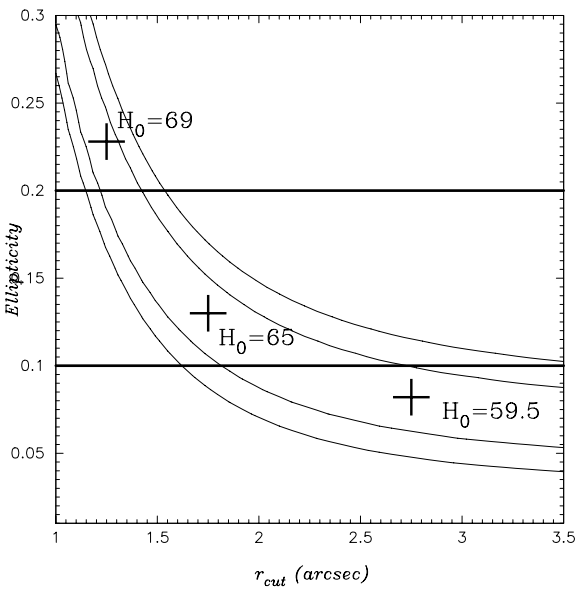


Fig. 15. Results of the model fitting when exploring the ellipticity/cut radius space. The lines show the best models, i.e., they show the area where the models fit the data at 1σ (inner lines) and 3σ (outer lines). Values for H_0 are given for different models among the most likely. The horizontal lines give the plausible range of ellipticities, given the HST images. The plot displayed here uses $\Omega = 0.3$, $\lambda = 0.7$.

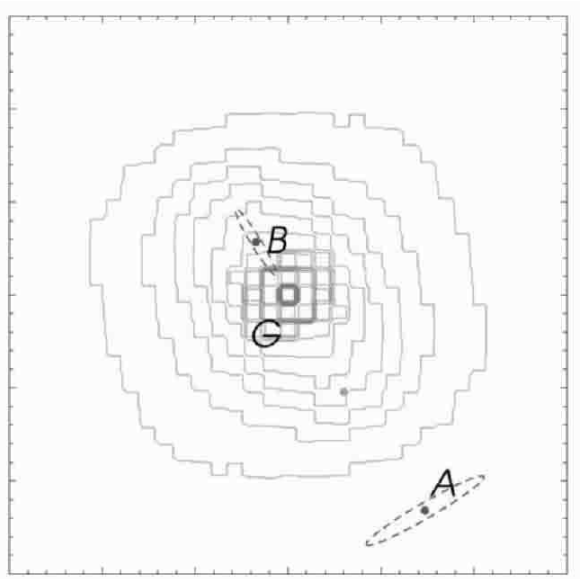


Fig. 16. Mass distribution found with the pixelated models with cosmology $\Omega = 0.3$, $\lambda = 0.7$. Almost no ellipticity is found. The contour levels represent $\kappa = 1/3$, 2/3, 1, etc. The scale is $3''$ on a side and the astrometry is the same as for the analytical models. The dashed ellipses around the quasar images represent the magnification matrix, i.e., the axes are proportional to the eigenvalues and the orientation corresponds to the eigenvectors. The spot between the quasar images is the position of the lensed source in the source plan.

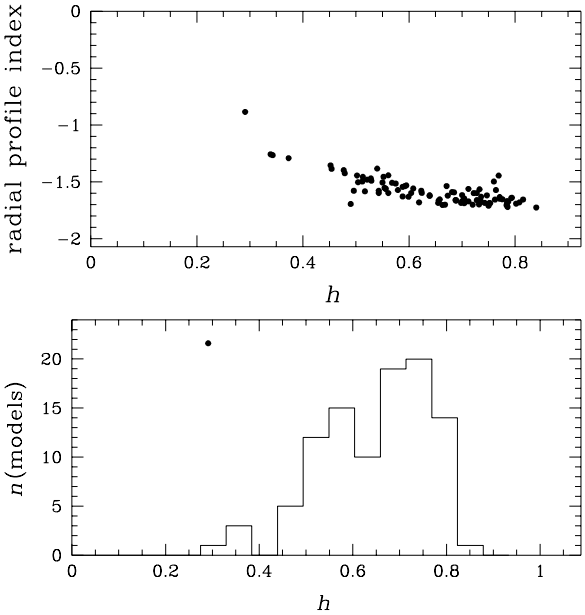


Fig. 17. *Top:* radial index profile vs. H_0 for one hundred different non-parametric models, showing that all the galaxy models have a steep mass profile (<-0.5). *Bottom:* probability density for H_0 for the same models. Units on the X axis of both figures is in h_{100}. The median value of the distribution is 65 km s^{-1} Mpc^{-1}. The black dot marks the location of an isothermal mass profile (radial profile index $= -1$).

6.1. Analytical models

Our analytic model uses the mass profile of Kneib et al. (1996): a truncated Pseudo-Isothermal-Elliptical-Mass-Distribution (PIEMD). Truncated PIEMD are elliptical mass distributions smoothly truncated at radius $r_{\rm cut}$. For radii smaller (respectively larger) than $r_{\rm cut}$, the projected surface mass density profile is varying as r^{-1} (respectively r^{-3}). The interest in such profile is their ability of characterizing any ellipticity in the mass distribution as well as having a total finite mass. We fit the model to the publicly available HST/WFPC2 data (which offers better resolution and sampling than NICMOS) obtained by Kochanek et al., and use the emission line flux ratio of 3.7 calculated from our VLT spectra. During the fit, the astrometry of the quasar images relative to the lens is fixed, as well as the redshift of the source and lens. The free parameters include the velocity dispersion, ellipticity, which is here defined as $[a^2 - b^2]/[a^2 + b^2]$ where a and b are the long and short axes of the lens, and cut radius of the lens.

A common problem in lens modeling is the mass-sheet degeneracy. In other words, several mass profiles and in particular mass profiles of different compactness, will reproduce the same time-delay (Gorenstein et al. 1988). One has therefore to constrain the models using observational data and explore the widest range of physically acceptable models. A first constraint comes from the HST images: the lens is almost round. After PSF-subtraction of the quasar images we fit the shape of the lensing galaxy and obtain an ellipticity of about 0.1–0.2. Assuming that the mass distribution follows the light distribution we can restrict ourselves to this range of ellipticities. Figure 15 shows a family of models exploring the ellipticity vs. $r_{\rm cut}$ space and we see that little spread in the values of H_0 is observed in the range of ellipticities 0.1–0.2. We assume ellipticity $\varepsilon = 0.15$ which implies $r_{\rm cut} = 1.6''$ and $H_0 = 66 \pm 8$ km s^{-1} Mpc^{-1} with additional systematic errors of $\pm$ 3 km s^{-1} Mpc^{-1} due to the limited range of ellipticity. We also try to investigate the existence of a galaxy core. For this we scan the possible values for the core radius. The lens model excludes any value of $r_{\rm core}$ larger than 0.02 arcsec. Within this limit, the core radius has basically no effect on the determination of H_0, so the choice of a given core radius is not critical. In our fiducial model, we use a core radius of $\sim$0.002 arcsec which corresponds to $\sim$10 pc. Using this, and keeping the other parameters free, we find a lens with the parameters summarized in Table 2. We show in Table 3 the effect of a change in cosmology. Due to the relatively low redshift of the lensing galaxy the influence of a change in cosmology is small compared to the measurement errors.

If we take the currently most popular cosmology, i.e., $\Omega = 0.3$, $\lambda = 0.7$, and $\Delta t = 103 \pm 12$ days, we find $H_0 = 66 \pm 8$ km s^{-1} Mpc^{-1} with an additional estimated

Table 2. Model parameters for HE 2149−2745. The values between brackets are *fixed* during the fit, the others are fitted. The core radius is negligible.

Parameter	Fit
Ω, λ	[0.3, 0.7]
Ellipticity	0.13 ± 0.05
PA (degrees)	62 ± 5
Vel. disp. ($\mathrm{km\,s^{-1}}$)	198 ± 10
$r_{\rm cut}$	[1.25″]
Core radius	[0.002″= 0.01 kpc]
time-delay	[103 days]

Table 3. Influence of the cosmology on the modeling of HE 2149−2745. Values of H_0 are listed for an Einstein–deSitter Universe ($\Omega = 1.0$, $\lambda = 0.$), an open Universe ($\Omega = 0.3$, $\lambda = 0.$) and a flat Universe with non-zero cosmological constant ($\Omega = 0.3$, $\lambda = 0.7$). The model parameters are fixed and set to the ones in Table 2.

Cosmology	H_0 (km s^{-1} Mpc^{-1})
$\Omega = 0.3$, $\lambda = 0.7$	66 ± 8
$\Omega = 0.3$, $\lambda = 0.0$	67 ± 8
$\Omega = 1.0$, $\lambda = 0.0$	61.5 ± 8

systematic error of $\pm$ 3 km s^{-1} Mpc^{-1} due to parameter choices.

6.2. Pixelated models

The pixelated models of Saha & Williams (1997) and Williams & Saha (2000) were also applied to HE 2149−2745. While the mass distribution resulting from these models is not as well related to the physical parameters of the lens, they allow us to explore a wide range of lens shapes and to estimate the robustness of the time-delay conversion. Figure 16 shows the mass distribution found by the models. During the fit, the ellipticity of the mass distribution was kept free. The program reconstructs almost round mass distributions, as does the analytical model (Fig. 15). We also examine the impact of a change in the compactness of the mass profile on the derived value for H_0. Figure 17 shows the result of a Monte-Carlo simulation where 100 models were run with different indices for the lens shape. The density index in Fig. 17 represents the logarithmic projected density gradient in the vicinity of the images (cf. Williams & Saha 2000). The upper panel of the figure shows that most models predict relatively steep/concentrated mass profiles.

In the lower panel of Fig. 17 we display the H_0 probability distribution. The mean of the distribution peaks at $H_0 = 65 \pm 15\,\mathrm{km\,s^{-1}\ Mpc^{-1}}$ at the 2-σ level and $H_0 = 65 \pm 8\,\mathrm{km\,s^{-1}\ Mpc^{-1}}$ at the 1-σ level.

7. Summary – conclusions

We have presented the first result of a long-term photometric monitoring campaign undertaken at ESO between 1998 and 2000 with the 1.54-m Danish telescope. Our V and i light curves allow us to measure a time-delay of $\Delta t = 103 \pm 12$ days between the two quasar images of HE 2149−2745.

From VLT spectroscopy, we have derived a tentative estimate of the lens redshift to be $z = 0.489$. Applying both analytic and numerical lens models to the case of HE 2149−2745, we derive $H_0 = 66 \pm 6\,\mathrm{km\,s^{-1}\ Mpc^{-1}}$ with an additional systematic error of $\pm 3\,\mathrm{km\,s^{-1}\ Mpc^{-1}}$ in the case of the analytic models, due the limited range of the ellipticity. The derived mass models are relatively compact, although not as compact as the light profile of the galaxy. An extra source of systematics might be introduced by the uncertainty on the lens redshift estimate. This is however not critical for the determination of H_0 as the error is dominated by the uncertainty in the time-delay measurement. As HE 2149−2745 shows smooth light curves, it is likely that the situation can be improved by continued monitoring. With an improved time-delay it would also be highly desirable to re-determine the lens redshift more precisely.

Our monitoring program of HE 2149−2745 is the first to be carried out in two bands on such a regular basis and over such a long time scale. Given the error bars, we do not see any significant colour variation over the 900 days of observation. Moreover, our spectra of the two quasar images show that the flux ratios in the broad emission lines behave differently for the continuum flux ratio, and that the flux ratio measured in the BAL structure of the source follows the behavior as the continuum region. Such behavior can be explained both by microlensing or by differential extinction by the lensing galaxy, or both. So far, the data do not allow us to distinguish between the two possible explanations. In order to confirm microlensing, one would need for example to know the time-scale of the putative event, i.e., to measure the absolute magnification of the event and its duration. This would not only allow us to confirm microlensing, but also to use it to map the radial structure of the central AGN in the source. Although the Einstein radius crossing time is long for HE 2149−2745, of the order of 10 years, much shorter microlensing events, such as a caustic crossings, can occur. Conducting a long-term spectrophotometric monitoring could therefore allow us to probe the AGN size HE 2149−2745.

Acknowledgements. We thank IJAF and ESO for granting us observing time for this project on a flexible basis. We are very grateful to the 2.2-m team for their support and enthusiasm. Most of the monitoring observations presented here have been carried out during short periods of time allocated during the scheduled runs of regular observers. We appreciated very much the enthusiasm of all the observers who accepted to perform the observations for us. Some of them, present at the telescope for long periods, contributed a lot to our program. It is a pleasure to thank in particular B. Milvang-Jensen, L. Fogh-Olsen, S. Frandsen, L. Hansen, H. Kjeldsen, J. Knude and G. Israel. We thank Lutz Wisotzki for letting us use his EFOSC spectrum and Prasenjit Saha for help with the non-parametric models. IB was supported by Pôle d'Attraction Interuniversitaire, P4/05 (SSTC,

Belgium). FC acknowledges financial support through Chilean grant FONDECYT/3990024. Additional support from the European Southern Observatory, through ECOS/CONICYT grant C00U05, CNRS/CONICYT grant 8730 and Marie Curie grant MCFI-2001-00242 are also gratefully acknowledged. JH is supported by the Danish Natural Science Research Council (SNF). JPK thanks CNRS for support.

References

Angonin, M. C., Remy, M., Surdej, J., & Vanderriest, C. 1990, A&A, 233, L5
Burud, I., Hjorth, J., Jaunsen, A. O., et al. 2000, ApJ, 544, 117
Courbin, F., Magain, P., Kirkove, M., & Sohy, S. 2000a, ApJ, 539, 1136
Courbin, F., Lidman, C., Meylan, G., Kneib, J.-P., & Magain, P. 2000b, A&A, 360, 853
Fassnacht, C. D., Pearson, T. J., Readhead, A. C. S., et al. 1999, ApJ, 527, 498
Gorenstein, M. V., Shapiro, I. I., & Falco, E. E. 1988, ApJ, 327, 693
Hartig, G. F., & Baldwin, J. A. 1986, ApJ, 302, 64
Hjorth, J., Burud, I., Jaunsen, A. O., et al. 2001, in Gravitational Lensing: Recent progress and future goals, ed. T. Brainerd, & C. Kochanek, ASP Conf. Ser., in press
Hutsemékers, D. 1993, A&A, 280, 435
Kinney, A. L., Calzetti, D., Bohlin, R. C., et al. 1996, ApJ, 467, 38
Kneib, J.-P., Ellis, R. S., Smail, I., Couch, W. J., & Sharples, R. M. 1996, ApJ, 471, 643
Kochanek, C. S., Falco, E. E., Impey, C., et al. `http://cfa-www.harvard.edu/glensdata/`
Kochanek, C. S., Falco, E. E., Impey, C. D., et al. 2000, ApJ, 543, 131
Koopmans, L. V. E., de Bruyn, A. G., Xanthopoulos, E., & Fassnacht, C. D. 2000, A&A, 356, 391
Krolik, J. 1999, in Active galactic nuclei: From the central black hole to the galactic environment. Princeton Series in Astrophysics, ed. J. P. Ostriker (Princeton University Press)
Kurtz, M. J., & Mink, D. J. 1998, PASP, 110, 934
Lidman, C., Courbin, F., Kneib, J.-P., et al. 2000, A&A, 364, L62
Magain, P., Courbin, F., & Sohy, S. 1998, ApJ, 494, 452
Mathis, J. S. 1990, ARA&A, 28, 37
Mould, J. R., Akeson, R. L., Bothun, G. D., et al. 1993, ApJ, 409, 14
Nadeau, D., Racine, R., Doyon, R., & Arboit, G. 1999, ApJ, 527, 46
Nemiroff, R. J. 1988, ApJ, 335, 593
Osterbrock, D. E. 1989, Astrophysics of Gaseous Nebulae and Active Galactic Nuclei (Universtiy Science Books)
Pei, Y. C. 1992, ApJ, 395, 130
Refsdal, S. 1964, MNRAS, 128, 307
Saha, P., & Williams, L. L. R. 1997, MNRAS, 292, 148
Schechter, P. L., Bailyn, C. D., Barr, R., et al. 1997, ApJ, 475, L85
Schild, R. E. 1990, AJ, 100, 1771
Schneider, P., & Wambsganss, J. 1990, A&A, 237, 42
Schneider, P., Ehlers, J., & Falco, E. E. 1992, Gravitational lenses (Springer, Berlin)
Sembach, K. R., Danks, A. C., & Savage, B. D. 1993, A&AS, 100, 107
Tonry, J., & Davis, M. 1979, AJ, 84, 1511
Vanderriest, C., Schneider, J., Herpe, G., et al. 1989, A&A, 215, 1
Wambsganss, J., Schneider, P., & Paczynski, B. 1990, ApJ, 358, L33
Wambsganss, J., & Paczynski, B. 1991, AJ, 102, 854
Williams, L. L. R., & Saha, P. 2000, AJ, 119, 439
Wisotzki, L., Koehler, T., Kayser, R., & Reimers, D. 1993, A&A, 278, L15
Wisotzki, L., Koehler, T., Ikonomou, M., & Reimers, D. 1995, A&A, 297, L59
Wisotzki, L., Koehler, T., Lopez, S., & Reimers, D. 1996, A&A, 315, L405

Troisième partie

Quasars de type BAL : polarisation

Article 10

A procedure for deriving accurate linear polarimetric measurements

H. Lamy, D. Hutsemékers : The Messenger 96, 25 (1999)

Dans cet article, nous décrivons une méthode permettant de mesurer de façon précise la polarisation linéaire d'objets ponctuels lorsque ceux-ci sont observés à l'aide d'une caméra CCD et d'un prisme de type Wollaston. Nous notons des déformations assez importantes des images et montrons qu'elles affectent peu la qualité des mesures.
(N.B. La qualité des figures de l'article étant assez médiocre, nous reprenons les figures originales en supplément).

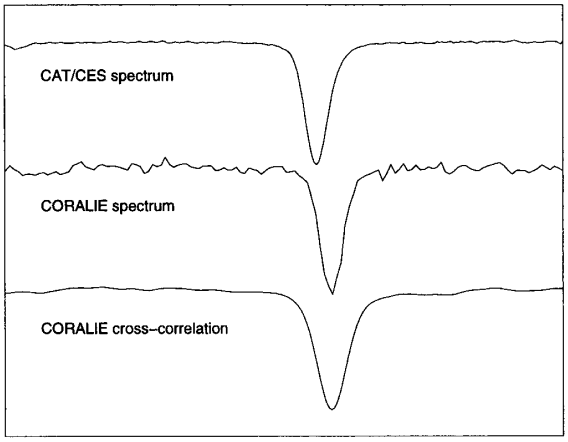


Figure 3: A Si II 4130Å line profile obtained with the CAT/CES is compared with one obtained with CORALIE and a cross-correlation profile derived from the CORALIE spectrum. Integration times were 25 minutes for the CAT spectrum and 17 minutes for the CORALIE spectrum.

For a previous application of mode identification in a pulsating star by means of cross-correlation functions we refer to Mathias & Aerts (1996). Another possibility to continue our monitoring is by means of FEROS. Up to now, we did not yet observe slowly pulsating B stars with this instrument, but we expect to find results comparable to those obtained with CORALIE.

3. Many Thanks

As already mentioned, a study as the one that we are undertaking is very challenging from an observational point of view. On the other hand, long-term monitoring is the only way to obtain meaningful results in the field of asteroseismology of early-type stars. Obviously, the OPC members judged that the scientific rationale of our proposals is important. We would like to thank both ESO and the Geneva Observatory for the generous awarding of telescope time to our long-term project.

We realise that the spectroscopic study of pulsating stars, one of the main subjects of our work in astronomy during the past 10 years, would not have been possible without an instrument like the CAT/CES. This combination of telescope and spectrograph was a cornerstone for the observational research performed at our institute, and several other astronomers, who now occupy key positions in important astronomical institutes, also made largely use of the CAT to develop their careers.

References

Aerts, C., 1994, Mode identification in pulsating stars, In IAU Symposium 162: Pulsation, Rotation and Mass Loss in Early-Type Stars, eds. L.A. Balona, H.F. Henrichs & J.M. LeContel, Kluwer Academic Publishers, 75.

Aerts, C., De Cat, P., Peeters, E., et al., 1999, Selection of a sample of bright southern Slowly Pulsating B stars for long-term photometric and spectroscopic monitoring, *A&A* **343**, 872.

Aerts, C., De Cat, P., Waelkens, 1998a, Slowly Pulsating B Stars – New Insights from Hipparcos, In *IAU S185*: New eyes to see inside the Sun and stars, eds. F. L. Deubner, J. Christensen-Dalsgaard, D. Kurtz, Kluwer Academic Publishers, 295.

Aerts, C., De Mey, K., De Cat, P., Waelkens, C., 1998b, Pulsations in early-type binaries, In *A Half Century of Stellar Pulsation Interpretations*, eds. P.A. Bradley & J.A. Guzik, A.S.P. Conference Series, Vol. **135**, 380.

Baade, D., 1998, Pulsations of OB-stars: new observations, In *IAU S185*: New eyes to see inside the Sun and stars, eds. F.L. Deubner, J. Christensen-Dalsgaard, D. Kurtz, Kluwer Academic Publishers, 347.

Dziembowski, W.A., Pamyatnykh, A.A., 1993, The opacity mechanism in B-type stars. I – Unstable modes in β Cephei star models, *MNRAS* **262**, 204.

Dziembowski, W.A., Jerzykiewicz, M., 1996, Asteroseismology of the β Cephei stars. I. 16 (EN) Lacertae, *A&A* **306**, 436.

Dziembowski, W.A., Jerzykiewicz, M., 1999, Asteroseismology of the β Cephei stars. II. 12 (DD) Lacertae, *A&A* **341**, 480.

Lomb, N.R., Shobbrook, R.R., 1975, New radial velocities and further photometric observations of λ Sco and κ Sco, *MNRAS* **173**, 709.

Mathias, P., Aerts, C., 1996, A spectroscopic analysis of the δ Scuti star 20 CVn, *A&A* **312**, 905.

Waelkens, C., 1987, Rotation and pulsation-mode-selection in B-type stars, In Stellar Pulsation, eds. A.N. Cox, W.M. Sparks, S.G. Starrfield, Springer-Verlag, 75.

Waelkens, C., Aerts, C., Kestens, E., et al., 1998, *A&A* **330**, 215.

Winget, D.E., Nather, R.E., Clemens, J.C., et al. ,1991, Asteroseismology of the DOV star PG1159–035 with the Whole Earth Telescope, *ApJ* **378**, 326.

A Procedure for Deriving Accurate Linear Polarimetric Measurements[1]

*H. LAMY and D. HUTSEMÉKERS**

Institut d'Astrophysique, Université de Liège, Belgium; e-mail: lamy@astro.ulg.ac.be, hutsemek@astro.ulg.ac.be

We present here a procedure written within the ESO MIDAS reduction package with the aim of deriving semi-automatically linear polarisation data from CCD images obtained with beam-splitters such as those available at the ESO 3.6-m telescope equipped with EFOSC2 or at the VLT equipped with FORS1. This method is adequate for point-like objects and was used for measuring quasar polarisation (cf. Hutsemékers et al. 1998). We also report on the detection of a significant image deformation effect, most probably due to the recent addition to EFOSC2 of a rotatable half-wave plate.

Polarimetry with EFOSC2

With EFOSC2, polarimetry is performed by inserting in the parallel beam a Wollaston prism which splits the incoming light rays into two orthogonally po-larised beams separated by a small angle (typically 20″). Every object in the field has therefore two images on the CCD detector (see Figure 1). In order to avoid any overlapping of different images and to reduce the sky contribution, an aperture mask is put at the focal plane of the telescope. The normalised Stokes parameters (NSPs), q and u, fully describing the linear polarisation, are then computed from the fluxes measured in the two orthogonally polarised images. Two frames with the Wollaston prism rotated by 45° are necessary to determine the NSPs. Additional frames may be considered although the quasi-perfect transmission of the Wollaston generally makes two orientations sufficient (Serkowski 1974; di Serego Alighieri 1989). Usually the orientations at 270° and 225° are taken and

$$q = \frac{I^{\rm u}_{270} - I^{\rm l}_{270}}{I^{\rm u}_{270} + I^{\rm l}_{270}}, \quad u = \frac{I^{\rm u}_{225} - I^{\rm l}_{225}}{I^{\rm u}_{225} + I^{\rm l}_{225}}, \qquad (1)$$

[1] See note on page 31.

*Chercheur Qualifié au Fonds National de la Recherche Scientifique (Belgium).

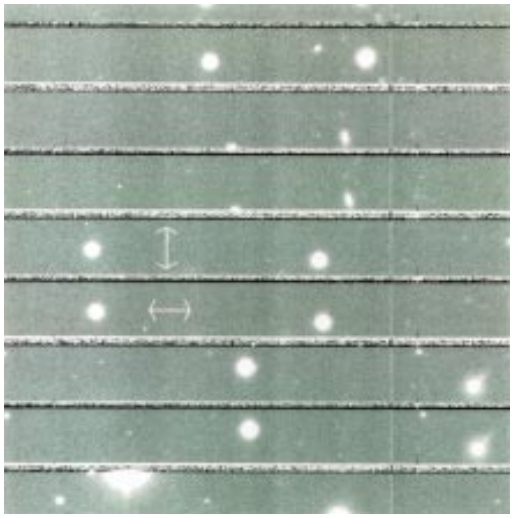


Figure 1: Example of a CCD frame obtained with EFOSC2, a Wollaston prism in the grism wheel and a mask at the focal plane of the telescope. Every object in the field has two orthogonally polarised images separated by ~ 20″ and called upper and lower images in the text. The arrows illustrate the direction of the polarisation of the two images. The y-axis is defined along the columns of the CCD, which is roughly the direction of the splitting. The detector was the Loral/Lesser CCD #40 with a pixel size of 0.160″ on the sky. The target was the quasar M08.02, observed on April 27, 1998 in the V filter with an exposure time of 300 s. It has a degree of polarisation $p \simeq 1.4\%$.

where $I^{\rm u}_{\alpha}$ and $I^{\rm l}_{\alpha}$ respectively represent the integrated fluxes from the upper and the lower images of the object produced by the Wollaston prism set at a position angle α. The associated errors, σ_q and σ_u, are calculated by computing the errors from the read-out noise and the photon noise in the object and the sky background and then by propagating these errors in Eq.1. The degree of polarisation is given by $p = \sqrt{q^2+u^2}$ and the polarisation position angle by $\theta = 1/2 * \arctan(u/q)$. The angles are measured relative to the instrument reference frame such that the observation of at least one polarimetric standard star is required for determining the polarisation position angle zero point.

Within this observing mode, the whole instrument has to be rotated, which means significant time-loss mainly due to re-pointing the objects. The insertion of a rotating half-wave plate (HWP) as the first optical element in the parallel beam significantly fastens the procedure by keeping EFOSC fixed (Schwartz & Guisard, 1995). Usually, four frames with the HWP orientated at 0°, 22.5°, 45° and 67.5° are taken and the NSPs are derived using the following formulae (e.g. di Serego Alighieri 1998):

$$q = \frac{R_q - 1}{R_q + 1} \text{ where } R_q = \frac{I^{\rm u}_0 / I^{\rm l}_0}{I^{\rm u}_{45} / I^{\rm l}_{45}}, \quad (2)$$

$$u = \frac{R_u - 1}{R_u + 1} \text{ where } R_u = \frac{I^{\rm u}_{22.5} / I^{\rm l}_{22.5}}{I^{\rm u}_{67.5} / I^{\rm l}_{67.5}},$$

$I^{\rm u}_{\beta}$ and $I^{\rm l}_{\beta}$ respectively denoting the integrated fluxes from the upper and the lower images of the object produced by the Wollaston prism. β is the position angle of the HWP. The polarisation degree, the polarisation position angle and the associated errors are calculated as above. In principle each NSP may also be evaluated from a single frame using Eq.1 such that, if we call q_0 (resp. q_{45}) the NSP calculated from the fluxes measured on the frame obtained with the HWP set at position angle 0° (resp. 45°), we should have $q_0 \simeq -q_{45}$.

Since the polarisation observed in extragalactic objects is usually ~ 1%, a careful subtraction of the sky background and an accurate determination of the object intensities $I^{\rm u}$ and $I^{\rm l}$ are essential to achieve a good estimate of the NSPs. In the next section we describe a MIDAS procedure written with the aim of optimising these two constraints.

The Reduction Procedure

In order to accurately measure $I^{\rm u}$ and $I^{\rm l}$, the first step is to subtract locally the sky background. Since the latter is usually polarised, this must be done independently for each orthogonally polarised image. For that purpose, two strips centered on the object are first extracted. Then the local sky is evaluated by fitting a bi-dimensional polynome to values of the background measured in small boxboxes free of cosmic rays and faint objects. The best results were obtained with polynomes of degree one. The small boxes are chosen in the upper and in the lower strips at exactly the same locations with respect to the object, taking into account a possible misalignment between the direction of the image splitting and the columns of the CCD.

Secondly, we noted after several trials that the usual standard aperture photometric methods available in MIDAS are not accurate enough for polarimetry: these procedures generally measure the total flux inside a given circle, taking entirely into account those pixels which are only partially contained in the circle. This is particularly problematic when the pixel size is large. Instead, we determine the center and the width of the object image at subpixel precision by fitting a bi-dimensional gaussian profile. Then, by means of a FORTRAN code, we integrate the flux in a circle of same center and arbitrary radius, taking into account only those fractions of pixels inside the circle. This was achieved on the basis of simple geometrical considerations. The NSPs may then be evaluated for any reasonable value of the aperture radius, expressed in units of the mean gaussian width $\sigma = (2\ln 2)^{-1/2}$FWHM/2, which is assumed to be identical for both the upper and lower images of the object. In order to take as much flux as possible without too much sky background, we adopt the radius $R/\sigma = 2.5$ which generally fulfils these requirements. Typical results obtained with the Wollaston prism only (i.e. without a HWP) indicate that, within the error bars, the measured NSPs are very stable against aperture radius variation, therefore giving confidence in the method.

With the aim of providing a semi-automatic and easy-to-use tool for extracting polarimetric data, two procedures have been implemented in MIDAS. The first one measures the intensities of the object and that of the background for any desired value of the aperture radius.

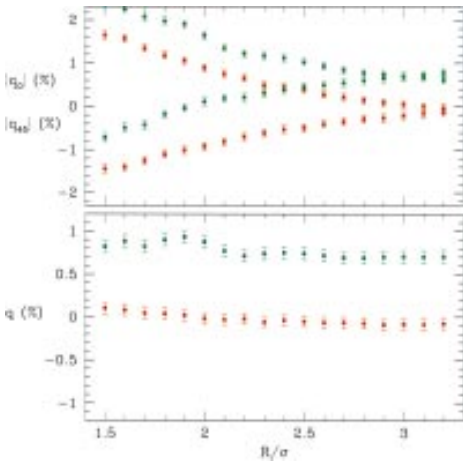


Figure 2: Upper panel: The normalised Stokes parameters, q_0 and q_{45}, are represented in absolute values as a function of the aperture radius expressed in units of the gaussian width of the image, for a polarised and an unpolarised quasar. These data were obtained on April 27–28, 1998 with EFOSC2 equipped with a 20″ Wollaston prism and a Half-Wave Plate set at 0° and 45°. The quasars were observed in the V filter with a typical exposure time of 300s for a given orientation. The pixel size was 0.130″ on the sky. Lower panel: The normalised Stokes parameter, q, computed according to Eq. 2 (see text). q is essentially stable against radius variation indicating that the effect described in the text is corrected.

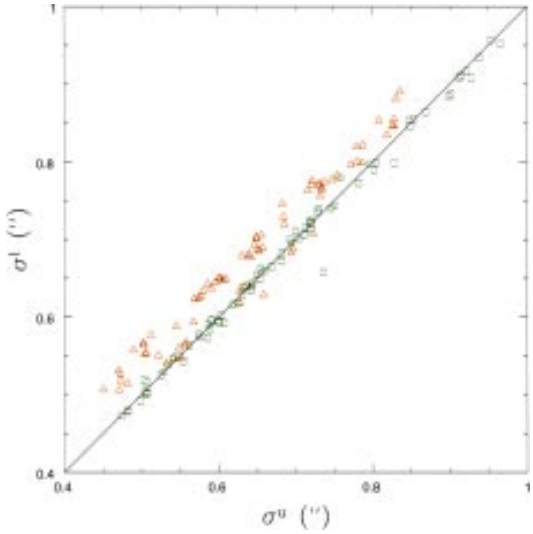


Figure 3: The gaussian widths of the lower images, σ^l, are represented as a function of the widths of the upper ones, σ^u, for all quasars observed during the nights 27–28 April 1998. Note that four HWP orientations have been obtained for each object and are presented here. The green squares represent σ_x and the red triangles σ_y. Most of the objects show an elongation along the direction of the Wollaston splitting (y-axis). The gaussian widths are expressed in arcsecond. The lack of corresponding red triangles in the right top corner corresponds to the second image deformation described in the text, affecting objects with wider profiles only.

The second one combines these measurements to provide the NSPs, the errors, the degree of polarisation and the polarisation position angle as a function of the aperture radius. The procedures can be made available as such to anyone interested.

Image Deformations and Their Effect on the Measurements

While the dependence of the NSPs against radius variation is quite flat when using the Wollaston without HWP, a different behaviour is found when adding the HWP. As previously stated, q_0 and q_{45} should be identical in absolute value apart from a small difference due to instrumental polarisation. However, it appears that $|q_0|$ and $|q_{45}|$ measured for a given aperture radius significantly differ. This is illustrated in the upper panel of Figure 2: for small radii, $|q_0|$ and $|q_{45}|$ appear quite different (sometimes ≥ 1%), while they finally tend towards the same value as the radius increases. For $R/\sigma \geq 3$, they are equal within the error bars. The two curves have nearly symmetrical shapes with respect to the expected behaviour (i.e. a flat curve with $|q_0|$ and $|q_{45}|$ identical). This effect is detected for polarised and unpolarised objects.

By fitting a bi-dimensional gaussian profile to the object, we have measured the widths σ_x and σ_y of the upper and lower orthogonally polarised images of the object. Figure 3 represents σ^l_x (resp σ^l_y), measured from the lower image, as a function of σ^u_x (resp σ^u_y), measured from the upper image, for every CCD frame obtained during the nights April 27–29, 1998. It appears clearly that the lower images are systematically more elongated along the y-axis than the upper images, while their widths are nearly identical along the x-axis direction. The mean difference between σ^l_y and σ^u_y is ~ 0.08″. This difference is more or less constant whatever the mean width of the gaussian profile. It is also independent of the HWP position angle. As a consequence, for a given aperture radius, we measure less flux in the upper images than in the lower ones. Therefore, for small radii, $|q_0|$ appear larger and $|q_{45}|$ smaller than the actual values. As the aperture radius increases, the total flux of the lower image is progressively taken into account and this effect vanishes, $|q_0|$ and $|q_{45}|$ tending towards the same value, in agreement with the behaviour seen in Figure 2. Note that there are a few frames on which the object images have $\sigma^u_y \sim \sigma^l_y$ which precisely corresponds to those cases where the $|q_0|$and $|q_{45}|$ curves are more similar.

Fortunately, due to the fact that the image deformations are independent of the HWP orientation, this effect is well corrected when determining a given NSP by combining the intensities from two frames according to Eq. 2. This is illustrated in the lower panel of Figure 2 which shows the expected flat curves. We may therefore conclude that two frames with the HWP set at angles separated by 45° are necessary to accurately evaluate one of the NSPs. If only a single frame is obtained, the NSP has to be measured with a radius large enough to minimise the effect. In this latter case, the radius $R/\sigma = 3$ is generally sufficient and the additional noise due to the background not too large. Note that, in fact, none of the two orthogonally polarised images is actually circular, as illustrated in Figure 4. But only the image deformations differentially affecting the upper and lower images have an effect on the NSPs measurements. It is important to emphasise that these effects were not visible on frames obtained previously with the Wollaston prism only, suggesting that the HWP is most probably responsible for the observed image deformations.

The image deformations described here appear much more complex than the expected behaviour due to the Wollaston chromatism only (e.g. di Serego Alighieri et al. 1989). Such an effect is important to further investigate and understand since it may affect imaging polarimetry with high spatial resolution instruments as will be available on the VLT.

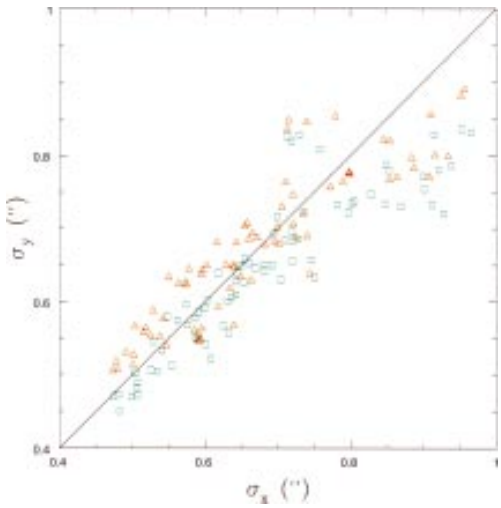


Figure 4: The gaussian width σ_y is represented as a function of σ_x for the upper (green squares) and the lower (red triangles) object images considering the same data as in Figure 3. The gaussian widths are expressed in arcseconds. The general trend is that upper images have $\sigma^u_x > \sigma^u_y$ while the lower images have $\sigma^l_x < \sigma^l_y$. For images with larger profiles, both images flatten ($\sigma_x > \sigma_y$), the difference being roughly constant.

Acknowledgements

This research is supported in part by contract ARC94/99-178 and by contract PAI P4/05. We also thank Marc Remy for providing us with the FORTRAN code.

References

di Serego Alighieri S. 1989, In:Grosbøl P.J. et al (eds.) 1st ESO/ST-ECF, Data Analysis Workshop, 157.

di Serego Alighieri S. 1998, in *Instrumentation for Large Telescopes*, Ed. J.M. Rodriguez Espinosa, Cambridge University Press, 287.

Hutsemékers D., Lamy H. & Remy M. 1998, *A&A* **340**, 371.

Schwarz H., Guisard D. 1995, *The Messenger* **81**, 9.

Serkowski K., 1974, in Methods of Experimental Physics, vol. 12, part A, eds. M.L. Meeks & N.P. Carleton (New York: Academic Press), 361

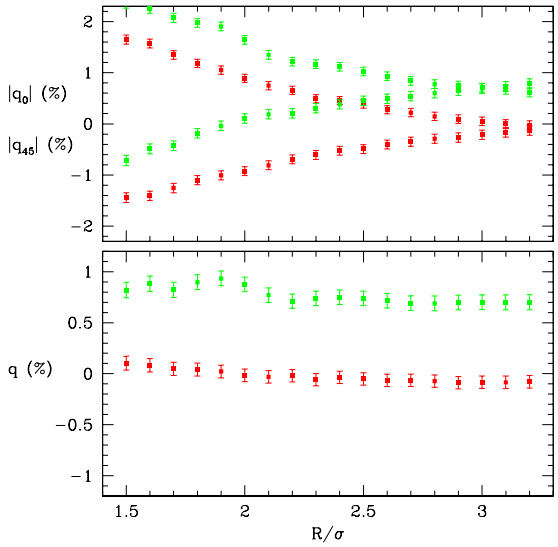
Erratum

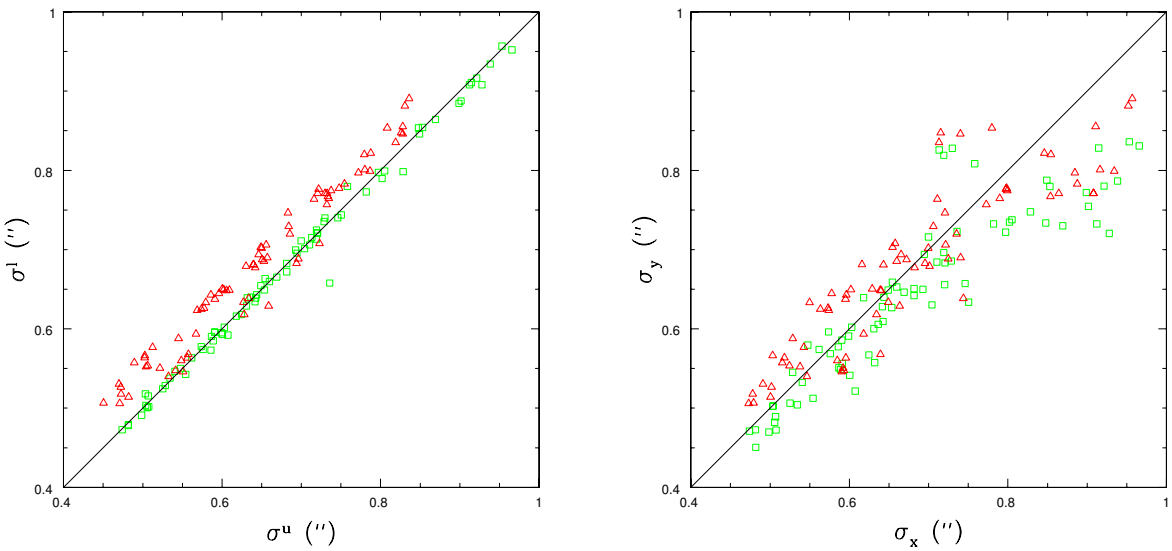
In the June issue of *The Messenger* (No. 96), page 26 (article by H. Lamy and D. Hutsemékers), formula 2 should read:

$$q = \frac{R_q - 1}{R_q + 1} \text{ where } R_q^2 = \frac{I_0^{\mathrm{u}} / I_0^{\mathrm{l}}}{I_{45}^{\mathrm{u}} / I_{45}^{\mathrm{l}}}, \quad (2)$$

$$u = \frac{R_u - 1}{R_u + 1} \text{ where } R_u^2 = \frac{I_{22.5}^{\mathrm{u}} / I_{22.5}^{\mathrm{l}}}{I_{67.5}^{\mathrm{u}} / I_{67.5}^{\mathrm{l}}},$$

Addendum





The original figures 2, 3 and 4. For captions, see text.

Article 11

Optical polarization of 47 quasi-stellar objects : the data

H. Lamy, D. Hutsemékers : Astron. Astrophys. Suppl. 142, 451 (2000)

Dans cet article, nous présentons des mesures de la polarisation linéaire de 47 quasars dont 27 quasars de type BAL. Les procédures d'observation et de réduction des données sont décrites en détail. Une attention particulière est portée à la discussion des contaminations possibles –instrumentales et/ou interstellaire– sur base notamment de la mesure simultanée de la polarisation d'étoiles du champ.

ASTRONOMY & ASTROPHYSICS
SUPPLEMENT SERIES

Astron. Astrophys. Suppl. Ser. **142**, 451–456 (2000)

Optical polarization of 47 quasi-stellar objects: The data⋆,⋆⋆

H. Lamy and D. Hutsemékers⋆⋆⋆

Institut d'Astrophysique, Université de Liège, 5 Av. de Cointe, B-4000 Liège, Belgium

Received October 18, 1999; accepted January 3, 2000

Abstract. New broad-band linear polarization measurements are presented for a sample of 47 QSOs which includes 27 broad absorption line QSOs and 2 gravitational lens candidates.

Key words: quasars: general — quasars: absorption lines — gravitational lensing — polarization

1. Introduction

Since the systematic surveys of Moore & Stockman (1981, 1984), the optical linear polarization has been recognized as an important quantity for understanding the nature of quasi-stellar objects (QSOs), namely due to the fact that polarization is an indicator of departures from spherical symmetry. This is particularly true for the broad absorption line (BAL) QSOs which appear systematically more polarized than other radio-quiet QSOs.

The new data presented here have been obtained to complement our recent study of BAL QSO polarization (Hutsemékers et al. 1998), as well as to further investigate the discovery of large-scale coherent orientations in the distribution of quasar polarization vectors (Hutsemékers 1998). While the results of these investigations will be published elsewhere (Hutsemékers & Lamy, in preparation), the present paper provides the full set of new polarimetric data, with details on the observations, the data reduction, and the measurements.

2. The observations

The polarimetric observations were carried out during several runs at the European Southern Observatory (ESO La Silla, Chile) from 1996 to 1999, using the 3.6 m telescope equipped with the EFOSC camera and spectrograph. In 1996, the instrument was EFOSC1 and the detector a 512×512 TeK CCD (ESO#26) with a pixel size of 27 μm corresponding to $0\farcs605$ on the sky (Melnick et al. 1989). Later, EFOSC1 was replaced by EFOSC2, and the detector was a 2048×2048 Loral/Lesser CCD (ESO#40) with a pixel size of 15 μm corresponding to $0\farcs157$ on the sky (Patat 1999). The latter CCD was used in a 2×2 binning mode, except in October 98.

With EFOSC, polarimetry is performed by inserting in the parallel beam a Wollaston prism which splits the incoming light rays into two orthogonally polarized beams. Each object in the field has therefore two images on the CCD detector, separated by $10''$ or $20''$ (depending on the Wollaston), and orthogonally polarized. To avoid image overlapping, one puts at the telescope focal plane a special mask made of alternating transparent and opaque parallel strips whose width corresponds to the splitting. The object is positioned at the centre of a transparent strip which is imaged on a region of the CCD chosen as clean as possible. The final CCD image then consists of alternate orthogonally polarized strips of the sky, two of them containing the polarized images of the object itself (di Serego Alighieri 1989, 1998; Lamy & Hutsemékers 1999). Note that the polarization measurements do not depend on variable transparency or seeing since the two orthogonally polarized images of the object are simultaneously recorded. The $20''$ Wollaston was used during the September 96, April 98, and September 99 observing runs, while the $10''$ Wollaston was used in October 98 and April 99.

In order to derive linear polarization measurements, i.e. the two normalized Stokes parameters q and u, frames must be obtained with at least two different orientations of the Wollaston. With EFOSC1, this was done by rotating the whole instrument by 45° (usually at the adapter angles 270° and 225°) such that, for each object, two frames were secured (Melnick et al. 1989). The excellent transmission of the Wollaston makes these two

⋆ Tables 3 and 4 are also available in electronic form at the CDS via anonymous ftp to cdsarc.u-strasbg.fr (130.79.128.5) or via http://cdsweb.u-strasbg.fr/Abstract.html

⋆⋆ Based on observations collected at the European Southern Observatory (ESO, La Silla).

⋆⋆⋆ Also, Chercheur Qualifié au Fonds National de la Recherche Scientifique (FNRS, Belgium).

orientations sufficient (di Serego Alighieri 1989). With EFOSC2, a half-wave plate (HWP) is inserted in the optical path and four frames with the HWP at position angles 0°, 22.5°, 45°, and 67.5° were obtained, without the need of rotating the whole instrument (Schwarz & Guisard 1995).

Most observations were done with the Bessel V filter. A few additional ones were obtained with the Gunn i filter. Typical exposure times are around 5 minutes per frame. Seeing was around $1''.2$ except in September 99 ($\sim 5''$). In addition, polarimetric calibration stars were observed in the same filters in order to unambiguously fix the zero-point of the polarization position angle and to check the whole observing and reduction process. The observed standard stars are given in Table 1.

Table 1. Polarized calibration stars

Date	Object	Ref
11-09-96	HD 161291	1
27-04-98	HD 111579, HD 155197, HD 298383	2,3
28-04-98	HD 155197	2,3
18-10-98	HD 298383	2
13-04-99	HD 164740, HD 126593, HD 161291, HD 298383	1,2
14-04-99	HD 111579, HD 126593, HD 161291, HD 298383	1,2
07-09-99	HD 283812	2,4

References: (1): Schwarz 1987; (2) Turnshek et al. 1990; (3) Schmidt et al. 1992; (4) Whittet et al. 1992.

Table 2. Residual instrumental polarization

Date	$\overline{q}_\star$ (%)	$\overline{u}_\star$ (%)	$\overline{\sigma}_\star$ (%)	$n_\star$
04/98	−0.07	+0.01	0.17	15
04/99	+0.00	+0.19	0.17	16

3. Data reduction

Considering first the two frames obtained with the EFOSC1 rotated at 270° and 225°, the normalized Stokes parameters q and u are given by

$$q = \frac{I^{\rm u}_{270} - I^{\rm l}_{270}}{I^{\rm u}_{270} + I^{\rm l}_{270}} \quad \text{and} \quad u = \frac{I^{\rm u}_{225} - I^{\rm l}_{225}}{I^{\rm u}_{225} + I^{\rm l}_{225}}, \tag{1}$$

where $I^{\rm u}$ and $I^{\rm l}$ respectively refer to the intensities integrated over the upper and lower orthogonally polarized images of the object.

When the four frames with the HWP oriented at 0°, 22.5°, 45° and 67.5° are considered, the normalized Stokes parameters are derived using the following formulae:

$$\begin{aligned} q &= \frac{R_q - 1}{R_q + 1} \quad \text{where} \quad R_q^2 = \frac{I^{\rm u}_0 / I^{\rm l}_0}{I^{\rm u}_{45} / I^{\rm l}_{45}}, \\ u &= \frac{R_u - 1}{R_u + 1} \quad \text{where} \quad R_u^2 = \frac{I^{\rm u}_{22.5} / I^{\rm l}_{22.5}}{I^{\rm u}_{67.5} / I^{\rm l}_{67.5}}, \end{aligned} \tag{2}$$

$I^{\rm u}_\beta$ and $I^{\rm l}_\beta$ respectively denoting the intensities integrated over the upper and the lower images of the object, β representing the position angle of the HWP. This combination of four frames obtained with different HWP orientations not only removes most of the instrumental polarization (di Serego Alighieri 1998[1]), but is essential for correcting the effects of image distortions introduced by the HWP (Lamy & Hutsemékers 1999). Note that q and u are measured with respect to the instrumental reference frame.

It is clear from these relations that intensities must be determined with the highest accuracy. For this, the data were first corrected for bias and dark emission, and flat-fielded. A plane was locally fitted to the sky around each object image, and subtracted from each image individually. Since it appeared that standard aperture photometry was not accurate enough, we have measured the object center at subpixel precision by fitting a 2D Gaussian profile and integrated the flux in a circle of same center and arbitrary radius by taking into account only those fractions of pixels inside the circle. With this method, the Stokes parameters may be computed for any reasonable radius of the aperture circle. They were found to be stable against radius variation, giving confidence in the method even when the object images are distorted (Lamy & Hutsemékers 1999). In order to take as much flux as possible with not too much sky background, we fixed the aperture radius at $\alpha \times [(2 \ln 2)^{-1/2}$ HWHM], where $\alpha = 2.5$ with EFOSC1 and $\alpha = 3.0$ with EFOSC2 to account for the image elongation introduced by the HWP. HWHM represents the mean half-width at half-maximum of the Gaussian profile. Note that in the few cases where the objects are resolved into multiple components, we use the smallest rectangular aperture encompassing all the components. The whole procedure has been implemented within the ESO MIDAS reduction package.

First applied to the calibration stars, the method provides polarization degrees in excellent agreement with the published values. During some nights more than one star has been observed (Table 1) in order to check the stability and the reliability of the zero-point offset of the polarization position angle. For all stars observed during a given night, the values of the angle offset do agree within 1°, which is quite small given the fact that the EFOSC2 HWP is not achromatic.

The normalized Stokes parameters q and u were then computed for the QSO sample, and modified according to the zero-point offset determined for each night independently. The uncertainties σ_q and σ_u are evaluated by

[1] We confirm the low intrumental polarization measured by di Serego Alighieri (1998). Indeed, on 27 April 1998, we have observed an unpolarized standard star (HD 154892, from Turnshek et al. 1990) for which we measured $p_{\rm V} = 0.06 \pm 0.02\,\%$, using Eq. (2).

Table 3. Polarimetric measurements

Object	z	Date	Filter	q (%)	u (%)	σ (%)	$q_\star$ (%)	$u_\star$ (%)	$\sigma_\star$ (%)
B0059−2735*	1.59	11-09-96	V	1.38	−0.45	0.15	-	-	-
B0059−2735*	1.59	11-09-96	i	2.06	−1.14	0.17	-	-	-
B0846+1540*	2.91	14-04-99	V	0.43	−0.48	0.12	-	-	-
B0856+1714*	2.32	14-04-99	V	0.70	0.20	0.17	0.10	0.13	0.03
B1009+0222*	1.35	13-04-99	V	0.06	−0.58	0.08	0.07	0.26	0.07
J 1053−0058*	1.55	13-04-99	V	−1.90	0.16	0.08	-	-	-
J 1104−0004*	1.35	13-04-99	V	0.49	0.14	0.13	0.16	−0.02	0.05
J 1141−0141*	1.27	13-04-99	V	−0.10	0.56	0.16	0.14	0.01	0.08
B1151+1145	0.18	28-04-98	V	−0.74	−0.24	0.06	−0.14	−0.24	0.04
B1157−2354*	2.10	27-04-98	V	−1.38	−0.24	0.04	0.00	0.04	0.04
B1157−2354*	2.10	14-04-99	V	−1.33	−0.38	0.05	−0.03	0.18	0.05
B1157+0128	1.99	13-04-99	V	0.16	0.93	0.07	0.21	−0.09	0.10
B1158+0045	1.38	13-04-99	V	−0.37	0.42	0.10	−0.16	0.10	0.04
B1203+1530*	1.63	13-04-99	V	0.75	1.54	0.10	0.18	−0.02	0.17
B1205+1436*	1.64	27-04-98	V	0.58	−0.51	0.07	-	-	-
B1210+1942	1.24	13-04-99	V	−0.29	0.34	0.08	−0.19	0.35	0.11
B1215+1244*	2.08	28-04-98	V	0.45	0.35	0.17	-	-	-
B1216+1103*	1.62	27-04-98	V	−0.41	0.48	0.09	−0.85	0.09	0.24
B1219+1244*	1.31	27-04-98	V	0.29	−0.57	0.10	−0.32	−0.24	0.11
B1222+1437	1.55	27-04-98	V	−0.22	0.19	0.06	−0.08	−0.04	0.05
J 1225−0150*	2.04	14-04-99	V	−0.43	−0.48	0.14	−0.12	0.27	0.05
B1228+1216*	1.41	27-04-98	V	−0.04	−0.11	0.06	0.21	0.48	0.22
B1230+1705*	1.42	27-04-98	V	−0.35	−0.10	0.09	−0.09	0.24	0.06
B1230−2347	1.84	28-04-98	V	−0.11	0.04	0.08	-	-	-
B1234−0209	1.62	27-04-98	V	−0.51	0.32	0.07	−0.30	0.33	0.10
B1235−1813	2.19	13-04-99	V	0.97	−0.14	0.05	-	-	-
B1235+1807*	0.45	14-04-99	V	0.05	0.29	0.17	0.17	0.42	0.03
B1238−0944	2.09	28-04-98	V	−0.24	0.07	0.06	-	-	-
B1239+0955*	2.01	27-04-98	V	0.58	−0.49	0.06	0.03	−0.12	0.03
B1239+1435	1.95	28-04-98	V	0.06	0.13	0.10	0.21	0.58	0.20
B1242+0006	2.08	28-04-98	V	−0.15	0.21	0.08	−0.10	0.05	0.07
J 1252+0053*	1.69	14-04-99	V	−0.02	−0.02	0.06	-	-	-
B1256−1734	2.06	27-04-98	V	−0.78	0.58	0.08	0.28	0.23	0.08
B1258−1627	1.71	28-04-98	V	−0.13	−0.52	0.07	−0.13	−0.05	0.04
B1305+0011	2.11	27-04-98	V	0.30	−0.58	0.14	0.05	0.33	0.06
B1333+2840*	1.91	13-04-99	V	4.66	−3.39	0.11	−0.15	0.31	0.24
B1334+2614*	1.88	13-04-99	V	−0.14	0.01	0.08	-	-	-
B1416−1256	0.13	28-04-98	V	−0.21	0.35	0.08	−0.49	0.54	0.07
B1429−0053	2.08	13-04-99	V	0.29	0.37	0.09	−0.36	0.16	0.06
B1429−0036*	1.18	14-04-99	V	−0.06	0.15	0.10	-	-	-
B1443+0141*	2.45	13-04-99	V	1.00	−0.68	0.15	−0.60	−0.13	0.10
B1451−3735	0.31	14-04-99	V	0.11	−0.05	0.05	−0.23	0.16	0.06
B1500+0824	3.94	14-04-99	V	−1.09	−0.19	0.28	−0.26	0.16	0.12
B2118−4303*	2.20	28-04-98	V	−0.11	−0.65	0.11	-	-	-
B2149−2745*	2.03	18-10-98	V	−0.13	0.07	0.10	0.00	0.25	0.15
B2226−3905	1.13	07-09-99	V	−0.13	0.16	0.09	-	-	-
B2240−3702*	1.83	11-09-96	V	1.16	1.75	0.08	-	-	-
B2240−3702*	1.83	11-09-96	i	1.33	0.73	0.10	-	-	-
B2329−3828	1.19	07-09-99	V	−0.12	−0.42	0.08	-	-	-
B2341−2333*	2.82	18-10-98	V	−0.28	−0.58	0.11	−0.03	0.39	0.13

Table 4. Final polarimetric data

Object	q (%)	u (%)	p (%)	σ_p (%)	p_0 (%)	$p_{\rm ISM}$ (%)	θ (°)	σ_θ (°)
B0059−2735*	1.38	−0.45	1.45	0.23	1.43	0.16	171	5
B0059−2735*	2.06	−1.14	2.35	0.24	2.34	0.16	166	3
B0846+1540*	0.43	−0.67	0.80	0.21	0.77	0.17	151	8
B0856+1714*	0.70	0.01	0.70	0.24	0.66	0.09	0	10
B1009+0222*	0.06	−0.77	0.77	0.19	0.75	0.06	137	7
J 1053−0058*	−1.90	−0.03	1.90	0.19	1.89	0.17	90	3
J 1104−0004*	0.49	−0.05	0.49	0.21	0.45	0.12	177	13
J 1141−0141*	−0.10	0.37	0.38	0.23	0.32	0.06	53	21
B1151+1145	−0.67	−0.25	0.72	0.18	0.70	0.01	100	7
B1157−2354*	−1.31	−0.25	1.33	0.17	1.32	0.44	95	4
B1157−2354*	−1.33	−0.57	1.45	0.18	1.44	0.44	102	4
B1157+0128	0.16	0.74	0.76	0.18	0.74	0.01	39	7
B1158+0045	−0.37	0.23	0.44	0.20	0.40	0.01	74	14
B1203+1530*	0.75	1.35	1.54	0.20	1.53	0.22	30	4
B1205+1436*	0.65	−0.52	0.83	0.18	0.81	0.03	161	6
B1210+1942	−0.29	0.15	0.33	0.19	0.28	0.10	76	19
B1215+1244*	0.52	0.34	0.62	0.24	0.58	0.06	17	12
B1216+1103*	−0.34	0.47	0.58	0.19	0.55	0.02	63	10
B1219+1244*	0.36	−0.58	0.68	0.20	0.65	0.02	151	9
B1222+1437	−0.15	0.18	0.23	0.18	0.17	0.19	65	30
J 1225−0150*	−0.43	−0.67	0.80	0.22	0.77	0.10	119	8
B1228+1216*	0.03	−0.12	0.12	0.18	0.00	0.17	142	-
B1230+1705*	−0.28	−0.11	0.30	0.19	0.25	0.05	101	22
B1230−2347	−0.04	0.03	0.05	0.19	0.00	0.57	72	-
B1234−0209	−0.44	0.31	0.54	0.18	0.51	0.08	72	10
B1235−1813	0.97	−0.33	1.02	0.18	1.00	0.09	171	5
B1235+1807*	0.05	0.10	0.11	0.24	0.00	0.07	32	-
B1238−0944	−0.17	0.06	0.18	0.18	0.00	0.18	80	-
B1239+0955*	0.65	−0.50	0.82	0.18	0.80	0.00	161	6
B1239+1435	0.13	0.12	0.18	0.20	0.00	0.05	21	-
B1242+0006	−0.08	0.20	0.22	0.19	0.14	0.00	56	39
J 1252+0053*	−0.02	−0.21	0.21	0.18	0.14	0.00	132	37
B1256−1734	−0.71	0.57	0.91	0.19	0.89	0.27	71	6
B1258−1627	−0.06	−0.53	0.53	0.18	0.50	0.12	132	10
B1305+0011	0.37	−0.59	0.70	0.22	0.67	0.02	151	9
B1333+2840*	4.66	−3.58	5.88	0.20	5.88	0.03	161	1
B1334+2614*	−0.14	−0.18	0.23	0.19	0.16	0.03	116	34
B1416−1256	−0.14	0.34	0.37	0.19	0.33	0.56	56	16
B1429−0053	0.29	0.18	0.34	0.19	0.30	0.17	16	18
B1429−0036*	−0.06	−0.04	0.07	0.20	0.00	0.16	107	-
B1443+0141*	1.00	−0.87	1.33	0.23	1.31	0.27	159	5
B1451−3735	0.11	−0.24	0.26	0.18	0.21	0.56	147	25
B1500+0824	−1.09	−0.38	1.15	0.33	1.10	0.08	100	9
B2118−4303*	−0.04	−0.66	0.66	0.20	0.63	0.16	133	9
B2149−2745*	−0.13	0.07	0.15	0.20	0.00	0.14	76	-
B2226−3905	−0.13	0.16	0.21	0.19	0.12	0.00	65	45
B2240−3702*	1.16	1.75	2.10	0.19	2.09	0.00	28	3
B2240−3702*	1.33	0.73	1.52	0.20	1.51	0.00	14	4
B2329−3828	−0.12	−0.42	0.44	0.19	0.40	0.00	127	14
B2341−2333*	−0.28	−0.58	0.64	0.20	0.61	0.02	122	9

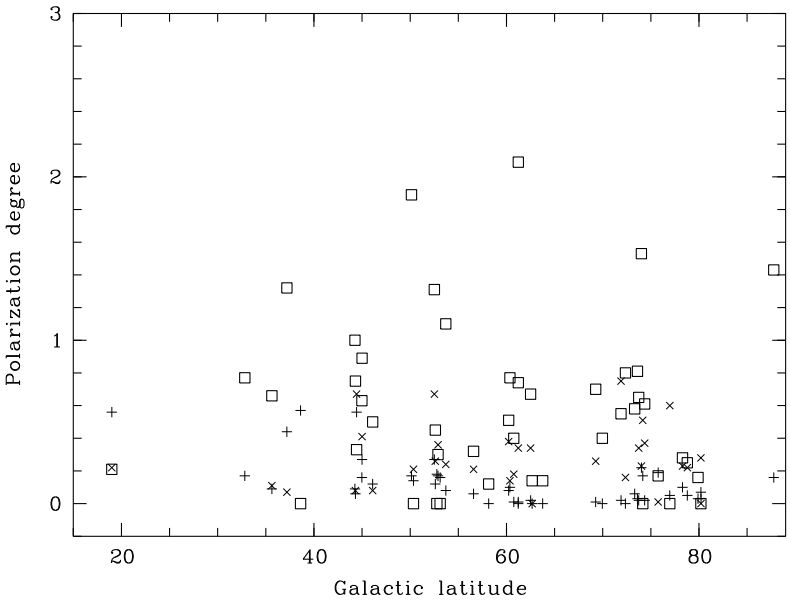


Fig. 1. The QSO polarization degree p_0 (in %) [□] is represented here as a function of the Galactic latitude of the objects ($|b_{II}|$, in degree), together with the de-biased polarization degree of field stars [×] (also corrected for the small systematic trend reported in Table 2), and the maximum interstellar polarization degree p_{ISM} derived from the Burstein & Heiles (1982) reddening maps [+]. Only B1333+2840 (p_0 = 5.9%) is not represented here

computing the errors on the intensities I^u and I^l, from the read-out noise and from the photon noise in the object and the sky background (after converting the counts in electrons), and then by propagating these errors in Eqs. (1) or (2). Uncertainties are typically around 0.1% for both q and u.

Since on most CCD frames field stars are simultaneously recorded, one can in principle use them to estimate the residual instrumental polarization, and to correct frame-by-frame the QSO Stokes parameters. However, the field stars (even when combined in a single "big" one per frame) are often fainter than the QSO, and a frame-by-frame correction introduces uncertainties on the QSO polarization larger than the instrumental polarization itself. We then computed the weighted average ($\overline{q}_\star$ and $\overline{u}_\star$) and dispersion ($\overline{\sigma}_\star$) of the normalized Stokes parameters of field stars considering the ($n_\star$) frames obtained during a given run. These values are given in Table 2 for the two runs with enough data. Note that possible contamination by interstellar polarization is included in the uncertainties. These values indicate that the residual instrumental polarization is small, as expected since most of the instrumental polarization is removed by the observing procedure. We nevertheless take it into account in a rather conservative way by subtracting the systematic $\overline{q}_\star$ and $\overline{u}_\star$ from the QSO q and u, and by adding quadratically the errors. For those objects observed in other runs, no systematic correction was applied; only the errors were similarly combined assuming, quite reasonably, that they are typical of the instrument.

4. The results

Table 3 lists the QSO position-name (B1950 or J2000), its redshift z, the date of observation (dd-mm-yy), the filter used, the QSO normalized Stokes parameters q and u, the uncertainty σ of the Stokes parameters[2], as well as the field star normalized Stokes parameters $q_\star$ and $u_\star$ and the associated uncertainty $\sigma_\star$. The normalized Stokes parameters are given in the equatorial reference frame. Objects marked with an asterisk are BAL QSOs (cf. Brotherton et al. 1998; Green et al. 1997; Korista et al. 1993; Schmidt & Hines 1999; Stocke et al. 1992; Hewitt & Burbidge 1993 and references therein).

The final values of the QSO normalized Stokes parameters q and u, corrected for the residual systematic instrumental polarization (cf. Table 2) are given in Table 4. Then, from these values, the polarization degree is evaluated with $p = (q^2 + u^2)^{1/2}$. The error on the polarization degree is estimated by $\sigma_p = (\sigma^2 + \overline{\sigma}_\star^2)^{1/2}$ taking into account the values of Table 2. Note that the complex statistical behavior of the polarization degree should be kept in mind (Serkowski 1962; Simmons & Stewart 1985). Indeed, since p is always a positive quantity, it is biased at low signal-to-noise ratio. A reasonably good estimator of the true polarization degree, noted p_0, is computed from p and σ_p using the Wardle & Kronberg (1974) method (Simmons & Stewart 1985). The polarization position angle θ is obtained by solving the equations $q = p\cos 2\theta$ and $u = p\sin 2\theta$, while the uncertainty of the polarization

[2] Note the u Stokes parameter of B1219+1244 may be more uncertain than reported due to a possible contamination of the object image in one of the four frames.

position angle θ is estimated from the standard Serkowski (1962) formula where p_0 is used instead of p to avoid biasing, i.e. $\sigma_\theta = 28\overset{\circ}{.}65\,\sigma_p/p_0$. All these quantities are given in Table 4. Note that due to the HWP chromatism over the V band, an additional error on $\theta \leq 2-3°$ should probably be accounted for (cf. the wavelength dependence of the polarization position angle offset in di Serego Alighieri 1998).

Since nearly all objects in the sample are at high galactic latitudes ($|b_{II}| > 30°$, except B1451 − 3735), the contamination by interstellar polarization in the Galaxy is expected to be small. This may be verified using the Burstein & Heiles (1982) reddening maps[3]. The maps provide $E(B-V)$ values from which the interstellar polarization is estimated with the relation $p_{ISM} \leq 8.3\%\ E(B-V)$ (Hiltner 1956). These upper limits on p_{ISM} are reported in Table 4. All but four are smaller than 0.3%, indicating a negligible contamination by the Galaxy. Polarization of faint field stars recorded on the CCD frames also provide an estimate of the interstellar polarization. The dispersion of their Stokes parameters (Table 2) indicates that actually both the instrumental and interstellar polarization are small. This is illustrated in Fig. 1, where the QSO polarization is compared to the field star polarization (interstellar + instrumental), and to the maximum interstellar polarization derived from the Burstein & Heiles maps. We may therefore safely conclude that virtually any QSO with $p_0 \geq 0.6\%$ is intrinsically polarized, in good agreement with our previous results (Hutsemékers et al. 1998), and with those of Berriman et al. (1990) obtained for low-polarization Palomar-Green QSOs. Note that several objects with $p_0 < 0.6\%$ have a polarization position angle similar to that of field stars, indicating that contamination is probably real at these low polarization levels (while no deviation from uniformity is found in the distribution of angle difference for objects with $p_0 \geq 0.6\%$).

For some QSOs of our sample (B0059 − 2735, B1157 − 2354, B1429 − 0053, B2240 − 3702), polarimetric measurements have been obtained at different epochs with the same filter and instrumentation (cf. Hutsemékers et al. 1998). The agreement is generally excellent, providing no evidence for polarization variability. Only the polarization degree of B1429 − 0053 is marginally different, possibly in relation with its suspected gravitationally lensed nature.

5. Conclusions

New broad-band linear polarization measurements have been obtained for a sample of 47 QSOs down to an accuracy of $\sim$ 0.2%. Most data are first-time measurements. The sample includes 27 BAL QSOs and 2 gravitational lens candidates (B1429 − 0053 and B2149 − 2745). With previous surveys by Hutsemékers et al. (1998) and Schmidt & Hines (1999), approximately 70 BAL QSOs have now measured polarization.

The present data show little contamination by interstellar polarization, and virtually any QSO with $p \geq 0.6\%$ is intrinsically polarized. Nine objects have $p \geq 1.0\%$, and one BAL QSO, B1333+2840, has $p = 5.9\%$. No polarization variability is detected, except, possibly, for the gravitational lens candidate B1429 − 0053.

Acknowledgements. It is a pleasure to thank Ingunn Burud for her participation in the September 99 observations, and Pierre Leisy for efficient support. This research is supported in part by contracts ARC 94/99-178 and PAI P4/05.

[3] The data files and routines were obtained from Schlegel 1998, via http://astro.berkeley.edu/davis/dust/data/bh/index.html

References

Berriman G., Schmidt G.D., West S.C., Stockman H.S., 1990, ApJS 74, 869
Brotherton M.S., van Breugel W., Smith R.J., et al., 1998, ApJ 505, L7
Burstein D., Heiles C., 1982, AJ 87, 1165 (BH)
di Serego Alighieri S., 1989, in 1st ESO/ST-ECF Data Analysis Workshop, Grosbøl P.J. et al. (eds.), p. 157
di Serego Alighieri S., 1998, in Instrumentation for Large Telescopes, Rodriguez Espinosa J.M. (ed.). Cambridge University Press, p. 287
Green P.J., Aldcroft T.L., Mathur S., Schartel N., 1997, ApJ 484, 135
Hewitt A., Burbidge G., 1993, ApJS 87, 451
Hiltner W.A., 1956, ApJS 2, 389
Hutsemékers D., 1998, A&A 332, 410
Hutsemékers D., Lamy H., Remy M., 1998, A&A 340, 371
Lamy H., Hutsemékers D., 1999, The Messenger 96, 25 (Erratum: The Messenger 97, 23)
Korista K.T., Voit G.M., Morris S.L., Weymann R.J., 1993, ApJS 88, 357
Melnick J., Dekker H., D'Odorico S., 1989, EFOSC, ESO operating manual No. 4, Version 2, ESO
Moore R.L., Stockman H.S., 1981, ApJ 243, 60
Moore R.L., Stockman H.S., 1984, ApJ 279, 465
Patat F., 1999, EFOSC2 user's manual, Version 1, ESO
Schmidt G.D., Elston R., Lupie O.L., 1992, AJ 104, 1563
Schmidt G.D., Hines D.C., 1999, ApJ 512, 125
Schwarz H.E., 1987, in Polarimetry with EFOSC, ESO Internal Memorandum Dec. 1987
Schwarz H.E., Guisard D., 1995, The Messenger 81, 9
Serkowski K., 1962, in Advances in Astron. and Astrophys., Kopal Z. (ed.). Academic Press 1, p. 289
Simmons J.F.L., Stewart B.G., 1985, A&A 142, 100
Stocke J.T., Morris S.L., Weymann R.J., Foltz C.B., 1992, ApJ 396, 487
Turnshek D.A., Bohlin R.C., Williamson II R.L., Lupie O.L., Koornneef J., Morgan D.H., 1990, AJ 99, 1243
Wardle J.F.C., Kronberg P.P., 1974, ApJ 194, 249
Whittet D.C.B., Martin P.G., Hough J.H., Rouse M.F., Bailey J.A., Axon D.J., 1992, ApJ 386, 562

Article 12

Polarization properties of a sample of Broad Absorption Line and gravitationally lensed quasars

D. Hutsemékers, H. Lamy, M. Remy : Astron. Astrophys. 340, 371 (1998)

Sur base de nouvelles mesures, nous présentons ici notre première étude systématique de la polarisation linéaire des quasars de type BAL.

Tout d'abord nous comparons la polarisation des quasars en fonction de leur type : BAL avec raies de haute ionisation en absorption (HIBAL), BAL avec raies de haute et faible ionisation en absorption (LIBAL) et non-BAL. Nous trouvons notamment que presque tous les quasars très polarisés appartiennent à la classe des quasars LIBAL et qu'au sein d'une même classe de quasar, la polarisation varie entre zéro et une valeur maximale, cette valeur maximale étant plus élevée pour les quasars BAL (et particulièrement LIBAL) que pour les quasars non-BAL.

Nous tentons ensuite de relier la polarisation à d'autres propriétés des quasars BAL, comme la pente du continuum, ou encore des indices caractérisant l'intensité ou le profil des raies spectrales. Nous montrons qu'il existe une corrélation significative entre la polarisation du continuum et l'indice de détachement des raies en absorption, dans le sens où les quasars montrant des profils de type P Cygni apparaissent plus polarisés. Cette relation est particulièrement claire pour les quasars LIBAL.

Enfin, nous montrons que ces résultats sont compatibles avec un modèle axisymétrique "disque + vent" de la région du quasar à l'origine des raies BAL, profils de raies et polarisation du continuum variant avec la géométrie et l'orientation du système.

Astron. Astrophys. 340, 371–380 (1998)

ASTRONOMY AND ASTROPHYSICS

Polarization properties of a sample of broad absorption line and gravitationally lensed quasars⋆,⋆⋆

D. Hutsemékers⋆⋆⋆, H. Lamy, and M. Remy

Institut d'Astrophysique, Université de Liège, 5 av. de Cointe, B-4000 Liège, Belgium

Received 20 July 1998 / Accepted 29 September 1998

Abstract. New broad-band linear polarization measurements have been obtained for a sample of 42 optically selected QSOs including 29 broad absorption line (BAL) QSOs. The polarization properties of different sub-classes have been compared, and possible correlations with various spectral indices searched for.

The main results of our study are: (1) Nearly all highly polarized QSOs of our sample belong to the sub-class of BAL QSOs with low-ionization absorption features (LIBAL QSOs). (2) The *range* of polarization is significantly larger for LIBAL QSOs than for high-ionization (HI) BAL QSOs and non-BAL QSOs. (3) There is some indication that HIBAL QSOs as a class may be more polarized than non-BAL QSOs and therefore intermediate between LIBAL and non-BAL QSOs, but the statistics are not compelling from the sample surveyed thus far. (4) For LIBAL QSOs, the *continuum* polarization appears significantly correlated with the *line profile* detachment index, in the sense that LIBAL QSOs with P Cygni-type profiles are more polarized. No correlation was found with the strength of the low- or the high-ionization absorption features, nor with the strength or the width of the emission lines.

These results are consistent with a scenario in which LIBAL QSOs constitute a different class of radio-quiet QSOs with more absorbing material and more dust. Higher maximum polarization can therefore be reached, while the actually measured polarization depends on the geometry and orientation of the system as do the line profiles. The observed correlation is interpreted within the framework of recent "wind-from-disk" models.

Key words: polarization – galaxies: quasars: absorption lines – galaxies: quasars: general – cosmology: gravitational lensing

1. Introduction

Broad absorption line quasi-stellar objects (BAL QSOs) are characterized by the presence in their spectra of broad, often deep, absorption troughs in the resonance lines of highly-ionized species like C IV, Si IV, or N V. These BALs appear blueshifted with respect to the corresponding emission lines. They are generally attributed to the ejection of matter at very high velocities ($\sim$0.1 c). About 12% of optically selected QSOs have BALs in their spectra, although this fraction could be underestimated if at least some BAL QSOs have their continuum more attenuated than non-BAL QSOs (Goodrich 1997). Apparently all BAL QSOs are radio-quiet[1] (Stocke et al. 1992). A recent account of BAL QSO properties may be found in Arav et al. (1997).

The fact that the broad emission line properties are essentially similar for BAL and non-BAL QSOs suggests that all radio-quiet QSOs could have a BAL region (BALR) of small covering factor, the BAL QSOs themselves being those objects with the BALR along the line of sight (e.g. Weymann et al. 1991, hereafter WMFH). Alternately, BAL and non-BAL QSOs may constitute two physically distinct populations of objects, BAL QSOs possibly representing an early stage in an evolutionary process towards normal QSOs (e.g. Boroson & Meyers 1992).

As first noticed by Stockman, Moore & Angel (1984), a number of BAL QSOs show high optical polarization ($\geq$ 3%) in the continuum while other radio-quiet QSOs (i.e. non-BAL ones) have generally low polarization ($\leq$ 1%). This important result has been recently confirmed by Hines & Schmidt (1997) on the basis of a larger sample. The fact that there is little or no variability of the polarization clearly distinguishes BAL QSOs from the so-called blazars. Since polarization is sensitive to the geometry of the objects (without spatially resolving them), a detailed understanding of BAL QSO polarization properties may provide important clues on the nature of the outflows and the status of these objects among AGN.

In this view, we have started a systematic polarimetric study of BAL QSOs. The present paper is devoted to the analysis of new broad-band polarization measurements obtained for a sam-

⋆ Tables 2 and 3 are also available in electronic form at the CDS via anonymous ftp to cdsarc.u-strasbg.fr (130.79.128.5) or via http://cdsweb.u-strasbg.fr/Abstract.html

⋆⋆ Based on observations collected at the European Southern Observatory (ESO, La Silla)

⋆⋆⋆ Also, Chercheur Qualifié au Fonds National de la Recherche Scientifique (FNRS, Belgium)

[1] There is only one known candidate radio-loud BAL QSO, 1556+3517, recently discovered by Becker et al. (1997). But Clavel (1998) finds that its radio-loudness is marginal after correcting for reddening

ple of 29 BAL QSOs, to which a number of normal radio-quiet QSOs have been added for comparison. Since an important issue is the study of possible correlations between polarization and other spectral characteristics, the objects have been essentially picked out from the WMFH sample which provides many useful quantitative spectral indices. Further, at least one BAL QSO is known to be gravitationally lensed. Its polarization could then be affected or induced by microlensing effects, i.e. by the selective magnification of some regions. We have therefore added to our sample several gravitationally lensed non-BAL QSOs with the aim of detecting any possible polarization difference.

The paper is organized as follows: the observing strategy and techniques are described in Sect. 2, as well as the methods for reducing the data and extracting accurate measurements. Instrumental polarization and de-biasing are also discussed in this section. In Sect. 3, the final sample of observed objects is detailed, sub-classes are defined, and several quantities characterizing the optical spectra are presented. Results are given in Sect. 4, including correlation searches between the various quantities. Conclusions and discussion form the last section.

2. Polarimetric observations and data reduction

The polarimetric observations were carried out on March 14–17 and September 3–6, 1994, at the European Southern Observatory (ESO La Silla, Chile), using the 3.6m telescope equipped with the EFOSC1 camera and spectrograph. The detector was a 512×512 TeK CCD (ESO#26) with a pixel size of 27 μm corresponding to $0''.605$ on the sky.

With EFOSC1, polarimetry is performed by inserting in the parallel beam a Wollaston prism which splits the incoming light rays into two orthogonally polarized beams. Each object in the field has therefore two images on the CCD detector, separated by about $20''$ and orthogonally polarized. To avoid image overlapping, one puts at the telescope focal plane a special mask made of alternating transparent and opaque parallel strips whose width corresponds to the splitting. The object is positioned at the centre of a transparent strip which is imaged on a region of the CCD chosen as clean as possible. The final CCD image then consists of alternate orthogonally polarized strips of the sky, two of them containing the polarized images of the object itself (Melnick et al. 1989, di Serego Alighieri 1989).

In order to derive linear polarization measurements, i.e. the two normalized Stokes parameters q and u, frames must be obtained with at least two different orientations of the Wollaston prism. This was done by rotating the whole EFOSC1 instrument by 45° (usually at the adapter angles 270° and 225°). For each object, two frames are therefore obtained. Typical exposure times are around 600s per frame, generally split into two shorter exposures. All observations were done with the Bessel V filter (ESO#553). The seeing was typically between $1''$ and $2''$, and the nights were photometric most of the time. Note that the polarization measurements do not depend on variable transparency or seeing since the two orthogonally polarized images of the object are simultaneously recorded. Finally, polarimetric calibration stars were observed (HD90177, HD161291, and HD164740; Schwarz 1987) in order to unambiguously fix the zero-point of the polarization position angle and to check the whole observing and reduction process.

Considering the two frames obtained with the instrument rotated at 270° and 225°, the normalized Stokes parameters are given by

$$q = \frac{I^1_{270} - I^2_{270}}{I^1_{270} + I^2_{270}}, \qquad u = \frac{I^1_{225} - I^2_{225}}{I^1_{225} + I^2_{225}}, \tag{1}$$

where I^1 and I^2 respectively refer to the intensities integrated over the two orthogonally polarized images of the object, background subtracted (Melnick et al. 1989). At this stage, the sign of q and u is arbitrary. It is clear from these relations that intensities must be determined with the highest accuracy. For this, the data were first corrected for bias and dark emission, and flat-fielded. A plane was locally fitted to the sky around each object image, and subtracted from each image individually. Since it appeared that standard aperture photometry was not accurate enough due to the rather large pixel size, we have measured the object center at subpixel precision by fitting a 2D gaussian profile and integrated the flux in a circle of same center and arbitrary radius by taking into account only those fractions of pixels inside the circle. With this method, the Stokes parameters may be computed for any reasonable radius of the aperture circle. They were found to be stable against radius variation, giving confidence in the method. In order to take as much flux as possible with not too much sky background, we finally fixed the aperture radius at $2.5\,(2\,\ln 2)^{-1/2}$ HW, where HW is the mean half-width at half-maximum of the gaussian profile. Note that in the few cases where the objects are resolved into multiple components, we use the smallest square aperture encompassing all the components. The whole procedure has been implemented within the ESO MIDAS reduction package. Applied to calibration stars, it provides polarization measurements in good agreement with the tabulated values. The zero-point of the polarization position angle is also determined from these stars, and the sign of q and u accordingly fixed. The uncertainties σ_q and σ_u are evaluated by computing the errors on the intensities I^1 and I^2 from the readout noise and from the photon noise in the object and the sky background (after converting the counts in electrons), and then by propagating these errors in Eq. 1. Uncertainties are typically around 0.15% for both q and u.

Since on most CCD frames field stars are simultaneously recorded, one can in principle use them to estimate the instrumental polarization, and to correct frame-by-frame the quasar Stokes parameters, following a method described by di Serego Alighieri (1989). However, the field stars (even when combined in a single "big" one per frame) are often fainter than the quasar, and a frame-by-frame correction introduces uncertainties on the quasar polarization larger than the instrumental polarization itself. Therefore, we tried to empirically correlate the instrumental polarization with observational parameters like the observing time or the position of the telescope, in order to check for possible variation and/or to derive a useful relation. Since no significant variation was found, we have finally computed the weighted average and dispersion of the normalized Stokes pa-

Table 1. Instrumental polarization

Date	$\overline{q}_\star$ (%)	$\sigma_{q_\star}$ (%)	$\overline{u}_\star$ (%)	$\sigma_{u_\star}$ (%)
03/94	+0.02	0.18	−0.10	0.34
09/94	+0.16	0.24	−0.30	0.29

rameters of field stars (a single "big" one per frame) considering all frames obtained during a given run. These values are given in Table 1. They indicate that the instrumental polarization is small. We take it into account in a rather conservative way by subtracting the systematic $\overline{q}_\star$ and $\overline{u}_\star$ from the quasar q and u, and by adding quadratically the errors. The final, corrected, values of the normalized Stokes parameters q and u are given in Table 2, together with the uncertainties. Note that possible contamination by interstellar polarization is included in the uncertainties (see also Sect. 4.1).

Then, from these values, the polarization degree is evaluated with $p = (q^2 + u^2)^{1/2}$, while the polarization position angle θ is obtained by solving the equations $q = p\cos 2\theta$ and $u = p\sin 2\theta$. The error on the polarization degree is estimated by $\sigma_p = (\sigma_q + \sigma_u)/2$, although the complex statistical behavior of the polarization degree should be kept in mind (Serkowski 1962, Simmons & Stewart 1985). Indeed, since p is always a positive quantity, it is biased at low signal-to-noise ratio. A reasonably good estimator of the true polarization degree, noted p_0, is computed from p and σ_p using the Wardle & Kronberg (1974) method (Simmons & Stewart 1985). Finally, the uncertainty of the polarization position angle θ is estimated from the standard Serkowski (1962) formula where p_0 is used instead of p to avoid biasing, i.e. $\sigma_\theta = 28\overset{\circ}{.}65\,\sigma_p/p_0$. All these quantities are given in Table 2. Also reported are the redshift z of the objects, the quasar sub-type (cf. Sect. 3.1), and $p_{\rm ISM}$, an upper limit to the galactic interstellar polarization along the object line of sight (cf. Sect. 4.1)

3. The observed sample and its characteristics

The observed QSOs were essentially chosen from the WMFH sample, which is a set of BAL and non-BAL QSOs from the Large Bright Quasar Survey (LBQS, cf. Hewett et al. 1995), augmented by several BAL QSOs from other sources. The selection was achieved during the observations depending on the QSO observability (position on the sky) and magnitude (priority to the brighter objects). A priority was also given to the BAL QSOs with low-ionization features. Five objects observable in the southern sky were added: 3 BAL QSOs from the Hartig & Baldwin (1986, hereafter HB) sample (0254-3327, 0333-3801, 2240-3702), and 2 non-BAL QSOs from the LBQS (2114-4346, 2122-4231). Finally, an additional 7 true or possible gravitationally lensed optically selected QSOs (cf. the compilation by Refsdal & Surdej 1994) were included in the sample.

The final sample then consists of 42 moderate to high redshift optically selected QSOs (cf. Tables 2 & 3). It contains 29 BAL QSOs, 12 non-BAL QSOs, and 1 "intermediate" object (2211-1915, cf. WMFH). 8 of them are true or possible gravitationally lensed QSOs, including 2 BAL QSOs: 1413+1143 and 1120+0154[2].

Among the 42 optically selected QSOs, 36 are definitely radio-quiet while only 1 is radio-loud (2211-1915, the "intermediate" object) (Stocke et al. 1992, Hooper et al. 1995, Véron & Véron 1996, Djorgovski & Meylan 1989, Bechtold et al. 1994, Reimers et al. 1995). The 5 remaining objects (3 BAL QSOs and 2 non-BAL QSOs: 0333-3801, 0335-3339, 2154-2005, 2114-4346, 2122-4231) have apparently not been measured at radio-wavelengths. However, they are most probably radio-quiet too (Stocke et al. 1992, Hooper et al. 1995).

3.1. The low-ionization BAL QSOs

Approximately 15% of BAL QSOs have deep low-ionization BALs (Mg II λ 2800 and/or Al III λ 1860) *in addition* to the usual high-ionization BAL troughs (WMFH, Voit et al. 1993). These objects might be significantly reddened by dust (Sprayberry & Foltz 1992). They also possibly constitute a physically different class of BAL QSOs (Boroson & Meyers 1992).

While objects with strong low-ionization (LI) features are recognized as LIBAL QSOs by most authors, the classification of objects with weaker features is controversial. We therefore define three categories of LIBAL QSOs: strong (S), weak (W), and marginal (M) LIBAL QSOs. The strong and weak LIBAL QSOs in our sample were all considered and first classified as such by WMFH. The strong ones are 0059-2735, 1011+0906, 1232+1325 and 1331-0108; the weak ones are 0335-3339, 1231+1320, 2225-0534 and 2350-0045 (WMFH "a" parameter < 1). But the classification by WMFH is rather conservative and includes only clear LIBAL QSOs, while several authors have reported faint LIBAL features in a number of other objects. We classify the latter objects as marginal LIBAL QSOs. These are 0043+0048, 1246-0542 and 2240-3702 (HB), 1413+1143 (Hazard et al. 1984, Angonin et al. 1990), 1120+0154 (Meylan & Djorgovski 1989), and 1212+1445 (this work). The marginal LIBAL QSOs are characterized by very weak Mg II and/or Al III BALs. The asymmetry of the Mg II or C III] emission lines, when cut on the blue side, is also considered as evidence for marginal LIBALs. Note finally that line strengths may be variable in some objects and that weak LIBALs could have been observed only once (namely due to possible microlensing effects as suspected in e.g. 1413+1143; Angonin et al. 1990, Hutsemékers 1993).

The remaining BAL QSOs are classified as high ionization (HI) only, except 0903+1734 and 1235+0857 which are unclassified, the Mg II line being outside the observed spectral range and no Al III BAL being detected. These classifications are summarized in Tables 2 and 3. Note that most spectra available in the literature were carefully re-inspected to check for the consistency of the classification. Altogether, the strong, weak and marginal LIBAL QSOs constitute approximately 50% of our

[2] Note that 1120+0154 = UM425 was only recently recognized as a BAL QSO (Michalitsianos & Oliversen 1995)

Table 2. Polarimetric results

Object	z	Type	q (%)	σ_q (%)	u (%)	σ_u (%)	p (%)	σ_p (%)	p_0 (%)	$p_{\rm ISM}$ (%)	θ (°)	σ_θ (°)
0006+0230	2.096	10	0.04	0.27	−0.10	0.31	0.11	0.29	0.00	0.08	145	–
0013−0029	2.084	10	−0.65	0.30	−0.79	0.35	1.03	0.33	0.97	0.07	115	10
0019+0107	2.124	20	0.13	0.27	0.88	0.30	0.89	0.29	0.85	0.10	41	10
0021−0213	2.296	20	0.65	0.30	−0.25	0.34	0.70	0.32	0.63	0.17	170	14
0025−0151	2.072	20	−0.37	0.26	0.24	0.31	0.44	0.28	0.37	0.15	74	22
0029+0017	2.226	20	0.54	0.32	−0.52	0.35	0.75	0.34	0.68	0.10	158	14
0043+0048	2.141	50	−0.14	0.27	−0.07	0.31	0.16	0.29	0.00	0.02	103	–
0059−2735	1.594	30	1.56	0.26	−0.44	0.31	1.62	0.29	1.60	0.16	172	5
0137−0153	2.232	20	−0.61	0.27	0.94	0.31	1.12	0.29	1.08	0.08	61	8
0142−1000	2.719	11	0.00	0.29	−0.28	0.33	0.28	0.31	0.00	0.08	135	–
0145+0416	2.029	20	−0.42	0.30	−2.67	0.34	2.70	0.32	2.68	0.21	131	3
0254−3327	1.862	20	−0.20	0.36	−0.02	0.40	0.20	0.38	0.00	0.04	93	–
0333−3801	2.210	20	0.01	0.26	0.83	0.30	0.83	0.28	0.78	0.00	45	10
0335−3339	2.258	40	0.02	0.33	0.60	0.35	0.60	0.34	0.53	0.00	44	19
0903+1734	2.776	60	−0.47	0.21	0.80	0.36	0.93	0.29	0.88	0.12	60	9
1009−0252	2.745	11	0.94	0.22	−0.07	0.38	0.95	0.30	0.90	0.07	178	9
1011+0906	2.262	30	0.60	0.23	−2.04	0.37	2.12	0.30	2.10	0.06	143	4
1029−0125	2.038	20	−0.54	0.24	−0.99	0.38	1.13	0.31	1.09	0.21	121	8
1104−1805	2.303	11	0.18	0.20	0.24	0.35	0.30	0.27	0.17	0.27	27	45
1115+0802	1.722	11	−0.02	0.19	0.68	0.35	0.68	0.27	0.63	0.17	46	12
1120+0154	1.465	51	1.84	0.19	0.63	0.35	1.95	0.27	1.93	0.17	9	4
1146+0207	2.055	10	0.22	0.25	−0.42	0.39	0.47	0.32	0.39	0.08	149	23
1208+1011	3.803	11	−0.18	0.24	0.30	0.37	0.35	0.30	0.23	0.00	60	38
1208+1535	1.956	20	−0.17	0.36	−0.11	0.47	0.20	0.42	0.00	0.28	107	–
1212+1445	1.621	50	0.98	0.23	1.06	0.36	1.45	0.30	1.42	0.25	24	6
1231+1320	2.386	40	0.59	0.25	−0.45	0.39	0.74	0.32	0.68	0.10	162	14
1232+1325	2.363	30	−1.95	0.30	−0.53	0.40	2.02	0.35	1.99	0.11	98	5
1235+0857	2.885	60	1.68	0.22	1.55	0.37	2.29	0.29	2.27	0.00	21	4
1246−0542	2.222	50	0.35	0.20	−0.84	0.36	0.91	0.28	0.87	0.07	146	9
1309−0536	2.212	20	0.78	0.21	−0.03	0.36	0.78	0.28	0.73	0.13	179	11
1331−0108	1.867	30	1.01	0.27	1.59	0.35	1.88	0.31	1.86	0.09	29	5
1413+1143	2.542	51	−0.78	0.25	1.32	0.36	1.53	0.31	1.50	0.00	60	6
1429−0053	2.084	11	0.95	0.18	0.31	0.40	1.00	0.29	0.96	0.18	9	9
1442−0011	2.215	20	0.16	0.22	−0.18	0.37	0.24	0.30	0.00	0.25	156	–
2114−4346	2.041	10	−0.11	0.29	−0.22	0.34	0.24	0.31	0.00	0.15	122	–
2122−4231	2.266	10	−0.01	0.27	−0.12	0.31	0.12	0.29	0.00	0.17	133	–
2154−2005	2.028	20	0.26	0.26	−0.70	0.30	0.75	0.28	0.69	0.07	145	12
2211−1915	1.951	10	0.14	0.27	0.03	0.31	0.14	0.29	0.00	0.08	6	–
2225−0534	1.981	40	3.58	0.27	−2.51	0.31	4.37	0.29	4.36	0.33	162	2
2230+0232	2.147	10	−0.36	0.28	−0.57	0.31	0.68	0.29	0.62	0.38	119	14
2240−3702	1.835	50	0.92	0.26	1.88	0.30	2.10	0.28	2.08	0.00	32	4
2350−0045	1.626	40	−0.58	0.27	−0.16	0.31	0.60	0.29	0.53	0.24	98	16

Object Type: First digit: (1) non-BAL QSOs + one intermediate object, (2) HIBAL QSOs, (3) Strong LIBAL QSOs, (4) Weak LIBAL QSOs, (5) Marginal LIBAL QSOs, (6) unclassified BAL QSOs; Second digit: (1) objects identified as true or possible gravitationally lensed QSOs

BAL QSO sample (but this is not representative of the actual proportion of LIBAL QSOs among BAL QSOs since priority was given to these objects).

3.2. The BAL QSO spectral characteristics

WMFH provide a series of spectral indices characterizing the absorption and emission features of BAL QSOs. For the absorption lines, they define the balnicity index (BI, in km s^{-1}) which is a modified velocity equivalent width of the C IV BAL, and the detachment index (DI, unitless) which measures the onset velocity of the strongest C IV BAL trough in units of the adjacent emission line half-width, that is, the degree of detachment of the absorption line relative to the emission one (see also HB who first distinguish between detached and P Cygni-type BAL profiles). Estimates of BI are also given by Korista et al. (1993) for most objects of our sample, such that we adopt for BI an average of these values and those from WMFH. WMFH also

Table 3. BAL QSO spectral characteristics

Object	Type	BI	DI	C IV HW	C III] HW	C IV EW	C III] EW	Fe II 2400 EW	Fe II 2070 EW	$\alpha_{\rm B}$	$\alpha_{\rm R}$
0019+0107	20	2305	4.65	1432	4193	7.5	18.1	21.99	5.96	0.73	0.68
0021−0213	20	5180	3.14	3077	3856	7.7	17.2	46.74	3.56	0.66	0.68
0025−0151	20	2878	2.97	1645	2528	10.9	23.4	19.90	1.96	0.34	1.07
0029+0017	20	5263	2.45	1857	3219	15.1	31.7	27.34	4.99	0.55	1.13
0043+0048	50	4452	10.06	987	1586	2.8	12.5	44.66	4.80	−0.13	0.77
0059−2735	30	11054	1.18	–	–	–	–	40.91	8.36	1.50	1.59
0137−0153	20	4166	2.41	1935	3125	8.2	22.6	35.95	6.32	1.01	1.26
0145+0416	20	4765	3.96	2341	–	12.5	–	33.10	5.36	0.96	0.42
0254−3327	20	694	1.08	1640	3125	8.1	22.5	23.00	2.40	0.64	0.91
0333−3801	20	3432	3.28	5450	3063	7.5	6.3	37.00	6.60	0.56	0.07
0335−3339	40	7460	15.90	599	–	1.7	–	95.66	14.16	1.91	1.74
0903+1734	60	9776	4.34	1548	5630	4.7	26.5	–	4.90	1.54	0.59
1011+0906	30	5587	6.84	3232	3754	7.9	11.1	40.91	9.16	1.95	1.51
1029−0125	20	1849	2.22	1645	3400	8.0	23.2	42.96	4.41	0.83	1.47
1120+0154	51	415	0.79	1343	–	8.5	–	–	–	0.45	1.25
1208+1535	20	4545	4.64	2709	5222	6.3	24.0	23.98	6.92	0.42	1.06
1212+1445	50	3619	6.05	1741	2363	3.8	4.9	25.29	3.37	1.51	1.08
1231+1320	40	3473	6.38	2612	4492	7.5	18.6	42.59	7.19	2.15	0.22
1232+1325	30	12620	1.84	3870	7123	17.5	42.9	58.76	11.80	2.38	0.92
1235+0857	60	815	0.42	1296	3840	10.4	24.0	–	3.00	1.04	0.45
1246−0542	50	4309	6.60	1587	3699	4.8	20.1	44.29	4.21	1.84	0.88
1309−0536	20	5363	5.10	3812	5128	8.1	23.7	36.42	5.19	1.41	0.90
1331−0108	30	7912	1.15	1935	3212	6.2	13.8	18.07	6.95	2.66	1.62
1413+1143	51	6621	1.50	1683	2937	18.8	35.0	–	1.89	1.72	0.63
1442−0011	20	5143	2.83	3522	5481	14.6	20.0	25.81	4.12	0.58	1.16
2154−2005	20	963	6.42	2438	3392	11.3	26.9	21.91	4.47	0.41	0.62
2225−0534	40	7903	0.48	1509	3251	11.3	43.4	53.38	7.67	1.68	2.21
2240−3702	50	8539	0.69	1940	3000	7.7	16.2	–	3.80	1.08	1.40
2350−0045	40	6964	5.08	1761	–	14.3	–	54.78	5.71	1.01	1.03

Object Type: First digit: (2) HIBAL QSOs, (3) Strong LIBAL QSOs, (4) Weak LIBAL QSOs, (5) Marginal LIBAL QSOs, (6) unclassified BAL QSOs; Second digit: (1) objects identified as true or possible gravitationally lensed QSOs. Units are given in the text

provide "clever" half-widths at half-maximum (HW, in km s^{-1}) and equivalent widths (EW, in Å) for the C IV, C III] and Fe II emission lines. For a more detailed definition of these indices, see WMFH.

For a few objects (0254-3327, 0333-3801, 2240-3702, and 1120+0154), some spectral indices were not provided. We therefore computed them using C IV spectra published by Korista et al. (1993) and Steidel & Sargent (1992). The spectra were digitally scanned, and the measurements done following the prescriptions given by WMFH. The measurements were also done for spectra of objects with published indices: a good agreement was found, giving confidence in our new values. For the C III] and Fe II emission lines, half-widths and equivalent widths were simply rescaled from those measured by HB. All these quantities are reported in Table 3.

In addition, we have evaluated the slope of the continuum using BAL QSO spectra digitally scanned from the papers by WMFH, HB, and Steidel & Sargent (1992). After some trials, we realized that some spectra cannot be easily fitted with a single power-law continuum: the slope often breaks roughly near C III], probably due to reddening and/or extended Fe II emission (compare for example the spectra of 1246-0542 and 1442-0011 in WMFH). We therefore decided to fit the continuum blueward and redward of C III], independently. The derived slopes $\alpha_{\rm B}$ and $\alpha_{\rm R}$ are given in Table 3, assuming a power-law continuum $F_\nu \propto \nu^{-\alpha}$. The values of $\alpha_{\rm B}$ and $\alpha_{\rm R}$ are affected by large uncertainties (not smaller than $\Delta\alpha \sim 0.3$), mainly due to the difficulty to accurately identify the continuum when the BALs are very large, when the Fe II emission/absorption is strong, or when the Mg II absorption is wide.

4. The results

4.1. Contamination by interstellar polarization

Since all objects in the sample are at high galactic latitudes ($|b_{\rm II}| > 35°$), the contamination by interstellar polarization in the Galaxy is expected to be negligible. This may be verified using the Burstein & Heiles (1982, hereafter BH) reddening maps[3]. The maps provide E(B-V) values from which the inter-

[3] The data files and routines were obtained from Schlegel 1998, via http://astro.berkeley.edu/davis/dust/data/bh/index.html

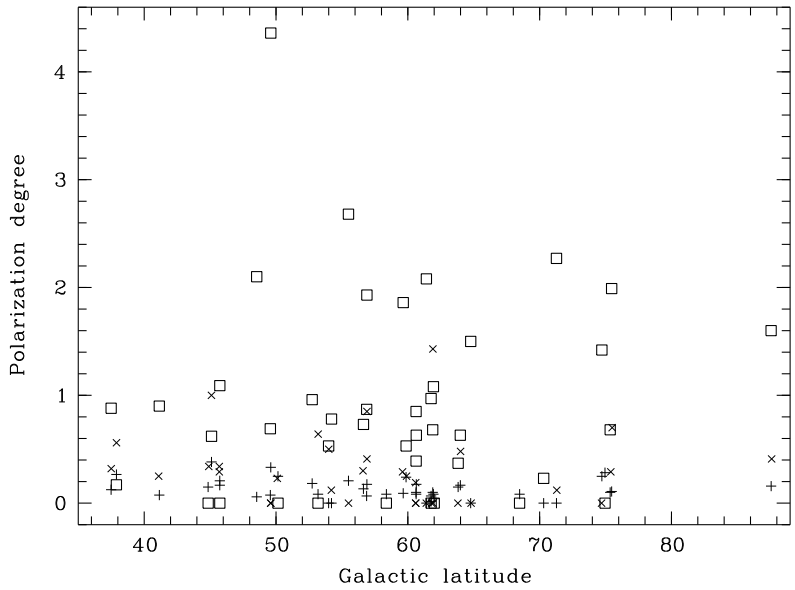


Fig. 1. The QSO polarization degree p_0 (in%) [□] is represented here as a function of the Galactic latitude of the objects ($|b_{II}|$, in degree), together with the de-biased polarization degree of field stars [×] (also corrected for the small systematic trend reported in Table 1), and the maximum interstellar polarization degree p_{ISM} derived from the Burstein & Heiles (1982) reddening maps [+]

stellar polarization is estimated with the relation $p_{ISM} \leq 8.3\%$ E(B-V) (Hiltner 1956). These upper limits on p_{ISM} are reported in Table 2. All but two are smaller than 0.3%, indicating a very small contamination by the Galaxy.

Polarization of faint field stars recorded on the CCD frames may also provide an estimate of the interstellar polarization. The dispersion of their Stokes parameters (Table 1) indicates that actually *both* instrumental and interstellar polarization are small. This is further illustrated in Fig. 1, where the QSO polarization is compared to the field star polarization (interstellar + instrumental), and to the maximum interstellar polarization derived from the BH maps. The absence of correlation between the field star polarization and the BH interstellar polarization suggests that instrumental polarization dominates field star polarization (although one cannot exclude that a few of them are intrinsically polarized). In addition, no deviation from uniformity was found in the distribution of the acute angle between quasar and field star polarization vectors measured on the same frame. These results confirm the insignificance of interstellar polarization in our sample.

We may therefore safely conclude that virtually any quasar with $p_0 \geq 0.5\%$ (or $p \geq 0.6\%$) is intrinsically polarized (cf. Fig. 1 and Table 1), in good agreement with the results obtained by Berriman et al. (1990) for low-polarization Palomar-Green (PG) QSOs.

4.2. Polarization variability

For some BAL QSOs of our sample, previous polarimetric measurements are available in the literature, and may be used for comparison. In Table 4, we list first epoch measurements obtained in 1977–1981. For all these objects, and within the limits of uncertainty, the values of the polarization position angles are in excellent agreement with ours (Table 2).

Table 4. Previous polarimetric measurements

Object	Date	p (%)	σ_p (%)	θ (°)	σ_θ (°)
0019+0107	11-05-78	0.93	0.26	24	8
0043+0048	11-05-78	0.33	0.38	103	25
0145+0416	10-23-81	0.58	0.68	131	34
0254−3327	10-24-81	0.62	1.16	154	54
1246−0542	4-05-78	1.87	0.31	139	5
1309−0536	6-09-78	2.33	0.57	179	7
1413+1143	6-06-81	3.39	0.48	49	4
2225−0534	9-11-77	4.09	0.79	166	6

From Moore & Stockman 1981, 1984, and Stockman et al. 1984

On the contrary, our values of p are generally smaller than or equal to the previous ones. However variability cannot be invoked since the observed differences are most likely due to the fact that the old measurements were done in white light and using detectors more sensitive in the blue, i.e. in a wavelength range where polarization is suspected to be higher (cf. Stockman et al. 1984, and more particularly the case of 1246-0542). Note further that those objects with null polarization ($p \leq \sigma_p$) are identical, except 0145+0416 which we find significantly polarized. But 0145+0416 is also the only object in our sample not far from a bright star which might contaminate the measurements. Its variability can nevertheless not be excluded.

In conclusion, we find no evidence in our sample of BAL QSOs for the strong polarization variability (in degree or angle) which characterizes blazars, confirming on a larger time-scale the results of Moore & Stockman (1981). This does not preclude the existence of small variations like those reported by Goodrich & Miller (1995) for 1413+1143.

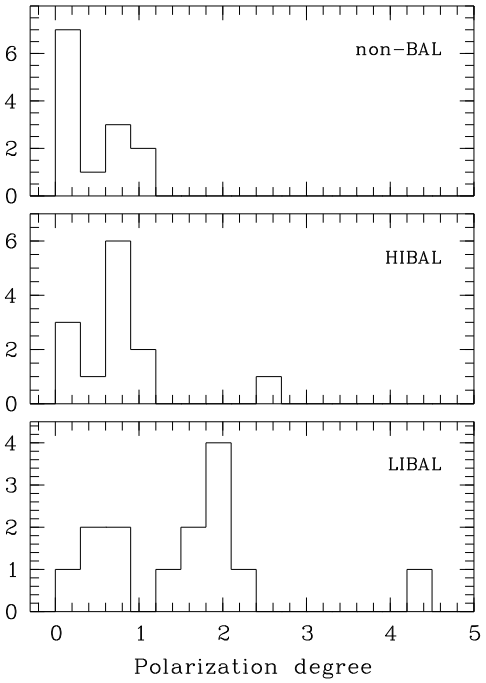


Fig. 2. The distribution of the polarization degree p_0 (in%) for the three main classes of QSOs. Non-BAL QSOs include the intermediate object. LIBAL QSOs contain the three sub-categories, i.e. strong, weak and marginal LIBAL QSOs

4.3. Polarization versus QSO sub-types

Before discussing the polarization properties of the different QSO sub-types, it is important to note that our sample is quite homogeneous in redshift (as from WMFH). Therefore, the polarization we measure in the V filter roughly refers to the same rest-frame wavelength range, such that differences between quasar sub-types will not be exaggerately masked by a possible wavelength dependence of the polarization. Also, spectral lines generally contribute little to the total flux in the V filter, and our polarimetric measurements largely refer to the polarization in the continuum.

Fig. 2 illustrates the distribution of p_0 for non-BAL, HIBAL and LIBAL QSOs. It immediately appears that nearly all QSOs with high polarization ($p_0 \geq 1.2\%$) are LIBAL QSOs. Only two other objects have high polarization (cf. Table 2): 1235+0857 which is unclassified (and therefore could be a LIBAL QSO), and 0145+0416 which has uncertain measurements (cf. Sect. 4.2). Also important is the fact that not all LIBAL QSOs do have high polarization (like 0335-3339 or 1231+1320 which are bona-fide ones; cf. WMFH and Voit et al. 1993). Further, although the strongest LIBAL QSOs are all highly polarized, there is apparently no correlation between the LIBAL strength and the polarization degree (cf. 2225-0534 or 1120+0154 which are weak and marginal LIBAL QSOs, respectively). This suggests that polarization is not systematically higher in LIBAL QSOs, but that its *range* is wider than in other QSOs. Although less polarized, several HIBAL QSOs also have intrinsic polarization ($p_0 \geq 0.5\%$), and apparently more often than non-BAL QSOs.

Table 5. Comparison of p_0 for various pairs of samples

Sample 1	Sample 2	n_1	n_2	$P_{\rm K-S}$
non-BAL	BAL	13	29	0.0253
non-BAL	LIBAL	13	14	0.0076
non-BAL	HIBAL	13	13	0.2914
non-BAL	HIBAL-	13	12	0.3973
LIBAL	HIBAL	14	13	0.0267
LIBAL	HIBAL-	14	12	0.0096
PG QSOs	non-BAL	88	13	0.1752
PG QSOs	BAL	88	29	0.0000
PG QSOs	LIBAL	88	14	0.0002
PG QSOs	HIBAL	88	13	0.0238
PG QSOs	HIBAL-	88	12	0.4282

The PG QSO sample is from Berriman et al. (1990), Seyfert galaxies and BAL QSOs excluded. HIBAL- refers to the HIBAL QSOs of our sample minus 0145+0416

The distribution of non-BAL QSOs peaks near $p_0 \sim 0\%$ with a mean value $< p_0 > \simeq 0.4\%$. It is in good agreement with the distribution found by Berriman et al. (1990) for low-polarization PG QSOs. The distribution of LIBAL QSOs is wider with a peak displaced towards higher polarization ($p_0 \sim 2\%$), and with $< p_0 > \simeq 1.5\%$. The distribution of HIBAL QSOs looks intermediate peaking near $p_0 \sim 0.7\%$, and with $< p_0 > \simeq 0.7\%$.

To see whether these differences are statistically significant, a two-sample Kolmogorov-Smirnov (K-S) statistical test (from Press et al. 1989) has been used to compare the observed distributions of p_0. In Table 5, we give the probability that the distributions of two sub-samples are drawn from the same parent population, considering various combinations. We also include a comparison with the polarization of PG QSOs (after de-biasing the polarization degrees as described in Sect. 2). The number of objects involved in the sub-samples (n_1 and n_2) are given in the table. The difference between LIBAL and non-BAL QSOs appears significant ($P_{\rm K-S} < 0.01$) as well as the difference between LIBAL and HIBAL QSOs. However, no significant difference between HIBAL and non-BAL QSOs can be detected. Comparison with PG QSOs confirms these results. It also suggests that the distributions of non-BAL, HIBAL, and PG QSOs do not significantly differ, although the latter objects have much lower redshifts and were measured in white light (any marginal difference with HIBAL QSOs is due to the polarization of 0145+0416, which is uncertain).

These results suggest that the polarization of LIBAL QSOs definitely differs from that of non-BAL and HIBAL QSOs, showing a distribution significantly extended towards higher polarization. On the contrary, no significant difference is found between HIBAL and non-BAL QSOs. The difference, if any, is small and would require a larger sample and more accurate measurements to be established.

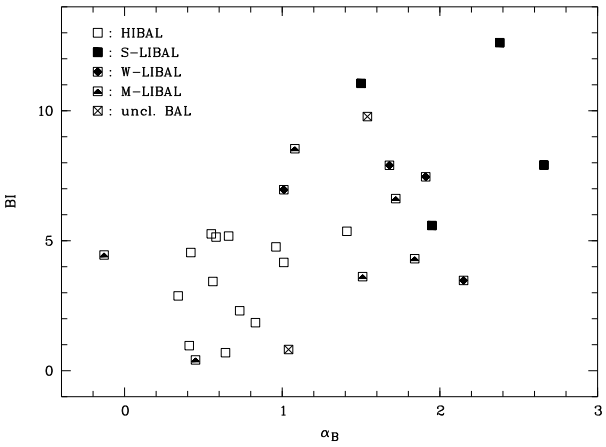


Fig. 3. The correlation between the balnicity index BI (in 10^3 km s^{-1}) and the slope of the continuum $\alpha_{\rm B}$ for all BAL QSOs of our sample

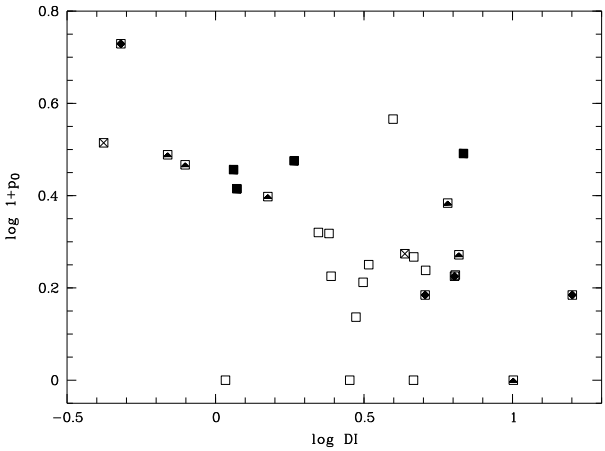


Fig. 4. The correlation between the polarization degree p_0 (in%) and the line profile detachment index DI for all BAL QSOs of our sample. Symbols are as in Fig. 3. The correlation is especially apparent for the QSOs of the LIBAL sample

Finally, no polarization difference was found when comparing the gravitationally lensed QSOs to other non-BAL or BAL QSOs. When polarized, their polarization is essentially related to their BAL nature. Small variations due to microlensing in either component can nevertheless be present (Goodrich & Miller 1995).

4.4. BAL QSO polarization versus spectral indices

The previous results suggesting a different behavior of LIBAL QSOs, it is important to recall that these QSOs also differ by the strength of their high-ionization features and the slope of their continuum (WMFH, Sprayberry & Foltz 1992). This is clearly seen in Fig. 3, using our newly determined continuum slopes. LIBAL QSOs (including several marginal ones) appear to have the highest balnicity indices and the most reddened continua. These differences are significant: the probability that the distribution of BI (resp. $\alpha_{\rm B}$) in HIBAL and LIBAL QSOs is drawn from the same parent population is computed to be $P_{\rm K-S}$ = 0.008 (resp. 0.002). In addition BI and $\alpha_{\rm B}$ seem correlated. Possible correlations may be tested by computing the Kendall (τ) and the Spearman (r_s) rank correlation coefficients (Press et al. 1989; also available in the ESO MIDAS software package). The probability P_τ that a value more different from zero than the observed value of the Kendall τ statistic would occur by chance among uncorrelated indices is P_τ = 0.003, for n = 29 objects. The Spearman test gives P_{r_s} = 0.001. This indicates a significant correlation between BI and $\alpha_{\rm B}$ in the whole BAL QSO sample.

Possible correlations between the polarization degree p_0 and the various spectral indices were similarly searched for by computing the Kendall τ and the Spearman r_s statistics. The resulting probabilities P_τ and P_{r_s} are given in Table 6, for the whole BAL QSO sample and for LIBAL QSOs only. Note that similar results are obtained when using p instead of p_0. From this table, it appears that the polarization degree is significantly correlated with the slope of the continuum $\alpha_{\rm B}$, and with the line profile detachment index DI.

Table 6. Analysis of correlation between p_0 and various indices

	BAL QSOs			LIBAL QSOs		
Index	P_τ	P_{r_s}	n	P_τ	P_{r_s}	n
BI	0.198	0.179	29	0.226	0.169	14
DI	0.007	0.014	29	0.004	0.009	14
C IV HW	0.968	0.857	28	0.158	0.158	13
C III] HW	0.880	0.845	24	0.325	0.405	10
C IV EW	0.334	0.331	28	0.075	0.078	13
C III] EW	0.546	0.612	24	0.325	0.446	10
Fe II 2400 EW	0.632	0.553	24	0.303	0.391	11
Fe II 2070 EW	0.358	0.321	28	0.667	0.571	13
$\alpha_{\rm B}$	0.007	0.004	29	0.582	0.459	14
$\alpha_{\rm R}$	0.393	0.375	29	0.061	0.086	14

The correlation with $\alpha_{\rm B}$ disappears when considering LIBAL QSOs only, although p_0 and $\alpha_{\rm B}$ still span a large range of values. Most probably, this correlation is detected in the whole BAL QSO sample as a consequence of the different distributions of both $\alpha_{\rm B}$ and p_0 in the LIBAL and HIBAL QSO sub-samples (Figs. 2 and 3).

On the contrary, the correlation with the detachment index holds for the whole BAL QSO sample as well as for the LIBAL QSO sub-sample. It is illustrated in Fig. 4. In fact, the correlation appears dominated by the behavior of LIBAL QSOs. HIBAL QSOs roughly follow the trend, but their range in DI is not large enough to be sure that they behave similarly[4]. It is interesting to remark that the observed correlation is stable – and even slightly better – if we assume that the polarization degree increases towards shorter wavelengths, i.e. if p_0 is redshift-dependent. This

[4] Note that the apparent difference between the distributions of DI for LIBAL and HIBAL QSOs is not significant ($P_{\rm K-S}$ = 0.179)

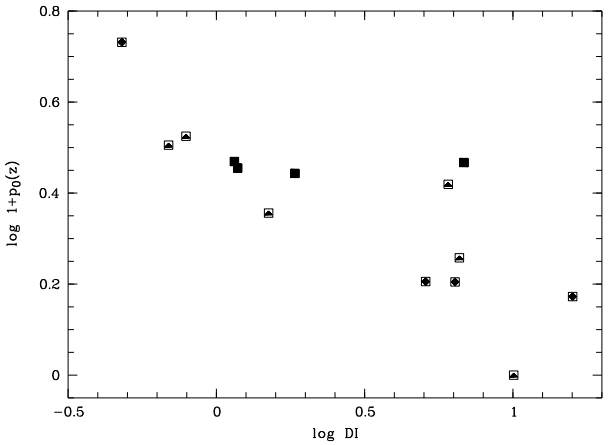


Fig. 5. The correlation between the redshift-corrected polarization degree $p_0(z)$ (in%) and the line profile detachment index DI for LIBAL QSOs only. We assume $p_0(z) = p_0(\frac{3}{1+z})$, i.e. a λ^{-1} dependence of p_0. Symbols are as in Fig. 3

is as illustrated in Fig. 5 for the LIBAL QSO sub-sample, assuming a reasonable λ^{-1} dependence (e.g. Cohen et al. 1995). In this case, P_τ = 0.0006 and P_{r_s} = 0.0003.

No other correlation of p_0, namely with the balnicity index, or with emission line indices is detected.

5. Discussion and conclusions

New broad-band linear polarization measurements have been obtained for a sample of 42 optically selected QSOs including 29 BAL QSOs (14 LIBAL and 13 HIBAL). The polarization properties of the different sub-classes have been compared, and possible correlations with various spectral indices searched for. The main results of our study are:

- Nearly all highly polarized QSOs of our sample belong to the LIBAL class (provided that BAL QSOs with weaker low-ionization features are included in the class).
- The *range* of polarization is significantly larger for LIBAL QSOs than for HIBAL and non-BAL QSOs. It extends from 0% to 4.4%, with a peak near 2%.
- There is some indication that HIBAL QSOs as a class may be more polarized than non-BAL QSOs and therefore intermediate between LIBAL and non-BAL QSOs, but the statistics are not compelling from the sample surveyed thus far.
- We confirm the fact that LIBAL QSOs (including weaker ones) have larger balnicity indices and more reddened continua than HIBAL QSOs.
- The *continuum* polarization appears correlated with the *line profile* detachment index, especially in the LIBAL QSO subsample.
- No correlation is found between polarization and the strength of the low- or the high-ionization absorption features, nor with the strength or the width of the emission lines. The apparent correlation between polarization and the slope of the continuum is probably due to the different distribution of these quantities within the HIBAL and LIBAL sub-samples.

The fact that LIBAL QSOs have different polarization properties is an additional piece of evidence that these objects could constitute a different class of radio-quiet QSOs, as suggested by several authors (WMFH, Sprayberry & Foltz 1992, and Boroson & Meyers 1992), HIBAL QSOs being much more similar to non-BAL QSOs. The higher maximum polarization observed in LIBAL QSOs is probably related to the larger amount of absorbing material and/or dust, either via the presence of additional scatterers (dust or electrons), or via an increased attenuation of the direct continuum.

The correlation between the continuum polarization and the detachment index was unexpected, especially since the latter index is a rather subtle characteristic of the line profiles which involves both absorption and emission components. The correlation is in the sense that LIBAL QSOs with detached C IV profiles are less polarized in the continuum, while those with P Cygni-type C IV profiles are more polarized. The most obvious explanation for such a correlation is that the high-ionization line profiles and the continuum polarization both depend on the geometry and/or the orientation of the LIBAL QSOs. This would explain that a range of polarization degrees is in fact observed, the maximum value being characteristic of the class. It is not excluded that HIBAL QSOs behave similarly within a smaller polarization range.

Murray et al. (1995) proposed a BAL flow model which accounts for many of the observed BAL profiles including the detached ones. Instead of being accelerated radially from a central source, the flow emerges from the accretion disk at some distance from the central source. It is then exposed to the continuum radiation and accelerated, rapidly reaching radial trajectories. The wind has naturally a maximum opening angle, and may produce polarization in the continuum via electron scattering. Other recent models are also based on such a "wind-from-disk" paradigm, and may result in roughly similar geometry and kinematics although acceleration mechanisms, photoionization, cloud size and filling factor could significantly differ (de Kool & Begelman 1995, Königl & Kartje 1994, Emmering et al. 1992).

Murray et al. (1995) show that for a flow seen nearly along the disk, P Cygni-type profiles with black troughs at low velocities are naturally produced. For the flow seen at grazing angle along the upper edge of the wind, high-velocity detached absorptions are obtained. Since the direct continuum is expected to be more attenuated for lines of sight near the disk, the continuum polarization is expected to be higher for orientations which produce P Cygni-type profiles than for orientations which produce detached profiles. This is in good qualitative agreement with the observed correlation. This mechanism has already been proposed by Goodrich (1997) to explain the higher polarization of some PHL5200-like (i.e. P Cygni-type) BAL QSOs. The polarization being uncorrelated with the slope of the continuum in the LIBAL QSO sub-sample, this differential attenua-

tion should be dominated by electron scattering in the wind. In fact, the electron scattering models of Brown & McLean (1977) also account for the observed behavior. For the cylindrical sector geometry which roughly characterizes the "wind-from-disk" models, Brown & McLean (1977) found that the observed polarization is given by $p \propto n_0 R \sin\phi \cos^2\phi \sin^2 i$, where i is the inclination of the system ($i = 0°$ for the disk in the plane of the sky), ϕ the opening half-angle of the wind, R its maximum extension, and n_0 a uniform electron density. With this geometry, polarization is higher along the equatorial line of sight (i = 90°) than along any other line of sight, again in good agreement with the observed correlation. In addition to this orientation effect within the LIBAL QSO sub-class, we see that the higher wind opacities (from either density or size) or the larger covering factors (up to $\phi \sim 35°$) which possibly distinguish LIBAL QSOs from HIBAL QSOs lead to higher maximum polarizations, as observed. While these models are certainly too simple to reproduce quantitatively the observations, the good overall agreement is encouraging.

A problem with the "wind-from-disk" model is that low-ionization features are assumed to be formed near the disk and therefore only observable for nearly equatorial lines of sight (Murray et al. 1995); low-ionization absorption troughs and high-ionization detached profiles are apparently mutually exclusive. Since this is not the case observationally, we have to admit that low-ionization features could form at large distance from the core also along inclined views. In this case, low-ionization features could be observed not only at the low-velocity end of the high-ionization troughs, but also at higher velocities. And indeed, more complex velocity structures are observed in the low-ionization troughs of two LIBAL QSOs with detached C IV profiles, 0335-3339 and 1231+1320 (Voit et al. 1993), giving some support to this hypothesis. Assuming more extended LIBAL regions would also imply that LIBAL and HIBAL QSOs are different objects, in agreement with other studies (e.g. Boroson & Meyers 1992). Possibly, the efficiency of the X-ray shielding could make the difference.

While unexpected a priori, the correlation found between LIBAL QSO line profiles and continuum polarization fits reasonably well the "wind-from-disk" models, without the need of ad-hoc explanations. Clearly, the possibility of more extended LIBAL regions should be investigated theoretically. More detailed polarization differences between objects with detached and with P Cygni-type profiles should be carefully investigated, namely using spectropolarimetry. Also, possible differences between the X-ray properties of LIBAL and HIBAL QSOs would be worthwhile to detect.

Acknowledgements. This research is supported in part by the contract ARC 94/99-178, and a project funded by SSTC/ Prodex. We would like to thank Jean Surdej for reading the manuscript, and the referee for useful comments.

References

Angonin M.C., Remy M., Surdej J., Vanderriest C., 1990, A&A 233, L5
Arav N., Shlosman I., Weymann R.J., 1997, Mass Ejection from Active Galactic Nuclei. ASP Conference Series 128, San Francisco
Bechtold J., Elvis M., Fiore F., et al., 1994, AJ 108, 374
Becker R.H., Gregg M.D., Hook I., et al., 1997, ApJ 479, L93
Berriman G., Schmidt G.D., West S.C., Stockman H.S., 1990, ApJS 74, 869
Boroson T.A., Meyers K.A., 1992, ApJ 397, 442
Brown J.C., McLean I.S., 1977, A&A 57, 141
Burstein D., Heiles C., 1982, AJ 87, 1165 (BH)
Clavel J., 1998, A&A 331, 853
Cohen M.H., Ogle P.M., Tran H.D., et al., 1995, ApJ 448, L77
de Kool M., Begelman M.C., 1995, ApJ 455, 448
di Serego Alighieri S., 1989, In: Grosbøl P.J. et al. (eds.) 1^{st} ESO/ST-ECF, Data Analysis Workshop, 157
Djorgovski S., Meylan G., 1989, In: Moran J.M. et al. (eds.) Gravitational Lenses. Lect. Notes Phys. 330, 173
Emmering R.T., Blandford R.D., Shlosman I., 1992, ApJ 385, 460
Goodrich R.W., Miller J.S., 1995, ApJ 448, L73
Goodrich R.W., 1997, ApJ 474, 606
Hartig G.F., Baldwin J.A., 1986, ApJ 302, 64 (HB)
Hazard C., Morton D.C., Terlevich R., McMahon R., 1984, ApJ 282, 33
Hewett P.C., Foltz C.B., Chaffee F.H., 1995, AJ 109, 1498
Hiltner W.A., 1956, ApJS 2, 389
Hines D.C., Schmidt G.D., 1997, In: Arav N. et al. (eds.) Mass Ejection from Active Galactic Nuclei. ASP Conference Series 128, 59
Hooper E.J., Impey C.D., Foltz C.B., Hewett P.C., 1995, ApJ 445, 62
Hutsemékers D., 1993, A&A 280, 435
Königl A., Kartje J.F., 1994, ApJ 434, 446
Korista K.T., Voit G.M., Morris S.L., Weymann R.J., 1993, ApJS 88, 357
Melnick J., Dekker H., D'Odorico S., 1989, EFOSC, ESO operating manual No 4, Version 2, ESO
Meylan G., Djorgovski S., 1989, ApJ 338, L1
Michalitsianos A.G., Oliversen R.J., 1995, ApJ 439, 599
Moore R.L., Stockman H.S., 1981, ApJ 243, 60
Moore R.L., Stockman H.S., 1984, ApJ 279, 465
Murray N., Chiang J., Grossman S.A., Voit G.M., 1995, ApJ 451, 498
Press W.H., Flannery B.P., Teukolsky S.A., Vetterling W.T., 1989, Numerical Recipes, Cambridge University Press
Refsdal S., Surdej J., 1994, Rep. Prog. Phys. 56, 117
Reimers D., Bade N., Schartel N., et al., 1995, A&A 296, L49
Schwarz H.E., 1987, In: Polarimetry with EFOSC. ESO Internal Memorandum Dec. 1987
Serkowski K., 1962, In: Kopal Z. (ed.) Advances in Astronomy and Astrophysics. Academic Press 1, 289
Simmons J.F.L., Stewart B.G., 1985, A&A 142, 100
Sprayberry D., Foltz C.B., 1992, ApJ 390, 39
Steidel C.C., Sargent W.L.W. 1992, ApJS 80, 1
Stocke J.T., Morris S.L., Weymann R.J., Foltz C.B., 1992, ApJ 396, 487
Stockman H.S., Moore R.L., Angel J.R.P., 1984, ApJ 279, 485
Véron M.-P., Véron P., 1996, A Catalogue of Quasars and Active Nuclei (7th Edition), ESO Scientific Report 17
Voit G.M., Weymann R.J., Korista K.T., 1993, ApJ 413, 95
Wardle J.F.C., Kronberg P.P., 1974, ApJ 194, 249
Weymann R.J., Morris S.L., Foltz C.B., Hewett P.C., 1991, ApJ 373, 23 (WMFH)

Article 13

The optical polarization of radio-loud and radio-intermediate Broad Absorption Line quasi-stellar objects

D. Hutsemékers, H. Lamy : Astron. Astrophys. 358, 835 (2000)

Afin de comprendre l'origine de la polarisation plus élevée des quasars BAL et plus particulièrement de tester l'hypothèse qu'elle serait due au fait que le continu direct des quasars BAL est plus atténué que celui des quasars non-BAL, nous analysons ici les corrélations possibles entre la puissance radio des quasars BAL, leur polarisation et une série d'indices spectraux. A cet effet, de nouvelles mesures de polarisation ont été obtenues.

L'analyse statistique indique l'absence de corrélations significatives entre le rapport de flux radio / optique $R^\star$ et la polarisation, ainsi qu'entre $R^\star$ et la vitesse terminale du flux de matière, ne confirmant pas les analyses antérieures basées sur de plus petits échantillons.

Astron. Astrophys. 358, 835–840 (2000)

ASTRONOMY AND ASTROPHYSICS

The optical polarization of radio-loud and radio-intermediate broad absorption line quasi-stellar objects⋆

D. Hutsemékers[1,2,⋆⋆] **and H. Lamy**[2]

[1] European Southern Observatory, Casilla 19001, Santiago 19, Chile
[2] Institut d'Astrophysique, Université de Liège, 5 av. de Cointe, 4000 Liège, Belgium

Received 6 January 2000 / Accepted 14 April 2000

Abstract. On the basis of a sample of approximately 50 broad absorption line quasi-stellar objects (BAL QSOs), we investigate possible correlations between BAL QSO radio properties and other spectral characteristics, including polarization. For this purpose new polarization data have been obtained.

The main result of our statistical study is the absence of significant correlations between the radio-to-optical flux ratio $R^\star$ and all other quantities: the polarization p_0 of the continuum, the slope of the continuum, the balnicity and detachment indices which characterize the BAL profiles, and the terminal velocity of the flow $v_{\rm max}$. The claimed anticorrelation between $R^\star$ and $v_{\rm max}$ is therefore not confirmed, as well as the correlation between $R^\star$ and p_0 predicted by some models. Although marginally significant, the only possible correlations occur for the BAL QSOs with low-ionization troughs.

Key words: galaxies: quasars: absorption lines – galaxies: quasars: general – polarization

1. Introduction

About 12% of optically-selected QSOs exhibit broad absorption lines (BALs) in their spectrum, that is resonance line absorption troughs that extend blueward of the emission lines up to $\sim 0.1\,c$. Since the continuum and emission line properties of most BAL QSOs are not found to significantly differ from those of normal (non-BAL) QSOs, it is generally thought that rapidly moving absorbing matter exists in all (at least all radio-quiet) QSOs with a small covering factor, the BAL QSOs being those objects with the absorption region (the BALR) along the line of sight (Junkkarinen 1983, Weymann et al. 1991). Alternatively, if one focuses on the different behavior of the rarer objects with low-ionization absorption troughs, BAL QSOs could constitute a distinct population of QSO, possibly in a different evolutionary stage (Boroson & Meyers 1992). An important characteristic of BAL QSOs is the absence of powerful radio-sources among them (Stocke et al. 1992, Kuncic 1999).

The hypothesis that all radio-quiet QSOs are surrounded by a BALR implies that all differences between BAL and non-BAL QSOs are due to orientation. There are at least two important differences between BAL and non-BAL QSOs: as a class, BAL QSOs are more polarized than non-BAL QSOs (Stockman et al. 1984, Hutsemékers et al. 1998, Schmidt & Hines 1999), and they are more frequently found among radio-intermediate QSOs (Francis et al. 1993). To interpret these differences within the orientation –or unification– model, Goodrich (1997) has suggested that at least some BAL QSOs must have an attenuated direct continuum along our line of sight, such that the scattered light is more important in the total light we see, and then the observed polarization is larger than in non-BAL QSOs. Such an attenuation simultaneously explains why some BAL QSOs dominate the radio-intermediate class: the optical continuum is fainter, and the ratio of radio to optical fluxes is higher. This also means that the true fraction of BAL QSOs in optically-selected samples could be severely underestimated (Goodrich 1997).

The main goal of the present paper is to verify a direct consequence of this interpretation: the existence of a correlation between the optical continuum polarization of BAL QSOs and their radio-to-optical flux ratio. We have therefore compiled linear polarization measurements for a sample of BAL QSOs with known radio properties, essentially taken from the Stocke et al. (1992) VLA radio survey. Additional polarization data have been obtained for BAL QSOs with more extreme radio properties, including the five radio-loud BAL QSOs recently discovered by Brotherton et al. (1998). Furthermore, we investigate possible correlations between absorption line indices and radio properties, and more particularly the claimed anticorrelation between the terminal velocity of the flow and the radio-to-optical flux ratio (Weymann 1997). This relation, if confirmed, provides strong contraints on theoretical models, and may constitute a clue to the radio-loud / radio-quiet dichotomy in QSOs (Murray et al. 1995, Kuncic 1999).

The paper is organized as follows: in Sect. 2, we present the data, new measurements and compilation. The statistical analysis and the results are presented in Sect. 3. Discussion and conclusions form the last section.

⋆ Based on observations collected at the European Southern Observatory (ESO, La Silla)

⋆⋆ Also, Chercheur Qualifié au Fonds National de la Recherche Scientifique (FNRS, Belgium)

Table 1. The sample of BAL QSOs with measured radio flux and polarization

Object	z	Type	BI	$v_{\max}$	DI	$\alpha_{\rm B}$	p_0	$\log R^\star$	$\log L_{\rm rad}$	Ref
B0004+0147	1.71	4	255	>25000	-	-	1.26	< 0.04	< 24.50	3
B0019+0107	2.12	2	2305	13383	4.65	0.73	0.85	< -0.14	< 24.59	1
B0021−0213	2.30	2	5180	12545	3.14	0.66	0.63	< 0.10	< 24.69	1
B0025−0151	2.07	2	2878	22415	2.97	0.34	0.37	< -0.01	< 24.70	1
B0029+0017	2.23	2	5263	10738	2.45	0.55	0.68	< 0.05	< 24.62	1
B0043+0048	2.14	5	4452	17705	10.06	−0.13	0.00	0.76	25.78	1
B0059−2735	1.59	3	11054	18544	1.18	1.50	1.60	< 0.09	< 24.49	1
B0137−0153	2.23	2	4166	9126	2.41	1.01	1.08	0.65	25.26	1
B0145+0416	2.03	2	4765	14480	3.96	0.96	2.68	< -0.50	< 24.38	1
B0146+0142	2.89	-	5523	20866	4.87	0.79	1.21	< -0.56	< 24.87	3
B0226−1024	2.26	2	7373	21834	4.72	0.88	2.50	< -0.38	< 24.76	3
B0254−3327	1.86	2	694	4223	1.08	0.64	0.00	< 0.54	< 24.73	1
B0846+1540	2.91	-	-	-	-	-	0.77	< -0.26	< 24.78	2
B0856+1714	2.32	-	8590	16802	5.43	-	0.66	1.05	25.65	2
B0903+1734	2.78	-	9776	16480	4.34	1.54	0.88	< -0.35	< 24.84	1
B0932+5006	1.91	4	6636	18157	3.88	0.93	1.38	< -0.39	< 24.55	3
B0946+3009	1.22	2	-	-	-	-	0.84	: −1.75	: 23.20	3
B1009+0222	1.35	2	1565	12029	2.02	-	0.75	0.49	24.49	2
B1011+0906	2.26	3	5587	>25000	6.84	1.95	2.10	< -0.38	< 24.67	1
B1029−0125	2.04	2	1849	18738	2.22	0.83	1.09	< 0.11	< 24.56	1
J 1053−0058	1.55	3	255	5300	1.20	0.74	1.89	1.98	25.84	2
J 1104−0004	1.35	3	-	-	-	-	0.45	2.49	25.90	2
B1120+0154	1.47	5	415	9884	0.79	0.45	1.93	< -0.50	< 24.16	1
J 1141−0141	1.27	3	-	-	-	-	0.32	1.73	24.98	2
B1212+1445	1.62	5	3619	19189	6.05	1.51	1.42	0.11	24.62	1
B1216+1103	1.62	2	4792	11900	4.66	0.18	0.55	< 0.24	< 24.50	2
J 1225−0150	2.04	2	3900	24300	7.20	1.50	0.77	1.38	25.19	2
B1228+1216	1.41	2	496	21512	7.17	-	0.00	< -0.38	< 24.17	2
B1230+1705	1.42	2	-	-	-	-	0.25	: −0.09	: 24.23	2
B1231+1320	2.39	4	3473	>25000	6.38	2.15	0.68	< -0.01	< 24.62	1
B1232+1325	2.36	3	12620	>25000	1.84	2.38	1.99	< 0.08	< 24.67	1
B1235+0857	2.89	-	815	4997	0.42	1.04	2.27	0.08	25.09	1
B1235+1807	0.45	3	-	-	-	-	0.00	0.71	24.22	2
B1246−0542	2.22	5	4309	22995	6.60	1.84	0.87	0.06	25.14	1
J 1252+0053	1.69	2	130	15400	5.20	0.64	0.14	2.01	25.73	2
B1254+0443	1.02	2	-	-	-	-	0.58	−0.84	24.01	3
B1309−0536	2.21	2	5363	>25000	5.10	1.41	0.73	< -0.77	< 24.25	1
B1331−0108	1.87	3	7912	21963	1.15	2.66	1.86	0.61	25.24	1
B1333+2840	1.91	2	2357	9448	2.20	0.77	5.88	< -0.03	< 24.59	2
B1413+1143	2.54	5	6621	12351	1.50	1.72	1.50	0.29	25.55	1
B1429−0036	1.18	2	-	-	-	-	0.00	< -0.07	< 24.13	2
B1442−0011	2.22	2	5143	21963	2.83	0.58	0.00	: −0.19	: 24.52	1
B1443+0141	2.45	-	7967	24673	3.26	0.60	1.31	< -0.16	< 24.69	2
B1700+5153	0.29	3	-	-	-	-	0.58	0.56	24.39	3
B2225−0534	1.98	4	7903	15512	0.48	1.68	4.36	< 0.09	< 24.78	1
B2240−3702	1.84	5	8539	23253	0.69	1.08	2.08	< -0.30	< 24.47	1
B2241+0016	1.39	2	-	-	-	-	0.57	< 0.15	< 24.30	3
B2341−2333	2.82	-	-	-	-	-	0.61	0.19	25.23	2
B2350−0045	1.63	4	6964	22995	5.08	1.01	0.53	< 0.28	< 24.50	1

Units: BI and $v_{\max}$ are in km s^{-1}, p_0 in%, and $L_{\rm rad}$ in W Hz^{-1}. Uncertain radio measurements are indicated (:)
Object Type: (2) HIBAL QSOs, (3) Strong LIBAL QSOs, (4) Weak LIBAL QSOs, (5) Marginal LIBAL QSOs
References for polarization: (1) Hutsemékers et al. 1998, (2) Lamy & Hutsemékers 2000, (3) Schmidt & Hines 1999

2. The data

The considered sample is constituted of BAL QSOs with measured radio flux and good quality broad-band polarization data compiled from the literature. It also includes polarization measurements specifically obtained for the present study. This sample is given in Table 1. Table 2 contains additional BAL QSOs

for which only radio flux and absorption line indices are available.

Tables 1 and 2 list the QSO position-name (B1950 or J2000), the redshift z, and the object type / classification which depends on the presence of low-ionization BAL troughs. The balnicity index BI, the maximum velocity $v_{\rm max}$, and the detachment index DI are quantities which characterize the BALs, while $\alpha_{\rm B}$ is the continuum power-law index, and p_0 the debiased polarization degree. $R^\star$ is the K-corrected radio-to-optical flux ratio, and $L_{\rm rad}$ the radio power at 5 GHz. Details on these quantities are given below.

2.1. The radio data

Most radio measurements are from the Stocke et al. (1992) BAL QSO VLA radio survey at 5 GHz. This sample provides a homogeneous set of K-corrected radio-to-optical flux ratios, and of radio powers in W Hz^{-1}, K-corrected to 5 GHz in the QSO rest-frame.

For only one object of our previous polarization survey (Hutsemékers et al. 1998, hereafter Paper I), B1120+0154 (= UM425), an additional radio measurement is found in the literature (Meylan & Djorgovski 1989). It is included in Table 1 after computing $R^\star$ and $L_{\rm rad}$ following the prescriptions of Stocke et al. (1992).

Since then, a handful of radio-loud BAL QSOs has been discovered by Brotherton et al. (1998). These five unusual objects (with J2000 coordinates) are also included in our sample. The K-corrected radio-to-optical flux ratios are from Brotherton et al. (1998), while the radio powers have been computed and K-corrected to 5 GHz according to Stocke et al. (1992). None of these formally radio-loud[1] BAL QSOs appear to be powerful radio sources (i.e. all have $\log R^\star \lesssim 2.5$; see also the discussion by Kuncic 1999).

2.2. The polarization

Most polarization data come from our previous survey (Paper I). However this sample was not chosen to investigate possible correlations with radio properties, and additional measurements were needed. Using the ESO 3.6m telescope + EFOSC, we then obtained new broad-band linear polarization data for 16 BAL QSOs, most of them with extreme radio properties, i.e. with the highest $R^\star$ values or with stringent upper limits. These data are presented in Lamy & Hutsemékers (2000) with full account of the observation and reduction details. We also refer the reader to Paper I and to Lamy & Hutsemékers (1999) for details related to our previous survey and to reduction procedures. The polarization degree p_0 reported in Table 1 is debiased according to the Wardle & Kronberg (1974) method. Typical uncertainties of the polarization degree are 0.2–0.3%.

[1] QSOs with $\log R^\star \geq 1$ are considered as formally radio-loud. As a definition of radio-intermediate QSOs, we adopt $0 < \log R^\star < 1$, in order to encompass objects classified as such by Francis et al. (1993). Radio-quiet QSOs have $\log R^\star \leq 0$

Independently of our survey, Schmidt & Hines (1999) have recently published a large number of BAL QSO polarization data, obtained mostly in white light. For the sake of homogeneity, we consider in Table 1 only the BAL QSOs of their sample with polarization degrees sufficiently accurate, i.e. with $\sigma_p \leq 0.4\%$, σ_p denoting the uncertainty of the observed polarization degree p. This constraint, also applied to our data, is important since several BAL QSOs have low polarization levels ($p \leq 1\%$). 8 BAL QS0s from the Schmidt & Hines (1999) sample and with available radio measurements are then added to our sample. Their polarization degrees have been similarly debiased. The data of Schmidt & Hines (1999) also confirm our previous measurement of the polarization of B0145+0416, which was questioned in Paper I. Note finally that their spectropolarimetric data clearly show that broad-band polarization measurements represent fairly well the polarization of the continuum.

2.3. The spectral indices

Weymann et al. (1991) provide a series of useful spectral indices to characterize the absorption features of BAL QSOs. They define the balnicity index BI which is a modified velocity equivalent width of the C IV $\lambda1549$ BAL, and the detachment index DI which measures the onset velocity of the strongest C IV BAL trough in units of the adjacent emission line half-width, that is the degree of detachment of the absorption line relative to the emission one (cf. Weymann et al. 1991 for more details). C IV BI and DI are reported in Tables 1 and 2. When BI are also given by Korista et al. (1993), we adopt an average of these values and those of Weymann et al. (1991). For the radio-loud BAL QSOs, BI are from Brotherton et al. (1998). We do not consider BI measured from other BAL troughs.

For a few BAL QSOs of our sample, the C IV DI are not given by Weymann et al. (1991). Therefore, as in Paper I, we have computed them by using good quality published spectra, when available. The spectra were digitally scanned, and the measurements done following the prescriptions by Weymann et al. (1991). The new measurements make use of spectra published by Korista et al. (1993) and Brotherton et al. (1998), and are reported in Tables 1 and 2 together with values from Paper I. Only one object (B0004+0147) with a spectrum in Korista et al. (1993) has no measured DI, due to an unusual emission line profile.

In addition to BI and DI, we have also reported in Tables 1 and 2 the maximum velocity in the C IV BAL trough, $v_{\rm max}$, which provides an estimate of the terminal velocity of the flow. For the radio-loud BAL QSOs, values of $v_{\rm max}$ are given by Brotherton et al. (1998). For other objects, $v_{\rm max}$ is evaluated from the Korista et al. (1993) and Steidel & Sargent (1992) spectra, by measuring, from the blue to the red, the wavelength at which the absorption first drops $\sim 10\%$ below the flux level defined by the local continuum (cf. also Lee & Turnshek 1995). Narrow or weak high-velocity absorption features are not taken into account. Further, at velocities higher than $\sim$25000 km s^{-1}, C IV BALs may be contaminated by the Si IV emission line, such

Table 2. Additional BAL QSOs with measured radio flux and BAL indices

Object	z	Type	BI	$v_{\max}$	DI	$\alpha_{\rm B}$	$\log R^\star$	$\log L_{\rm rad}$
B0135−4001	1.85	-	3577	17834	7.38	-	< -0.46	< 24.53
B0324−4047	3.06	-	3614	19899	5.00	-	< -0.19	< 25.21
B1208+1535	1.96	2	4545	17770	4.64	0.42	< -0.03	< 24.60
B1235+1453	2.68	-	2658	13835	3.55	1.01	< 0.13	< 24.92
B1240+1607	2.36	2	2867	21382	4.47	1.06	< 0.09	< 24.71
B1243+0121	2.79	-	5953	15319	2.35	1.17	< -0.03	< 24.84
B1303+3048	1.76	2	1897	10996	2.27	0.57	< -0.42	< 24.60
B1314+0116	2.69	-	2626	13899	7.41	0.64	< -0.03	< 24.77
B1336+1335	2.43	-	5973	15448	1.18	-	< 0.52	< 24.85
B1414+0859	2.64	-	3516	>25000	11.00	-	< 0.49	< 24.70
B1504+1041	3.07	-	4140	17834	3.23	-	< 0.71	< 24.91
B2201−1834	1.82	5	1613	19963	2.19	2.37	< -0.34	< 24.55
B2212−1759	2.21	-	2221	8480	6.70	-	< -0.14	< 24.70

Units and Object Type are as in Table 1

that the measurement of $v_{\max}$ becomes inaccurate. We therefore limit $v_{\max}$ to 25000 km s^{-1} from the C IV emission centroid, in agreement with the definition of BI (Weymann et al. 1991). This limit constitutes, in a few cases, a lower limit to the true $v_{\max}$.

Finally, we have measured the slope of the continuum as in Paper I. Using spectra published by Weymann et al. (1991) and by Brotherton et al. (1998), a power-law continuum $F_\nu \propto \nu^{-\alpha}$ was fitted blueward of C III] λ1909 (cf. Paper I). The resulting index $\alpha_{\rm B}$ is provided in Tables 1 and 2.

2.4. The LIBAL / HIBAL classification

Approximately 15% of BAL QSOs have deep low-ionization BALs (Mg II λ2800 and/or Al III λ1860) in addition to the usual high-ionization troughs (Weymann et al. 1991, Voit et al. 1993). These objects could be significantly reddened by dust (Sprayberry & Foltz 1992). Since they have no or very weak [O III] λ5007 emission compared to other objects, Boroson & Meyers (1992) have argued that LIBAL QSOs are not seen along a preferred line of sight but could constitute a physically different class of BAL QSOs.

In Paper I, we have defined three categories of LIBAL QSOs: strong (S), weak (W), and marginal (M) LIBAL QSOs. Indeed, in addition to the strong and weak LIBAL QSOs, first classified as such by Weymann et al. (1991), several authors have reported faint LIBAL features in a number of other objects (Hartig & Baldwin 1986, Hazard et al. 1984). We have classified the latter objects as marginal LIBAL QSOs. They are characterized by very weak Mg II and/or Al III BALs. The asymmetry of the Mg II or C III] emission lines, when cut on the blue side, is also considered as evidence for marginal LIBALs (Hartig & Baldwin 1986). BAL QSOs with no evidence for low-ionization features are classified as high-ionization (HI) BAL QSOs. Objects with poor quality spectra, or objects with no Al III BAL and Mg II outside the observed spectral range, remain unclassified (cf. Paper I for additional details and examples). It is important to note that the present classification somewhat differs from other classifications found in the literature. Most often, the BAL QSOs defined in the literature as low-ionization BAL QSOs are the S-LIBALs or the S-LIBALs + W-LIBALs, while the high-ionization BAL QSOs are anything else, including M-LIBALs and unclassified objects.

Our classification is summarized in Tables 1 and 2. It is based on a careful inspection of good-quality spectra available in the literature (Brotherton et al. 1998, Foltz et al. 1987, 1989, Hewett et al. 1991, Steidel & Sargent 1992, Turnshek et al. 1985, Turnshek & Grillmair 1986, Turnshek 1988, Wampler 1983, Weymann et al. 1991). Several BAL QSO sub-types were already given and discussed in Paper I.

3. Results of statistical tests

Before presenting the results of the statistical tests, it is immediately clear from Table 1 that radio-intermediate and radio-loud BAL QSOs are not the most polarized objects. Among the five radio-loud BAL QSOs from Brotherton et al. (1998), only one, J1053-0058, which belongs to the LIBAL class, is significantly polarized with $p_0 \simeq 1.9\%$. It is particularly interesting to note that J1053-0058 has the smallest detachment index among the radio-loud BAL QSOs, in good agreement with the anticorrelation between p_0 and DI found in Paper I[2].

Since $R^\star$ and $L_{\rm rad}$ are often upper limits, the search for possible correlations between $\log R^\star$ (or $\log L_{\rm rad}$) and other BAL QSO properties must rely on survival analysis. We then use the standard survival analysis tests available in the ASURV Rev. 1.3 package (LaValley et al. 1992). Several sub-samples are considered: LIBAL QSOs, HIBAL QSOs, and BAL QSOs with $z > 1.5$. The latter limit corresponds to the redshift at which the C IV BAL starts to be detected in the visible. Probabilities (P) that the observed statistics occur by chance among indices uncorrelated with $\log R^\star$ are summarized in Table 3, using the generalized Kendall τ and Spearman ρ rank order correlation coefficients, and the Cox proportional hazard model (LaValley

[2] The anticorrelation between p_0 and DI is confirmed and even more significant when taking into account the polarization data presented here (i.e. with 37 BAL QSOs instead of 29 in Paper I)

Table 3. Analysis of correlation of various indices with $\log R^\star$

	p_0	BI	DI	$\alpha_{\rm B}$	$-v_{\rm max}$	
All BALs	0.09	0.45	0.93	0.61	-	C
	0.11	0.44	0.92	0.58	0.20	K
	0.05	0.45	0.72	0.91	0.15	S
	−	−	−	+	+	
	49/28	51/38	50/37	41/30	51/38	n/m
HI BALs	0.29	0.44	0.85	0.35	-	C
	0.97	0.16	0.71	0.22	0.93	K
	0.49	0.24	0.72	0.83	0.62	S
	−	−	−	+	+	
	22/14	20/15	20/15	18/14	20/15	n/m
LI BALs	**0.03**	0.56	0.38	0.50	-	C
	0.03	0.58	0.74	0.51	**0.04**	K
	0.03	0.95	0.70	0.65	0.06	S
	−	+	+	−	+	
	20/10	17/11	16/10	16/10	17/11	n/m
All BALs	0.19	0.38	0.75	0.70	-	C
$z > 1.5$	0.32	0.49	0.71	0.67	0.24	K
	0.11	0.30	0.85	0.89	0.15	S
	−	−	−	−	+	
	37/24	48/36	47/35	40/29	48/36	n/m

This table gives the probabilities that the observed statistics (Cox, Kendall, Spearman) occur by chance among uncorrelated quantities. n is the number of objects considered in the correlation analysis, and m the number of objects with $\log R^\star$ upper limits. The sign of the correlation is also given, from the sign of the Spearman ρ. The three less accurate values of $\log R^\star$ are considered as detections, although the results are unchanged if they are not taken into account. The Cox model cannot be used to test correlations with $-v_{\rm max}$, since $-v_{\rm max}$ is also left-censored. Some results, obtained with very few detections and given here for completeness, must be seen with caution

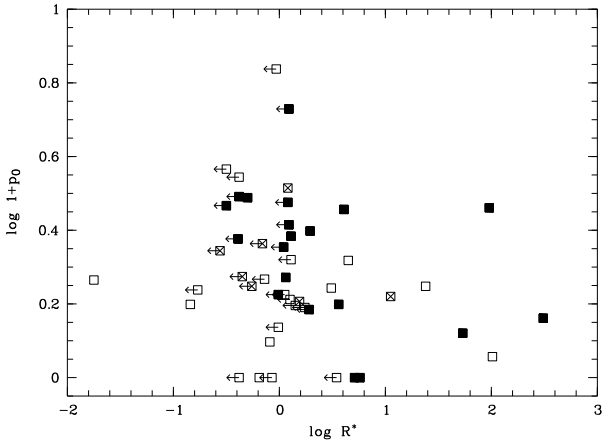


Fig. 1. The BAL QSO polarization, p_0, is plotted here against the radio-to-optical flux ratio, $R^\star$. Censored data points are indicated. Open squares represent HIBAL QSOs, filled squares LIBAL QSOs, and squares with a cross unclassified BAL QSOs

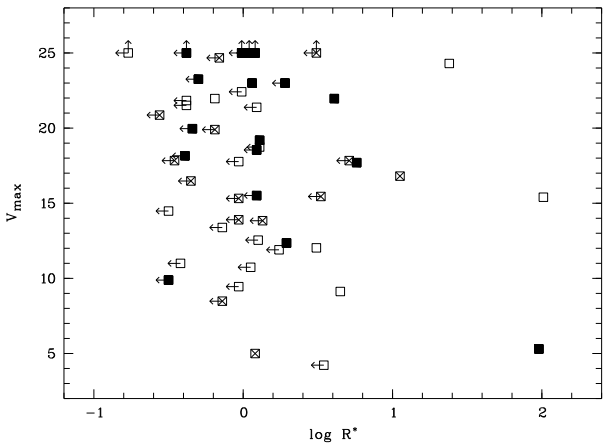


Fig. 2. The C IV BAL maximum velocity, $v_{\rm max}$, is plotted here against the radio-to-optical flux ratio, $R^\star$. Censored data points are indicated. Open squares represent HIBAL QSOs, filled squares LIBAL QSOs, and squares with a cross unclassified BAL QSOs

et al. 1992, Isobe et al. 1986). Results from Table 3 indicate that $\log R^\star$ is essentially uncorrelated with the other quantities ($P \geq 0.05$), except within the LIBAL QSO sub-sample. The statistical analysis includes the few radio-loud BAL QSOs. Indeed, these objects, although formally radio-loud, are not powerful radio-sources and mostly in the radio-quiet / radio-loud transition region. However, since the original suggestion by Goodrich (1997) only includes formally radio-intermediate objects, we have also considered the sample of BAL QSOs with $\log R^\star < 1$. In this case, the results of Table 3 are basically unchanged, P being only slightly higher for the weak correlations detected in the LIBAL QSO sub-sample. Finally the same statistical analysis has been carried out considering $\log L_{\rm rad}$ instead of $\log R^\star$, with the result that $\log L_{\rm rad}$ is totally uncorrelated with the other quantities, whatever the sub-sample.

Within the LIBAL QSO sub-sample, the statistical tests suggest the existence of a weakly significant anticorrelation between $\log R^\star$ and p_0 ($P \leq 0.05$ for all tests), and a marginally significant anticorrelation between $\log R^\star$ and $v_{\rm max}$ ($P \leq 0.05$ for only one test). We have therefore plotted p_0 and $v_{\rm max}$ against $\log R^\star$ in Figs. 1 and 2. The anticorrelations do not appear very convincing. And indeed, if we delete only one object from the LIBAL QSO sub-sample (e.g. B2225-0534 in Fig. 1, and J1053-0058 in Fig. 2), the statistical tests indicate that the correlations are not significant any longer. Further, if one restricts the LIBAL QSO sub-sample to high-redshift objects ($z > 1.5$), the correlation between p_0 and $\log R^\star$ disappears ($P > 0.35$ with n/m = 15/9), suggesting a possible bias. Note that due to the limited sample of LIBAL QSOs, no distinction between LIBAL sub-types was made.

In view of the apparently different behavior of LIBAL QSOs, we have also compared the distribution of $\log R^\star$ for the LIBAL and HIBAL QSO sub-samples, again using standard survival analysis tests from the ASURV package. Tests include the Logrank test, and the Gehan, Peto & Peto, and Peto & Prentice generalized Wilcoxon tests (LaValley et al. 1992,

Feigelson et al. 1985). The probability that the two samples (25 HIBALs and 21 LIBALs) are drawn from the same parent population is found to range from 0.06 to 0.09, depending on the test. This means that no significant difference in the distribution of $\log R^\star$ is detected when comparing the LIBAL and HIBAL QSO sub-samples.

4. Discussion and conclusions

On the basis of a sample of approximately 50 BAL QSOs, we have investigated possible correlations between BAL QSO radio properties and other spectral characteristics, including polarization and the terminal velocity of the flow.

The main result of our statistical study is the absence of correlations between the radio-to-optical flux ratio, $R^\star$, and all other quantities: polarization and slope of the continuum, balnicity and detachment indices, and the terminal velocity of the flow. The anticorrelation between $R^\star$ and $v_{\rm max}$ claimed by Weymann (1997) and Kuncic (1999) is therefore not confirmed. Furthermore, we do not support the relation between $R^\star$ and p_0 suggested by the model of Goodrich (1997), even if we restrict our sample to the formally radio-intermediate objects.

The only possible correlations occur within the LIBAL QSO sub-sample, which, once more, seems to behave differently. But the significance is marginal and additional data are necessary. It is nevertheless important to remark that, if real, the relation between $R^\star$ and p_0 is opposite to the prediction of Goodrich (1997) who suggests that p_0 would be higher for objects with large $R^\star$ as a result of a stronger attenuation of the UV rest-frame continuum.

It is also interesting to note that $R^\star$ is uncorrelated with the continuum power-law index $\alpha_{\rm B}$, i.e. with dust extinction (Sprayberry & Foltz 1992). This is in agreement with the results of Hall et al. (1997) who found, from the distribution of optical / near-infrared colours, that the excess of BAL QSOs among radio-intermediate QSOs cannot be attributed to extinction.

Within the unification scheme, different orientation and attenuation of the continuum are probably necessary to explain the different polarization properties of BAL and non-BAL QSOs (Goodrich 1997). Our results indicate that this interpretation cannot simultaneously explain the excess of BAL QSOs among radio-intermediate QSOs. Another interpretation of BAL QSO radio properties is therefore needed.

Alternatively, we may abandon the hypothesis that all observed differences between BAL and non-BAL QSOs are only due to different orientations. The BAL phenomenon may then be seen as an evolutionary mass-loss phase, and properties like polarization could be related to the presence of ejected material. The range of BAL QSO radio properties can also be explained considering models like that of Kuncic (1999) which associates the BAL region with a poorly collimated and weakly radio-emitting jet. The lack of correlation between $v_{\rm max}$ and $R^\star$ does not support this model, although it should be pointed out that it does not necessarily refute it. Indeed, the relation between $v_{\rm max}$ and $R^\star$ may depend on several other parameters, like the covering factor or the orientation of the jet. In this view, the eventual detection of a significant anticorrelation between $v_{\rm max}$ and $R^\star$ within a larger LIBAL QSO sub-sample would fix some of these parameters, and provide useful constraints on the models.

Acknowledgements. The SIMBAD database operated by the CDS has been consulted. HL is supported in part by contracts ARC 94/99-178 and PAI P4/05. The referee is acknowledged for useful comments.

References

Boroson T.A., Meyers K.A., 1992, ApJ 397, 442
Brotherton M.S., van Breugel W., Smith R.J., et al., 1998, ApJ 505, L7
Feigelson E.D., Nelson P.I., 1985, ApJ 293, 192
Foltz C.B., Chaffee F.H., Hewett P.C., et al. 1987, AJ 94, 1423
Foltz C.B., Chaffee F.H., Hewett P.C., et al. 1989, AJ 98, 1959
Francis P.J., Hooper E.J., Impey C.D., 1993, AJ 106, 417
Goodrich R.W., 1997, ApJ 474, 606
Hall P.B., Martini P., DePoy D.L., Gatley I., 1997, ApJ 484, L17
Hartig G.F., Baldwin J.A., 1986, ApJ 302, 64
Hazard C., Morton D.C., Terlevich R., McMahon R., 1984, ApJ 282, 33
Hewett P.C., Foltz C.B., Chaffee F.H., 1991, AJ 101, 1121
Hutsemékers D., Lamy H., Remy M., 1998, A&A 340, 371 (Paper I)
Isobe T., Feigelson E.D., Nelson P.I., 1986, ApJ 306, 490
Junkkarinen V.T., 1983, ApJ 265, 73
Korista K.T., Voit G.M., Morris S.L., Weymann R.J., 1993, ApJS 88, 357
Kuncic Z., 1999, PASP 111, 954
Lamy H., Hutsemékers D., 1999, The Messenger 96, 25 (Erratum: The Messenger 97, 23)
Lamy H., Hutsemékers D., 2000, A&AS 142, 451
LaValley M., Isobe T., Feigelson E.D., 1992, BAAS 24, 839
Lee L.W., Turnshek D.A., 1995, ApJ 453, L61
Meylan G., Djorgovski S., 1989, ApJ 338, L1
Murray N., Chiang J., Grossman S.A., Voit G.M., 1995, ApJ 451, 498
Schmidt G.D., Hines D.C., 1999, ApJ 512, 125
Sprayberry D., Foltz C.B., 1992, ApJ 390, 39
Steidel C.C., Sargent W.L.W., 1992, ApJS 80, 1
Stocke J.T., Morris S.L., Weymann R.J., Foltz C.B., 1992, ApJ 396, 487
Stockman H.S., Moore R.L., Angel J.R.P., 1984, ApJ 279, 485
Turnshek D.A., Foltz C.B., Weymann R.J., et al., 1985, ApJ 294, L1
Turnshek D.A., Grillmair C.J., 1986, ApJ 310, L1
Turnshek D.A. 1988, in: Blades J.C. et al. (eds), QSO absorption Lines: Probing the Universe, Cambridge, p. 17
Voit G.M., Weymann R.J., Korista K.T., 1993, ApJ 413, 95
Wampler E.J., 1983, A&A 122, 54
Wardle J.F.C., Kronberg P.P., 1974, ApJ 194, 249
Weymann R.J., Morris S.L., Foltz C.B., Hewett P.C., 1991, ApJ 373, 23
Weymann 1997, in: Arav N., et al. (eds), Mass Ejection from Active Galactic Nuclei, ASP Conference Series 128, p. 3

Article 14

The polarization properties of Broad Absorption Line QSOs : observational results

D. Hutsemékers, H. Lamy : in Mass Outflow in Active Galactic Nuclei : New Perspectives, D.M. Crenshaw et al. (eds.), A.S.P. Conference Series 255, 207 (2002)

Cette contribution résume les principaux résultats des deux articles précédents tout en tenant compte de nouvelles mesures obtenues entretemps.

La différence de polarisation entre quasars LIBAL, HIBAL et non-BAL est confirmée ainsi que les corrélations mises en évidence dans l'article 12 et notamment la relation entre la polarisation du continuum et l'indice de détachement des raies BAL.

En addendum, nous présentons la spectropolarimétrie de six quasars BAL dont le mirage gravitationnel H1413+117. Nous dégageons quelques tendances générales et plus particulièrement une relation possible entre l'indice de détachement des raies BAL et la profondeur de l'absorption dans le spectre polarisé.

Mass Outflow in Active Galactic Nuclei: New Perspectives
ASP Conference Series, Vol. 255, 2002
D.M. Crenshaw, S.B. Kraemer, and I.M. George

The Polarization Properties of Broad Absorption Line QSOs: Observational Results

D. Hutsemékers[1]

European Southern Observatory, Chile

H. Lamy

University of Liège, Belgium

Abstract. Correlations between BAL QSO intrinsic properties and polarization have been searched for. Some results are summarized here, providing possible constraints on BAL outflow models.

1. Introduction

From 1994 to 1999 we have obtained broad-band linear polarization measurements for a sample of approximately 50 Broad Absorption Line (BAL) QSOs using the ESO 3.6m telescope at La Silla (Chile).
On the basis of this sample plus additional data compiled from the literature, possible correlations between BAL QSO intrinsic properties and polarization have been searched for. Here we present some of our most interesting results, updated with recent data.

2. Analysis and results

A careful distinction between BAL QSO subtypes has been done. In addition to the BAL QSOs with high-ionization (HI) absorption features only, we have distinguished BAL QSOs with strong (S), weak (W), and marginal (M) low-ionization (LI) absorption troughs (Hutsemékers et al. 1998, 2000 for details).
Several indices are used to quantify the spectral characteristics: the balnicity index (BI) which is a modified velocity equivalent width of the C IV BAL, the detachment index (DI) which measures the degree of detachment of the absorption trough relative to the emission line, the maximum velocity $v_{\rm max}$ in the C IV BAL, and the power-law index α of the continuum.
Although most BAL QSOs are radio-quiet, some of them appear radio-moderate, and radio-to-optical flux ratios $R^\star$ were also collected.
Correlations and sample differences were searched for by means of the usual statistical tests. Survival analysis was used for censored data (mainly $R^\star$). While the study of polarization was our main goal, correlations between different in-

[1]Also Research Associate FNRS, University of Liège, Belgium

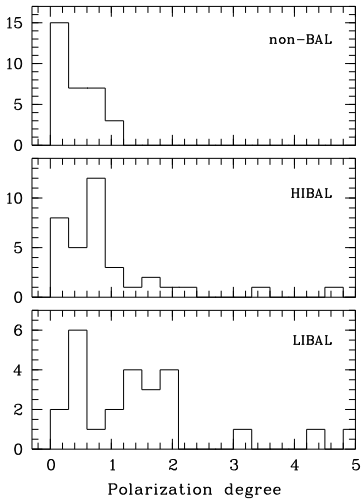


Figure 1. The distribution of the polarization degree p_0 (in %) for the three main classes of QSOs. LIBAL QSOs contain the three sub-categories, i.e. strong, weak and marginal LIBAL QSOs. Data are from H1998, S1999, L2000, O2000 (a LIBAL QSO with p_0=7.5 and the unclassified BAL QSOs are not represented here)

dices have also been considered.
Results presented by Hutsemékers et al. (1998, 2000; H1998, H2000) are updated with polarimetric data from Schmidt & Hines (1999; S1999), Lamy & Hutsemékers (2000; L2000), and Ogle et al. (2000; O2000). Only polarimetric measurements with $\sigma_p \leq 0.4\%$ are taken into account, such that the debiased polarization degree p_0 has a typical uncertainty σ_p = 0.2-0.3%. The radio-loud BAL QSOs recently discovered in the FIRST survey (Becker et al. 2000; B2000) are included in the present study.

• Evidence for polarization differences between low- and high-ionization BAL QSOs
The distribution of the polarization degree p_0 for the three main classes of QSOs is illustrated in Fig. 1. We can see that the bulk of QSOs with $p_0 > 1.2\%$ belong to the sub-class of LIBAL QSOs. Note that not all LIBAL QSOs are highly polarized. As a class, HIBAL QSOs appear less polarized than LIBAL QSOs and more polarized that non-BAL QSOs. They seem to have intermediate properties. All these differences are statistically significant ($P_{\rm K-S} \geq 99\%$).

• The correlation between the balnicity and the slope of the continuum
In addition to their higher polarization, it is seen from Fig. 2 that most LIBAL QSOs have also larger balnicities and more reddened continua than HIBAL QSOs. Considering the whole BAL QSO sample (i.e. HI+LI BALs), a significant ($P_\tau \geq 99\%$) correlation is found between the balnicity index BI and the slope of the continuum. Since LIBAL QSOs as a class are more reddened and

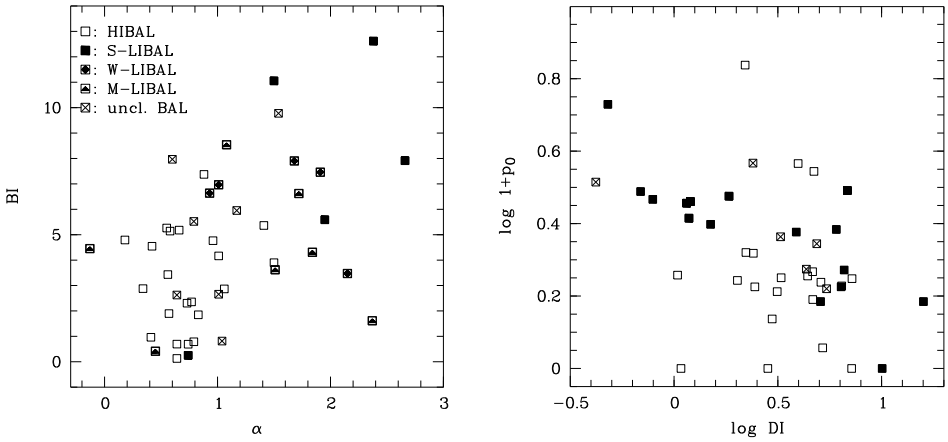


Figure 2. **Left**: the correlation between the balnicity index BI (in 10^3 km s^{-1}) and the power-law index α ($F_\nu \propto \nu^{-\alpha}$). The 3 subcategories of LIBAL QSOs are distinguished here. Data and objects are from H1998, L2000, H2000. **Right**: the correlation between the polarization degree p_0 (in %) and the line profile detachment index DI. The correlation is especially apparent for the LIBAL QSOs (filled squares). Data from H1998, S1999, L2000

more polarized than HIBAL QSOs, it also results a correlation between the power-law index and the polarization, although less convincing.

• The correlation between the polarization of the continuum and the line profile detachment index

Among several possible correlations of the polarization with spectral indices like the balnicity index, the equivalent width and the velocity width of C IV and C III], the only significant ($P_\tau \geq 99\%$) correlation we found is a correlation with the line profile detachment index, quite unexpectedly. Fig. 2 illustrates the correlation between the polarization degree p_0 and the line profile detachment index DI for all BAL QSOs of our sample. The correlation is especially apparent and significant for the LIBAL QSOs. It indicates that the BAL QSOs with P Cygni-type line profiles (DI$\ll$) are the most polarized.

• The absence of correlation between the polarization and $R^\star$

If the higher polarization of BAL QSOs as a class is due to an attenuation of the direct continuum with respect to the scattered one –at least in some objects– (Goodrich 1997), then we expect the polarization to be correlated with the radio-to-optical flux ratio. In Fig. 3, the BAL QSO polarization p_0 is plotted against the radio-to-optical flux ratio $R^\star$. No correlation is seen, as confirmed by the statistical tests. Note that the distribution of $R^\star$ is not found to differ between the HIBAL and LIBAL subsamples

• The absence of correlation between the terminal velocity and $R^\star$

In order to investigate the claimed anticorrelation between the terminal velocity of the flow and the radio-to-optical flux ratio (Weymann 1997), we have plotted

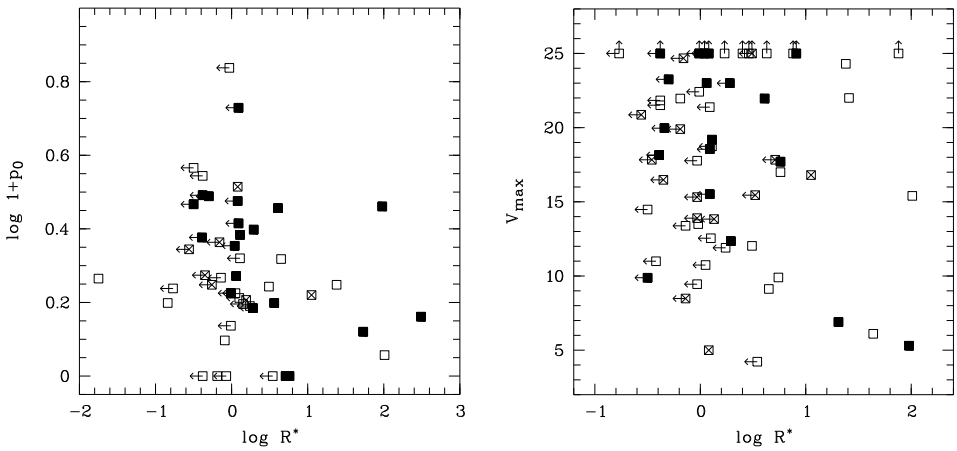


Figure 3. **Left**: The polarization degree p_0 plotted against the radio-to-optical flux ratio $R^\star$. Data are from H2000. **Right**: the maximum velocity $v_{\rm max}$ in the C IV BAL (in 10^3 km s^{-1}) is plotted against the radio-to-optical flux ratio $R^\star$. Data from H2000, B2000. In both figures, open squares represent HIBAL QSOs, filled squares LIBAL QSOs, and squares with a cross unclassified BAL QSOs, while arrows indicate censored data points

in Fig. 3 the maximum velocity $v_{\rm max}$ in the C IV BAL against the radio-to-optical flux ratio $R^\star$. No correlation is found, as confirmed by the statistical tests.

3. Conclusions

Our results show that polarization is correlated with BAL QSO line profiles and types, emphasizing the extreme behavior of LIBAL QSOs already reported by several studies. These results could provide constraints on the BAL outflow models and geometry. As discussed by Hutsemékers et al. (1998), they are consistent with the Murray et al. (1995) disk-wind model.

References

Becker, R. et al. 2000, ApJ 538, 72 [B2000]
Goodrich, R. 1997, ApJ 474, 606
Hutsemékers, D., Lamy, H., Remy, M. 1998, A&A 340, 371 [H1998]
Hutsemékers, D., Lamy, H. 2000, A&A 358, 835 [H2000]
Lamy, H., Hutsemékers, D. 2000, A&AS 142, 451 [L2000]
Murray, N. et al. 1995, ApJ 451, 498
Ogle, P. et al. 2000, ApJS 125, 1 [O2000]
Schmidt, G., Hines, D. 1999, ApJ 512, 125 [S1999]
Weymann, R. 1997, ASP Conf 128, 3

Addendum
Spectropolarimetry of BAL QSOs : new data and trends

Spectropolarimetric data are given for six BAL QSOs (Fig. 1). The observations were carried out as described in Paper 15, and will be discussed in details in a forthcoming paper (Lamy & Hutsemékers 2003). Here, we only present a few results.

First, the main features of BAL QSO spectropolarimetry can be observed in our data : a net increase of the polarization in the broad absorption lines, and the fact that BALs are often seen in the polarized spectrum while emission lines are usually not (Ogle et al. 2000). These properties may be interpreted by electron scattering of the continuum either within the BAL flow or within a separated "polar" region (Ogle et al. 2000).

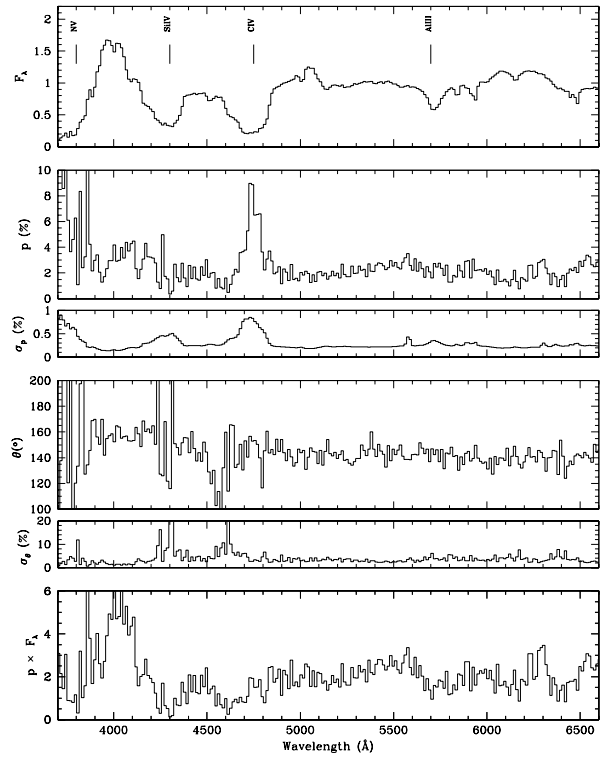
An interesting new result is the different behavior of objects with detached troughs like Q1246−0542 and objects with P Cygni profiles like Q2225−0534 : absorption in the polarized spectrum seems deeper for P Cygni BALs than for detached BALs. In order to quantify these properties, and to search for correlations with other parameters, we have measured a series of spectropolarimetric indices for the objects of our sample, augmented with those from Ogle's atlas. In Fig. 2 we show the possible relation between SI, the ratio of the CIV absorption depths measured in the polarized and the total spectra, and the BAL detachment index DI. If real, this relation supports the interpretation of the DI / p_0 correlation and the BAL QSO model depicted in Papers 12–14. Indeed, if detached BALs are related to a disk inclined with respect to the line of sight, polarized radiation can escape the flow without being re-absorbed, while for P Cygni type BALs the disk is seen nearly edge-on and the polarized flux is more often re-absorbed .

Spectropolarimetry of the gravitationally lensed BAL QSO H1413+117 is illustrated in Figs. 1 and 3. First note that with P Cygni type BALs, H1413+117 does follow the general DI / p_0 and DI / SI trends. Its polarization properties are quite similar to those of other BAL QSOs except that the broad emission lines are polarized as the continuum and are well seen in the polarized flux (Fig. 1). This object also shows a net rotation of the polarization angle within the absorption lines suggesting the existence of at least two sources and/or mechanisms of polarization. Remarkably, only the "disk" absorption is seen in the polarized spectrum (Fig. 3), i.e. along the line of sight from which the scattered continuum emerges. These characteristics can be interpreted in the framework of the two-component outflow model proposed in Paper 8. Assuming that the observed polarization is a combination of perpendicular polarizations due to scattering in the polar component of the wind and in the disk, the continuum (or the emission lines) scattered in the wind can be re-absorbed in the disk, such that only this absorption is detected in the polarized spectrum. In the absorption lines, the relative importance of the wind and the disk contributions then changes, leading to the observed rotation of the polarization angle.

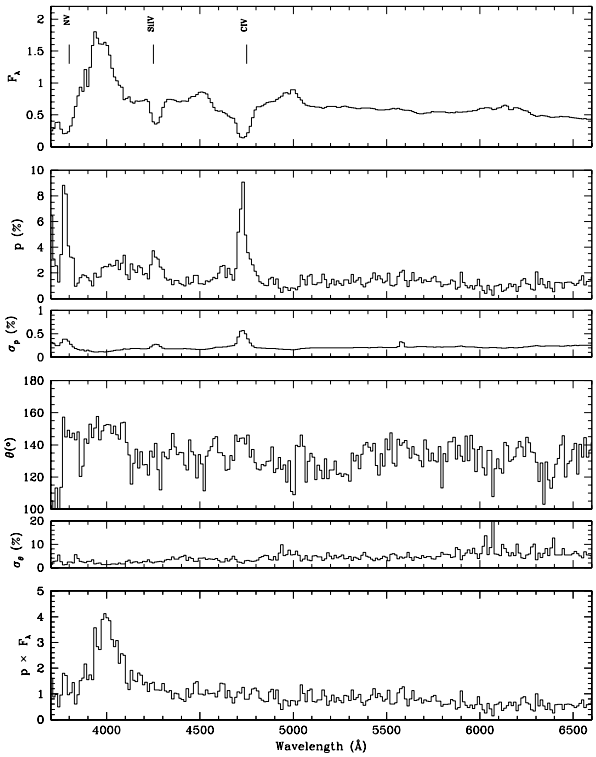
References

- Lamy, H., Hutsemékers, D., 2003, A&A, in preparation
- Ogle, P., et al., 2000, ApJS 125, 1, and references therein

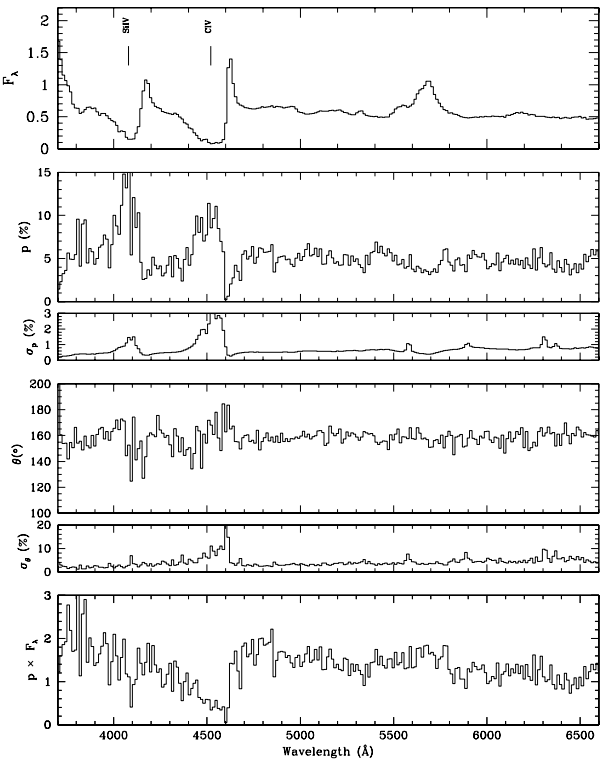
Q1011+0906



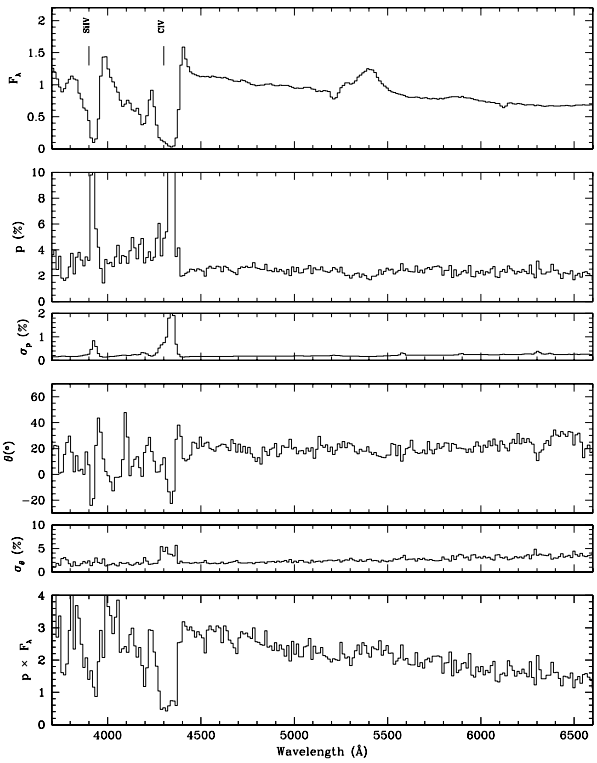
Q1246−0542



Q2225−0534



Q2240−3702



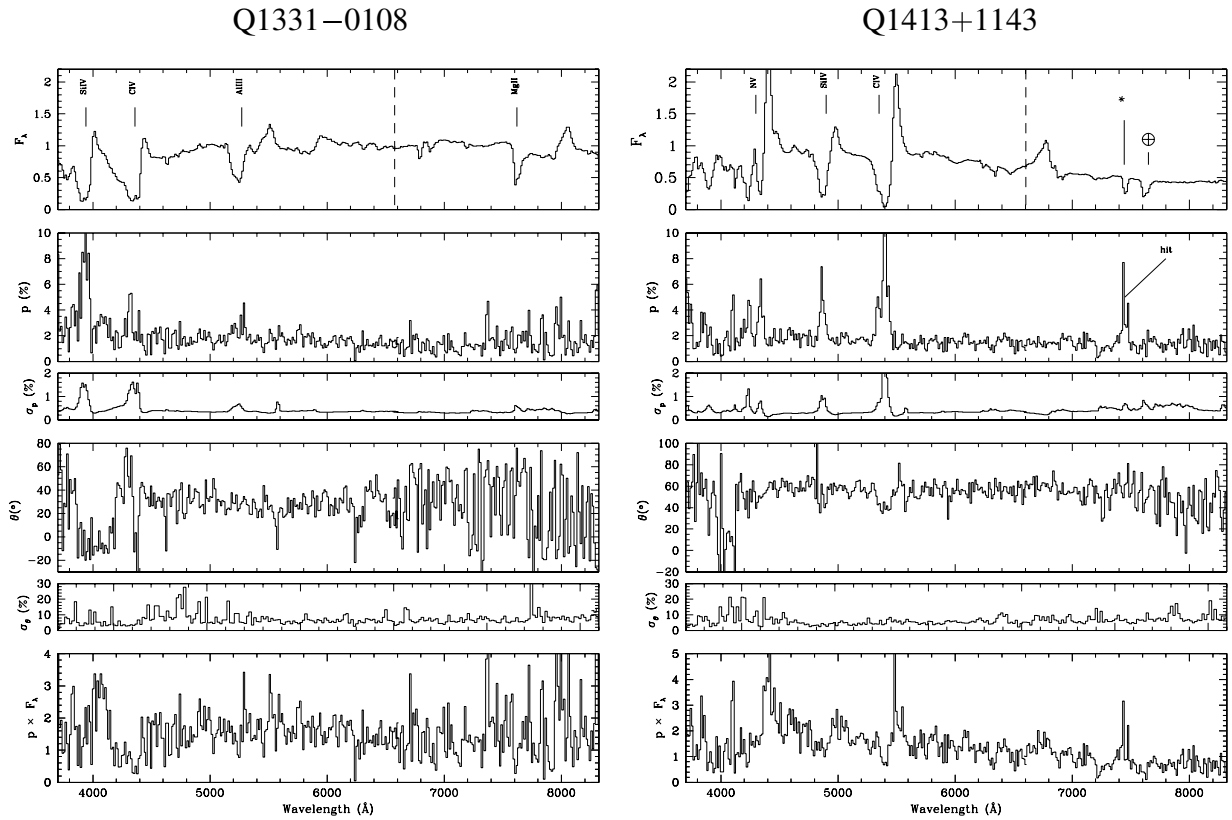


Fig. 1 : Spectropolarimetry of six BAL QSOs. For each object we show the total flux F_λ (in relative units), the polarization degree p and σ_p the uncertainty of p (in %) , the polarization position angle θ and σ_θ the uncertainty of θ (in degree), and the polarized flux $p \times F_\lambda$.

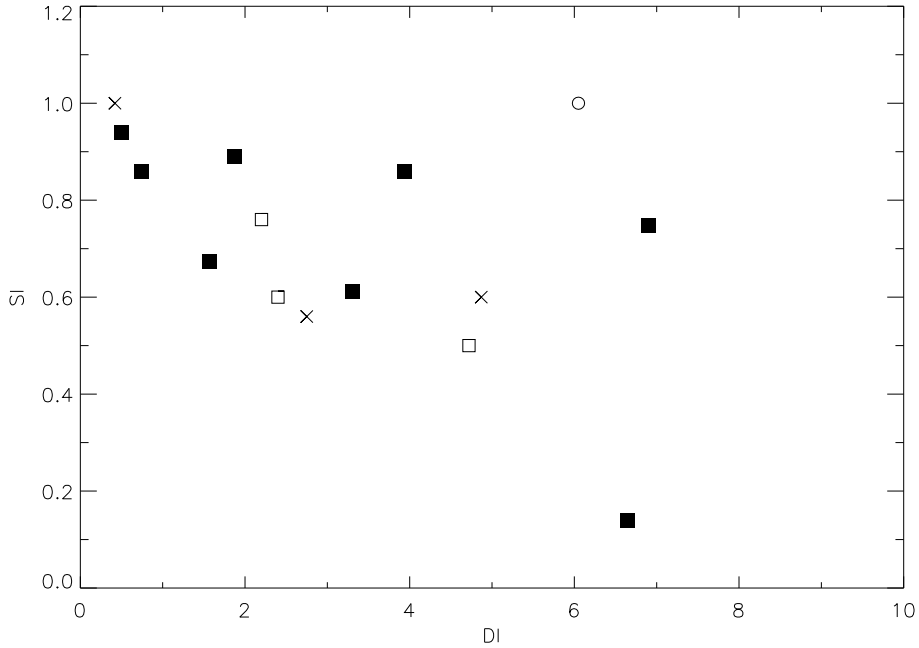


Fig. 2 : The possible correlation between the detachment index DI and SI, the ratio of the CIV absorption depths measured in the polarized and the total spectra. LIBAL QSOs are represented by filled squares, HIBAL QSOs by open squares, unclassified BAL QSOs by crosses. A doubtful measurement is indicated by the open circle. The probability that the correlation is due to chance only is P = 3% with the doubtful data point and P = 0.5% without this point.

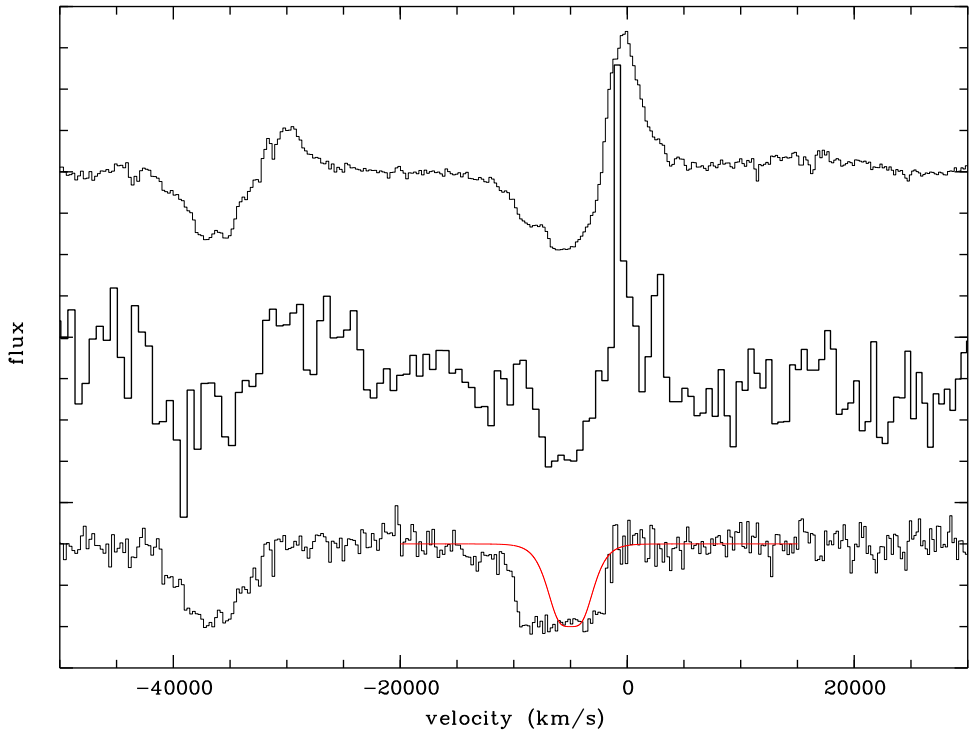


Fig. 3 : The polarized flux[1] $q' \times F_\lambda$ of H1413+117 (= Q1413+1143) is plotted here on a velocity scale in the quasar rest-frame, together with the total flux (upper spectrum), and the absorption profile derived from the microlensing analysis (lower spectrum, cf. Paper 8). As in Paper 8 (cf. Fig. 2 of the update), the model for the disk absorption is superimposed on the total absorption. Remarkably, only this absorption is seen in the polarized spectrum.

[1]The Stokes parameter q' is the Stokes q rotated in the quasar frame i.e. $q' = q\cos 2\theta_c - u \sin 2\theta_c$ where θ_c is the position angle of the quasar continuum polarisation. $\theta_c = 60^o$ for H1413+117 (Fig. 1)

Article 15

Spectropolarimetry of the iron low-ionization Broad Absorption Line quasar Q0059-2735

H. Lamy, D. Hutsemékers : Astron. Astrophys. 356, L9 (2000)

Q0059-2735 : a hybrid Starburst / Broad Absorption Line QSO ? Clues from Spectropolarimetry

D. Hutsemékers, H. Lamy : in Mass Outflow in Active Galactic Nuclei : New Perspectives, D.M. Crenshaw et al. (eds.), A.S.P. Conference Series 255, 211 (2002)

Nous présentons ici des observations spectropolarimétriques du quasar BAL Q0059-2735. Ce quasar possède la particularité rare de montrer des raies de FeII en absorption.

Nous trouvons que la polarisation du continuum augmente régulièrement vers les courtes longueurs d'onde, l'angle de polarisation subissant une légère rotation. C'est une indication de l'existence de deux mécanismes à l'origine de la polarisation du continuum.

Dans les raies BAL fortement ionisées, la polarisation augmente considérablement par rapport à la polarisation du continuum. Par contre, les raies de FeII en absorption ne sont pas plus polarisées que le continuum, tout en étant bien visibles dans le spectre polarisé. Ce comportement différent des raies de FeII indique une localisation et/ou une géométrie de leur région de formation différente de celle à l'origine des raies plus ionisées.

Nous montrons que les caractéristiques observationnelles de Q0059-2735 sont compatibles avec un modèle hybride quasar + starburst, l'absorption du FeII étant plutôt liée à du gaz éjecté par des supernovae.

Astron. Astrophys. 356, L9–L12 (2000)

ASTRONOMY AND ASTROPHYSICS

LETTER

Letter to the Editor

Spectropolarimetry of the iron low ionization broad absorption line quasar Q 0059-2735⋆

H. Lamy and D. Hutsemékers⋆⋆,⋆⋆⋆

Université de Liège, Institut d'Astrophysique et de Géophysique, 5, Avenue de Cointe, 4000 Liège, Belgium

Received 27 January 2000 / Accepted 2 March 2000

Abstract. We present optical (ultraviolet rest-frame) spectropolarimetric observations of the rare iron low ionization broad absorption line (BAL) QSO Q 0059-2735. The continuum polarization increases to the blue with a regular rotation of the polarization position angle, suggesting that at least two mechanisms are at the origin of the polarization. There is also some evidence for dilution by a Fe II pseudo-continuum in emission. In the broad absorption lines, the polarization strongly rises, with the largest values ever reported. On the contrary, the Fe II blends in absorption are not more polarized than the continuum, while they are clearly visible in the polarized flux. These different polarization properties of Fe II absorption lines suggest a different origin and/or geometry. The observed properties of Q 0059-2735 are consistent with a hybrid QSO / starburst model.

Key words: galaxies: quasars: absorption lines – galaxies: quasars: individual: – polarization

1. Introduction

Broad absorption line (BAL) QSOs are a class of QSOs with broad, often deep, absorption troughs of high-ionization species like C IV, Si IV or N V, blueshifted with respect to the corresponding emission lines. These BALs are observed in $\sim 12\,\%$ of optically selected QSOs and are generally interpreted in terms of material outflowing at very high velocities ($\sim 0.1c$). Since the emission lines and continuum properties of BAL and non-BAL QSOs appear essentially similar (Weymann et al 1991), all radio-quiet (RQ) QSOs may have a broad absorption region of small covering factor, the QSOs being classified as BAL QSOs when the line-of-sight intercepts absorbing material. On the other hand, the BAL QSOs may form a different class of objects with large covering factor, possibly in an early stage of an evolutionary process towards normal QSOs (e.g. Boroson & Meyers 1992).

Among the BAL QSOs, $\sim 15\,\%$ constitute a sub-class with additional low-ionization broad absorption troughs: the low-ionization (LI) BAL QSOs. These QSOs generally have redder continua, stronger optical Fe II emission and very weak [O III] emission while detectable. These properties are consistent with LIBAL QSOs being more dusty (Boroson & Meyers 1992, Sprayberry & Foltz 1992).

Q 0059-2735 (z = 1.59) is a peculiar member of the LIBAL QSO class. First, the large Balmer decrement and the optical / near-infrared color index indicate an unusually high amount of dust in its surroundings (Egami et al. 1996). Also, the emission lines from highly ionized species are particularly weak and narrow (Hazard et al. 1987). But, most striking, is the fact that its rest-frame ultraviolet spectrum contains many narrow absorption lines (NAL) from highly-excited metastable levels of iron-peak elements, which sometimes blend in broad troughs, then forming a complex absorption spectrum (Hazard et al. 1987, Wampler et al. 1995). Up to now only three other QSOs are known to show similar properties, forming the class of *iron* LIBAL QSOs, of which Q 0059-2735 is often considered as the prototype (Becker et al. 1997, Brotherton et al. 1997). Detailed analysis of high-resolution spectra suggests that Fe II absorption may originate from low ionization condensations embedded in a hotter BAL flow (Wampler et al. 1995). An alternative model is that Q 0059-2735 is a mixture of a QSO and a starburst galaxy (Cowie et al. 1994, Egami et al. 1996). In this view, the Fe II absorption could be related to gas swept up by supernova explosions in the starburst galaxy.

Like several other LIBAL QSOs, Q 0059-2735 is significantly polarized in the continuum (Hutsemékers et al. 1998), providing us with the possibility of carrying out a detailed spectropolarimetric study. Such observations are presented here with the aim of better understanding the geometry of this object as well as the origin of the Fe II absorption lines.

2. Observations and data reduction

The observations were carried out with the ESO 3.6m telescope at the European Southern Observatory (La Silla, Chile) on September 10-12, 1996. The telescope was equipped with EFOSC1 and a Wollaston prism, giving two orthogonally polarized bi-dimensional spectra of the object and of the sky, sepa-

⋆ Based on observations collected at the European Southern Observatory, La Silla, Chile

⋆⋆ Also, Chercheur Qualifié au Fonds National de la Recherche Scientifique (FNRS, Belgium)

⋆⋆⋆ Present address: ESO, Casilla 19001, Santiago, Chile

rated by 20" on the CCD detector. The detector was a 512×512 TeK CCD (ESO#26) with a pixel size of 27 μm corresponding to 0.″605 on the sky (Melnick et al. 1989). Two exposures with the Wollaston prism rotated by 45° were secured to obtain the two Stokes parameters fully describing the linear state of polarization. A mask was used in order to avoid overlapping of the sky spectra. The spectrum covers the useful 3700–8700 Å spectral range after combining the B300 and R300 grisms. The spectral resolution is 6.3 Å per pixel. For each grism and position angle of the Wollaston, three frames were taken for a total exposure time of 90 minutes.

All reductions were performed using procedures developed within the ESO MIDAS software package. After the usual bias and flat-field corrections, one-dimensionnal spectra were carefully extracted and calibrated in wavelength and flux, independently for the ordinary and extraordinary spectra. The standard star EG274 (Stone & Baldwin 1983, Baldwin & Stone, 1984), assumed to be unpolarized, was observed with the same setup and used for the flux calibration and for an estimate of the instrumental polarization. For each of the two spectra of the object, the sky was averaged using the nearest adjacent strips of same polarization on either side of the object. These sky spectra were then individually extracted and calibrated before subtraction from the object spectra. The one-dimensional spectra were rebinned on a linear wavelength scale with 13 Å pixels, (approximately corresponding to 2 original pixels) in order to increase the signal-to-noise ratio while keeping a good spectral resolution. Finally, these spectra were combined with the usual formulae to derive the q and u normalized Stokes parameters. (cf. di Serego Alighieri 1998). The associated errors were calculated by propagating the errors from the photon noise in the object and sky spectra. Note the instrumental polarization measured from EG274 was found to be low ($\sim 0.3\,\%$). A spectropolarimetric standard star, HD161291, was observed with the same setup in order to fix the zero point of the polarization position angle (PA) and to check the whole procedure. The interstellar polarization curve of HD161291 was found to be in excellent agreement with that measured by di Serego Alighieri et al. (1994) with the same setup, and with the parameters given by Serkowski et al. (1975)

Note that other BALQSOs were observed at the same time and compared to spectropolarimetric data available in the literature (Cohen et al. 1995, Goodrich & Miller 1995, Schmidt & Hines 1999). Our results appear in good agreement, giving additional confidence in the observation / reduction process. More details about these observations will be given elsewhere.

3. Results

3.1. Analysis of data

The optical (UV rest-frame) spectropolarimetric results for Q 0059-2735 are displayed in Fig. 1. The polarization degree p, the polarization position angle θ and the associated uncertainties σ_p and σ_θ have been computed from the q and u normalized Stokes parameters using the usual formulae (e.g. di Serego Alighieri 1998). The combined B300 and R300 spectra are presented.

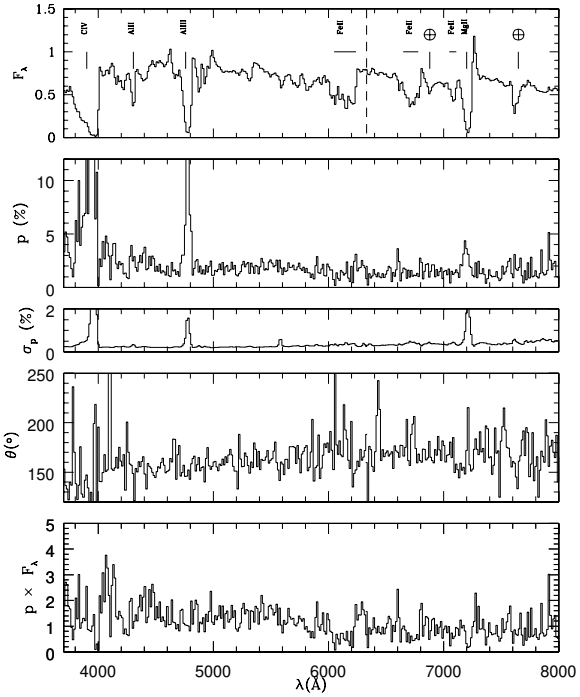


Fig. 1. Spectropolarimetry of Q0059-2735. From top to bottom: (1) The total flux, F_λ, in arbitrary units (2) The degree of polarization, p (3) The uncertainty on the degree of polarization, σ_p (4) The polarization position angle, θ (5) The polarized flux, $p \times F_\lambda$ in arbitrary units. The B300 and R300 spectra were cut on their reddest and bluest parts respectively, and linked together at the wavelength indicated by the vertical dashed line. The less interesting part above 8000 Å is not shown here. Note finally that p in C IV and Al III, and σ_p in C IV are truncated; peak values are given in Table 2

Moreover, the continuum polarization has been measured from the Stokes q, u spectra in wavelength bands selected after a careful inspection of the high-resolution spectra of Wampler et al (1995) in order to avoid the numerous Fe II narrow absorption lines. The continuum defined in that way is the sum of the QSO continuum and of the possible pseudo-continuum formed by the Fe II emission. The measurements are reported in Table 1. The continuum polarization of Q 0059-2735 slightly decreases towards the red (from 2% to 1%). These values are in good agreement with our previous broad-band polarimetry measurements: $p_V = 1.62 \pm 0.29\,\%$ and $1.45 \pm 0.23\,\%$ (Hutsemékers et al 1998, Lamy & Hutsemékers 2000). However, at the red end of the spectrum, the polarization starts rising again. This is confirmed by the value measured in the Gunn i filter during the same run ($p_i = 2.45 \pm 0.24\,\%$, Lamy & Hutsemékers 2000). The polarization position angle slightly rotates along the blue part of the spectrum. This rotation could indicate the presence of two polarization mechanisms, or the sum of two polarized components coming from distinct regions. Indeed, in this latter case, if the relative importance of one component compared to the other one changes with wavelength, one also expects a rota-

Table 1. Continuum polarization

	$\overline{p}$	$\overline{\sigma_p}$	$\overline{\theta}$	$\overline{\sigma_\theta}$
$\lambda\lambda\,4400-4600$	1.98	0.05	152	1
$\lambda\lambda\,5000-5200$	1.70	0.06	160	1
$\lambda\lambda\,5600-5800$	1.67	0.07	166	2
$\lambda\lambda\,6250-6400$	1.52	0.08	170	2
$\lambda\lambda\,7350-7500$	0.85	0.10	169	4
$\lambda\lambda\,7750-8000$	1.57	0.12	166	3

Table 2. BAL trough polarization

	$\overline{p}$	$\overline{\sigma_p}$	p_{peak}	$\sigma_{p_{peak}}$
C IV λ 1549	8.99	0.16	48.0	3.32
Al II λ 1671	2.65	0.18	3.92	0.34
Al III λ 1857	7.32	0.25	17.2	1.60
Mg II λ 2798	2.14	0.46	4.36	0.94
Fe II λ 2380	0.97	0.09	2.45	0.38
Fe II λ 2600	1.20	0.12	2.74	0.32
Fe II λ 2750	1.11	0.18	1.64	0.34

tion of the polarization PA. Again, in the red part of the spectra, this rotation stops and the value of θ measured in the Gunn i filter ($\theta_i = 166 \pm 3\,\%$) is close to the one measured redward of Mg II.

We have also measured the polarization in the BAL troughs. Peak and integrated values are given in Table 2. To calculate the integrated values, we assumed a power-law for the continuum using the spectral indices ($\alpha_B = 1.50$ and $\alpha_R = 1.59$) measured in Hutsemékers et al. (1998) and we defined the broad absorption lines as those regions of the spectra dipping 10% or more below the estimated continuum, thus following the prescriptions of Weymann et al (1991) for C IV. Then the q and u spectra were averaged over the BALs and combined to obtain the $\overline{p}$ values given in Table 2. As previously observed in many other BAL QSOs (Goodrich & Miller 1995, Ogle 1997, Schmidt & Hines 1999), the degree of polarization strongly increases in the BAL troughs. However, in Q 0059-2735, the peak values reached in the C IV and Al III BALs are unusually high (respectively 48 % and 17 % measured on the spectrum rebinned to 13 Å), larger than observed in any other BAL QSO (Schmidt & Hines 1999). Note that these are not spurious results since adjacent pixels have also high values. They may even be lower limits since we do not resolve the peak. These large values preclude resonance scattering in the BAL lines as the main polarizing mechanism (Lee et al. 1994). The LI BALs Al II and Mg II are also polarized but at a lower level above the continuum. It is interesting to remark that the polarization peak in Mg II seems to correspond to the higher velocity part of the BAL. A possible rotation of θ across C IV and Mg II may be present but the signal-to-noise ratio is too low to distinguish from the regular rotation accross the continuum. In the polarized flux, while the BAL C IV and Mg II appear quite clearly, there is no indication of the presence of the BAL Al III, even in the non-rebinned data.

Also remarkable is the different behavior of the Fe II absorption blends which, contrary to what happens in other BALs, show no significant polarization increase in the absorption troughs (Table 2), although the degree of polarization varies across the blends in a complicated way. However, some of these blends appear in the polarized flux, clearly for Fe II λ 2380 and Fe II λ 2600, and marginally for Fe II λ 2750. A few other NALs may also be visible in the polarized flux (e.g. Ni II or Zn II) but higher S/N data should be obtained to confirm them.

Finally, the polarization of the Mg II emission line appears similar to that of the continuum. On the other hand, while no C IV broad emission is seen in the direct flux, a broad emission seems present in the polarization spectrum and more particularly in the polarized flux.

3.2. Comparison with similar objects

A few other QSOs also exhibit narrow absorption lines from metastable levels of iron FIRST J 0840+3633 and J 1556+3517, Becker et al. 1997; Hawaii 167, Cowie et al. 1994), and spectropolarimetric data have been obtained for two of them (J 0840+3633 and J 1556+3517, Brotherton et al. 1997).

J 0840+3633 has essentially the same spectral features as Q 0059-2735 albeit with deeper absorption troughs (Becker et al. 1997). The polarization significantly increases in the LI BALs Al III and Mg II although not as much as for Q 0059-2735 (peak values around 8 %). It rises weakly in the Fe II blends at 2600 Å and 2750 Å and drops in Fe II 2380 Å (Brotherton et al. 1997). The polarization PA rotates accross these Fe II blends in a complex manner. All these lines including the Al III BAL are strongly apparent in the polarized flux.

J 1556+3517 has a much more heavily absorbed and reddened continuum and no prominent emission lines (Becker et al. 1997). It also has polarimetric characteristics completely different from other BAL QSOs. The degree of polarization in the continuum is high (p = 7 % around 7000 Å) and rises strongly to the blue (p = 13 % around 5000 Å). Moreover, it dramatically *decreases* to zero in the broad absorption lines (including in the Fe II blends), indicating that the scattered flux is completely absorbed at these wavelengths (Brotherton et al. 1997). The polarization PA rotates accross the broad absorption lines and the Fe II blends.

4. Discussion and conclusions

Since the continuum polarization slightly rises towards the blue and since the QSO is redder than typical radio-quiet QSOs, the polarization may be attributed to dust scattering. However, a wavelength-independent scattering by free electrons is also possible if a dilution by an unpolarized red component is present. The latter may be due to a wavelength-dependent extinction stronger for the direct rays than for the scattered ones, or to the pseudo-continuum formed by the blends of numerous unpolarized Fe II narrow emission lines, as suggested for J 0840+3633 and PHL 5200 (Brotherton et al. 1997, Cohen et al. 1995, Wills et al. 1985). If true, we would expect a rise of polarization redward of Mg II, where optical Fe II lines are much weaker

($\lambda \geq 7750$ Å, Wills et al. 1985). And indeed, although the quality of the measurements is poorer in this region, the values in Table 1 as well as our Gunn i measurement confirm this rise at the red end of our spectra. However, the still higher p at the blue end of the spectrum and the regular rotation of the polarization PA cannot be explained by the Fe II dilution alone. It is therefore likely that at least one other mechanism acts simultaneously, dust scattering and/or differential extinction. Note that dust scattering of the C IV broad emission line photons in the vicinity of the broad absorption line region (BALR) could explain their destruction in the direct flux and their presence in the polarized flux.

In agreement with the standard interpretation of BAL QSO spectropolarimetry (Cohen et al. 1995, Schmidt & Hines 1999), the rise of polarization in the BAL troughs suggests that the scattered continuum is less absorbed in the BALR than the direct unpolarized continuum. Furthermore, the fact that some BALs (e.g. C IV) are seen in the polarized flux indicates that the scattered flux crosses the BALR in regions of lower opacity. However, the absence of Al III in the polarized flux suggests that the scattered flux misses the region of the BALR where Al III is formed. This behavior is not unique among BAL QSOs: in the polarized flux of Q 1246-0542 there is apparently no trace of any BAL, including C IV (Schmidt & Hines 1999[1]). In the case of Q 0059-2735, this suggests that the low-ionization Al III BALR is less extended than the high-ionization one, and does not cover the scattering region. On the contrary, the Fe II absorption blends are detected in the polarized flux, while they are not significantly more polarized than the continuum. Thus, the iron absorbing gas must intercept both the polarized and unpolarized continua with roughly the same opacity, suggesting a different location and/or geometry for the Fe II absorbing region. Compared to other low-ionization BALs, the behavior of the Mg II BAL is quite striking since it appears more polarized than the continuum (although not as much as Al III), while it is seen in the polarized flux like Fe II. These intermediate properties may indicate a hybrid origin for the Mg II BAL.

Our results are consistent with the interpretation that the spectrum of Q 0059-2735 is a superposition of a BAL QSO spectrum and of a starburst one, the starburst being at the origin of the Fe II NALs and of the unusually large reddening (cf. Cowie et al. 1994; Egami et al. 1996). In this model, Q 0059-2735 is seen along a line of sight close to the dusty equatorial plane. In the framework of the disk-wind model for the QSO BALR, such an orientation could explain the presence of low ionization troughs, the very deep and steep CIV absorption trough, and the high degree of polarization in the continuum (cf. Murray et al. 1995, Hutsemékers et al. 1998). Free electrons and/or dust scatter the continuum photons along lines of sight that cross parts of the BALR where the opacity is still large for C IV, and much smaller for Al III and Mg II, the latter ones originating much closer to the disk as suggested by Murray et al. (1995).

[1] Note that we confirm the absence of BAL in the polarized flux of Q1246-0542 on the basis of new data obtained with a better signal-to-noise ratio (Lamy & Hutsemékers 2000, in preparation)

Within this model, the Fe II absorption blends are produced beyond the BALR, in material swept up by the strong winds of supernovae in the starburst (Hazard et al. 1987, Norman et al. 1994). The BAL Mg II could be hybrid, partly formed in the QSO disk-wind and partly in the starburst. The fact that the Mg II polarization peak does not exactly correspond to the BAL peak could support this hypothesis, although data with higher spectral resolution are needed to confirm it.

Since J 0840+3633 has basically the same properties as Q 0059-2735, this QSO + starburst model may apply as well, assuming that the scattered flux now crosses the low-ionization BALR (Al III is detected in the polarized flux). The smaller peak values of the BAL polarization in J 0840+3633 are compatible with this hypothesis, the scattered flux crossing regions of higher opacity than in Q 0059-2735.

Acknowledgements. This research is supported in part by the contracts ARC 94/99-178, and by PAI P4/05.

References

Baldwin J.A., Stone R.P.S., 1984, MNRAS, 206, 241
Becker R.H., Gregg M.D., Hook I., et al., 1997, ApJ 479, L93
Boroson T.A., Meyers K.A., 1992, ApJ 397,442
Brotherton, M.S., Tran, H.D., Van Breugel, W., Dey, A., Antonucci, R., 1997, ApJL 487, L113
Cohen, M.H., Ogle, P.M., Tran, H.D., Vermeulen, R.C., Miller, J.S., Goodrich, R.W., Martel, A.R., 1995, ApJ 448, L77
Cowie L.L., Songaila A., Egami E., et al., 1994, ApJ 432, L83.
di Serego Alighieri S., Cimatti A., Fosbury R.A.E., 1994, ApJ 431, 123
di Serego Alighieri S., 1998, in Instrumentation for Large Telescopes, Eds. J.M. Rodriguez Espinosa, Cambridge University Press, 287
Egami, E., Iwamuro, F., Maihara, T., Oya, S., Cowie, L.L., 1996, AJ 112, 73
Glenn, J., Schmidt, G.D., Foltz, C.B., 1994, ApJ 434, L47
Goodrich R.W., Miller J.S., 1995, ApJ 448, L73
Hazard C., Mc Mahon R.G., Webb J.K., Morton D.C., 1987, ApJ 323, 263
Hines, D.C., Wills, B., 1995, ApJ 448, L69
Hutsemékers, D., Lamy, H., Remy, M., 1998, A&A 340, 371
Kartje J.F., 1995, ApJ 452, 565
Lamy, H., Hutsemékers, D., 2000, A&AS, in press
Lee H.W., Blandford R.D., Western L., 1994, MNRAS 267, 303
Melnick J., Dekker H., D'odorico S., 1989, EFOSC, ESO operating manual n4, Version 2, ESO
Murray N., Chiang J., Grossman S.A., Voit G.M., 1995, ApJ 451, 498
Norman C.A., Bowen D.V., Heckman T., Blades C., Danly L., 1996, ApJ 472, 73
Ogle P.M., 1997, in ASP Conf. Ser. 128, Mass ejection from AGN, ed. N. Arav, I. Shlosman, R.J. Weymann (San Francisco:ASP), 78
Schmidt G.D., Hines D.C., 1999, ApJ 512, 125
Serkowski K., Matthewson D.S., Ford V.L., 1975, ApJ 196, 261
Sprayberry, D., Foltz, C.B., 1992, ApJ 390, 39
Stocke J.T., Morris S.L., Weymann R.J., Foltz C.B., 1992, ApJ 396, 487
Stockman H.S., Moore R.L., Angel J.R.P., 1984, ApJ 279, 485
Stone R.P.S., Baldwin J.A., 1983, MNRAS 204, 347
Wampler, E.J., Chugai, N.N., Petitjean, P., 1995, ApJ 443, 586
Weymann R.J., Morris S.L., Foltz C.B., Hewett P.C., 1991, ApJ 373, 23
Wills B.J., Netzer H., Wills D., 1985, ApJ 288, 94

Mass Outflow in Active Galactic Nuclei: New Perspectives
ASP Conference Series, Vol. 255, 2002
D.M. Crenshaw, S.B. Kraemer, and I.M. George

Q0059-2735: A Hybrid Starburst / Broad Absorption Line QSO? Clues from Spectropolarimetry

D. Hutsemékers[1]

European Southern Observatory, Chile

H. Lamy

University of Liège, Belgium

Abstract. Spectropolarimetric data support the hybrid BALQSO / Starburst model proposed for the iron Lo-BAL QSO Q0059-2735.

1. Q0059-2735 and the Hybrid BALQSO / Starburst model

Q0059-2735 (z =1.59) is one of the extreme and very rare low-ionization broad absorption line (Lo-BAL) QSOs which exhibit narrow absorption lines (NALs) from metastable levels of Fe II. Q0059-2735 is often considered as the prototype of the "iron Lo-BAL" QSO class.
A hybrid BAL QSO / Starburst model has been proposed for Q0059-2735 by Cowie et al. (1994) and Egami et al. (1996). These authors suggest a model in which the central (BAL) QSO is surrounded by a dusty shell of young stars contributing to the excess of UV continuum, and at the origin of the Fe II NALs. The mixture of starburst and reddened quasar properties appears in varying degree as a function of wavelength, and could be the signature of a younger stage in the quasar evolutionary sequence. A couple of BAL QSOs with characteristics supporting this interpretation were recently found by Becker et al. (1997).
Since Q0059-2735 is polarized like many other low-ionization BAL QSOs, we have investigated its UV rest-frame polarized spectrum.

2. Clues from Spectropolarimetry

Spectropolarimetric data have been obtained for Q0059-2735 with the ESO 3.6m telescope at La Silla, and are presented in Lamy & Hutsemékers (2000).
In agreement with the standard interpretation of BAL QSO spectropolarimetry (Cohen et al. 1995, Schmidt & Hines 1999), the rise of polarization in the BAL troughs (cf. Fig. 1 and Table 2 in Lamy & Hutsemékers 2000) suggests that the scattered continuum is less absorbed in the BAL region (BALR) than the direct unpolarized continuum. The fact that some BALs (e.g. C IV) are also seen in the polarized flux indicates that the scattered flux crosses the BALR in regions of

[1]Also Research Associate FNRS, University of Liège, Belgium

lower opacity. However, the absence of Al III in the polarized flux of Q0059-2735 suggests that the scattered flux misses the region of the BALR where Al III is formed. This behavior is not unique among BAL QSOs: in the polarized flux of Q1246-0542 there is apparently no trace of any BAL, including C IV. In the case of Q0059-2735, this suggests that the low-ionization Al III BALR is less extended than the high-ionization one, and does not cover the scattering region. On the other hand, the Fe II absorption blends are detected in the polarized flux, while they are not significantly more polarized than the continuum. Thus, the iron absorbing gas must intercept both the polarized and unpolarized continua with roughly the same opacity, suggesting a different location and/or geometry of the Fe II absorbing region. Compared to the other low-ionization BALs, the behavior of the Mg II BAL is quite striking since it appears more polarized than the continuum (although not as much as Al III), while it is seen in the polarized flux, like Fe II. These intermediate properties may indicate a hybrid origin of the Mg II BAL.

These results are consistent with the interpretation that the spectrum of Q0059-2735 is a superposition of a BAL QSO spectrum and a starburst one, the starburst being at the origin of the Fe II NALs (Cowie et al. 1994; Egami et al. 1996). In this model, Q0059-2735 is seen along a line of sight close to the dusty equatorial plane. In the framework of the disk-wind model of the BALR, such an orientation could explain the presence of low ionization troughs, the very deep and steep C IV absorption trough, and the high degree of polarization in the continuum (cf. Murray et al. 1995, Hutsemékers et al. 1998). Free electrons and/or dust scatter the continuum photons along lines of sight that cross the BALR where the opacity is still large for C IV, and much smaller for Al III and Mg II, the latter ions being located much closer to the disk as suggested by Murray et al. (1995). Within this model, the Fe II NALs are produced beyond the BALR, in material swept up by the strong winds of supernovae in the starburst (Hazard et al. 1987, Norman et al. 1994), such that the scattered and direct continua are similarly absorbed. The Mg II BAL could be hybrid, partly formed in the QSO disk-wind and partly in the starburst. The fact that the polarization in the Mg II BAL is not the highest at exactly the wavelength at which the BAL profile is the deepest could support this hypothesis, although data with higher spectral resolution are needed.

References

Becker, R.H. et al. 1997, ApJ479, L93

Cohen, M.H. et al. 1995, ApJ448, L77

Cowie, L.L. et al. 1994, ApJ432, L83

Egami, E. et al. 1996, AJ112, 73

Hazard, C. et al. 1987, ApJ323, 263

Hutsemékers, D. et al. 1998, A&A340, 371

Lamy, H., Hutsemékers, D. 2000, A&A356, L9

Murray, N. et al. 1995, ApJ451, 498

Norman, C.A. et al. 1996, ApJ472, 73

Schmidt, G.D., Hines, D.C., 1999, ApJ512, 125

Quatrième partie

Orientation à grande échelle de la polarisation des quasars

Article 16

Evidence for very large-scale coherent orientations of quasar polarization vectors

D. Hutsemékers : Astron. Astrophys. 332, 410 (1998)

Dans cet article, nous rapportons la découverte d'un effet d'orientation à très grande échelle de la polarisation des quasars.

Sur base d'un nouvel échantillon de quasars polarisés, nous trouvons dans un premier temps que dans une région du ciel, les angles de polarisation des quasars ne sont pas orientés de façon aléatoire comme on pourrait s'y attendre mais concentrés autour d'une certaine direction.

Dans le but de vérifier ce résultat surprenant, nous avons rassemblé un grand nombre de données polarimétriques à partir de la littérature. En appliquant des critères de qualité stricts afin d'éliminer au mieux une contamination possible par notre Galaxie, nous avons construit un échantillon de 170 quasars avec des mesures de polarisation fiables. Pour traiter le problème quantitativement, nous avons développé des tests statistiques adaptés au problème ainsi qu'une méthode de visualisation des résultats.

Appliqués à notre échantillon de 170 objets, deux tests statistiques différents montrent qu'avec un niveau de signification de l'ordre de 1%, les vecteurs polarisation des quasars ne sont pas distribués aléatoirement sur le ciel ; au contraire, ils apparaissent orientés de façon cohérente sur de très grandes échelles spatiales. Le fait que les vecteurs polarisation d'objets situés le long de la même ligne de visée mais à des redshifts plus petits ne sont pas orientés de la même façon indique qu'il ne s'agit ni d'un biais instrumental ni d'un effet dû à la polarisation par des poussières de notre Galaxie.

Les échelles auxquelles cet effet d'orientation est observé suggèrent un effet d'importance cosmologique. Plusieurs interprétations possibles sont discutées.

Astron. Astrophys. 332, 410–428 (1998)

ASTRONOMY
AND
ASTROPHYSICS

Evidence for very large-scale coherent orientations of quasar polarization vectors⋆,⋆⋆

D. Hutsemékers⋆⋆⋆

Institut d'Astrophysique, Université de Liège, 5 av. de Cointe, B-4000 Liège, Belgium

Received 21 July 1997 / Accepted 17 December 1997

Abstract. On the basis of a new sample of quasar optical polarization measurements, we have found that, in a region of the sky, the quasar polarization vectors are not randomly oriented as naturally expected, but appear concentrated around one preferential direction.

In order to verify this surprising although preliminary result, we have compiled a large sample of quasar polarization measurements from the literature. With quite severe criteria to eliminate at best the contamination by our Galaxy, a sample of 170 quasars with good quality polarization measurements has been defined. Maps in redshift slices reveal a few regions where the polarization vectors are apparently aligned. To handle the problem more quantitatively, non-parametric 3D statistical tests were designed, as well as a method for visualizing spatially the results. The significance is evaluated through Monte-Carlo simulations.

Applied to our sample of 170 polarized quasars, two different statistical tests provide evidence, with significance levels of 0.005 and 0.015 respectively, that the optical polarization vectors of quasars are not randomly distributed over the sky but are coherently oriented on very large spatial scales. This orientation effect appears spatially delimited in the 3D Universe, mainly occuring in a few groups of 10-20 objects. The polarization vectors of objects located along the same line of sight but at different redshifts do not appear accordingly aligned. Essentially for this reason, instrumental bias and contamination by interstellar polarization in our Galaxy are unlikely to be responsible for the observed effect.

The very large scale at which this local orientation effect is observed indicates the presence of correlations in objects or fields on spatial scales $\sim 1000\,h^{-1}$ Mpc at redshifts $z \simeq$ 1-2, suggesting an effect of cosmological importance. Several possible and testable interpretations are discussed.

Key words: large-scale structure of the Universe – quasars: general – polarization – methods: statistical

1. Introduction

In the framework of a study of polarization properties of broad absorption line quasars, we have recently obtained new optical polarization measurements for a sample of moderate to high-redshift quasars (Hutsemékers et al. 1998). Significantly polarized objects were found. During the analysis of the data, we realized that in some regions of the sky the quasar polarization position angles are apparently not randomly distributed within 180° as naturally expected, but appear concentrated around one direction. Moreover, it was possible to delineate a contiguous volume in the three-dimensional space in which all objects have their polarization position angles within 80°. Although we are dealing with small numbers, the probability of such a situation is already small, but not meaningful since one may have picked out a peculiar configuration out of a random process. It nevertheless prompted us to see in the literature how the polarization position angles are distributed for quasars located in the same volume of the Universe. Five additional polarized quasars were found in the specified region, with the surprising result that their polarization position angles are concentrated around the same direction, giving a first evidence for some kind of coherent orientation on very large spatial scales. These preliminary results motivated us to carry out a more detailed statistical study of the distribution of quasar polarization position angles, using a sample, as large as possible, of measurements compiled from the literature.

In Sect. 2, we report in more detail the first evidence for spatially coherent orientations of quasar polarization vectors. In Sect. 3, we discuss the selection of a large sample of optical polarization measurements from data available in the literature. A preliminary analysis is given in Sect. 4, where we also

Send offprint requests to: D. Hutsemékers

⋆ Tables 2 and 3 are also available in electronic form at the CDS via anonymous ftp to cdsarc.u-strasbg.fr (130.79.128.5) or via http://cdsweb.u-strasbg.fr/Abstract.html

⋆⋆ Based in part on observations collected at the European Southern Observatory (ESO, La Silla)

⋆⋆⋆ Also, Chercheur Qualifié au Fonds National de la Recherche Scientifique (FNRS Belgium)

present maps of quasar polarization vectors in redshift slices. Since a quantitative statistical method is needed, we propose in Sect. 5 dedicated non-parametric statistical tests, together with a method for visualizing the results. Basically the tests measure the circular dispersion of polarization position angles for groups of neighbours in the three-dimensional space, the significance being evaluated through Monte-Carlo simulations. The results of the statistical tests are given in Sect. 6, providing evidence for polarization vector "alignments" on very large spatial scales. Since it is clear that the presence of such an effect may be of great importance for cosmology, some possible interpretations are discussed in Sect. 7, as well as possible biases in the data, the latter being essentially ruled out. Final conclusions form the last section.

2. First evidence from a small sample

With the aim of studying the polarization of broad absorption line (BAL) quasars, we have obtained optical linear polarization measurements for a sample of 42 moderate to high-redshift optically selected quasars. The observations were carried out at the European Southern Observatory (ESO) with the 3.6m telescope, during two runs in 1994. The telescope was equipped with the EFOSC camera set up in its imaging polarimetry mode (see e.g. di Serego Alighieri 1989). The details of these observations and their analysis are reported elsewhere (Hutsemékers et al. 1998).

Out of the 42 quasars, 20 were observed during the first observing run, all of them at high northern galactic latitudes b_{II}. 15 quasars appear significantly polarized, i.e. with $p \geq 2\,\sigma_p$, p denoting the measured degree of polarization (expressed in %), and σ_p the uncertainty. Since the uncertainties of these measurements are typically around 0.3%, this corresponds to values of p larger than 0.6 %, values from which one may consider the polarization to be intrinsic to the quasars (Berriman et al. 1990). This also corresponds to a maximum uncertainty $\sigma_\theta \simeq 14°$ for the polarization angle θ[1], σ_θ being evaluated using the standard relation $\sigma_\theta = 28.^\circ65\ \sigma_p/p$ (e.g. Clarke & Stewart 1986).

While we naturally expect the quasar polarization angles to be randomly distributed between 0° and 180°, it appears that 11 out of the 15 polarized objects have their angles θ distributed within the limited range $\Delta\theta = 83°$. More interestingly, we can define a contiguous volume in the three-dimensional (3D) space, limited by redshifts $z \leq 2.3$ and right ascensions $\alpha \geq 11^h\ 15^m$, where all the quasars, i.e. 7 objects, have their polarization angles between 146° and 46°, i.e. in the range $\Delta\theta = 80°$ (cf. Table 1). The probability that such a situation occurs by chance is of the order of a few percent, but completely meaningless since evaluated *a posteriori*. However, if an orientation effect[2] is indeed present, these observations can be used to predict that, in the volume delimited in redshift and right ascension by our first set of 7 objects (i.e. $11^h15^m \leq \alpha \leq 14^h29^m$ and $1.465 \leq z \leq 2.222$) , every significantly polarized quasar should have a polarization angle between 146° and 46°. Assuming that the distribution of position angles is only due to chance, the probability to find n objects, different from those of the first set, within this angle range is simply $(80/180)^n$.

Table 1. The two quasar samples showing polarization vector alignments: the first, from our observations, suggesting the effect, and the second, from the literature, confirming it

Object	b_{II}	z	p	σ_p	θ	σ_θ	Ref
1115+080	+61	1.722	0.68	0.27	46	12	0
1120+019	+57	1.465	1.95	0.27	9	4	0
1212+147	+75	1.621	1.45	0.30	24	6	0
1246−057	+57	2.222	0.91	0.28	146	9	0
1309−056	+57	2.212	0.78	0.28	179	11	0
1331−011	+60	1.867	1.88	0.31	29	5	0
1429−008	+53	2.084	1.00	0.29	9	9	0
1222+228	+82	2.046	0.84	0.24	150	8	2
1246−057	+57	2.222	2.06	0.29	150	4	2
1255−316	+31	1.924	2.20	1.00	153	12	4
1303+308	+85	1.770	1.12	0.56	170	14	3
1309−216	+41	1.491	12.30	0.90	160	2	4
1309−056	+57	2.212	2.33	0.57	179	7	2
1354−152	+45	1.890	1.40	0.50	46	10	4

References: (0) Hutsemékers et al. 1998, (2) Stockman et al. 1984, (3) Moore & Stockman 1984, (4) Impey & Tapia 1990

To check this, we have compiled quasar optical polarization measurements from all major surveys available in the literature (see next section). Adopting the same quality requirements on the data, i.e. $\sigma_\theta \leq 14°$and $p \geq 0.6\%$, 7 polarized objects are found in the volume previously defined in right ascension and redshift (cf. Table 1). Two objects (1246-057 and 1309-056) are common with our first set, and their published polarization angles are in excellent agreement with our measurements (the differences in the polarization degree p are most probably due to the fact that the measurements were not done in the same filters). It came as a surprise that all of the 5 remaining objects have angles within the range predicted from our first sample, a situation which has a probability of only 1.7% to occur by chance.

More confidence within this preliminary result can be gained from the fact that we had a priori no reason to fix the lower limit in z as in our first sample (except for being able to compute a probability *a priori*), and that if we adopt $z \geq 1.0$ instead of 1.465, 4 polarized objects (1127-145, 1246+377, 1254+047,

[1] The polarization position angle, or simply polarization angle, θ, is expressed in degrees from 0° to 180°, and counted from the north-south direction in the equatorial coordinate system, clockwise if east is to the right. Polarization *vectors* refer to non-oriented lines of arbitrary length centred at the object position with a direction fixed by the polarization angle

[2] It is important to note that throughout this paper we will speak of *alignments* or *coherent orientations*, although the polarization vectors are generally poorly aligned, i.e. for example when the polarization angles are distributed within 80-90°, instead of spanning 180° as expected from a uniform distribution

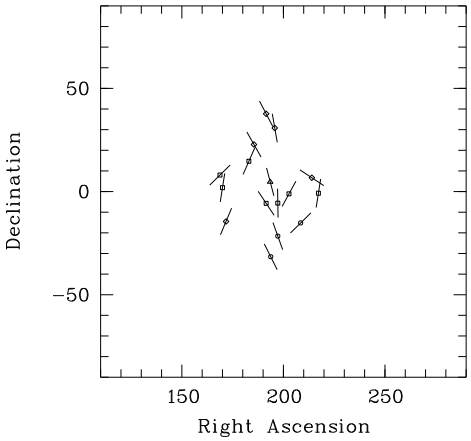


Fig. 1. A map of the polarization vectors of *all* polarized ($p \geq 0.6\%$ and $\sigma_\theta \leq 14^\circ$) quasars found in the literature with right ascensions $11^h15^m \leq \alpha \leq 14^h29^m$, and redshifts $1.0 \leq z \leq 2.3$ (i.e. the objects from Table 1, plus 4 additional ones mentionned in the text). The vector length is arbitrary. The different symbols refer to different catalogues: Stockman et al. 1984, and Moore & Stockman 1984 [losanges], Berriman et al. 1990 [triangles], Impey & Tapia 1990, and Impey et al. 1991 [circles], Hutsemékers et al. 1998 [squares]

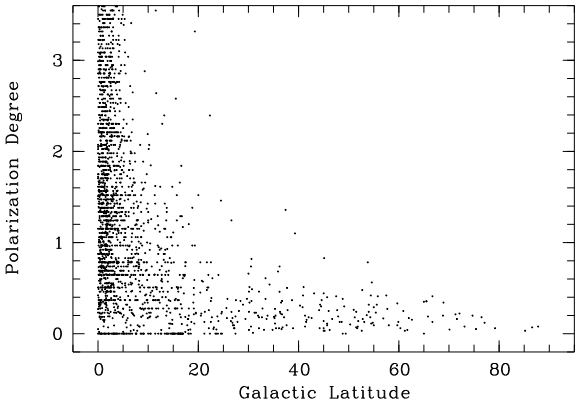


Fig. 2. The polarization degree (p in %) of distant ($d \geq 400$pc) stars of our Galaxy as a function of their galactic latitude $|b_{II}|$. All data are from the catalogue of Axon & Ellis (1976). The plot has been truncated to $p = 3.6\%$ to emphasize the behavior of low-polarization objects, while keeping all stars with $|b_{II}| \geq 20^\circ$

and 1416+067) may be added to the sample, 3 of them with polarization vectors accordingly aligned (cf. Tables 2 and 3). Also, if we plot on a map all the objects considered up to now (Fig. 1), a structure is apparent in the sense that the polarization vectors are better aligned at the centre of the group: all quasars with $12^h22^m \leq \alpha \leq 13^h09^m$ (i.e. 8 objects) have $146^\circ \leq \theta \leq 179^\circ$ ($\Delta\theta = 33^\circ$), suggesting a much more significant effect. It is clear from Fig. 1 that, if quasar polarization vectors are coherently oriented, this occurs on very large spatial scales.

These preliminary results provide a first, moderate, evidence for a coherent orientation effect of quasar polarization vectors in a limited, although very large, region of the sky. The fact that objects from different surveys, observed with different instrumentations, behave similarly indicates that the effect is unlikely to be due to an instrumental bias. These results motivate the construction of a larger sample from the literature to investigate if statistically significant alignments may be detected in other regions of the sky, therefore providing more definite evidence for the physical reality of the effect.

3. The selection of a large sample from the literature

In order to have a larger sample of quasar polarization angles, we have compiled optical polarization measurements from all (to our knowledge) major surveys available in the literature i.e. those by Stockman et al. (1984), Moore & Stockman (1984), Berriman et al. (1990), Impey & Tapia (1990), Impey et al. (1991), Wills et al. (1992), and Hutsemékers et al. (1998). Several of these surveys contain new measurements together with a compilation of data from the literature. Here, we only consider objects for which the polarization angle and the redshift are given, and which are classified by the authors as quasars. Seyfert galaxies and radio-galaxies were discarded, while BL Lac objects included by the authors in their quasar samples were taken into account, the BL Lac nature being not the primary criterion of selection. Note that some polarization surveys only dedicated to BL Lac objects may be found in the literature. These were not considered in our compilation, not only because the nature of BL Lac objects and their relation to quasars is still unclear, but also because their redshifts are uncertain (when measured), and because it is often difficult to assess a unique value to their polarization angle. When more than one measurement is available in a given catalogue, we have taken the data obtained with the lowest uncertainty σ_p, whatever the value of p, θ, σ_θ, the filter in which it was observed, or the possible or known variability. Measurements with the smallest σ_p were preferred to those with the smallest σ_θ since σ_θ depends on p and may be biased. Our sample finally amounts to 525 measurements which correspond to 433 different quasars, several objects belonging to more than one catalogue.

Due to the fact that this is always a positive quantity, the polarization degree p is biased at low signal to noise (e.g. Clarke & Stewart 1986). It is important to note that the polarization position angle is *not* affected by such a bias; only the uncertainty σ_θ may be biased when computed using the standard formula $\sigma_\theta = 28.^\circ65\ \sigma_p/p$, as done in most surveys. Since in most catalogues the polarization measurements were not corrected for bias, we only consider the measured values of p as they are reported. The values of σ_θ were also used as reported, except for the Wills et al. (1992) sample where the uncertainties are not given. For this sample, σ_θ was re-computed using the standard formula.

Our compilation contains polarization measurements obtained with various filters, and even in white light, which, due to the range in redshift, correspond to quite different spectral

regions in the quasar rest frame. Any wavelength dependence of the polarization angle would contribute to smear out coherent orientation effects. Fortunately, while the degree of polarization may depend on wavelength, the quasar polarization angles show apparently little or no wavelength dependence in the optical to near-infrared spectral range, a characteristics which seems common to low and high polarization objects, as well as to BAL quasars (cf. e.g. Saikia & Salter 1988, the multi-wavelength studies by Stockman et al. 1984, Webb et al. 1993, and the spectro-polarimetric observations by de Diego et al. 1994, Smith et al. 1994, Cohen et al. 1995). This important property seems to extend to the ultraviolet (Impey et al. 1995), although up to now very few objects have been observed. Also, the time variability of the polarization degree and the position angle, which is observed in many strong radio sources (e.g. Saikia & Salter 1988, Impey et al. 1991), will add some noise to the orientation effects. We nevertheless prefer to keep these objects in the sample because they have generally high, well measured polarization which can definitely not be attributed to extinction in our Galaxy. Furthermore, it seems that for many blazars, the polarization angles do not vary within a very large range of values, at least in the considered sample (Impey et al. 1991). While these effects certainly affect our data to some extent, we emphasize that they can only act to reduce the deviation from an uniform distribution, and certainly not to produce coherent orientations.

Although we want to keep as many quasars as possible, it is useless to consider objects for which the polarization angle measurements are too uncertain. We therefore adopt the reasonable constraint $\sigma_\theta \leq 14°$, which is equivalent to $p \geq 2\,\sigma_p$. It is important to remark that with this signal to noise ratio, the bias on p is not larger than $\sim 10\%$ (cf. Wardle & Kronberg 1974).

Further, it is necessary to reduce as much as possible the contamination by extinction in our Galaxy. This is especially important in our case since this mechanism is well known to align polarization vectors. On the basis of the Burstein & Heiles (1982) extinction maps, Berriman et al. (1990) have evaluated the contribution of the galactic interstellar medium to the polarization of their objects, which are essentially low-polarization quasars. They conclude that virtually any measured value of p above 0.6% is intrinsic to the quasar. A similar conclusion is reached in Hutsemékers et al. (1998), using polarization measurements of faint stars located in the immediate vicinity of the quasars. We will therefore adopt this necessary cut-off value and consider only objects with $p \geq 0.6\%$. It is clear that the highest the cut-off value, the lower contamination one can expect. But our sample is dominated by low-polarization quasars, the number of which precisely peaks near 0.6% (cf. Berriman et al. 1990), such that choosing a higher cut-off value would dramatically decrease the number of objects in our sample.

It is also necessary to discard objects at low galactic latitude, the usual choice being $|b_{II}| \geq 20°$. However, looking at the Burstein & Heiles (1982) maps, there is still significant extinction between 20° and 30°, especially in the southern part of the sky: $E_{B-V} \simeq 0.09$ is not unusual, which corresponds to $p_{ISM} \lesssim 0.75\%$ using the standard formula $p_{ISM} \leq 8.3\,E_{B-V}$ (Hiltner 1956). This indicates that a more stringent cut-off could be valuable. In Fig. 2, we have used the compilation by Axon & Ellis (1976) to plot the polarization degree of galactic stars as a function of their galactic latitude. Only distant stars ($d \geq 400$ pc) are considered i.e. those lying beyond the local volume where most interstellar polarization is imprinted. Here also, choosing $|b_{II}| \geq 30°$ rather than $|b_{II}| \geq 20°$ appears safer to have less galactic contamination above p = 0.6%. Adopting this more stringent cut-off decreases the number of objects in the sample, but the effect is not so dramatic, first because the quasar distribution peaks around $|b_{II}| \simeq 40°$ (cf. Fig. 3), and second because the considered volume of the Universe also decreases, such that the number of objects per unit volume, which is an important quantity in 3D investigations, is essentially unaffected.

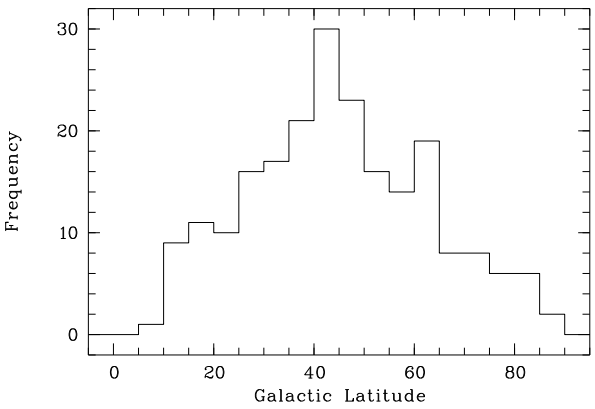


Fig. 3. The distribution in galactic latitude ($|b_{II}|$) of the quasars from our compilation. Only those objects with $p \geq 0.6\%$ and $\sigma_\theta \leq 14°$ are represented here

Finally, with the conditions $\sigma_\theta \leq 14°$, $p \geq 0.6\%$, $|b_{II}| \geq 30°$, and keeping only the best measurement when several are available (i.e. the ones with the smallest σ_p), our final sample amounts to 170 different polarized quasars. With the adopted constraints, we expect a priori little contamination by extinction in our Galaxy. The objects are given in Tables 2 and 3, with some of their characteristics. Note that the uncertainty of the polarization angle, σ_θ, is roughly uniformly distributed between 1° and 14°, and has therefore a mean value close to 7°.

4. Preliminary analysis of the sample

4.1. Are the polarization angles uniformly distributed?

We can test the hypothesis that the polarization angles in the final sample of 170 quasars are drawn from an uniform distribution using the Kuiper test (see e.g. Fisher 1993) which is similar to the well-known Kolmogorov-Smirnov test, but adapted to circular data. Due to the condition $|b_{II}| \geq 30°$, the objects lie in a biconical volume, whose northern and southern parts are essentially disconnected except at low redshift. We therefore consider subsamples at northern and southern galactic latitudes, and at low and high redshifts. The Kuiper test does not provide any ev-

Table 2. The final sample of 170 polarized quasars

Object	b_{II}	z	p	σ_p	θ	σ_θ	Ref
0003−066	−67	0.347	3.50	1.60	160	12	4
0003+158	−45	0.450	0.62	0.16	114	7	2
0013−004	−62	2.084	1.03	0.33	115	10	0
0017+154	−47	2.012	1.14	0.52	137	13	3
0019+011	−61	2.180	0.93	0.26	24	8	2
0021−022	−64	2.296	0.70	0.32	170	14	0
0024+224	−40	1.118	0.63	0.29	90	14	2
0029+002	−62	2.226	0.75	0.34	158	14	0
0050+124	−50	0.061	0.61	0.08	8	3	1
0051+291	−34	1.828	0.80	0.38	119	14	3
0059−275	−88	1.594	1.62	0.29	172	5	0
0100+130	−50	2.660	0.84	0.29	112	10	2
0106+013	−61	2.107	1.87	0.84	143	13	3
0110+297	−33	0.363	2.60	1.15	63	13	2
0117+213	−41	1.493	0.61	0.20	102	9	1
0119+041	−58	0.637	4.20	1.10	59	6	4
0123+257	−36	2.358	1.63	0.81	140	14	3
0130+242	−38	0.457	1.70	0.52	110	9	2
0133+207	−41	0.425	1.62	0.36	49	6	3
0137−018	−62	2.232	1.12	0.29	61	8	0
0137−010	−61	0.330	0.63	0.31	154	14	2
0145+042	−56	2.029	2.70	0.32	131	3	0
0146+017	−58	2.920	1.17	0.23	138	5	2
0148+090	−51	0.299	1.21	0.54	139	13	3
0159−117	−67	0.699	0.65	0.30	4	13	2
0202−172	−70	1.740	3.84	1.13	98	9	6
0205+024	−55	0.155	0.72	0.17	22	7	2
0208−512	−62	1.003	11.50	0.40	88	1	4
0214+108	−47	0.408	1.13	0.22	121	6	2
0226−038	−57	2.064	1.20	0.53	68	13	2
0232−042	−56	1.436	0.91	0.32	163	10	2
0332−403	−54	1.445	14.80	1.80	113	3	4
0333−380	−54	2.210	0.83	0.28	45	10	0
0336−019	−43	0.852	19.40	2.40	22	4	4
0348+061	−35	2.058	1.39	0.51	157	10	2
0350−073	−43	0.962	1.67	0.24	14	4	2
0402−362	−49	1.417	0.60	0.30	66	14	4
0403−132	−43	0.571	3.80	0.50	170	4	4
0405−123	−42	0.574	0.83	0.16	136	5	2
0414−060	−37	0.781	0.78	0.22	146	8	2
0420−014	−33	0.915	11.90	0.50	115	1	4
0438−436	−42	2.852	4.70	1.00	27	6	4
0451−282	−37	2.559	1.80	0.50	66	9	4
0454−234	−35	1.009	27.10	0.50	3	1	6
0506−612	−36	1.093	1.10	0.50	83	12	4
0537−441	−31	0.894	10.40	0.50	136	1	4
0804+499	+32	1.430	8.60	0.70	179	2	4
0836+710	+34	2.170	1.10	0.50	102	12	4
0839+187	+32	1.270	1.74	0.53	100	9	6
0844+349	+38	0.064	0.63	0.13	26	6	1
0848+163	+34	1.932	1.37	0.54	27	11	2
0850+140	+33	1.110	1.05	0.50	106	14	3
0851+202	+36	0.306	10.80	0.30	156	1	4
0855+143	+34	1.048	5.31	2.12	30	11	3
0903+175	+37	2.776	0.93	0.29	60	9	0
0906+430	+43	0.670	3.80	0.40	53	2	4
0906+484	+43	0.118	1.08	0.30	148	8	2
0923+392	+46	0.699	0.91	0.35	102	11	3
0946+301	+50	1.216	0.79	0.19	110	7	1
0953+254	+51	0.712	1.45	0.33	127	7	6
0954+556	+48	0.901	8.68	0.82	4	3	6
0954+658	+43	0.368	19.10	0.20	170	1	5
1001+054	+44	0.161	0.77	0.22	74	8	2
1004+130	+49	0.240	0.79	0.11	77	4	1
1009−028	+41	2.745	0.95	0.30	178	9	0
1011+091	+49	2.262	2.12	0.30	143	4	0
1012+008	+44	0.185	0.66	0.23	98	10	1
1029−014	+46	2.038	1.13	0.31	121	8	0
1038+064	+53	1.270	0.62	0.24	149	11	2
1048−090	+43	0.344	0.85	0.30	96	10	2
1049+616	+50	0.422	0.83	0.34	176	12	2
1055+018	+53	0.888	5.00	0.50	146	3	4
1100+772	+39	0.313	0.71	0.22	76	8	2
1114+445	+64	0.144	2.37	0.18	96	2	1
1115+080	+61	1.722	0.68	0.27	46	12	0
1120+019	+57	1.465	1.95	0.27	9	4	0
1127−145	+44	1.187	1.26	0.44	23	10	2
1128+315	+72	0.289	0.95	0.33	172	10	2
1151+117	+69	0.176	0.90	0.19	94	6	1
1156+295	+78	0.729	2.68	0.41	114	4	6
1208+322	+80	0.388	1.03	0.24	26	7	2
1212+147	+75	1.621	1.45	0.30	24	6	0
1216+069	+68	0.334	0.80	0.19	53	7	1
1222+228	+82	2.046	0.84	0.24	150	8	2
1229+204	+82	0.064	0.61	0.12	118	6	2
1231+133	+75	2.386	0.74	0.32	162	14	0
1232+134	+75	2.363	2.02	0.35	98	5	0
1235+089	+71	2.885	2.29	0.29	21	4	0
1244−255	+37	0.633	8.40	0.20	110	1	4
1246−057	+57	2.222	0.91	0.28	146	9	0
1246+377	+80	1.241	1.71	0.58	152	10	2
1252+119	+75	0.870	2.51	0.56	129	6	6
1253−055	+57	0.536	9.00	0.40	67	1	4
1254+047	+67	1.024	1.22	0.15	165	3	1
1255−316	+31	1.924	2.20	1.00	153	12	4
1303+308	+85	1.770	1.12	0.56	170	14	3
1308+326	+83	0.996	12.10	1.50	68	3	4
1309−216	+41	1.491	12.30	0.90	160	2	4
1309−056	+57	2.212	0.78	0.28	179	11	0
1318+290	+83	0.549	0.61	0.28	51	13	2
1321+294	+83	0.960	1.20	0.27	111	6	2
1322+659	+51	0.168	0.81	0.22	90	8	1
1328+307	+81	0.849	1.29	0.49	47	11	3
1331−011	+60	1.867	1.88	0.31	29	5	0
1334−127	+48	0.541	10.60	0.50	8	1	4
1340+289	+79	0.905	0.81	0.35	45	12	2
1347+539	+61	0.976	1.73	0.81	161	14	6
1351+640	+52	0.087	0.66	0.10	11	4	2
1354−152	+45	1.890	1.40	0.50	46	10	4
1354+213	+74	0.300	1.42	0.31	81	6	1
1411+442	+67	0.089	0.76	0.17	61	6	1
1413+117	+65	2.542	1.53	0.31	60	6	0

Table 3. The final sample of 170 polarized quasars (continued)

Object	b_{II}	z	p	σ_p	θ	σ_θ	Ref
1416−129	+45	0.129	1.63	0.15	44	3	1
1416+067	+61	1.439	0.77	0.39	123	14	2
1425+267	+69	0.366	1.42	0.23	74	5	2
1429−008	+53	2.084	1.00	0.29	9	9	0
1435−067	+47	0.129	1.44	0.29	27	6	1
1453−109	+41	0.940	1.64	0.54	59	9	3
1458+718	+42	0.905	1.41	0.60	108	12	6
1502+106	+55	1.839	3.00	0.60	160	5	4
1504−166	+35	0.876	5.30	0.70	52	4	4
1508−055	+43	1.191	1.51	0.46	67	9	2
1510−089	+40	0.361	1.90	0.40	79	6	4
1512+370	+59	0.371	1.10	0.23	109	6	2
1522+155	+53	0.628	7.90	1.46	32	5	3
1532+016	+43	1.420	3.50	0.20	131	2	4
1538+477	+52	0.770	0.90	0.14	65	4	1
1545+210	+50	0.266	1.03	0.20	4	5	2
1548+056	+42	1.426	4.70	1.10	14	7	4
1552+085	+43	0.119	1.88	0.23	75	3	1
1611+343	+47	1.401	1.68	0.67	134	11	3
1612+266	+45	0.395	1.24	0.56	81	13	2
1617+175	+41	0.114	0.94	0.17	79	5	1
1633+382	+42	1.814	2.60	1.00	97	11	4
1635+119	+35	0.146	0.82	0.38	175	13	2
1637+574	+40	0.745	2.40	0.80	170	9	5
1641+399	+41	0.594	4.00	0.30	103	2	4
1642+690	+37	0.751	16.60	1.70	8	3	4
1656+571	+38	1.290	1.34	0.31	51	7	6
1721+343	+32	0.206	0.74	0.16	143	6	2
1739+522	+32	1.375	3.70	0.20	172	2	4
2121+050	−30	1.878	10.70	2.90	68	6	4
2131−021	−36	0.557	16.90	4.00	93	1	4
2145+067	−34	0.990	0.61	0.23	138	11	2
2154−200	−50	2.028	0.75	0.28	145	12	0
2155−152	−48	0.672	22.60	1.10	7	2	4
2216−038	−47	0.901	1.09	0.44	139	11	2
2223−052	−49	1.404	13.60	0.40	133	1	4
2225−055	−49	1.981	4.37	0.29	162	2	0
2227−088	−52	1.562	9.20	0.87	173	3	6
2230+025	−45	2.147	0.68	0.29	119	14	0
2230+114	−39	1.037	7.30	0.30	118	1	4
2240−370	−61	1.835	2.10	0.28	32	4	0
2243−123	−57	0.630	1.25	0.26	156	6	6
2245−328	−63	2.268	2.30	1.10	73	13	4
2247+140	−39	0.237	1.39	0.38	75	8	2
2251+113	−42	0.323	1.00	0.15	49	4	2
2251+158	−38	0.859	2.90	0.30	144	3	4
2251+244	−31	2.328	1.34	0.67	113	14	3
2254+024	−49	2.090	1.67	0.75	2	13	6
2255−282	−65	0.926	2.00	0.40	112	6	4
2308+098	−46	0.432	1.14	0.16	105	4	2
2326−477	−64	1.302	1.00	0.30	103	8	4
2340−036	−61	0.896	0.87	0.25	130	8	2
2345−167	−72	0.576	4.90	1.50	70	8	4
2349−010	−60	0.174	0.91	0.21	143	7	2
2351−154	−72	2.665	3.73	1.56	13	12	2
2353+283	−33	0.731	1.43	0.54	76	11	3
2354−117	−70	0.949	2.00	0.40	105	6	4
2355−534	−62	1.006	3.70	0.60	126	4	4

References: (0) Hutsemékers et al. 1998, (1) Berriman et al. 1990, (2) Stockman et al. 1984, (3) Moore & Stockman 1984, (4) Impey & Tapia 1990, (5) Impey et al. 1991, (6) Wills et al. 1992

idence for significant deviations from a uniform distribution of angles, except in the subsample of 75 quasars which are located in the southern galactic hemisphere. In this case, the Kuiper statistic is evaluated to be $K_n = 1.694$, which indicates a rejection of the null hypothesis at the 5% significance level (cf. Arsham 1988), i.e. a marginal evidence for a deviation from uniformity.

We may also test the statistical isotropy of the histograms (cf. Fig. 4) using the Hawley & Peebles (1975) Fourier method. Similar results are obtained i.e. no significant deviation from a uniform distribution of angles, except in the southern subsample. If Δ_1 and Δ_2 denotes the coefficients of the wave model which describe the degree of deviation from isotropy, we have $\Delta_1 = -0.082$ and $\Delta_2 = -0.452$ assuming the polarization angles of the 75 quasars grouped in 18 bins of 10°. Then the probability that the total amplitude $\Delta = (\Delta_1^2 + \Delta_1^2)^{1/2}$ exceeds some chosen value is computed to be $P(>\Delta) = 2\%$, using $P(>\Delta) = \exp(-0.25\, n\, \Delta^2)$ where $n = 75$ (cf. Hawley & Peebles 1975). This indicates a moderate deviation from isotropy. The preferred orientation may be calculated from $\theta = 0.5 \arctan(\Delta_2/\Delta_1) \simeq 130°$ which corresponds to the peak seen in the histogram (Fig. 4).

Taking into account the fact that we have considered several subsamples with one moderate detection, we may conclude that there is only weak evidence that the distribution of quasar polarization angles deviates from uniformity.

4.2. Maps of quasar polarization vectors

In Fig. 5, maps of quasar polarization vectors are illustrated. The whole sky is split in two parts which correspond to the northern and southern galactic hemispheres. Nearly all of the 170 quasars of our sample are represented (except 5 objects with $z > 2.3$ located in the northern galactic hemisphere). The objects are represented in redshift slices whose values have been searched for and chosen to emphasize visible alignments. The region discussed in Sect. 2 (Fig. 1) is seen in the lower left frame (with $170° \leq \alpha \leq 220°$ and $1.0 < z \leq 2.3$). In the following, we will refer to it as to the region of (quasar polarization vector) alignments A1.

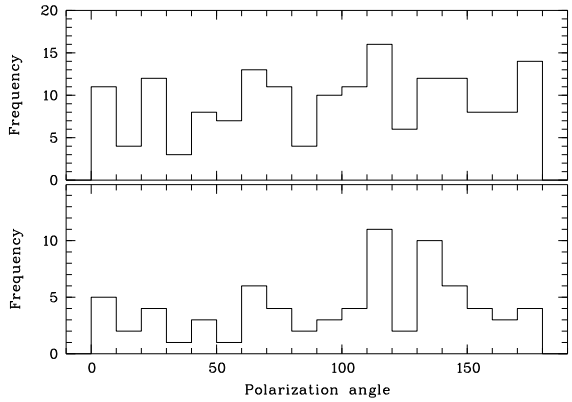


Fig. 4. Polarization angle histograms for the whole sample of 170 quasars (top), and for the 75 quasars located in the southern galactic hemisphere (bottom)

Although this may be quite subjective and dependent on the projection, at least 2 other large regions where quasar polarization vectors seem coherently oriented may be identified: a group of objects with polarization angles concentrated around $\theta \simeq 80°$ and located at roughly constant declination $\delta \sim 10°$ with $150° \leq \alpha \leq 250°$ and $0.0 < z \leq 0.5$ (region A2), and more particularly a well-defined group of 10 objects with $320° \leq \alpha \leq 360°$ and $0.7 < z \leq 1.5$, for which all polarization angles lie in the range $103° - 144°$ (region A3). The latter objects are the main contributors to the peak seen in the histogram of the southern subsample (Fig. 4). For these quasars, most measurements (i.e. 7 out of 10) are apparently taken from the same paper (Impey & Tapia 1990), giving the impression that we could have pointed out an instrumental bias. But one should recall that the paper by Impey & Tapia (1990) is also a compilation, and that 3 of these objects were in fact measured independently. Furthermore, for 2 of them (2223-052 and 2251+158) the polarization angles were re-measured by Wills et al. (1992) and are in excellent agreement, such that there is finally more evidence *against* an instrumental bias. Note that a confirmation of the reality of these alignments may simply be obtained by performing new optical polarization measurements for other quasars located in the same regions of the sky.

It is particularly interesting to notice that the alignments of quasar polarization vectors are spatially delimited, and more particularly in redshift: quasars located along the same line of sight but with lower or higher redshifts do not show the same trend. This indicates not only that a 3D analysis is essential, but also that instrumental or interstellar polarization are not likely to be responsible for the observed effect.

5. Statistical tests: formulation and description

5.1. A new dedicated statistical test

Apart from the fact that the identified polarization vector alignments are apparently localized in the 3D space, we have a priori no idea on their characteristics, nor on the physics responsible for them. Statistical tests should therefore be general enough, and if possible non-parametric, the main goal being the detection of the effect and the evaluation of its statistical significance. For this purpose, we design a rather simple measure of polarization vector alignments, which will be compared to simulations.

First, we adopt comoving distances calculated with

$$r(z) = \frac{2\,c}{H_0}\,(1 - (1+z)^{-1/2})\,, \tag{1}$$

where we assume a flat Universe with a cosmological deceleration parameter $q_0 = 0.5$. H_0 is the Hubble constant; its value is unimportant here since only relative distances are of interest. The distance from an object to another one is then computed using the rectangular coordinates

$$\begin{aligned} x &= r\,\cos\delta\cos\alpha\,, \\ y &= r\,\cos\delta\sin\alpha\,, \\ z &= r\,\sin\delta\,, \end{aligned} \tag{2}$$

α and δ denoting the right ascension and declination of the object in the equatorial coordinate system. A 2D analysis may be carried out by fixing $r = 1$ in Eq. 2.

For each group of n_v neighbouring quasars, we consider the local dispersion of polarization angles as a measure of their possible alignment. For evaluating a circular dispersion, there are several possibilities which are essentially related to the *mean* direction of the angles, or to the *median* direction (cf. Fisher 1993). After some experimentation, the dispersion related to the median was adopted, since it appeared slightly more efficient in detecting local deviations from uniform distributions of angles. For each object, we identify the n_v nearest neighbours in the 3D (or 2D) space, and compute (Fisher 1993)

$$d(\theta) = 90 - (1/n_v)\sum_{k=1}^{n_v} |90 - |\theta_k - \theta||, \tag{3}$$

where $\theta_1, \cdots, \theta_{n_v}$ are the polarization angles of the neighbouring objects. The central object is included in the n_v ones and in the sum (with $k = 1$). In this expression, it has been accounted for the fact that polarization angles are *axial* data, i.e. they do not span the whole circle but range from 0° to 180°. The mean dispersion of the polarization angles of the n_v objects around object i, hereafter noted D_i, is computed to be the minimum value of $d(\theta)$. If n represents the total number of objects in our sample, we adopt

$$S_D = \frac{1}{n}\,\sum_{i=1}^{n} D_i \tag{4}$$

as a statistic with one parameter n_v. If the polarization vectors are locally aligned, we expect S_D to be smaller than in models where polarization angles are distributed at random on the objects.

S_D measures the concentration of angles for groups of objects close to each other in space. We may also measure, in a

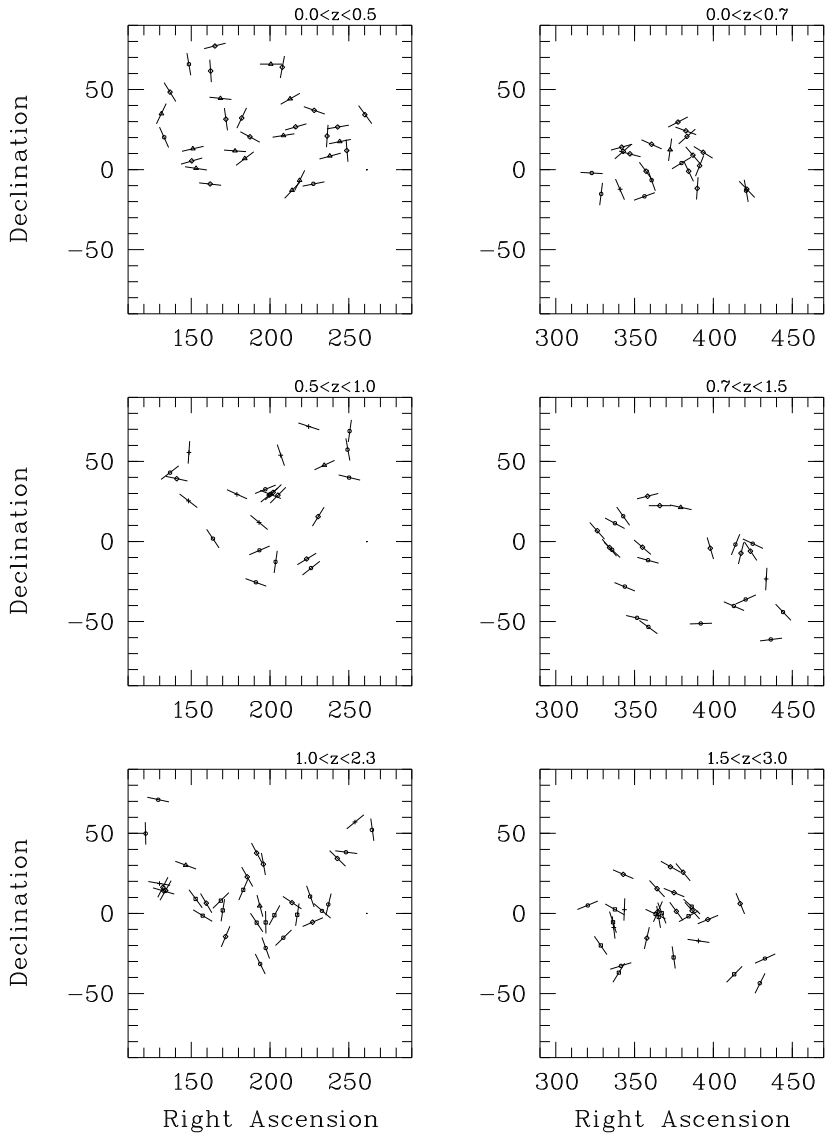


Fig. 5. Maps of quasar polarization vectors in the equatorial coordinate system (right ascensions are in degrees). Each frame is labeled with the redshift range. The different symbols refer to different catalogues: Stockman et al. 1984, and Moore & Stockman 1984 [losanges], Berriman et al. 1990 [triangles], Impey & Tapia 1990, and Impey et al. 1991 [circles], Wills et al. 1992 [crosses], Hutsemékers et al. 1998 [squares]

given volume, the spatial concentration of objects which have similar angles. The combination of both measures is expected to be more efficient for detecting local coherent orientations, for example if groups of aligned neighbours have different sizes, or if their shape is not spherical.

So, for each object i, we first compute an average direction of the polarization angles of its n_v nearest neighbours, including the object i itself. The average direction is taken to be the median direction $\tilde{\theta}$ which is the value of θ minimizing the function $d(\theta)$ in Eq. 3. The median is not always uniquely defined since $d(\theta)$ may not have a single minimun, or this minimum may be quite broad: this situation occurs when the angles tend to be uniformly distributed, and more particularly when n_v is small. In this case, we choose for the median direction the central value of the broadest minimum, taking into account the circular nature of the data. Note that other kinds of average directions may be considered, like the mean direction defined in the next section (Eq. 11) which provides comparable results.

To every object k taken among the n_v neighbours and whose polarization angle θ_k is close to the local median, i.e. objects for which $\Delta\theta_k \leq \Delta\theta_c$ where

$$\Delta\theta_k = 90 - |90 - |\theta_k - \tilde{\theta}|| \tag{5}$$

and $\Delta\theta_c$ is a critical value defined between 0° and 90° and fixed in advance, we attribute a weight w_k = 1, otherwise w_k = 0. Then, if $r(k, k')$ represents the distance from object k to

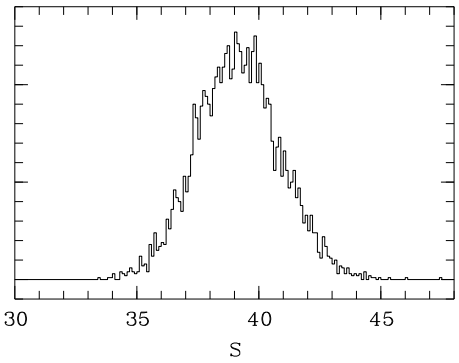


Fig. 6. An example of the S distribution obtained by running 5000 simulations, with n_v = 24 and $\Delta\theta_c$ = 60°. With the same parameters, the S statistic corresponding to our sample of 170 quasars is computed to be $S^\star$ = 33.°9

object k', we calculate the average distances

$$RC_i = \frac{\sum_{k=1}^{n_v-1}\sum_{k'=k+1}^{n_v} w_k w_{k'}\, r(k,k')}{\sum_{k=1}^{n_v-1}\sum_{k'=k+1}^{n_v} w_k w_{k'}}\,, \tag{6}$$

which refers to objects whose polarization angles are close to the median direction, and

$$RF_i = \frac{\sum_{k=1}^{n_v-1}\sum_{k'=k+1}^{n_v}(1-w_k)(1-w_{k'})\, r(k,k')}{\sum_{k=1}^{n_v-1}\sum_{k'=k+1}^{n_v}(1-w_k)(1-w_{k'})}\,, \tag{7}$$

which refers to objects whose polarization angles are far from the median direction, the ratio

$$R_i = RC_i/RF_i \tag{8}$$

providing a local measure of the spatial concentration of objects which have angles close to the median. R_i is expected to be around 1 when the angles are distributed at random on the different objects, and smaller than 1 when objects with similar angles are spatially concentrated. Its value is put equal to 1 when the number of objects with w_k = 1 or the number of objects with w_k = 0 is strictly smaller than 3.

We can now write the final statistic

$$S = \frac{1}{n}\sum_{i=1}^{n} D_i\, R_i\,, \tag{9}$$

which may be evaluated for different values of the parameters n_v and $\Delta\theta_c$. It is expected to be relatively small for samples in which local alignments of polarization vectors are present.

Since the quantities D_i and R_i are clearly not independent due to the overlapping regions over which they are calculated, the distribution of S and S_D must be obtained using simulations. For this, the positions of the objects are kept fixed, and the polarization angles randomly shuffled on the objects. With this method, each simulated configuration has the same angle histogram and object positions as the original sample, but any true correlation between angles and positions will have been erased, ensuring that we are essentially testing correlations between angle coherent orientations and object positions. Several thousand simulated configurations are computed for which the S and S_D statistics are evaluated. A typical example of the S distribution is illustrated in Fig. 6, for n_v = 24 and $\Delta\theta_c$ = 60°. With different values of the parameters, the distribution is shifted or its shape modified.

If $S^\star$ is the statistic measured for the original sample, the statistical significance of the test, or the probability that a value of S such that $S < S^\star$ would have been obtained by chance, may be estimated in computing the percentage of simulated configurations for which $S < S^\star$, up to a resolution fixed by the number of simulations.

Let us finally note that distributions resulting from randomly generated (instead of shuffled) angles have also been tried, and that they give nearly similar statistical significances.

5.2. The Andrews & Wasserman test

After the previously described test was implemented, and most results obtained, we became aware of the work by Bietenholz & Kronberg (1984), and Bietenholz (1986). These authors have re-analysed with appropriate statistical methods the claim by Birch (1982) that the offset between the position angle of an extragalactic radio source and the orientation of its radio polarization vector (corrected for Faraday rotation) is correlated with the source position on the celestial sphere. Although the results themselves may be of interest for the present study and will be discussed later, we consider here one of the proposed statistical tests which may be useful for our purpose: the non-parametric test originally due to Andrews & Wasserman.

The idea of the Andrews & Wasserman test is to compute for each object i, the mean direction $\bar\theta_i$ of its n_v neighbours, and to compare this local average to the actual polarization angle of the object i, θ_i. If angles are correlated to positions, one expects, on the average, θ_i to be closer to $\bar\theta_{j=i}$ than to $\bar\theta_{j\neq i}$.

So, for each object i, we consider the n_v nearest neighbours in the 2D or 3D space as in Sect. 5.1, and compute the mean resultant vector

$$\mathbf{Y}_i = \frac{1}{n_v}\,(\sum_{k=1}^{n_v}\cos 2\theta_k,\ \sum_{k=1}^{n_v}\sin 2\theta_k)\,, \tag{10}$$

where $\theta_1, \cdots, \theta_{n_v}$ are the polarization angles of the neighbouring objects, excluding i. The factor 2 accounts for the fact that the polarization angles are axial data. Then, if we let $\bar{\mathbf{Y}}_i$ denote the normalized vector $\mathbf{Y}_i$, the mean direction $\bar\theta_i$ is given by

$$\bar{\mathbf{Y}}_i = (\cos 2\bar\theta_i,\ \sin 2\bar\theta_i)\,. \tag{11}$$

As a measure of the closeness of θ_i and $\bar\theta_j$, one uses the inner (dot) product $\mathrm{D}_{i,j} = \mathbf{y}_i.\bar{\mathbf{Y}}_j$, where $\mathbf{y}_i = (\cos 2\theta_i,\ \sin 2\theta_i)$. If angles are correlated to positions, $\mathrm{D}_{i,j}$ is expected to be, on the average, larger for $j = i$ than for $j \neq i$. Then, to evaluate the statistic, one sorts the $\mathrm{D}_{i,j=1,n}$ values in increasing order, and notes r_i the rank of $\mathrm{D}_{i,j=i}$. Finally, the test statistic Z_c, which

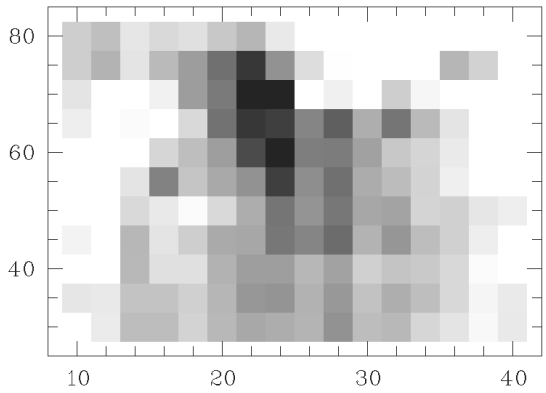


Fig. 7. Map of the significance level of the S statistical test applied to our sample of 170 quasars for various combinations of the parameters n_v (in abscissae) and $\Delta\theta_c$ (in ordinates). The significance level is represented on a logarithmic gray scale where white corresponds to log S.L.≥ -1.3 and black to log S.L.≤ -3

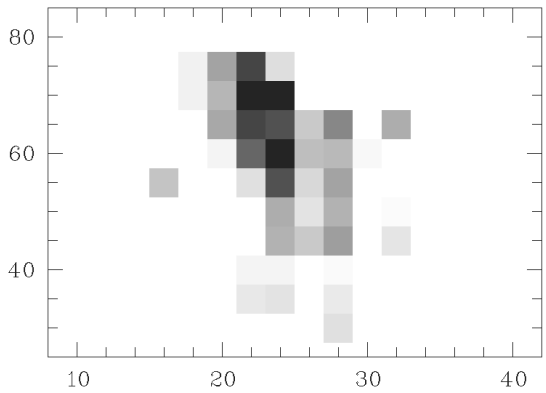


Fig. 8. Same as Fig. 7, but white corresponds to log S.L.≥ -2 and black to log S.L.≤ -3. The smallest value of the S.L. is $2\,10^{-4}$, for n_v = 22 and $\Delta\theta_c$ = 70°

is approximately normally distributed (cf. Bietenholz 1986), is written

$$Z_c = \frac{1}{n}\sum_{i=1}^{n} Z_i \qquad (12)$$

where

$$Z_i = \frac{\mathrm{r}_i - (n+1)/2}{\sqrt{n/12}}\,, \qquad (13)$$

n representing the total number of objects in our sample. Z_c is expected to be significantly larger than zero when the polarization angles are not randomly distributed on object positions. Again, the number of nearest neighbours n_v is a free parameter.

Although this test is normalized, the $\mathrm{D}_{i,j=1,n}$ are not independent, especially for large n_v. When applied to our sample, simulations were found necessary to obtain accurate statistical

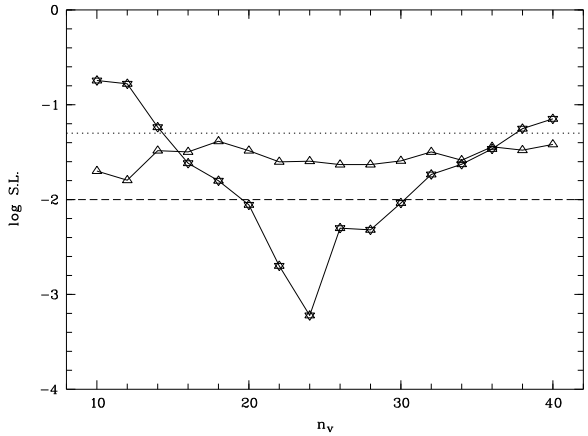


Fig. 9. The significance level of the S_D test (triangles) as a function of n_v for our sample of 170 quasars, together with the results of the S test for $\Delta\theta_c$ = 60° (stars). The dotted and dashed horizontal lines respectively indicate S.L. = 0.05 and 0.01

significances, i.e. to better than a factor 2-3. If $Z_c^\star$ is the statistic measured for the original sample, the statistical significance of the test may be evaluated by computing the percentage of simulated configurations for which $Z_c > Z_c^\star$.

5.3. A modified Andrews & Wasserman test

The original Andrews & Wasserman test may be modified in an interesting way. The length of the mean resultant vector $\mathbf{Y}_i$ provides in fact a natural measure of the dispersion of the angles, being large if the angles are concentrated around the mean direction (e.g. Fisher 1993). By using the dot product $\mathrm{D}_{i,j} = \mathbf{y}_i.\mathbf{Y}_j$ instead of $\mathrm{D}_{i,j} = \mathbf{y}_i.\bar{\mathbf{Y}}_j$, one gives more weight to the groups of objects for which the local average has actually a sense, i.e. to those for which the polarization vectors are coherently oriented. Apart from this, the statistic Z_c^m of this modified Andrews & Wasserman test is calculated in the same way.

5.4. Visualization of the results

The previous tests may tell us if a statistically significant orientation effect exists in the sample, or not. However, it would be interesting to know which groups of objects contribute the most to the effect, and if the groups visually identified in Fig. 5 have some statistical reality or not. For this, we use a method adapted from Dressler & Shectman (1988) which was proposed for detecting sub-structures in clusters of galaxies.

For each object i, a local statistic S_i has been defined: S_i = D_i, D_iR_i, Z_i or Z_i^m (cf. Eqs. 4, 9, 12). It may be evaluated for the original sample, $S_i^\star$, as well as for every simulated configuration, such that one can compute $< S_i >$, the average over the whole set of simulations, and σ_i, the corresponding standard deviation. Then we calculate

$$s_i = \frac{< S_i > - S_i^\star}{2\,\sigma_i}\,, \qquad (14)$$

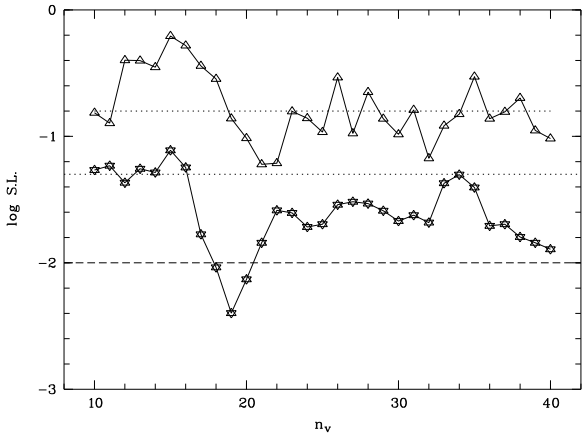


Fig. 10. The significance level of the Z_c and Z_c^m tests (respectively, triangles and stars) as a function of n_v for our sample of 170 quasars. For clarity, the Z_c results have been shifted upwards by 0.5. The dotted and dashed horizontal lines respectively indicate S.L. = 0.05 and 0.01

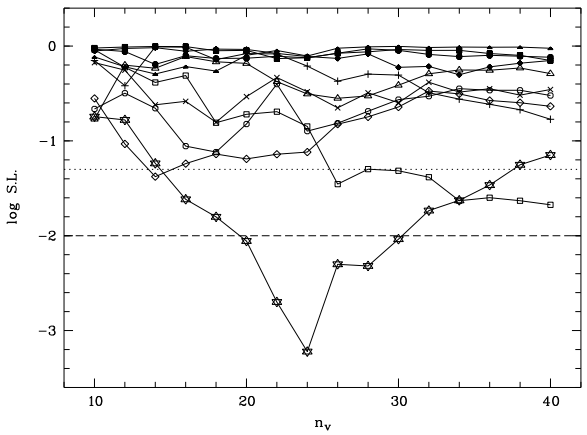


Fig. 11. The significance level of the S test ($\Delta\theta_c = 60°$) as a function of n_v for our sample of 170 quasars, when the test is applied to the real data (stars), and to the first ten randomized models (other symbols). The dotted and dashed horizontal lines respectively indicate S.L. = 0.05 and 0.01

which provides a measure of the local departure to random models. If we only consider the positive values of s_i when $S_i = D_i$ or $S_i = D_i R_i$, and the negative values of s_i when $S_i = Z_i$ or $S_i = Z_i^m$, one may draw around each object i a circle of radius

$$\rho_i \propto \exp|s_i| - 1\,, \tag{15}$$

such that the larger the circle, the larger the contribution of object i to a local orientation effect. Put on maps, clusters of large circles may help to identify regions in which polarization vector alignments prevail, if one carefully keeps in mind that the points are not statistically independent.

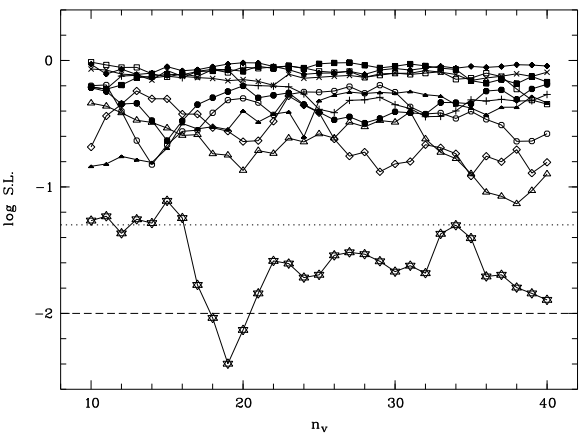


Fig. 12. The significance level of the Z_c^m test as a function of n_v for our sample of 170 quasars, when the test is applied to the real data (stars), and to the first ten randomized models (other symbols). The dotted and dashed horizontal lines respectively indicate S.L. = 0.05 and 0.01

6. Results from the statistical tests

The selected sample of 170 quasars has been analysed using the tests S, S_D, Z_c, and Z_c^m, and considering the objects located in the 3D space. The parameters have been varied around values expected from the preliminary analyses (Sects. 2 & 4), then largely explored to check the behavior and stability of the results. Finally, the test statistics have been computed for n_v between 10 and 40 nearest neighbours, and $\Delta\theta_c$ between 30° and 80°. Let us recall that n_v represents the number of neighbours including the central object for the S-type tests, while excluding it for the Z-type tests. As far as computing time is concerned, the Z-type tests are significantly faster than the S-type ones such that smaller increments in n_v were taken to allow a direct comparison of the results. In order to evaluate the significance level of the statistical tests, 5000 models with randomly shuffled angles have been considered. The tests were applied to each randomized model for the adopted range of parameters, and statistical distributions have been constructed for each n_v, or combination of n_v and $\Delta\theta_c$. The test statistics computed for the real data with a given set of parameters were then compared to the statistical distributions obtained with the same parameters.

The results of the S test, which depend on both n_v and $\Delta\theta_c$, are conveniently illustrated in Figs. 7 & 8, which represent maps of the significance level (S.L.) in the $(n_v, \Delta\theta_c)$-plane. Only S.L. evaluated to be lower than 0.05 (0.01) are illustrated in Fig. 7 (Fig. 8), the darker the points the smaller the S.L. We emphasize that the S.L. values are not independent. The variation with the parameters appears rather smooth, and a significant deviation from randomness is detected around $n_v \sim 24$ with $0.001 <$ S.L. < 0.01, quite independently of $\Delta\theta_c$ (Fig. 8). Significance levels as small as $2\,10^{-4}$ were measured but are not considered as representative. The values of n_v which minimize the S.L., although larger than the 10-15 coherently oriented objects

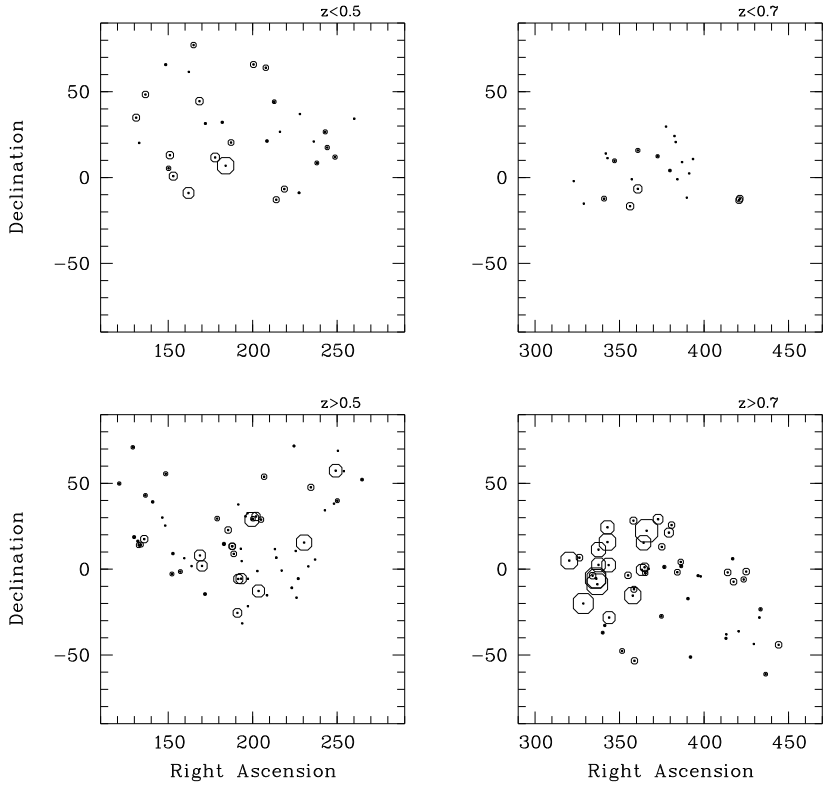


Fig. 13. Maps in the equatorial coordinate system of the local contributions to the significance level of the S test, for n_v = 24 and $\Delta\theta_c$ = 60°. Each frame is labeled with the redshift range

visually identified in Fig. 5, are in good agreement with the expected values since the number of neighbours used in the tests must necessarily encompass the physical structures, due to the way the tests are designed. In addition, these structures may be slanted with respect to the line of sight and contain more members than actually seen on projected maps.

The results of the S_D test, which do not depend on $\Delta\theta_c$, are given in Fig. 9 together with a representative example of the S test obtained for $\Delta\theta_c$ = 60°. As expected, the S_D test is less sensitive, although it indicates moderate deviation from randomness with 0.01 $<$ S.L. $<$ 0.05, quite independently of n_v. The S.L. of the Z-type tests are illustrated in Fig. 10. The Z_c^m test detects a deviation from uniformity for $n_v \simeq 18-20$ with S.L. $<$ 0.01, confirming the previous results. The Z_c test appears to be the less sensitive with a rather noisy S.L. It nevertheless indicates a moderate deviation from randomness near $n_v \sim 22$ with 0.01 $<$ S.L. $<$ 0.05. The slightly larger values of n_v obtained with the S test when compared to the Z_c^m test may probably be accounted for by the fact that one needs at least three mis-aligned objects among the n_v nearest neighbours for computing the distance ratio R_i (Eq. 8).

Although there is a good agreement between the values of n_v minimizing the significance level of the statistical tests and those expected from Fig. 5 (the results are not too dependent on $\Delta\theta_c$), the parameter values were in fact not exactly known a priori. It is therefore important to have an estimate of the significance independently of the values of $\Delta\theta_c$ and n_v. Since the results at different $\Delta\theta_c$ and n_v are not independent, we have computed for each of the 5000 randomized models the smallest S.L. given by the tests for whatever n_v and $\Delta\theta_c$ it occurs at, and constructed the distribution of these minimum values. Since the minimum S.L. does not occur at the same n_v or $\Delta\theta_c$ for the different realizations (cf. Figs. 11 & 12), S.L. have been used instead of statistics, the latter being not normalized. Then, the smallest S.L. for the real data, also evaluated whatever the value of n_v or $\Delta\theta_c$, has been compared to the previously obtained distribution, and a "global" S.L. derived. Considering the whole range of $\Delta\theta_c$ and n_v, i.e. $\Delta\theta_c$ = 30° to 80° and n_v = 10 to 40, the global S.L. is found to be equal to 0.005 for the S test. For the Z_c^m test, the global S.L. is 0.015 with n_v = 10 to 40. Since the parameter space has been more largely explored than necessary, these values may be seen as upper limits.

Now, it is interesting to see which groups of objects contribute the most to the deviation, and if they correspond, or not, to the regions of alignments visually identified in Sect. 4.2. The local contributions to the significance levels of the S and Z_c^m tests are illustrated for a representative case in Figs. 13 & 14 where the 170 quasars are plotted on maps comparable to those of Fig. 5, following the method described in Sect. 5.4. Note that we should not expect a one-to-one correlation between the quasars whose polarization vectors are apparently aligned and those associated with a small local significance level. On the

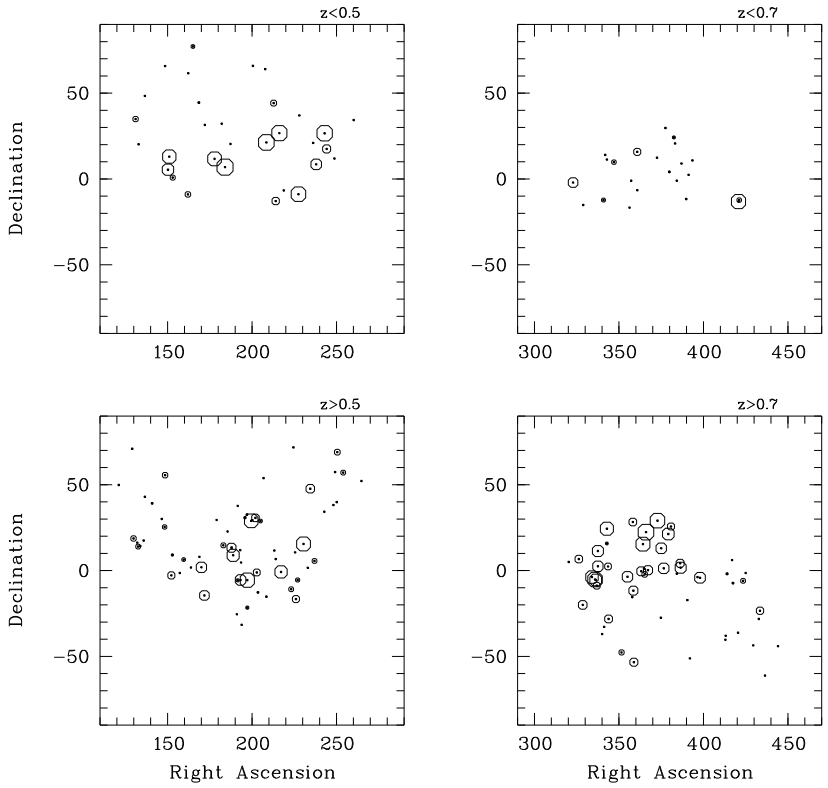


Fig. 14. Maps in the equatorial coordinate system of the local contributions to the significance level of the Z_c^m test, for n_v = 19. Each frame is labeled with the redshift range

maps, the larger and more numerous the circles, the larger the contribution to a local deviation from uniformity, although we re-emphasize that large circles are not independent. It can be seen from Figs. 13 & 14 that the strongest concentration of large circles roughly coincides with the high redshift region of alignments A3 ($320^\circ \leq \alpha \leq 360^\circ$; cf. Fig. 5 and Sect. 4.2). Nearby and also contributing is a small group of quasars located at $\alpha \sim 10^\circ$, $\delta \sim 20^\circ$, which may be identified on the high redshift ($z \geq 1.5$) map of Fig. 5; it could constitute an extension of region A3. Large regions with little or no circles are also seen: the contrast between the high and low redshift maps is particularly striking. This statistically confirms that the regions of polarization vector alignments are spatially delimited, namely in redshift. Significant local deviations from randomness also coincides with the high redshift region A1 ($170^\circ \leq \alpha \leq 220^\circ$), suggesting it is detected by the tests, although not as strongly as region A3. This difference may be due to the fact that the most aligned objects of region A1 lie in a relatively narrow region (cf. Sect. 2), while the tests are more efficient for detecting spherical structures. This nevertheless confirms the preliminary detection of region A1 reported in Sect. 2. Finally, the low redshift region A2 is also possibly detected, but mainly by the Z_c^m test. Note that similar conclusions are reached when considering other combinations of $\Delta\theta_c$ and n_v associated with small S.L. These results indicate that the statistically significant groups of objects are spatially delimited, namely in redshift, and that they correspond reasonably well to the regions visually identified in Fig. 5.

Finally, the statistical tests were run in 2D assuming all quasars located at the same distance, i.e. on the surface of a sphere (r = 1 in Eq. 2). The significance levels are definitely worse than in the 3D case. Typical results are illustrated in Fig. 15: for all n_v, S.L. > 0.01 with the S test, and S.L. > 0.05 with the Z_c^m test. This suggests weak to no real evidence for deviations from uniformity when the 3D positions of the objects are not fully taken into account.

6.1. The importance of the selection criteria

Our sample of 170 quasars was obtained by applying quite severe selection criteria to eliminate at best the contamination by our Galaxy (cf. Sect. 3). In order to know a posteriori if these were justified, we completely relax the constraints on b_{II} and p before applying the tests again. Although the size of the sample increases to 249 quasars, none of the S or Z-type tests indicate significant deviations from randomness, suggesting that the contamination is real when no selection is applied, in agreement with the study by Berriman et al. (1990, cf. Sect. 3). On the contrary, if the constraints are too strong, the sample is too small and significant results cannot be obtained. It is nevertheless interesting to note that with the condition $|b_{II}| \geq 35^\circ$ instead of $|b_{II}| \geq 30^\circ$, a deviation from uniformity is detected by both the

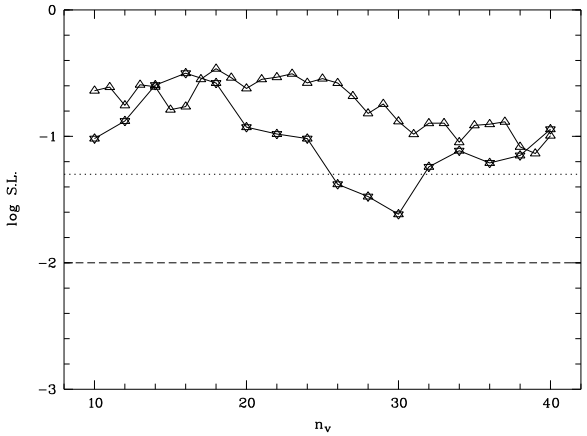


Fig. 15. The significance level of the Z_c^m and S tests (respectively, triangles and stars) as a function of n_v for our sample of 170 quasars, when all quasars are assumed located at the same distance (2D case). For the S test, $\Delta\theta_c$ = 60°. The dotted and dashed horizontal lines respectively indicate S.L. = 0.05 and 0.01

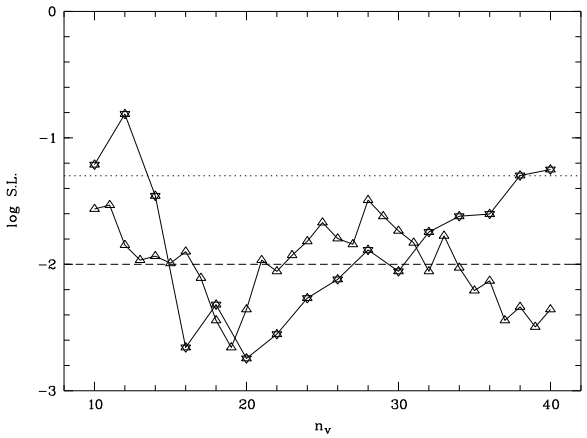


Fig. 16. The significance level of the Z_c^m and S tests (respectively, triangles and stars) as a function of n_v for a more constrained sample of 153 quasars. For the S test, $\Delta\theta_c$ = 60°. The dotted and dashed horizontal lines respectively indicate S.L. = 0.05 and 0.01

S and Z_c^m tests with a comparable to better S.L. (cf. Fig. 16), although the size of the sample has decreased to 153 objects.

6.2. The dependence on the coordinate system

The statistical tests used in the present paper are invariant under rotations of the polarization angles and of the coordinates of the sources α and δ. In fact, since only relative distances are of interest, the object position may be expressed in any coordinate system on the celestial sphere. But this is not true for the polarization angles which are defined relative to the meridians and depend on the polar axis. The importance for the statistical tests may be easily understood if one imagines a group of objects in the sky with aligned polarization vectors: if projected on the equatorial region of the celestial sphere, the alignment will be more or less conserved and detected by the tests. However, if one puts a pole just in the middle of the group, the projected angles will range from 0° to 180° and the alignment be undetected, although the dependence of the angles on positions is still highly organized. We therefore expect the significance level of our statistical tests to vary with the adopted polar axis.

To investigate this effect, we consider a new arbitrary northern pole, the equatorial coordinates of which are α_p, δ_p. In the associated new system of coordinates, the polarization angle θ_N of an object is given by

$$\tan(\theta - \theta_N) = \frac{\cos\delta_p \, \sin\left(\alpha_p - \alpha\right)}{\sin\delta_p \, \cos\delta - \sin\delta \, \cos\delta_p \, \cos\left(\alpha_p - \alpha\right)}, \quad (16)$$

where θ is the polarization angle in the equatorial coordinate system, and α, δ the equatorial coordinates of the object. For example, polarization angles projected in galactic coordinates are computed with α_p = 192° and δ_p = 27°, which are the equatorial coordinates of the North Galactic Pole. Since the polarization vectors are not oriented, only the polar direction is meaningful, and (α_p + 180°, δ_p) is equivalent to (α_p, $-\delta_p$).

For each pole (α_p, δ_p) we have therefore a different set of polarization angles for which the statistics and the significance levels may be computed. The results are illustrated in Fig. 17 which represents a map in the (α_p, δ_p)-plane of the statistic Z_c^m applied to our sample of 170 quasars and averaged over n_v = 17 to 23. Ideally one should have used S.L. instead of the statistic but at the cost of a too large amount of computing time. However, since the Z_c^m statistic is normalized, its values may be roughly seen as usual σ values, which is sufficient for the present purpose.

It is clear from Fig. 17 that the S.L. of the test depends on the adopted pole. Regions of higher and lower S.L. are clearly seen when compared to our previous results obtained in equatorial coordinates (δ_p = 90°); a spot of higher significance is identified near (130°, 35°). A very similar pattern with a spot near (120°, 35°) is observed using the S statistic suitably averaged over n_v and $\Delta\theta_c$, although this map appears less contrasted. For confirmation, the tests were run adopting the pole (125°, 35°), and the significance levels were computed. For all the S, S_D, Z_c, and Z_c^m tests, definitely lower S.L. are obtained over larger n_v ranges, S.L $< 10^{-3}$ being frequently observed. Typical examples, which should be compared to those in Fig. 10, are illustrated in Fig. 18; they were obtained by running 10000 simulations for the Z-type tests. Moreover, by visualizing the local S.L. as in Figs. 13 & 14, we have noticed that the increased significance of the tests is essentially due to the same groups of objects rather than to additional ones. Now, since the position of the spot does not correspond to the pole of an already known cosmical direction, like the Local Supercluster Pole (283°, 16°), the Cosmic Microwave Background Dipole (168°, −7°), or the direction to the Great Attractor (200°, −40°) (Bennett et al. 1996, Scaramella et al. 1989), it should not be considered as more than

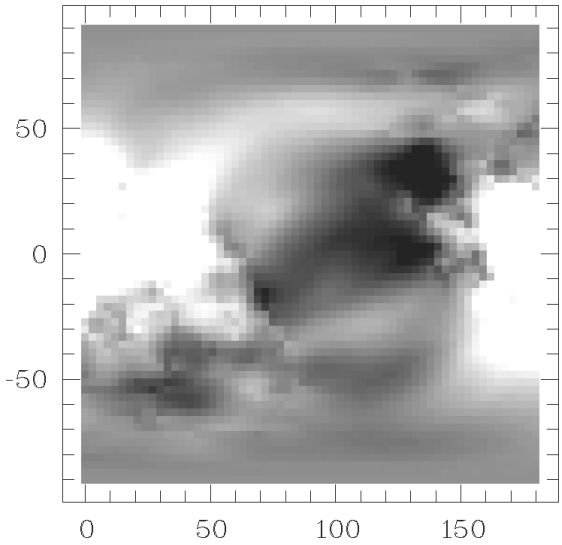


Fig. 17. Map of the Z_c^m statistic averaged over n_v = 17 to 23, as a function of the equatorial coordinates α_p (abscissae) and δ_p (ordinates) of an arbitrary northern pole. The statistic is represented on a logarithmic gray scale where white corresponds to $\overline{Z_c^m} \leq 1$ and black to $\overline{Z_c^m} \geq 3$. Note that $(\alpha_p + 180^\circ, \delta_p)$ is equivalent to $(\alpha_p, -\delta_p)$

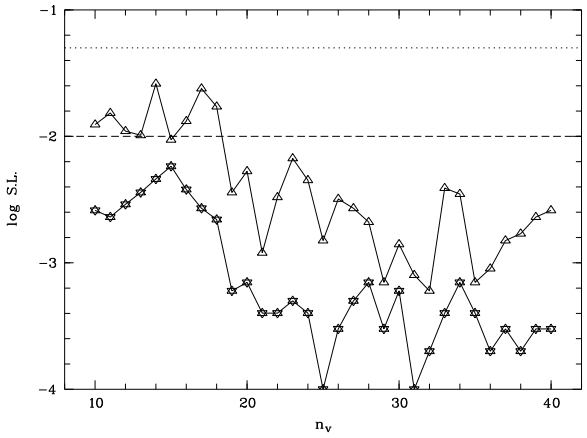


Fig. 18. The significance level of the Z_c and Z_c^m tests (respectively, triangles and stars) as a function of n_v for our sample of 170 quasars, with the polarization angles projected in a coordinate system of northern pole (α_p = 125°, δ_p = 35°). Note that for n_v = 25, the S.L. of the Z_c^m test is in fact unresolved, and therefore smaller than illustrated. The dotted and dashed horizontal lines respectively indicate S.L. = 0.05 and 0.01

a statistical fluctuation, probably due to the non-uniform distribution of coherently oriented objects in a rather limited sample. The important conclusion is that the significance of our previous results in equatorial coordinates appears intermediate and not exceptional.

6.3. Conclusions on test results

From the previous results, we may conclude that in our sample of 170 quasars, 3D statistical tests provide evidence that local alignments of polarization vectors are present, and that these cannot be ascribed to random fluctuations with global significance levels of 0.005 and 0.015, depending on the test. The higher significance reached in several cases cannot be considered as representative, but indicates that the reported significance levels are stable and not exceptional.

The tests show that the polarization vectors are coherently oriented in groups of $n_v \sim 20$ quasars, spatially delimited, and roughly corresponding to the regions visually identified on polarization vector maps. Large regions where angle distributions are compatible with random fluctuations are also seen.

7. Discussion

7.1. Are the alignments due to instrumental or interstellar polarization?

A first possible explanation for the observed polarization vector alignments is a strong instrumental bias which affects the measurements, at least for the quasars which participate to the effect. However this interpretation is unlikely since the objects with aligned polarization vectors were not measured by the same authors, nor using identical techniques (cf. Fig. 5, Sect. 4.2, and Tables 1, 2 and 3,). Also, objects measured in different surveys have polarization angles which are generally in good agreement. Furthermore, very large polarization degrees ($\geq$ 10%) are sometimes recorded and these cannot be easily ascribed to an instrumental effect. Finally, if instrumental polarization is responsible for the effect, one would expect the mean directions of the aligned polarization vectors to coincide with 0° or 90°, which is not the case.

Extinction by dust grains in our Galaxy is well known to polarize light from distant stars and to be at the origin of local alignments of polarization vectors (Mathewson & Ford 1970, Axon & Ellis 1976). Since this interstellar polarization certainly affects to some extent the quasar measurements, we have applied severe selection criteria to eliminate at best this contamination. As a whole, our final sample of 170 objects is most probably quite free of contamination, but a few affected objects may remain, and we cannot be sure a priori that these objects are not precisely those which participate to an alignment. The following discussion will therefore essentially concern the quasars belonging to the regions of alignments A1, A2 and A3, plus a few objects possibly connected to region A3 (cf. Sect. 6), i.e. a total of 43 objects.

First, if extinction in our Galaxy is the dominant mechanism of alignment, we would expect quasars located approximately along the same line of sight to have similar polarization angles independently of their redshift. The contrary is definitely observed (Fig. 5): alignments are well delimited in redshift (cf. region A3), with even different mean directions along the same

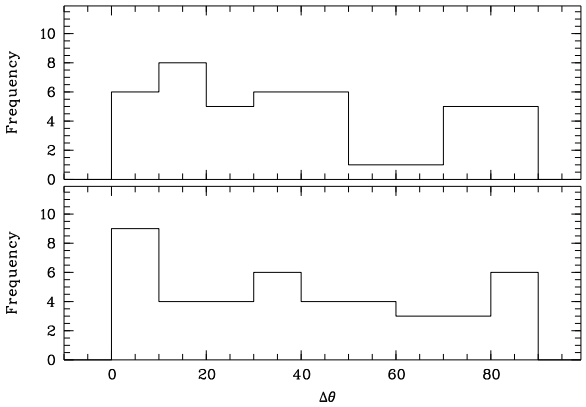


Fig. 19. Histograms of the polarization angle difference $\Delta\theta = 90 - |90 - |\theta - \theta_{star}||$, where θ refers to a quasar with aligned polarization vector and θ_{star} to the nearest galactic star on the celestial sphere. The stellar data are from the Axon & Ellis (1976) catalogue. Top: all stars are taken into account; bottom: only those stars with $d \geq 400$ pc are considered

line of sight (cf. regions A1 & A2). One might argue that the polarization degree might depend on redshift since it refers to different rest-frame spectral regions; in this case the quasar polarization could be significantly smaller for some redshift ranges and the contamination by the Galaxy larger. But, on the average, p is not smaller for quasars with aligned polarization vectors than for objects at lower or higher redshifts located along the same line of sight (cf. Tables 1, 2 and 3); moreover some of these quasars have very large p values which are difficult to ascribe to interstellar polarization, especially at high galactic latitudes. For comparison, if we consider distant stars located at high galactic latitudes (i.e. 150 stars with $d \geq 400$pc and $|b_{II}| \geq 30°$ from the catalogue of Axon & Ellis 1976), only 10 of them have $p \geq 0.6\%$ and 2 have $p \geq 1.0\%$ (cf. Fig. 2). Low polarizations ($p \leq 0.3\%$) are also reported by Berdyugin & Teerikorpi (1997) for stars close to the North Galactic Pole. In fact, the polarization degree of quasars with aligned polarization vectors is significantly higher than that of galactic stars located nearby on the celestial sphere, which is a direct consequence of our selection criteria. In addition, these quasars are not located in regions of particularly high extinction: when reported on the Burstein & Heiles (1982) extinction maps, nearly all objects are located in regions where interstellar $E_{B-V} \leq 0.03$, i.e. $p_{ISM} \leq 0.3\%$. In fact, the existence of a correlation between quasar structural axis and polarization angle indicates that the polarization is essentially intrinsic to the objects (Rusk 1990, Impey et al. 1991). This also means that the Galaxy should first de-polarize the light before producing alignments, such that even more obscuring material would be needed for affecting quasars than for affecting distant unpolarized stars.

Now, in order to compare the polarization angles themselves, we have searched in the Axon & Ellis (1976) catalogue the nearest polarized galactic star to each quasar which participates to an alignment. As seen in Fig. 19, no relation is found between the angles, i.e. no major concentration near $\Delta\theta \sim 0°$ in the histograms. Similar results are obtained when considering more than one nearest star. The three groups of aligned polarization vectors have also been compared to the global orientations seen throughout the Galaxy, namely on the maps of Axon & Ellis (1976) and Mathewson & Ford (1970) (see also Fig. 20). Such a comparison is rather subjective since it is often not easy to define a mean trend, especially at high galactic latitudes where fewer stars have been observed. Also, visual impressions depend on the used projection. However, the mean direction of region A1 ($170° \leq \alpha \leq 220°$) appears completely different from the galactic trend. Unfortunately nothing similar can be said about region A3 ($320° \leq \alpha \leq 360°$) due to the large dispersion of polarization vector orientations in the corresponding region of the Galaxy. Only a few (~ 5) quasars in the right part ($\alpha \geq 200°$) of the low-redshift region of alignments A2 (cf. Fig. 5) seem to have polarization vectors in the same direction as those of nearby stars, suggesting that their polarization could be of galactic origin. This region roughly corresponds to the North Polar Spur (Mathewson & Ford 1970, Berkhuijsen 1973). In fact, the small, moderately significant, excess seen in the first bin of one of the histograms of Fig. 19 ($d \geq 400$ pc) is due to these objects.

Statistical tests support this apparently weak contamination by instrumental and interstellar polarization. As expected, when the tests are applied to the sample of 150 galactic stars with $d \geq 400$pc and $|b_{II}| \geq 30°$, local deviations from uniformity are detected in 2D with a high significance. In fact, for $10 \leq n_v \leq 20$, $Z_c^m \simeq 6$ and S.L. is unresolved with 5000 simulations. Considering therefore the values of Z_c^m, one obtains a slightly better significance when angles are projected in galactic coordinates than in equatorial ones. On the contrary, for our sample of 170 quasars, the tests run in 2D (Fig. 15) do not detect anymore the significant effect observed in 3D, whatever the adopted coordinate system. Furthermore, neither the Celestial Pole nor the Galactic Pole correspond to a maximum of significance in Fig. 17, in agreement with the idea that the orientation effect is not due to an instrumental bias nor to a contamination by our Galaxy.

All these arguments concur to indicate that the observed polarization vector alignments are not likely to be an artefact due to instrumental polarization, or to result from interstellar polarization in our Galaxy. Since most knowledge of polarization by our Galaxy is from stars which, although distant, belong to it, one could invoke a different behavior of polarization in some remote regions of our Galaxy, or some unknown mechanisms. But even in this case it would be difficult to explain the redshift dependence of the observed alignments. We may therefore conclude that the observed alignments of quasar polarization vectors are most probably of extragalactic origin.

7.2. Are the alignments of cosmological origin?

The observed alignments of quasar polarization vectors may reflect an intrinsic property of the objects, or reveal a mechanism

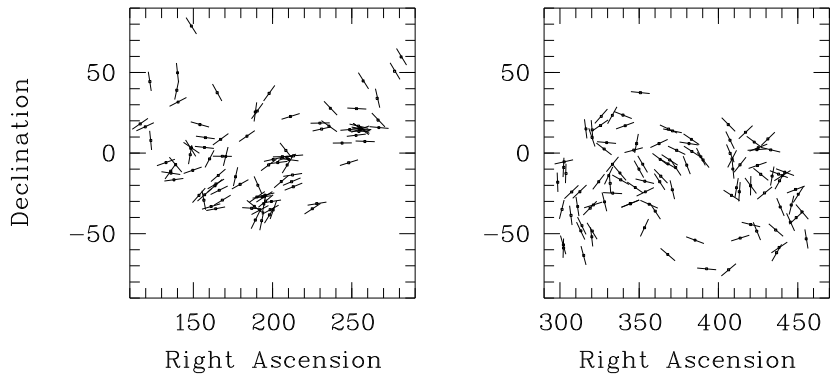


Fig. 20. Maps of galactic star polarization vectors projected in the equatorial coordinate system (right ascensions are in degrees). Data are from the Axon & Ellis (1976) catalogue. Only those stars with $d \geq 400$ pc and $|b_{II}| \geq 20°$ are represented

which affects light on its travel towards us. The fact that they are observed at high redshift, with different or no counterpart at lower redshift, indicates the existence of correlations in objects or fields on very large spatial scales; the fact that they are spatially delimited suggests that this is not a global effect at the scale of the Universe. The orientation effect is observed independently of the nature of the objects: it concerns both radio-quiet and radio-loud quasars, as well as BAL, high or low polarization objects. Let us recall that for at least part of our sample, polarization angles are related to the morphological axis of the objects, indicating that the bulk of polarization should originate in the quasar themselves.

Several mechanisms may affect light as it propagates through the Universe, the most simple naturally producing polarization vector alignments being dichroism, or selective absorption. As far as we know, the only known mechanism of this type is extinction by aligned dust grains, which could be located in galaxies along the line of sight (Webster et al. 1995, Masci & Webster 1995). For the intervening galaxies to act as analysers, one would require rather precise coherent orientations of their axis on large scales, but also a fine tuning between the original quasar polarization and the extinction in the galaxies. Moreover, one would expect strong reddening, which is certainly not true for the optically selected objects. Other light propagation effects rely on optical activity, or circular birefringence, which produces a rotation of the plane of polarization. The most common is the well-known Faraday rotation which essentially works at radio wavelengths, being proportional to the square of the wavelength. Possible mechanisms based on anisotropic cosmologies, interactions with cosmic strings, vortices or pseudoscalar fields have also been proposed, and some of them already ruled out (Brans 1975, Manohar 1988, Harvey & Nakulich 1989, Carroll et al. 1990, Carroll & Field 1991, Harari & Sikivie 1992, Masperi & Savaglio 1995). In general, if one starts with a random distribution of polarization vectors, rotation effects are unable to produce alignments. However, within regions permeated by some cosmic magnetic field, the polarization vectors may oscillate between their initial direction and that related to the field (Harari & Sikivie 1992) such that, on the average, the polarization vectors could appear coherently oriented. Interestingly enough, a small amount of dichroism is also expected in this case, through the conversion of photons into pseudoscalars. Such an effect would scramble but not completely wash away the correlation between polarization angles and morphological axes (which is not so tight indeed). Although it is far from clear whether this mechanism can work on the observed scales, it is also difficult on the observational point of view to explain why objects at higher redshifts along the same line of sight do not have accordingly aligned polarization vectors, and why alignments with different mean directions exist along the same line of sight (cf. regions A1 & A2). This remark indeed applies to every effect based on light propagation.

On the other hand, we may admit that the quasars themselves, i.e. their structural axes, are coherently oriented on large spatial scales, in agreement with the observed correlation between object structure and polarization. In this case, one must seek for a mechanism acting at the epoch of formation, like for example those proposed to explain the possible alignments of galaxy rotation axes in nearby clusters, although the latter phenomenon, still controversial, refers to much smaller scales (MacGillivray et al. 1982, Djorgovski 1987, and references therein). Coherent orientations of structural axes may provide evidence for a weak cosmological magnetic field (Reinhardt 1971). Although speculative, such a scenario could more naturally account for the different local behaviors and mean directions. Note that the correlation between structure and polarization angles is only established for some quasars of our sample, and not necessarily for those quasars which participate to an alignment (there are not enough measurements for the latter objects).

It is important to specify that the correlation between structural axes and polarization vectors which seems valid for most quasars (including BL Lac objects) arises between the *optical* polarization vector and the *core* structural axis as measured on milli-arcsecond (VLBI) scale, these two quantities being apparently always aligned (Rusk 1990, Impey et al. 1991). Larger (VLA) structures compared to optical polarization vectors show a bimodal distribution, with alignment for the low polarization quasars and anti-alignment for the highly polarized ones (Moore & Stockman 1984, Rusk 1990, Berriman et al. 1990). Bimodal distributions are also observed when radio polarization vectors and VLBI structure axes are compared (BL Lac objects

included), when radio polarization vectors and VLA structure axes are compared, and also when radio-galaxies are considered (Clarke et al. 1980, Rusk 1987, Rusk 1990, Cimatti et al. 1993, and references therein). These properties and the fact that the optical and radio polarization angles of quasars are weakly or not correlated (Rusk & Seaquist 1985, Impey & Tapia 1990, Rusk 1990) may explain why no deviation from uniformity has been reported in the distribution of radio polarization angles for samples mixing quasars and radio-galaxies[3] (Bietenholz 1986). Furthermore, since in the framework of unification models (e.g. Antonucci 1993, Urry & Padovani 1995), radio-galaxies are thought to be identical to quasars but differently oriented, it is not excluded that coherent orientation effects cannot be detected for these objects.

8. Conclusions and final remarks

In the present study, we find that the optical polarization vectors of quasars are not randomly distributed over the sky as naturally expected, but appear coherently oriented on very large spatial scales. Statistical tests indicate that this effect is significant.

This orientation effect appears spatially delimited in 3D, typically occuring in groups of 10-20 objects; apparently, not all quasars have aligned polarization vectors. The fact that the polarization vectors of objects approximately located along the same line of sight are not accordingly aligned constitutes a very important observational constraint. However, since only small numbers of objects with different redshifts can be found exactly in front of the regions of interest, especially at higher redshifts, it would be worthwhile to confirm this result with additional polarimetric observations. The orientation effect itself could be confirmed independently by obtaining new measurements for other quasars located in the identified regions of alignments, the preferential direction of polarization vectors being predicted. The data could then be analysed with simple binomial statistics (as in Sect. 2), with the advantage that the objects contributing to the significance correspond to those visually identified without any ambiguity.

Since instrumental bias and contamination by interstellar polarization in our Galaxy are apparently unlikely to be responsible for the observed effect, the very large scale at which it is observed suggests the presence of correlations in objects or fields on spatial scales $\sim 1000\,h^{-1}$ Mpc at redshifts $z \simeq$ 1-2, h being the Hubble constant in units of 100 km s^{-1} Mpc^{-1}. Although more objects are needed to determine the scale accurately, this is more comparable to the size of the Cosmic Microwave Background anisotropies detected by COBE (Smoot et al. 1992) than to the largest structures detected so far from galaxies or from quasar absorption line systems ($\lesssim 150\,h^{-1}$ Mpc, Einasto et al. 1997, Quashnock et al. 1996).

[3] We confirm the absence of deviation from randomness also in 3D by applying our statistical tests to approximately the same data set, i.e. a sample of $\sim$ 300 objects with known redshift from Simard-Normandin et al. 1981. But one should notice that the redshift distribution is quite different from that in our sample, with significantly more objects at lower redshifts

No definite interpretation exists for this orientation effect, given the data. Since polarization angles are apparently correlated to structural axes, it is tempting to admit that the objects themselves are coherently oriented, suggesting a primordial origin. However, it is not clear at all that this correlation is valid for those quasars with aligned polarization vectors. In order to check this, it would be worthwhile to obtain VLBI data for them, and to see if the structural axes are also coherently oriented. Furthermore, it will certainly be interesting to know if the different classes of objects (quasars, radio-galaxies, BL Lac objects, etc) behave similarly, or not.

Whatever its origin, this new effect, if confirmed, may be of great interest for cosmology, especially since different interpretations are subject to direct observational tests.

Acknowledgements. I am indebted to E. Gosset and M. Remy for many enlightning discussions on statistical methods. E. Gosset, H. Lamy, M. Remy, and J. Surdej are acknowledged for their remarks on the manuscript, as well as the referee for his careful reading and constructive comments. I also thank J.F. Claeskens and L. Querella for discussions on cosmological models. E. Gosset is acknowledged for providing me with his Kuiper test code, and V. Mortiaux for encoding the data from Simard-Normandin et al. The NASA Astrophysics Data System (ADS) has been consulted. The catalogue of Axon & Ellis has been retrieved in electronic form thanks to the Centre de Données Stellaires (CDS) in Strasbourg, France. This research is supported in part by contract ARC 94/99-178

References

Antonucci R. 1993, ARA&A 31, 473
Arsham H. 1988, J. Appl. Stat. 15, 131
Axon D.J., Ellis R.S. 1976, MNRAS 177, 499
Bennett C.L., Banday A.J., Górsky K.M. et al. 1996, ApJ 464, L1
Berdyugin A., Teerikorpi P. 1997, A&A 318, 37
Berkhuijsen E.M. 1973, A&A 24, 143
Berriman G., Schmidt G.D., West S.C., Stockman H.S. 1990, ApJS 74, 869
Bietenholz M.F. 1986, AJ 91, 1249
Bietenholz M.F., Kronberg P.P. 1984, ApJ 287, L1
Birch P. 1982, Nat 298, 451
Brans C.H. 1975, ApJ 197, 1
Burstein D., Heiles C. 1982, AJ 87, 1165
Carroll S.M., Field G.B., Jackiw R. 1990, Phys. Rev. D 41, 1231
Carroll S.M., Field G.B. 1991, Phys. Rev. D 43, 3789
Cimatti A., di Serego Alighieri S., Fosbury R.A.E., Salvati M., Taylor D. 1993, MNRAS 264, 421
Clarke D., Stewart B.G. 1986, Vistas in Astronomy 29, 27
Clarke J.N., Kronberg P.P., Simard-Normandin M. 1980, MNRAS 190, 205
Cohen M.H., Ogle P.M., Tran H.D. et al. 1995, ApJ 448, L77
de Diego J.A., Kidger M.R., Pérez E., Takalo L.O. 1994, ApJ 424, 76
di Serego Alighieri S. 1989, 1^{st} ESO/ST-ECF Data Analysis Workshop, Grosbøl P.J. et al. (eds), 157
Djorgovski S. 1987, in Nearly Normal Galaxies, Faber S.M. (ed.), Springer-Verlag New-York, p. 227
Dressler A., Shectman S.A. 1988, AJ 95, 985
Einasto J., Einasto M., Gottlöber S. et al. 1997, Nat 385, 139
Fisher N.I. 1993, Statistical Analysis of Circular Data, Cambridge University Press, Cambridge

Harari D., Sikivie P. 1992, Phys. Lett. B 289, 67
Harvey J.A., Nakulich S.G. 1989, Phys. Lett. B 217, 231
Hawley D.L., Peebles P.J.E. 1975, AJ 80, 477
Hiltner W.A. 1956, ApJS 2, 389
Hutsemékers D., Lamy H., Remy M. 1998, in preparation
Impey C.D., Lawrence C.R., Tapia S. 1991, ApJ 375, 46
Impey C.D., Malkan M.A., Webb W., Petry C.E. 1995, ApJ 440, 80
Impey C.D., Tapia S. 1990, ApJ 354, 124
MacGillivray H.T., Dodd R.J., McNally B.V., Corwin Jr H.G. 1982, MNRAS 198, 605
Manohar A. 1988, Phys. Lett. B 206, 276
Masci F.J., Webster R.L. 1995, PASA 12, 146
Masperi L., Savaglio S. 1995, Astroparticle Phys. 3, 209
Mathewson D.S., Ford V.L. 1970, Mem. R. Ast. Soc. 74, 139
Moore R.L., Stockman H.S. 1984 ApJ 279, 465
Quashnock J.M., Vanden Berk D.E., York D.G. 1996, ApJ 472, L69
Reinhardt M. 1971, Ap&SS 10, 363
Rusk R. 1987, in The Impact of VLBI on Astrophysics and Geophysics, Reid M.J. & Moran J.M. (eds.), IAU Symposium 129, Reidel Dordrecht, p. 161
Rusk R. 1990, J. R. Astron. Soc. Can. 84, 199
Rusk R., Seaquist E.R. 1985, AJ 90, 30
Saikia D.J., Salter C.J. 1988, ARA&A 26, 93
Scaramella R., Baiesi-Pillastrini G., Chincarini G., Vettolani G., Zamorani G. 1989, Nat 338, 562
Simard-Normandin M., Kronberg P.P., Button S. 1981, ApJS 45, 97
Smith P.S., Schmidt G.D., Jannuzi B.T., Elston R. 1994, ApJ 426, 535
Smoot G.F., Bennett C.L., Kogut A. et al. 1992, ApJ 396, L1
Stockman H.S., Moore R.L., Angel J.R.P. 1984, ApJ 279, 485
Urry C.M., Padovani P. 1995, PASP 107, 803
Wardle J.F.C., Kronberg P.P. 1974, ApJ 194, 249
Webb W., Malkan M., Schmidt G., Impey C.D. 1993, ApJ 419, 494
Webster R.L., Francis P.J., Peterson B.A., Drinkwater M.J., Masci F.J. 1995, Nat 375, 469
Wills B.J., Wills D., Breger M., Antonucci R.R.J., Barvainis R. 1992, ApJ 398, 454

This article was processed by the author using Springer-Verlag LaTeX A&A style file *L-AA* version 3.

Article 17

Confirmation of the existence of coherent orientations of quasar polarization vectors on cosmological scales

D. Hutsemékers, H. Lamy : Astron. Astrophys. 367, 381 (2001)

Dans le but de vérifier la possibilité d'une orientation cohérente de la polarisation des quasars sur de très grandes échelles (Article 16), nous avons obtenu de nouvelles mesures de polarisation pour un échantillon de quasars situés dans une région de l'Univers où les valeurs que peuvent prendre les angles de polarisation sont prédites à l'avance. L'hypothèse d'une distribution uniforme des angles de polarisation peut dès lors être analysée sur base d'un simple test binomial. Pour ce nouvel échantillon, cette hypothèse est rejetée avec un niveau de signification de 1,8%, apportant une confirmation indépendante à l'existence d'un effet d'alignement.

Au total, dans cette région du ciel, 25 quasars sur 29 ont leurs vecteurs polarisation alignés et ce sur une échelle de l'ordre du Gpc. Des tests statistiques globaux appliqués à l'échantillon total de 213 objets confirment les résultats précédents avec un niveau de signification de l'ordre de 0,1%.

Quelques contraintes sur le phénomène sont également obtenues. Tout d'abord nous trouvons que la polarisation est à peu près parallèle au plan du Superamas Local. Nous confirmons que les objets sur la même ligne de visée mais à des redshifts différents ne sont pas alignés de la même façon. Enfin, nous montrons que les corrélations entre les propriétés intrinsèques des quasars et leur polarisation ne sont pas détruites par l'effet d'alignement.

A&A 367, 381–387 (2001)
DOI: 10.1051/0004-6361:20000443
© ESO 2001

Astronomy & Astrophysics

Confirmation of the existence of coherent orientations of quasar polarization vectors on cosmological scales⋆

D. Hutsemékers[1,2,⋆⋆] and H. Lamy[2]

[1] European Southern Observatory, Casilla 19001, Santiago 19, Chile
[2] Institut d'Astrophysique, Université de Liège, 5 Av. de Cointe, 4000 Liège, Belgium

Received 4 September 2000 / Accepted 5 December 2000

Abstract. In order to verify the existence of coherent orientations of quasars polarization vectors on very large scales, we have obtained new polarization measurements for a sample of quasars located in a given region of the three-dimensional Universe where the range of polarization position angles was predicted in advance. For this new sample, the hypothesis of uniform distribution of polarization position angles may be rejected at the 1.8% significance level on the basis of a simple binomial test. This result provides an independent confirmation of the existence of alignments of quasar polarization vectors on very large scales. In total, out of 29 polarized quasars located in this region of the sky, 25 have their polarization vectors coherently oriented. This alignment occurs at redshifts $z \simeq 1{-}2$ suggesting the presence of correlations in objects or fields on Gpc scales. More global statistical tests applied to the whole sample of polarized quasars distributed all over the sky confirm that polarization vectors are coherently oriented in a few groups of 20–30 quasars. Some constraints on the phenomenon are also derived. Considering more particularly the quasars in the selected region of the sky, we found that their polarization vectors are roughly parallel to the plane of the Local Supercluster. But the polarization vectors of objects along the same line of sight at lower redshifts are not accordingly aligned. We also found that the known correlations between quasar intrinsic properties and polarization are not destroyed by the alignment effect. Several possible mechanisms are discussed, but the interpretation of this orientation effect remains puzzling.

Key words. cosmology: large-scale structure of the Universe – quasars: general – polarization

1. Introduction

Considering a sample of 170 optically polarized quasars with accurate polarization measurements, we recently found that quasar polarization vectors are not randomly oriented on the sky as naturally expected. Indeed, in some regions of the three-dimensional Universe (i.e. in regions delimited in right ascension, declination, and redshift), the quasar polarization position angles appear concentrated around preferential directions, suggesting the existence of large-scale coherent orientations – or alignments – of quasar polarization vectors (Hutsemékers 1998, hereafter Paper I).

Mainly because the polarization vectors of objects located along the same line of sight but at different redshifts are not accordingly aligned, possible instrumental bias and contamination by interstellar polarization are unlikely to be responsible for the observed effect (cf. Paper I for a more detailed discussion). The very large scale at which these coherent orientations are seen suggests the presence of correlations in objects or fields on spatial scales $\sim 1000h^{-1}$ Mpc at redshifts $z \simeq 1{-}2$, possibly unveiling a new effect of cosmological importance.

Although we found this orientation effect statistically significant, the sample is not very large, and further investigation is needed to confirm it, especially in view of its very unexpected nature. One of the simplest tests consists in measuring the polarization of a new sample of quasars located in one of the regions of the sky where an alignment was previously found and where we can predict in advance the range of polarization position angles. Such polarimetric observations have been recently carried out, and the results are presented here.

In Sect. 2, we present the new polarimetric observations, as well as a compilation of the most recent measurements from the literature. The results of the statistical analysis – confirming the orientation effect – are given in Sect. 3. Then, from the properties of the objects in the region of alignment we derive some constraints on possible interpretations. These are discussed in Sect. 4. Conclusions form the last section.

⋆ Based in part on observations collected at the European Southern Observatory (ESO, La Silla).
⋆⋆ Also, Chercheur Qualifié au Fonds National de la Recherche Scientifique (FNRS, Belgium).

2. New observations and compilation of data

In Paper I, we identified a region in the sky (region A1) where nearly all quasar polarization position angles lie in the range 146°–46°. This region is delimited in right ascension by $11^{\rm h}15^{\rm m} \leq \alpha \leq 14^{\rm h}29^{\rm m}$ and in redshift by $1.0 \leq z \leq 2.3$.

A new sample of quasars[1] located in this region was therefore selected, mainly from the quasar catalogues of Véron-Cetty & Véron (1998) and Hewitt & Burbidge (1993). This sample was observed during two runs at ESO La Silla in 1998 and 1999, using the ESO 3.6 m telescope equipped with EFOSC2 in its polarimetric mode. In order to minimize the contamination by interstellar polarization in our Galaxy, only objects at high galactic latitudes $|b_{\rm II}| \geq 35°$ were considered. The selection of the targets at the telescope was not random: the brightest objects were given higher priority as well as objects at the center of the alignment region where the orientation effect is suspected to be stronger. Also, radio-loud and broad absorption line (BAL) quasars were preferred since these objects are more likely to be significantly polarized (Impey & Tapia 1990; Hutsemékers et al. 1998; Schmidt & Hines 1999). In this view, 3 BAL quasars recently discovered by Brotherthon et al. (1998) were added to the sample. At the end, polarimetric data were secured for 28 quasars belonging to region A1, with a typical uncertainty of 0.2% on the polarization degree. About half of them appear significantly polarized. These data are presented in Lamy & Hutsemékers (2000) with full account of the observation and reduction details.

In the meantime, two major quasar polarimetric surveys – obviously not restricted to region A1 – have been published by Visvanathan & Wills (1998) and by Schmidt & Hines (1999). Several of their targets are located in region A1, but most of them are unfortunately redundant with ours and generally measured with less accuracy. All these new data have been compiled, also including a few additional measurements we did ourselves in the framework of a polarimetric study of radio-loud BAL quasars (Hutsemékers & Lamy 2000).

The new polarimetric data are summarized in Table 1. They refer to quasars distributed all over the sky, which complement the sample of 170 polarized quasars studied in Paper I. The 43 objects reported in the first part of Table 1 are significantly polarized and fulfil the criteria defined in Paper I: $p \geq 0.6\%$, $\sigma_\theta \leq 14°$, and $|b_{\rm II}| \geq 30°$, where p is the polarization degree and σ_θ the uncertainty of the polarization position angle θ. These constraints ensure that most objects are significantly and intrinsically polarized with little contamination by the Galaxy, and that the polarization position angles are measured with a reasonable accuracy (Paper I). If an object has been observed more than once, only the best value is kept i.e. the measurement with the smallest uncertainty $\sigma_{\rm p}$ on the polarization degree. Let us recall that our previous sample of

[1] All throughout this paper we use "quasar" without any distinction between quasars and quasi-stellar objects (QSOs).

Table 1. The additional sample of polarized quasars

Object (B1950)	$b_{\rm II}$ (°)	z	p (%)	$\sigma_{\rm p}$ (%)	θ (°)	σ_θ (°)	Ref
B0004+017	−59	1.711	1.29	0.28	122	6	8
B0010−002	−61	2.145	1.70	0.77	116	13	8
B0025−018	−64	2.076	1.16	0.52	109	13	8
B0046−315	−86	2.721	13.30	2.00	159	4	7
B0109−014	−64	1.758	1.77	0.35	76	6	8
B0117−180	−79	1.790	1.40	0.46	13	10	8
B0226−104	−62	2.256	2.51	0.25	165	3	8
B0422−380	−45	0.782	6.20	3.00	173	14	7
B0448−392	−40	1.288	2.90	1.00	49	10	7
B0759+651	+32	0.148	1.45	0.14	119	3	8
B0846+156	+33	2.910	0.80	0.21	151	8	9
B0856+172	+36	2.320	0.70	0.24	0	10	9
B0932+501	+47	1.914	1.39	0.16	166	3	8
B1009+023	+44	1.350	0.77	0.19	137	7	9
B1051−007	+50	1.550	1.90	0.19	90	3	9
B1157−239	+37	2.100	1.33	0.17	95	4	9
B1157+014	+61	1.990	0.76	0.18	39	7	9
B1203+155	+74	1.630	1.54	0.20	30	4	9
B1205+146	+74	1.640	0.83	0.18	161	6	9
B1215+127	+73	2.080	0.62	0.24	17	12	9
B1216−010	+61	0.415	6.90	0.80	8	3	7
B1219+127	+74	1.310	0.68	0.20	151	9	9
B1222−016	+60	2.040	0.80	0.22	119	8	9
B1235−182	+44	2.190	1.02	0.18	171	5	9
B1239+099	+72	2.010	0.82	0.18	161	6	9
B1256−220	+41	1.306	5.20	0.80	160	4	7
B1256−175	+45	2.060	0.91	0.19	71	6	9
B1302−102	+52	0.286	1.00	0.40	70	11	7
B1305+001	+62	2.110	0.70	0.22	151	9	9
B1333+286	+80	1.910	5.88	0.20	161	1	9
B1402+436	+68	0.324	7.55	0.22	33	1	8
B1443+016	+52	2.450	1.33	0.23	159	5	9
B1452−217	+33	0.773	12.40	1.50	60	3	7
B1500+084	+54	3.940	1.15	0.33	100	9	9
B1524+517	+52	2.873	2.71	0.34	94	4	8
B1556+335	+50	1.650	1.31	0.47	70	10	8
B2115−305	−44	0.980	3.40	0.40	67	3	7
B2118−430	−45	2.200	0.66	0.20	133	9	9
B2128−123	−41	0.501	1.90	0.40	64	6	7
B2135−147	−43	0.200	1.10	0.40	100	10	7
B2201−185	−51	1.814	1.43	0.51	7	10	8
B2341−235	−74	2.820	0.64	0.20	122	9	9
B2358+022	−58	1.872	2.12	0.51	45	7	8
B0019+011	−61	2.124	0.76	0.19	26	7	8
B0059−275	−88	1.590	1.45	0.23	171	5	9
B0146+017	−58	2.909	1.23	0.21	141	5	8
B0946+301	+50	1.216	0.85	0.14	116	5	8
B1011+091	+49	2.266	1.54	0.23	136	4	8
B1151+117	+69	0.180	0.72	0.18	100	7	9
B1246−057	+57	2.236	1.96	0.18	149	3	8
B1413+117	+65	2.551	2.53	0.29	53	3	8
B2240−370	−61	1.830	2.10	0.19	28	3	9

References: (7) Visvanathan & Wills 1998, (8) Schmidt & Hines 1999, (9) Lamy & Hutsemékers 2000.

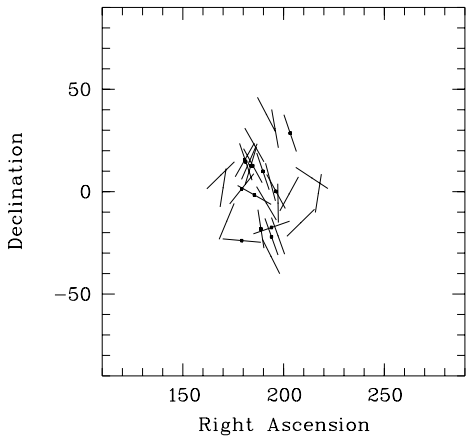


Fig. 1. A map of the polarization vectors of all significantly polarized ($p \geq 0.6\%$ and $\sigma_\theta \leq 14°$) quasars with right ascensions $11^{\rm h}15^{\rm m} \leq \alpha \leq 14^{\rm h}29^{\rm m}$, and redshifts $1.0 \leq z \leq 2.3$. The vector length is arbitrary. The 13 new objects are indicated by additional points

170 objects was similarly selected from 525 measurements compiled from the literature. The second part of Table 1 lists quasars already studied in Paper I, and for which better data (i.e. with a smaller $\sigma_{\rm p}$) have been obtained in the recent surveys. Note that these new measurements are in good agreement with the older ones, as well as measurements obtained by different authors, providing confidence in the quality of the data.

Together with the data from Paper I, the total sample of polarized quasars then amounts to 213 objects distributed all over the sky.

3. Statistical analysis and results

We first want to test the hypothesis that the polarization position angles of quasars located in region A1 preferentially lie in the interval [146°–46°] instead of being uniformly distributed. This angular sector was selected prior to the new observations – on the basis of the results of Paper I–, and the polarization position angles have been measured for a sample of quasars different from that one at the origin of the detection of the effect. Out of the 13 new significantly polarized quasars in region A1 (Table 1), 10 have their polarization position angles in the expected range. To test the null hypothesis H_0 of uniform distribution of circular observations against the alternative of sectoral preference, we may use a simple binomial test (e.g. Lehmacher & Lienert 1980; Siegel 1956). If $P_{\rm A}$ is the probability under H_0 that a polarization position angle falls in the angular sector [146°–46°], then $P_{\rm A} = 80°/180°$. If L denotes the number of polarization position angles falling in [146°–46°], L has a binomial distribution under H_0, such that the probability to have $L_\star$ or more polarization angles in [146°–46°] is

$$P(L \geq L_\star) = \sum_{l=L_\star}^{N} \left(\begin{array}{c} N \\ l \end{array} \right) P_{\rm A}^l \, (1 - P_{\rm A})^{N-l} \, . \qquad (1)$$

With $N = 13$ and $L_\star = 10$, we compute $P(L \geq 10) = 1.8\%$. This indicates that the hypothesis of uniform distribution of polarization position angles may be rejected at the 1.8% significance level in favour of coherent orientation.

A map of the quasar polarization vectors is illustrated in Fig. 1, including the objects from Paper I. An alignment is clearly seen, with a net clustering of polarization vectors around $\theta \sim 165°$–$170°$. Altogether, there are 29 significantly polarized quasars in this region, and 25 of them have their polarization vectors aligned i.e. their polarization position angles in the range 146°–46° (Tables 1 and 2, and Paper I). It is interesting to note that the effect is stable when we increase the polarization degree cutoff (then decreasing the probability of a possible contamination): out of 22 quasars with $p \geq 0.8\%$, 19 have their polarization vectors aligned, and out of 17 quasars with $p \geq 1.0\%$, 16 have their polarization vectors aligned.

Since in total 43 new polarized objects were found all over the sky, it is also interesting to re-run the global statistical tests used in Paper I. These tests are applied to the whole sample of 213 objects. The statistics basically measure the dispersion of polarization position angles for groups of $n_{\rm V}$ neighbours in the 3-dimensional space, the significance being evaluated through Monte-Carlo simulations, shuffling angles over positions. It is not our purpose to repeat here what was done in Paper I, but only to illustrate the trend with the larger sample. The significance levels of the statistical tests, i.e. the probabilities that the test statistics would have been exceeded by chance only, are given in Fig. 2 for the four tests considered in Paper I. Compared to Figs. 9 and 10 of Paper I, all the statistical tests indicate a net decrease of the significance level for the larger sample, strengthening the view that polarization vectors are not randomly distributed over the sky but are coherently oriented in groups of 20–30 objects. We note a shift of the minimum significance level towards slightly higher values of $n_{\rm V}$, as expected from the increase of the number density of the objects.

All these results confirm the existence of orientation effects in the distribution of quasar polarization vectors, and more particularly in the high-redshift region A1 where an independent test was performed.

4. Towards an interpretation

4.1. Observational constraints

First, it is important to note that the observational facts discussed in detail in Paper I and arguing against an instrumental bias and/or a contamination by interstellar polarization in our Galaxy are still valid. They are even

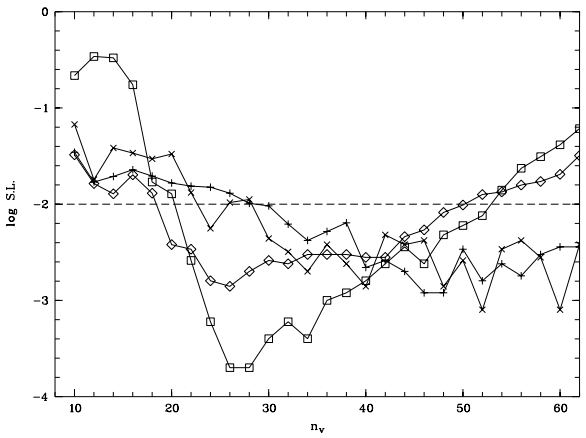


Fig. 2. The logarithmic significance level (S.L.) of the four statistical tests defined in Paper I, S with $\Delta\theta_c = 60°$ (□), S_D(◇), Z_c^m(+), Z_c(×), when applied to the new sample of 213 polarized quasars. n_v is the number of nearest neighbours around each quasar; it is involved in the calculation of averaged quantities. The dashed horizontal line indicates the 1% significance level

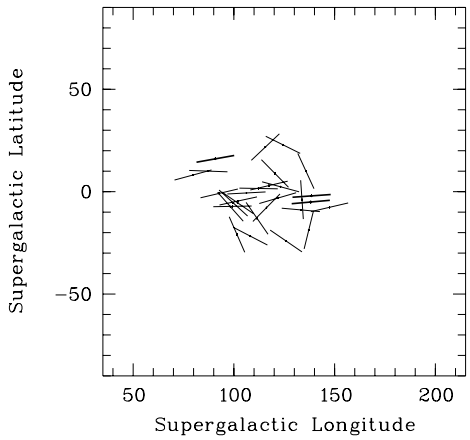


Fig. 3. A map in the supergalactic coordinate system of the polarization vectors of the 29 polarized quasars belonging to region A1. The vector length is arbitrary. Thicker lines refer to objects with $p \geq 5\%$

strengthened since additional objects have been observed, several of them by different authors with different instrumentations. For the new measurements presented here, the polarization of field objects has been measured simultaneously and found to be very small (Lamy & Hutsemékers 2000). The comparison of the quasar polarization position angles with those of neighbouring stars has also been reinvestigated for the new sample. Using the most recent compilation of Heiles (2000), we confirm the absence of correlation between quasar and Galactic star polarization angles, especially in region A1. And finally, the fact that the polarization vectors of quasars on the same line of sight but at lower redshifts are not accordingly aligned certainly remains one of the strongest arguments against artifacts.

Let us now discuss some observational results providing us with possible constraints on the phenomenon. This discussion is mostly based on quasars in region A1.

Looking at Fig. 1, we found – by chance – that the plane of the Local Supercluster (in the direction of its center) roughly passes through the structure formed by the aligned objects. We have then transformed the polarization position angles in the supergalactic coordinate system (de Vaucouleurs et al. 1991) using Eq. (16) of Paper I. A map is illustrated in Fig. 3. It shows a rough alignment of quasar polarization vectors with the supergalactic plane, the effect being more prominent for those objects close to the supergalactic equator. The most polarized objects (with $p \geq 5\%$) do follow the trend. This behavior is very reminiscent of the alignment of Galactic star polarization vectors with the Galactic plane (Mathewson & Ford 1970; Axon & Ellis 1976).

Other constraints come from the relation between quasar intrinsic properties and polarization. In Table 2, we give all quasars in region A1 with good polarization measurements, either polarized ($p \geq 0.6\%$ and $\sigma_\theta \leq 14°$ the latter constraint being equivalent to $p/\sigma_p \simeq 2$), or unpolarized ($p < 0.6\%$ with $\sigma_p \leq 0.3\%$). The quasar type is also given: broad absorption line (BAL), radio-loud non-BAL (RL), radio-quiet non-BAL (RQ), or optically selected non-BAL (O). We may first notice that the quasars with aligned polarization vectors do belong to all types, i.e. radio-quiet/optically selected (3 objects), radio-loud (9), or BAL (13). Note however that significantly polarized radio-quiet non-BAL quasars are definitely less numerous, and that two of them, B1115+080 and B1429−008, are possibly gravitationally lensed. Furthermore, we can see that the known polarization difference between BAL and non-BAL radio-quiet quasars also prevails in region A1 (Fig. 4). A Kolmogorov-Smirnov test gives a probability of only 0.6% that these two samples of are drawn from the same parent population. The illustrated distributions are also in good agreement with those reported by Hutsemékers et al. (1998). In addition, the distribution of p for non-BAL radio-quiet quasars is very similar to that found by Berriman et al. (1991) for the Palomar-Green quasar sample. This clearly indicates that, also in region A1, quasar polarization is related to the intrinsic properties of the objects.

4.2. Discussion

The apparent alignment of quasar polarization vectors with the supergalactic plane is very appealing as the starting point of an explanation, namely since this could decrease by more than one order of magnitude the scale at which a mechanism must act coherently. By analogy with the alignment of stellar polarization vectors with the plane of our Galaxy (Mathewson & Ford 1970; Axon & Ellis 1976), some dichroism could be achieved due to extinction by dust grains aligned in a magnetic field. Another

Table 2. Polarized and unpolarized quasars in region A1

Object (B1950)	z	p (%)	σ_p (%)	θ (°)	σ_θ (°)	Ref	Type
B1115+080	1.722	0.68	0.27	46	12	0	RQ
B1120+019	1.465	1.95	0.27	9	4	0	BAL
B1127−145	1.187	1.26	0.44	23	10	2	RL
B1138−014	1.270	0.38	0.23	53	21	9	BAL
B1138+040	1.876	0.10	0.24	36	-	1	RQ
B1157−239	2.100	1.33	0.17	95	4	9	BAL
B1157+014	1.990	0.76	0.18	39	7	9	RL
B1158+007	1.380	0.44	0.20	74	14	9	RL
B1203+155	1.630	1.54	0.20	30	4	9	BAL
B1205+146	1.640	0.83	0.18	161	6	9	BAL
B1206+459	1.158	0.24	0.17	132	20	1	RQ
B1210+197	1.240	0.33	0.19	76	19	9	RL
B1212+147	1.621	1.45	0.30	24	6	0	BAL
B1215+127	2.080	0.62	0.24	17	12	9	BAL
B1216+110	1.620	0.58	0.19	63	10	9	BAL
B1219+127	1.310	0.68	0.20	151	9	9	BAL
B1222−016	2.040	0.80	0.22	119	8	9	BAL
B1222+146	1.550	0.23	0.18	65	30	9	O
B1222+228	2.046	0.84	0.24	150	8	2	RL
B1225+317	2.200	0.16	0.24	150	-	2	RL
B1228+122	1.410	0.12	0.18	142	-	9	BAL
B1230−237	1.840	0.05	0.19	72	-	9	O
B1230+170	1.420	0.30	0.19	101	22	9	BAL
B1234−021	1.620	0.54	0.18	72	10	9	O
B1235−182	2.190	1.02	0.18	171	5	9	RL
B1238−097	2.090	0.18	0.18	80	-	9	O
B1239+099	2.010	0.82	0.18	161	6	9	BAL
B1239+145	1.950	0.18	0.20	21	-	9	RQ
B1241+176	1.273	0.12	0.19	120	-	1	RL
B1242+001	2.080	0.22	0.19	56	39	9	RQ
B1246−057	2.236	1.96	0.18	149	3	8	BAL
B1246+377	1.241	1.71	0.58	152	10	2	RL
B1247+267	2.038	0.41	0.18	97	12	1	RQ
B1248+401	1.030	0.20	0.19	3	-	1	RQ
B1250+012	1.690	0.21	0.18	132	37	9	BAL
B1254+047	1.024	1.22	0.15	165	3	1	BAL
B1255−316	1.924	2.20	1.00	153	12	4	RL
B1256−220	1.306	5.20	0.80	160	4	7	RL
B1256−175	2.060	0.91	0.19	71	6	9	RL
B1258−164	1.710	0.53	0.18	132	10	9	O
B1303+308	1.770	1.12	0.56	170	14	3	BAL
B1305+001	2.110	0.70	0.22	151	9	9	O
B1309−216	1.491	12.30	0.90	160	2	4	RL
B1309−056	2.212	0.78	0.28	179	11	0	BAL
B1317+277	1.022	0.15	0.20	94	-	2	RQ
B1329+412	1.930	0.36	0.21	83	16	1	RQ
B1331−011	1.867	1.88	0.31	29	5	0	BAL
B1333+286	1.910	5.88	0.20	161	1	9	BAL
B1334+262	1.880	0.23	0.19	116	34	9	BAL
B1338+416	1.219	0.37	0.19	67	15	1	RQ
B1354−152	1.890	1.40	0.50	46	10	4	RL
B1416+067	1.439	0.77	0.39	123	14	2	RL
B1429−008	2.084	1.00	0.29	9	9	0	RQ
B1429−006	1.180	0.07	0.20	107	-	9	BAL

References: (0) Hutsemékers et al. 1998, (1) Berriman et al. 1990, (2) Stockman et al. 1984, (3) Moore & Stockman 1984, (4) Impey & Tapia 1990, (7) Visvanathan & Wills 1998, (8) Schmidt & Hines 1999, (9) Lamy & Hutsemékers 2000.

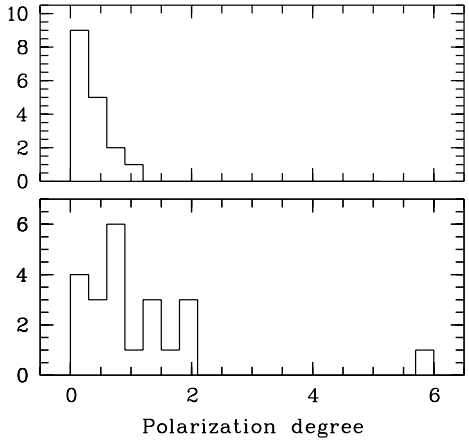


Fig. 4. The distribution of the polarization degree p (in %) for the quasars located in the region of alignment A1 (Table 2). Upper panel: radio-quiet (RQ+O) quasars. Lower panel: BAL quasars

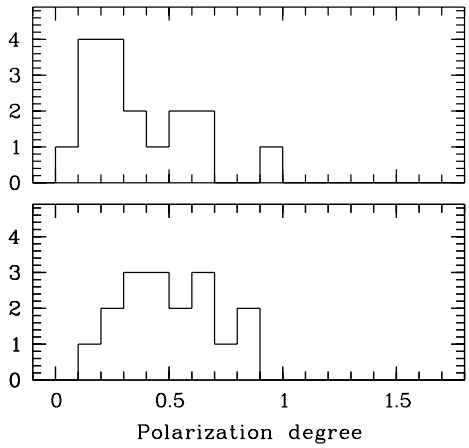


Fig. 5. The distribution of the polarization degree for the radio-quiet (RQ+O) quasars in region A1. The upper panel is an enlargement of that of Fig. 4 and refers to the observed polarization degree p (in %). The so-called polarization bias (due to the fact that p is always a positive quantity) affects the first bin (see also Berriman et al. 1991). The lower panel shows the distribution of the polarization degree after subtraction of a small but systematic polarization ($p_s = 0.25\%$, $\theta_s = 170°$)

possibility could be the conversion of photons into pseudo-scalars also within a magnetic field (Harari & Sikivie 1992; Gnedin & Krasnikov 1992; Gnedin 1994). In both cases the hypothetical magnetic field should be coherent on a ∼50 Mpc scale, which is only slightly larger than the large-scale magnetic field possibly detected by Vallée (1990) in the direction of the Virgo cluster. But this interpretation suffers some drawbacks: namely, it cannot explain why the polarization vectors of quasars at lower redshifts are not accordingly aligned (cf. Fig. 5 in Paper I).

It is therefore difficult to escape the conclusion that if a mechanism is able to produce the alignment of polarization vectors of high-redshift quasars by modifying the polarization state of photons during their travel towards us, this must happen at redshifts $z \gtrsim 1$ (for region A1), or all along the line of sight assuming a cumulative or oscillatory effect (see also discussion in Paper I). Interestingly, an oscillation of quasar polarization with cosmological distance has been predicted as the consequence of the conversion of photons into pseudo-scalars within a large-scale magnetic field permeating the intergalactic medium (Harari & Sikivie 1992; Gnedin & Krasnikov 1992; Gnedin 1994). However, this interpretation, like other mechanisms which affect light as it propagates towards us, cannot easily explain why correlations observed between quasar polarization and intrinsic properties are not washed away.

In this view we may ask ourselves how small could be the systematic polarization which, added to randomly oriented polarization vectors, can be at the origin of an orientation effect which involves nearly all polarized quasars of region A1. To simulate this, we have vectorially subtracted a systematic polarization p_s oriented at $\theta_s = 170°$ (the dominant direction, cf. Fig. 1) from all polarized and unpolarized quasars of region A1 (Table 2). Then we have re-selected a sample of significantly polarized quasars with the conditions $p \geq 0.6\%$ and $\sigma_\theta \leq 14°$. For $p_s = 0.25\%$, 29 quasars fulfil the conditions[2] and only 15 objects out of this new sample have their polarization position angles still in the range 146°–46°. This small systematic polarization seems therefore sufficient to produce the orientation effect, and small enough to preserve the difference between BAL and non-BAL quasars. However, as seen in Fig. 5, even such a small systematic polarization significantly modifies the polarization distribution of non-BAL radio-quiet quasars which appears depleted at polarization degrees $p \lesssim p_s$, and then quite different from the distribution found by Berriman et al. (1991) and Hutsemékers et al. (1998). If we further note that values of p_s higher than 0.25% are obviously needed to explain the alignment of the 16 objects with $p \geq 1.0\%$, we may conclude that it is quite difficult to invoke a systematic additional polarization along the line of sight without modifying the quasar intrinsic polarization properties. This simple test also provides additional evidence that a systematic instrumental effect is unlikely.

Although more subtle and speculative effects modifying the polarization of light along the line of sight can probably be imagined, we may admit on the other hand that the quasars themselves i.e. their structural axes are coherently oriented on Gpc scales. For radio-loud quasars, it is well known that the optical polarization is often parallel to the structural axis of the radio core (Rusk 1990; Impey et al. 1991). Unfortunately, only one polarized quasar in region A1 (B1127−145) is spatially resolved. It is however very interesting to note that this object has a core structure parallel to its polarization vector (Impey & Tapia 1990). In this view it is worth noting that possible coherence of morphological structures from the central engines of active galactic nuclei to superclusters has been suggested by West (1991, 1994), although this observation is apparently not confirmed at the supercluster scale (Jaaniste et al. 1998). From the theoretical point of view, some studies (Reinhardt 1971; Wasserman 1978) have pointed out the possible effects of magnetic fields on galaxy formation and orientation. Extrapolating, a correlation between quasar structural axes could be settled at the epoch of formation and related to very large-scale primordial magnetic fields possibly formed during inflation (Battaner & Florido 2000). Large-scale vorticity is another possibility, at least qualitatively. In this view, the apparent alignment found with the supergalactic plane is puzzling. However, coincidence cannot be ruled out, especially if we note that the polarization vectors of quasars belonging to the other regions of alignments (regions A2 and A3 in Paper I) do not show the same alignment with the plane of the Local Supercluster.

[2] The fact that this modified sample contains 29 objects exactly as the original one is only chance. Several objects are indeed different.

5. Conclusions

In order to verify the existence of very large-scale coherent orientations of quasars polarization vectors, we have obtained new polarization measurements for quasars located in a given region of the sky where the range of polarization position angles was predicted in advance. The statistical analysis of this new sample provides an independent confirmation of the existence of alignments of quasar polarization vectors at high redshifts. In total, out of 29 polarized quasars located in this region, 25 have their polarization vectors coherently oriented. Moreover, global statistical tests applied to the whole sample indicate that, with the increased size of the sample, the detection of the effect is stable and even more significant.

The increased size of the sample also allowed us to put some constraints on the phenomenon. We namely found that the polarization vectors of quasars in region A1 are apparently parallel to the plane of the Local Supercluster, while those of quasars at lower redshifts are not accordingly aligned. Furthermore, we found that the well-known correlations between quasar intrinsic properties and polarization also prevail for those quasars located in that region of alignment.

Mechanisms modifying the polarization somewhere along the line of sight could explain some results, but cannot easily fit all constraints, namely the fact that correlations between quasar intrinsic properties and polarization are not washed away. Another possibility is that the quasar structural axes themselves are coherently oriented. However, given the scales involved, a reasonable physical mechanism is far from obvious. Interestingly, in region A1, nine quasars with aligned polarization vectors are radio-loud, such that this hypothesis could be tested by simply mapping their radio core.

The interpretation of this orientation effect therefore remains puzzling. Nevertheless, the presence of coherent orientations at such large scales seems to indicate the existence of a new interesting effect of cosmological importance.

Acknowledgements. We are grateful to the referee for useful comments. The SIMBAD and NED databases have been consulted namely to classify some quasars in Table 2.

References

Axon, D. J., & Ellis, R. S. 1976, MNRAS, 177, 499
Battaner, E., & Florido, E. 2000, ASP Conf. Ser., 200, 144
Berriman, G., Schmidt, G. D., West, S. C., & Stockman, H. S. 1990, ApJS, 74, 869
Brotherton, M. S., van Breugel, W., Smith, R. J., et al. 1998, ApJ, 505, L7
de Vaucouleurs, G., de Vaucouleurs, A., Corwin, H. G., et al. 1991, Third Reference Catalogue of Bright Galaxies (Springer-Verlag)
Gnedin, Y. N., & Krasnikov, S. V. 1992, Sov. Phys. JETP, 75, 933
Gnedin, Y. N. 1994, Astron. Astrophys. Trans., 5, 163
Harari, D., & Sikivie, P. 1992, Phys. Lett. B, 289, 67
Heiles, C. 2000, AJ, 119, 923
Hewitt, A., & Burbidge, G. 1993, ApJS, 87, 451
Hutsemékers, D. 1998, A&A, 332, 410, Paper I
Hutsemékers, D., Lamy, H., & Remy, M. 1998, A&A, 340, 371
Hutsemékers, D., & Lamy, H. 2000, A&A, 358, 835
Impey, C. D., & Tapia, S. 1990, ApJ, 354, 124
Impey, C. D., Lawrence, C. R., & Tapia, S. 1991, ApJ, 375, 46
Jaaniste, J., Tago, E., Einasto, M., et al. 1998, A&A, 336, 35
Lamy, H., & Hutsemékers, D. 2000, A&AS, 142, 451
Lehmacher, W., & Lienert, G. A. 1980, Biom. J., 22, 249
Mathewson, D. S., & Ford, V. L. 1970, Mem. R. Ast. Soc., 74, 139
Moore, R. L., & Stockman, H. S. 1984, ApJ, 279, 465
Reinhardt, M. 1971, Ap&SS, 10, 363
Rusk, R. 1990, J. R. Astron. Soc. Can., 84, 199
Schmidt, G. D., & Hines, D. C. 1999, ApJ, 512, 125
Siegel, S. 1956, Nonparametric Statistics (McGraw-Hill)
Stockman, H. S., Moore, R. L., & Angel, J. R. P. 1984, ApJ, 279, 485
Vallée, J. P. 1990, AJ, 99, 459
Véron-Cetty, M. P., & Véron, P. 1998, ESO Scientific Report, 18
Visvanathan, N., & Wills, B. J. 1998, AJ, 116, 2119
Wasserman, I. 1978, ApJ, 224, 337
West, M. J. 1991, ASP Conf. Ser., 21, 290
West, M. J. 1994, MNRAS, 268, 79